

N° d'ordre :



# THÈSE

PRÉSENTÉE A

**L'UNIVERSITÉ BORDEAUX 1**

ÉCOLE DOCTORALE DES SCIENCES CHIMIQUES

Par Pinar, BATAT

POUR OBTENIR LE GRADE DE

DOCTEUR  
SPÉCIALITÉ : CHIMIE-PHYSIQUE

## **COMMUNICATION MOLECULAIRE PHOTO-IONIQUE: LES ETUDES ULTRARAPIDES DE COMPOSÉS SUPRAMOLÉCULAIRE**

Directeur de recherche : Dr. Gediminas Jonusauskas, LOMA et Dr. Nathan McClenaghan,  
ISM, Université Bordeaux 1

Soutenue le 24 Octobre 2011

Devant la commission d'examen formée de :

M. CAMPAGNA, Sebastino	Professeur	Rapporteur
M. GADONAS, Roaldas	Professeur	Rapporteur
Mme. FEDOROVA, Olga	Professeur	
M. OBERLE, Jean	Professeur	
M. JONUSAUSKAS, Gediminas	Chargé de Recherche	Directeur de thèse
M. McCLENAGHAN, Nathan	Chargé de Recherche	Directeur de thèse



*To my father-BABAMA-  
I hope you have been seeing this Dr.Batat*



# Acknowledgement

This thesis arose in years of research that has been done since I came to McClenaghan's group. By that time, I have worked with a great number of people whose contributions help me to write this thesis. It is a pleasure to convey my gratitude to them all in my humble acknowledgment.

In the first place I would like to express my gratitude to Dr. Gediminas Jonusauskas for his patience and ability of changing all miserable things to an advantage. This thesis would not have been possible without him. His exceptional scientist insight has inspired me and enriched my growth as a student, a researcher and a scientist. I am indebted to him more than he knows.

I gratefully acknowledge Nathan McClenaghan for his advice, supervision, and crucial contribution, which made him a backbone of this research and so to this thesis.

Many thanks go in particular to Christine Grauby-Heywang and Sophia Selektor to their valuable supervision. I am much indebted to Christine for using her precious times to read the chapter and gave her critical comments about it.

I would like to thank Dr. Martine Cantuel, Dr. Guillaume Vives, Dr. Aurélie Lavie-Cambot Ren-Wei Chang, Aurélien Ducrot and Robin Bofinger for providing many of the samples studied herein and their friendship.

I have been fortunate to come across many good friends, without them life would be bleak. Silvia- my dear neighbor-, Laura and Christine, thanks for being my family in France. I'd like to thank my family including Dilara as well as my friends Neslihan and Zeliha to their unlimited patience, love and support.

This doctoral thesis was financed by a French ministerial grant. Equally, I wish to acknowledge Région Aquitaine and ERC (FP7/2007-2013) "Ideas" program, grant agreement N° 208702. All the work presented in this thesis corresponds to and directly attributed to the objectives of the latter project ("COMMOTION").

Finally, I would like to express my apology everyone that I could not mention personally one by one.



## **Résumé**

Des molécules ou assemblages moléculaires organiques (dérivés d'hémicyanine ou du BODIPY) ont été étudiés en solution par des méthodes optiques complémentaires : absorption stationnaire et fluorescence, absorption transitoire et fluorescence résolue en temps (échelle femtoseconde et picoseconde). Ces méthodes ont permis de caractériser différents processus tels que le transfert de charge intramoléculaire, le transfert d'énergie et le transfert d'électron photoinduit. Elles ont ainsi permis de démontrer l'intérêt de certains chromophores de type AzaBODIPY émettant dans le proche IR, dans des applications d'imagerie et de thérapie photodynamique. La photostabilité et l'absorption à deux photons ont également été étudiées dans le cas d'autres dérivés du BODIPY pouvant être appliqués à la détection d'espèces ioniques. Dans le cas des hémicyanines, des dérivés amphiphiles dotés d'une couronne reconnaissant spécifiquement certains cations ont également été étudiés sous forme de films de Langmuir-Blodgett et en présence de différents cations, le but étant de former des membranes artificielles iono- et photosensibles.

## **Abstract**

Ultrafast femtosecond transient absorption measurements (30 fs FWHM pulses) and complementary picosecond spectroscopies (20 ps FWHM pulses, streak camera detection), as well as steady state absorption and fluorescence measurements, were used to study a range of molecules and molecular assemblies. Processes such as intramolecular charge transfer, electronic energy transfer and photoinduced electron transfer were characterized. Amphiphilic azacrown-containing hemicyanine dyes and resulting iono- and photosensitive artificial membranes were studied using Langmuir-Blodgett techniques in the presence of various cations. Among a range of other molecules studied, NIR emitting aza-BODIPY dyes were studied by time-resolved methods in order to investigate their suitability for Photodynamic Therapy applications and imaging. Differently functionalized BODIPY dyes were investigated with respect to photostability, two photon absorption and ion sensing.



## TABLE OF CONTENT

COMMUNICATION ENTRE MOLECULES PAR DES IONS PHOTOGUIDES .....	1
Acknowledgement.....	5
Introduction .....	13
Chapter 1 .....	15
Background & Theory.....	15
1.1. Transitions between Molecular States .....	15
1.2. Molecular Signal Processing .....	18
1.2.1. Fluorescence ON/OFF switching <sup>13</sup> .....	19
1.2.2. Signal processing by intensity or wavelength changes <sup>28</sup> .....	25
1.3. Cation Recognition Units .....	26
Chapter 2 .....	30
Experimental Methods .....	30
2.1. Steady-state Spectroscopy .....	30
2.1.1. Absorption .....	30
2.1.2. Emission .....	30
2.2. Time-resolved spectroscopy .....	31
2.2.1. Time-resolved fluorescence.....	31
2.2.2. Transient Absorption .....	31
2.3. Resolution of the rate equation.....	34
2.3.1. One level model.....	34
2.3.2. Two level model.....	35
Chapter 3 .....	37
Hemicyanine based artificial membranes .....	37
Introduction .....	37
PART I.....	44
3.1.1. Absorption and Fluorescence Spectra .....	44
3.1.2. Solvent Effects .....	45
3.1.3. Ion Complexation.....	51
3.1.4. Fluorescence Anisotropy <sup>11,10</sup> .....	55
3.1.5 Time-Resolved Study .....	59
Conclusion.....	62
PART II.....	63
3.2.1. Langmuir-Blodgett films (LB films) <sup>95-98</sup> .....	63
3.2.2. Isotherms .....	65
3.2.3. Absorption of LB films.....	68
3.2.4. Fluorescence Emission of LB Films.....	70

3.2.4. Fluorescence Microscopy on LB Films .....	72
3.2.6. Discussion .....	75
Chapter 4 .....	79
Fast Processes in BF <sub>2</sub> -dipyrrromethene (BODIPY) -type dyes.....	79
Introduction .....	79
PART I.....	90
Photophysics of Aza-BODIPYs (BF <sub>2</sub> -Azadipyrrromethenes):NIR Fluorophores and Photodynamic Therapy Agent .....	90
4.1.1. Introduction .....	90
4.1.2. Steady State studies.....	94
4.1.3. Time resolved Fluorescence .....	96
4.1.4. Fluorescence Anisotropy .....	97
4.1.5. Transient Absorption .....	98
4.1.6. Two Photon Absorption.....	107
4.1.7. Photostability.....	109
4.1.8. Conclusion.....	111
PART II.....	112
Photostable fluorescent perfluorophenyl BODIPY .....	112
4.2.1. Introduction .....	112
4.2.2. Structure .....	112
4.2.3. Steady State Absorption and Emission .....	114
4.2.4. Transient Absorption .....	115
4.2.5. Two Photon Absorption.....	116
4.2.6. Photodegradation.....	118
4.2.7. Conclusion.....	118
PART III.....	119
Ultrafast photoinduced electron transfer in BODIPY-BAPTA sensors .....	119
4.3.1. Introduction .....	119
4.3.2. Principles.....	120
4.3.3. Fluorescence Titration with Ca <sup>2+</sup> Analyte .....	122
4.3.4. Transient Absorption .....	124
4.3.5. Discussion .....	133
Chapter 5 .....	135
Photochemionics .....	135
Introduction .....	135
PART I.....	136

BAPTA-Anthracene systems.....	136
5.1.1. Introduction .....	136
5.1.2. Photochemistry of Anthracene.....	136
5.1.3. First Generation (G1) .....	139
5.1.4. Second Generation (G2).....	144
5.1.4. Third Generation (G3).....	149
5.1.5. Hydrolyzed molecules.....	152
5.1.6. Conclusion.....	154
PART II.....	155
Azobenzene-Lariat Ether System .....	155
5.2.1. Introduction .....	155
5.2.2. Steady State Absorption .....	157
5.2.3. Transient Absorption .....	158
5.2.4. Conclusion.....	159
General Conclusion .....	161
APPENDIX.....	165
Calculation of Photodegradation Quantum Yield .....	165
References .....	167



# Introduction

The difficulty in establishing communication between distinct functional molecules is one major obstacle to the development of integrated molecular networks, which are much smaller than currently used solid-state equivalents. Previous attempts to effect communication have been subject to strong constraints: strategies based on magnetic coupling only function at low temperatures or are intramolecular<sup>1</sup>; systems based on the transfer of energy are limited by the energy-wasting downhill nature of the process<sup>2</sup>; long distance electron transfer processes are strongly distance dependent<sup>3</sup> and sequential electron transfer processes are difficult to organize.

In our project, the study and combination of two complementary processes, the photoejection of an ion, “light-in, ion-out”, and ion-induced fluorescence, “ion-in, light-out”, will be harnessed to establish connection between distinct functional molecules. It is important to underline the fact that certain aspects of this functioning are particularly efficient in the human eye and ion-channels, using arrays of large biomolecules<sup>4</sup>. As vision is our busiest information channel, this demonstrates the efficiency that can be achieved by this approach. Separate processes of ion-ejection<sup>5</sup> and ion-detection<sup>6</sup> with artificial systems have been demonstrated with varying degrees of success in terms of efficiency.

During this project, complementary photocontrolled molecules were synthesized (thesis work of Aurélie Lavie Cambot and post-doc work of Guillaume Vives) and their photophysical studies are presented in this dissertation, with particular regard to processes of complexation, photo-decomplexation and fluorescence signalling of ions.

In the first chapter, fundamental aspects of photophysics and photochemistry will be highlighted. Processing signals via electron transfer and internal charge transfer will be discussed and Marcus theory of electron transfer will be summarized in this chapter.

The second chapter presents the experimental techniques and experimental setups that were used in this thesis. A detailed description of the simulation of data is also described. Each of the following chapters has a separate introduction highlighting previous work in detail specific to the individual chapter.

The third chapter discusses the application of amphiphilic azacrown-containing hemicyanine dyes as iono- and photosensitive artificial membranes. The chapter consists of two parts. The first part explains the behaviour of azacrown containing hemicyanine dyes in solution and its complexation with various cations. In the second part, the results obtained using Langmuir-Blodgett (LB) techniques in the presence of various cations are described. The changes of

absorption and emission spectra depending on concentration of metal cations in the subphase and the fluorescence microscopy images will be presented and the conclusions about the LB film structure and photophysical processes in the excited states will be drawn.

In the fourth chapter, BF<sub>2</sub>-dipyromethene (BODIPY) dyes in view of different applications will be reviewed in three parts. In the first part, photophysics of NIR-emitting BF<sub>2</sub>-Azadipyromethenes (Aza-BODIPY) dyes which have potential application in photodynamic therapy and NIR imaging is considered. The second part presents full photophysical characterization and stability of perfluoroBODIPY and iodoBODIPY dyes which may equally be used in fluorescence microscopy. BAPTA, a biocompatible Ca<sup>2+</sup> receptor coupled with BODIPY gives a molecular fluorescent signalling system. Ultrafast processes, notably ion-modulated photoinduced electron transfer in two different conjugates, are described in the third part.

In chapter five, various molecular compounds are considered where light is a stimulus to provoke ion-release. One of these compounds is BAPTA (1,2-bis(o-aminophenoxy)ethane-N,N,N',N'-tetraacetic acid) decorated with two anthracenes where photodimerization is anticipated to lower the calcium binding affinity, which will be introduced in the first part of the chapter. In the second part, an example of a lariat ether-azobenzene system, where ion release is anticipated to be based on the isomerisation of azobenzene is given.

The sixth chapter is the general discussion and conclusions concerning all systems.

# Chapter 1

## Background & Theory

### 1.1. Transitions between Molecular States

A primary light-matter interaction involves absorption of light energy<sup>7</sup>. Following absorption, a transition occurs between two states. The rate of the transition is given by Fermi Golden Rule which is developed from time-dependent perturbation theory. It defines a rate of transition from a single state to a density of states, which can be described as follows:

$$k_{f \leftarrow i} = 2\pi\hbar |V_{fi}|^2 \rho(E_{fi}) \quad (1)$$

where  $\rho(E_{fi})$  is the density of final states at the transition frequency and the modulus term is the perturbation that is driving the transition. The density of states is the total number of states at the energy  $E_{fi}$  that can be accessed by the perturbation. Considering absorption phenomenon, the perturbation is the light. Light is classically defined as a wave which has electric and magnetic fields oscillate orthogonally to each other. In the case of light-matter interaction, if the oscillating frequency of electric field of light is suitable, the perturbation can promote a transition to another quantum state with different electronic charge distribution. In other words, when a photon is absorbed by a system, the system has undergone an electric dipole transition. The amplitude of the oscillations of the electric dipole moment ( $\mu$ ) during an electric dipole transition between initial (i) and final (f) states is proportional to a matrix element, defined by

$$V_{fi} \sim \int \psi_f^* \hat{\mu} \psi_i d\tau \quad (2)$$

This matrix element is usually referred to as the transition dipole moment ( $V_{fi}$ ).

The wavefunction and probability density of a system in a stationary state is given as following:

$$\Psi_1 = \psi_1 e^{-\frac{iE_1 t}{\hbar}} \quad (3)$$

$$\Psi_1 \Psi_1^* = \psi^* \psi \quad (4)$$

The probability density for such a system is independent of time. If a photon-induced transition is in progress, the wavefunction is a mixture of the wavefunctions of two quantum states, having different energies, then the probability density of the system is no longer independent of time but contains terms that oscillate in time with a specific frequency and it is the transition dipole moment that governs the amplitude of the electric dipole moment during

the transition. Moreover if an electronic system is in a state that lies above (in energy) another state, then a transition to the lower energy state can occur with the concomitant emission of a photon that has a frequency equivalent to the energy difference between the two states. If the lower state is the ground state of the system then no further photon emission is possible because there is no state of lower energy with which to mix and to generate the required oscillatory perturbation. However when the ground state finds itself in the presence of a photon of matching frequency, the perturbing field can induce the necessary oscillations, causing the mix to occur, one result of which is the promotion of the system to the upper energy state and the annihilation of the photon. The process in which a lower energy state interacts with a photon to create a higher energy state with annihilation of the photon is termed stimulated absorption (usually simply absorption). The process in which an upper state creates a photon and in doing so populates a lower-lying state is termed spontaneous emission.

A photon with a frequency of  $\nu=(E_f-E_i)/h$  can provide the perturbation to induce lower state to generate a higher state, so a second photon of the same frequency can induce mixing of higher and lower states and is accompanied by the creation of a photon. This process is called stimulated emission and it is the inverse of stimulated absorption.

Fermi's golden rule provides a microscopic expression for the rate at which energy is absorbed from a beam of light. The Beer-Lambert law explains the attenuation of the light beam with a macroscopic expression, which is described below:

If a monochromatic beam of the light of intensity  $I_i$  is incident normally on a sample of thickness  $l$ , containing  $N$  molecules per litre absorbing the intensity of beam emerging the sample is  $I_{abs}$ .

$$I_{abs} = I_i e^{-\sigma.N.l} = I_i e^{-\mu.l} \quad (5)$$

$\sigma$  is defined as molecular absorption cross section,  $\mu$  is the absorption coefficient.

These parameters are commonly expressed in terms of molar extinction coefficient ( $\epsilon$ ), defined as:

$$I_{abs} = I_i 10^{-\epsilon.c.l} \quad (6)$$

The total energy of a molecule in its ground state is the sum of three components: Electronic ( $E_e$ ), vibrational ( $E_v$ ) and rotational ( $E_r$ ) energy<sup>8</sup>. Transitions involving  $E_v$  and  $E_r$  yield the vibrational and rotational absorption spectrum, which occurs in the infrared region. Transitions involving  $E_e$  yield the electronic absorption spectrum, which occurs in the visible, ultraviolet and near IR region. Since the total energy of ground and excited state has been

described as the sum of  $E_c+E_v+E_r$ , the wave function of a state can be expressed as the product of electronic ( $\Theta$ ) and nuclear ( $\Phi$ ) (vibrational and rotational) wave functions.

$$\psi = \Theta \cdot \Phi \quad (7)$$

This is the Born-Oppenheimer (BO) approximation, which also states that the rate of change of nuclear wavefunctions as the nuclear positions change is much smaller than the change in electronic wavefunctions<sup>9</sup>. It should be considered that nuclear motion occurs more slowly than the electronic motion, because the nuclei have higher mass than electrons.

The potential energy diagram of a molecule plots the total energy of the molecule as a function of the nuclear separation  $r$  and the wavefunction of  $\Psi$  approximate to those of the harmonic oscillator.

The Franck-Condon principle states that, because the time required for an electronic transition is negligible compared with that of the nuclear motion, the most probable transition is one which involves no changes in the nuclear coordinates. The transitions between two states are vertical. If we examine the nuclear wavefunctions for the ground and excited states, the overlap of wavefunctions between these two states will determine the intensity of the transition. After electronic transition, the excited state then adjusts its equilibrium electronic structure which can be different from ground state electronic structure.

Once the molecule is excited by absorption of a photon, it can return to the ground state following many possible deexcitation pathways<sup>10</sup>.

Relaxation of singlet excited state to ground state (singlet) accompanied by photon emission is called fluorescence. Fluorescence emission occurs from the lowest vibrational state to ground state. This is known as the Kasha rule which states that the emission occurs with noticeable yield only from the lowest excited state and is irrespective to the excitation wavelength<sup>11</sup>.

Fluorescence is a good analytical tool to obtain information about molecules and materials<sup>10</sup>. The parameters which can be obtained directly from the fluorescence emission such as emission wavelength shifts according to solvent, quantum yield and photostability gives information about the chemical and electronic structure. Fluorescence measurements of a system also give indirect information about the systems. For example some fluorescent probes attached to biological molecules like proteins give information about their conformation, while fluorescent probes attached to some molecular systems which can coordinate ions can be used as chemical detecting and signalling units.

Phosphorescence, which is another deexcitation pathway of an excited molecule, is defined as the emission due to transition between electronic states with different multiplicities. For molecules the ground state is a singlet state and the lowest excited state is a triplet state<sup>10</sup>.

If the excited molecule relaxes through another state with same multiplicity without emission, this process is called internal conversion. In internal conversion process the energy of the excited state is dissipated as heat (vibrations) to the environment.

The radiationless transition between states with different multiplicities is called intersystem crossing (ISC). ISC is forbidden but spin-orbit coupling between the orbital magnetic moment and the spin magnetic moment can be large enough to make it possible<sup>9</sup>.

In addition to the aforementioned processes such as conformational changes, energy transfer, excimer or exciplex formation, electron transfer, proton transfer and photochemical reactions involving chemical bond breaking or formation are also major photophysical and photochemical reactions which can occur under some special circumstances when molecules are in an excited state<sup>10</sup>.

## *1.2. Molecular Signal Processing*

In human sensing, receptors transduce chemical, electrical, mechanical and thermal stimulations into nerve impulses<sup>12</sup>. This process consists of many steps and each step takes place on a molecular level. Output signals of one step are input signals for another. Conceptually, similar procedures exist also in computers for data processing using electronic logic circuits. Nano-scaled logic circuits are made of sequences of molecular switches<sup>12</sup>. Artificial systems are able to in this way reproduce to some extent the functions of detecting and transmitting signals at the molecular level. Their development requires first of all a fundamental understanding of the behaviour of individual molecules in response to environmental stimulations.

In the scope of this thesis, different molecular systems will be presented, which have the functions of detecting or transmitting optical signals and may prove to be components of molecular logic circuits. As detailed above, the fluorescence emission is an ideal tool to get direct or indirect information about system.

The environmental changes on molecular systems cause changes of the fluorescence emission. This will allow us to use fluorescent molecules, principally supermolecules with fluorophores as signal processors. Not only the absence or presence of fluorescence can be used as signals but also the changes in intensity and quantum yield or the changes in emission wavelength or lifetime can be used as signals.

### 1.2.1. Fluorescence ON/OFF switching<sup>13</sup>

The advantage of fluorescence ON-OFF switching of molecular systems allows applications such as sensors and switches. They can be examined in two cases. In the first case, upon the excitation of the fluorophore, an electron is promoted to LUMO level. Subsequently, an electron is transferred from the HOMO level of the recognition unit to the now singly occupied HOMO level of fluorophore, which causes the quenching of fluorescence. Upon cation binding, the oxidation potential of the donor is changed so the relevant HOMO becomes lower in energy than HOMO level of the fluorophore. PET is no longer thermodynamically possible and fluorescence quenching is suppressed. In other words, fluorescence intensity is enhanced upon cation binding (Fig.1.1).

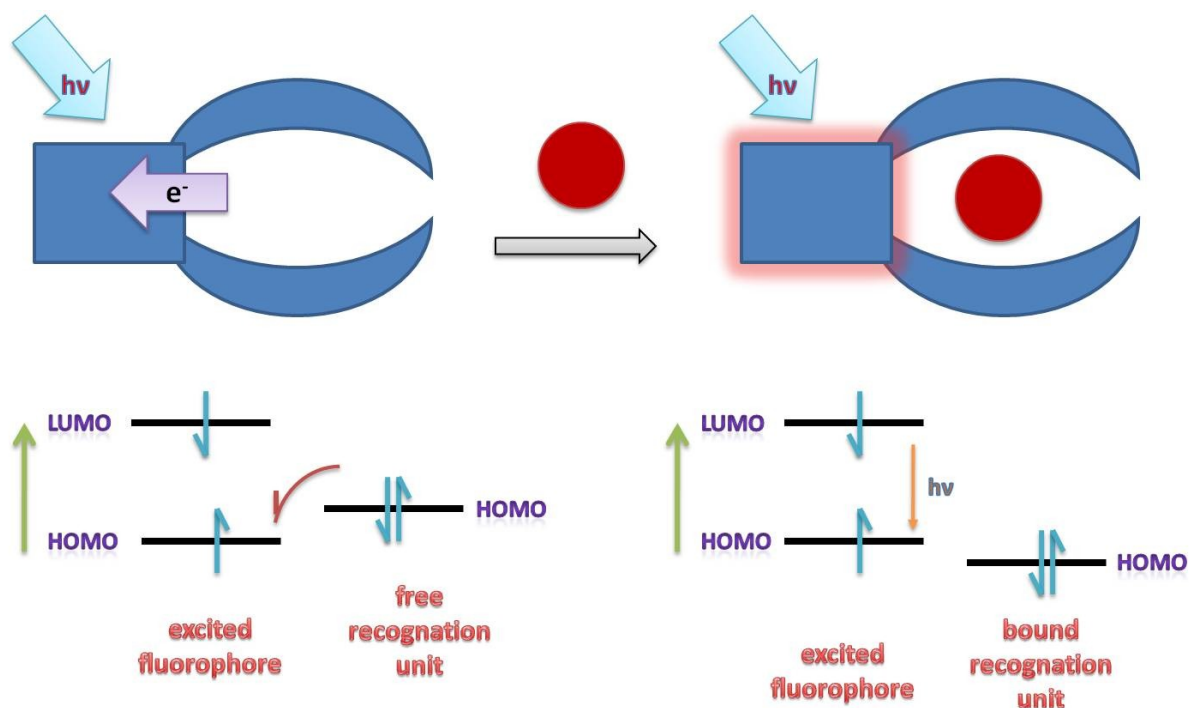


**Fig.1.1:** The mechanism of OFF/ON signalling of PET sensors (square block: fluorophore, hollow circle: receptor and red sphere: ion).

Fig.1.2 presents some examples of OFF/ON PET sensors. Compound **1**<sup>14</sup> is an early example which shows an increase in fluorescence intensity in the presence of  $\text{Ca}^{2+}$ . Compound **2** was developed in Valeur's laboratory and it responds to many different metal ions<sup>15,16</sup>. Compound **3**<sup>17</sup> is also a good guest binding fluorophore which is sensitive to  $\text{K}^+$  and  $\text{Ca}^{2+}$ . Compound **4**<sup>18</sup> and **5**<sup>19</sup> can give signals in the presence of  $\text{Zn}^{2+}$  and mostly be used in peptide research. All compounds lead a large fluorescence enhancement with  $\text{H}^+$  due to the incorporation nitrogen atoms.

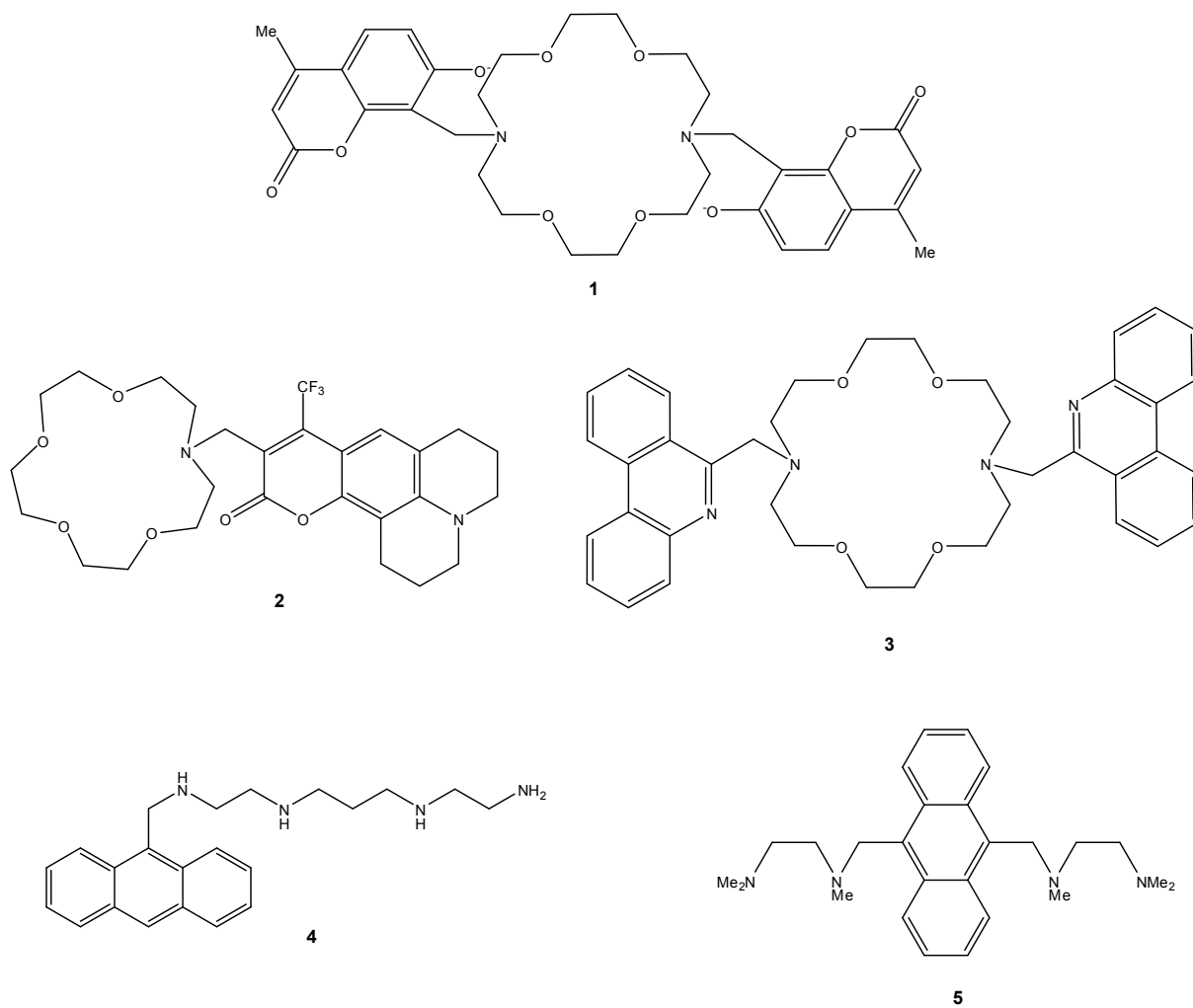


**Fig.1.2:** The chemical structures of some examples of OFF/ON PET sensors.

In the second case, the molecular system is fluorescent in the beginning. When recognition unit binds cation, the system becomes non-fluorescent due to electron transfer (Fig.1.3).

In this case, when the recognition unit bind a guest which can be a cation, a molecule, protons, etc., the electron transfer ability of the system can be increased by involving PET ability of the guest. Electron transfer direction can be towards or away from the guest depending on the redox potential of guest relative to redox potential of fluorophore<sup>6</sup>.

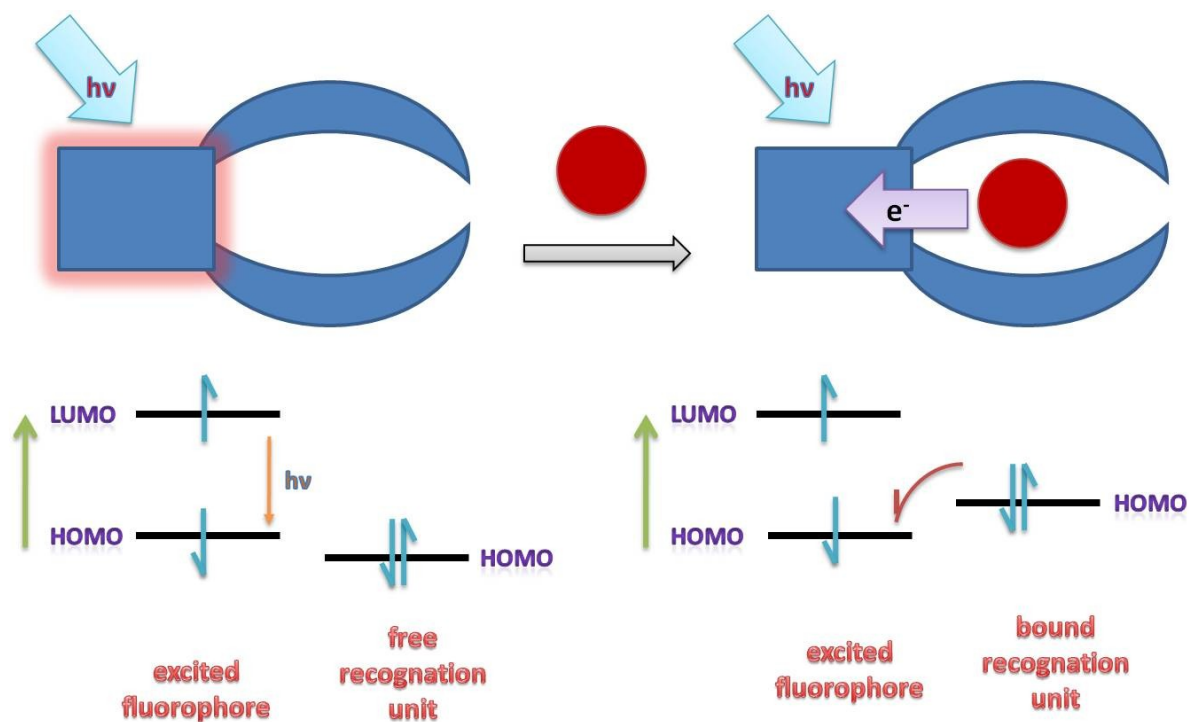


**Fig.1.3:** The mechanism of ON/OFF signalling of PET sensors.

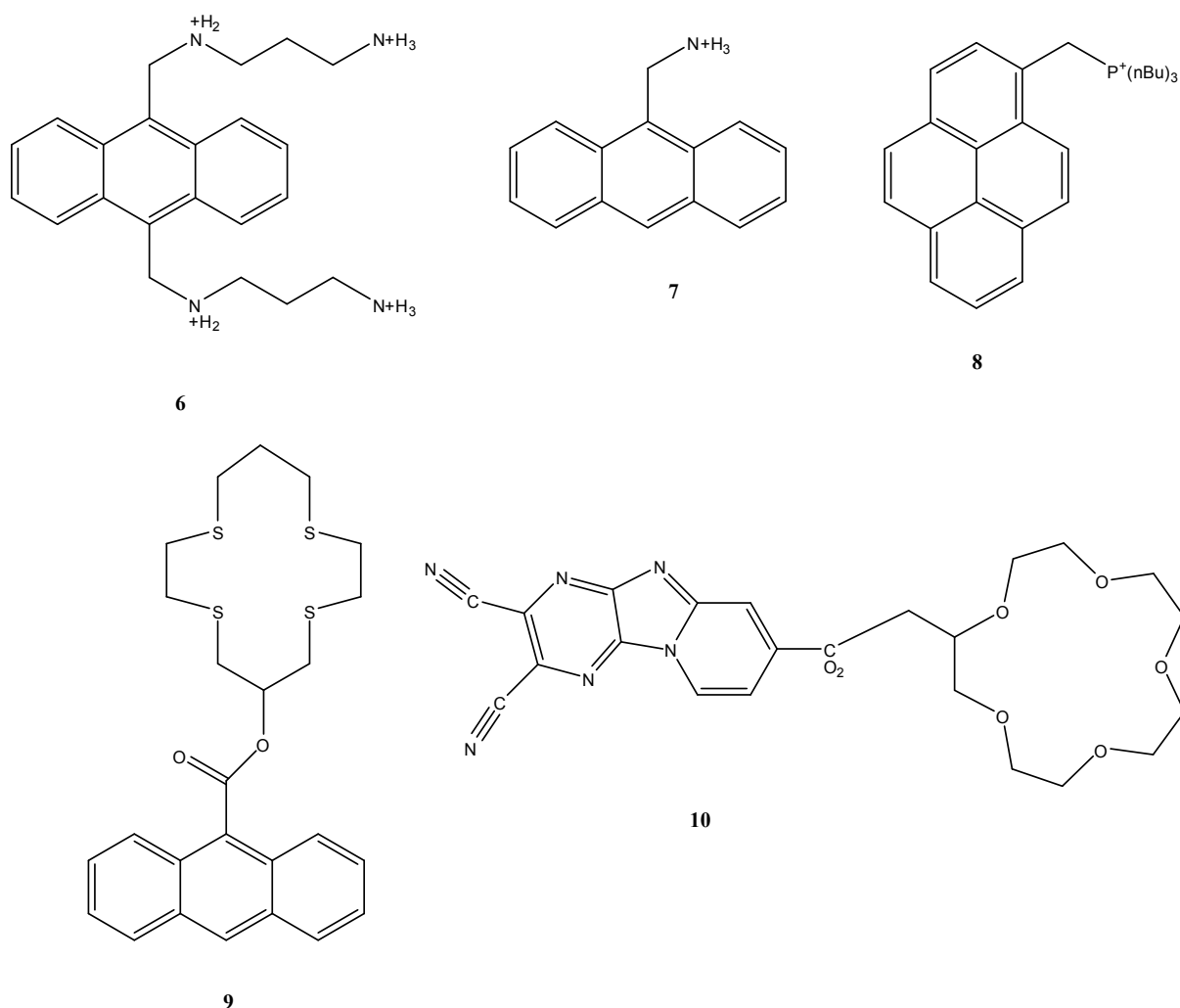


**Fig.1.4:** The chemical structures of some examples of ON/OFF PET sensors.

Compound **6**<sup>20</sup> and **7**<sup>21</sup> shown in Fig.1.4 are anthrylmethylammonium systems which lead ON/OFF signaling when they interact with DNA. Compound **8**<sup>22</sup> shows fluorescence quenching following binding with guanine-rich single stranded polynucleotides. Compound **9**<sup>23</sup> can both bind  $\text{Cu}^+$  and  $\text{Cu}^{2+}$  metal cations. The  $d^{10}$  electron configuration prevents PET process and **9**. $\text{Cu}^+$  is strongly emissive.  $d^9$  configuration triggers a demonstrable PET process and **9**. $\text{Cu}^{2+}$  shows zero fluorescence. Compound **10**<sup>24</sup> can fit two different receptors targeting  $\text{Ba}^{2+}$  and  $\text{SCN}^-$ . Switching OFF of the fluorescence is only achieved when both of the ion concentrations are of a sufficient level. This allows using **10** as a logic gate.

## Electron Transfer

Electron transfer is one of the basic phenomenon governing the metabolism and information transfer in living organisms, e.g. respiration (the way of humans and animals can get energy from food and oxygen), photosynthesis (the way of plants can make food), etc. Many examples of electron transfer can be found in chemistry and biochemistry<sup>7</sup>. In Fig.1.5, the energy potential for chemical reaction is shown. Y-axis is the energy and the x-axis is the reaction coordinate. Electron transfer can be defined as the crossing from the well of the reactants' potential energy surface (D, A: D is the electron donor and A is the electron acceptor) to the well of the products' potential energy surface.

According to the classical model, the transition between the donor D and acceptor A occurs assuming the horizontal Franck-Condon principle which is the nuclear configuration of the reactant and product is the same at the point of the transition state and the internal energy is conserved<sup>25</sup>. In semi-classical theory, this Franck-Condon principle is modified<sup>25, 26</sup>. The transfer of an electron between two species is essentially an instantaneous event compared to the slower nuclear motions which must take place in order to accommodate the "new" electronic configuration in the surrounding inner coordination shells. Nuclear changes occur prior to electron transfer and are made possible because of collision between reactants and surrounding molecules. Before the transfer of an electron, the nuclear geometry of the reactants, including the surrounding solvent molecules, must be converted into a high energy, nonequilibrium or distorted configuration.

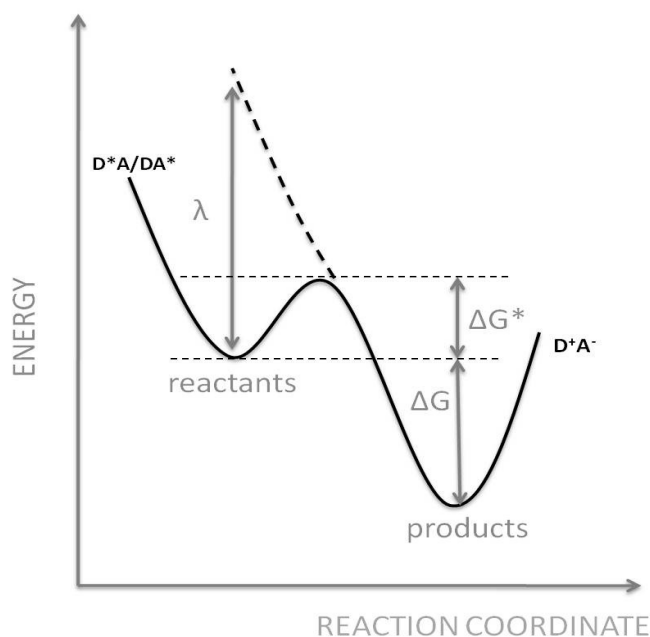


**Fig.1.5:** The potential energy surface description of electron transfer.

The parameters shown in the diagram are:  $\lambda$ , the reorganization energy, which represents the change in free energy if the reactant was distorted to the equilibrium configuration of the product without transferring the electron;  $\Delta G$  which is the difference in free energy between the equilibrium configurations of the reactant and product states (the driving force) and  $\Delta G^*$  which corresponds to the free energy of activation.

The rate constant for the reaction is:

$$k \sim e^{\frac{-\Delta G^*}{k_B T}} \quad (8)$$

Marcus developed an analysis of the electron transfer process based on parabolic surfaces to relate the electron transfer rate to the free energy of activation, described by the following relationship<sup>27</sup>:

$$\Delta G^* = \frac{(\Delta G + \lambda)^2}{4\lambda} \quad (9)$$

$$k_{ET} = A e^{-\frac{(\Delta G + \lambda)^2}{4\lambda RT}} \quad (10)$$

Here A is often expressed as an exponential term itself, dependent on distance  $r$  between the molecule or group which donates electron and the one which accepts the electron.

$$k_{ET} = C e^{-\beta r} e^{-\frac{(\Delta G + \lambda)^2}{4\lambda RT}} \quad (11)$$

C is a constant and  $\beta$  is a constant which depends on what is between the donor and the acceptor. Electrons travel through some materials more easily,  $\beta$  reflects this situation.

Here,  $\lambda$  the so called reorganization energy is composed of solvation ( $\lambda_0$ ) and vibrational ( $\lambda_i$ ) components:

$$\lambda = \lambda_0 + \lambda_i \quad (12)$$

In the solvation component, the ionic radii of reactants ( $a_1, a_2$ ), their centre-to-centre distance ( $R$ ), the optical ( $D_{op}$ ) and static ( $D_s$ ) dielectric constants of solvent and the amount of the charge transferred from one reactant to another are taken into account.

$$\lambda_0 = (\Delta e)^2 \left( \frac{1}{2a_1} + \frac{1}{2a_2} - \frac{1}{R} \right) \left( \frac{1}{D_{op}} - \frac{1}{D_s} \right) \quad (13)$$

The vibrational term is simplified by symmetrization approximation between the normal mode coordinates ( $Q_{i,j}$ ) and the reduced force constants of reactants.

$$\lambda_i = \frac{1}{2} \sum_j k_j (Q_i - Q_j)^2 \quad (14)$$

Equation 9 explains the relationship between the free energy of activation and driving force of electron transfer. The consequence of this explanation is that the electron transfer rate ( $k_{ET}$ ) should increase until a certain value of  $\Delta G$  is reached where the rate begins to fall again. The range of free energy values where the rate increases with increasing driving force is known as the “normal” region. The negative free energy values where the rate is predicted to diminish is described as the “inverted” region (Fig.1.6)<sup>26</sup>.

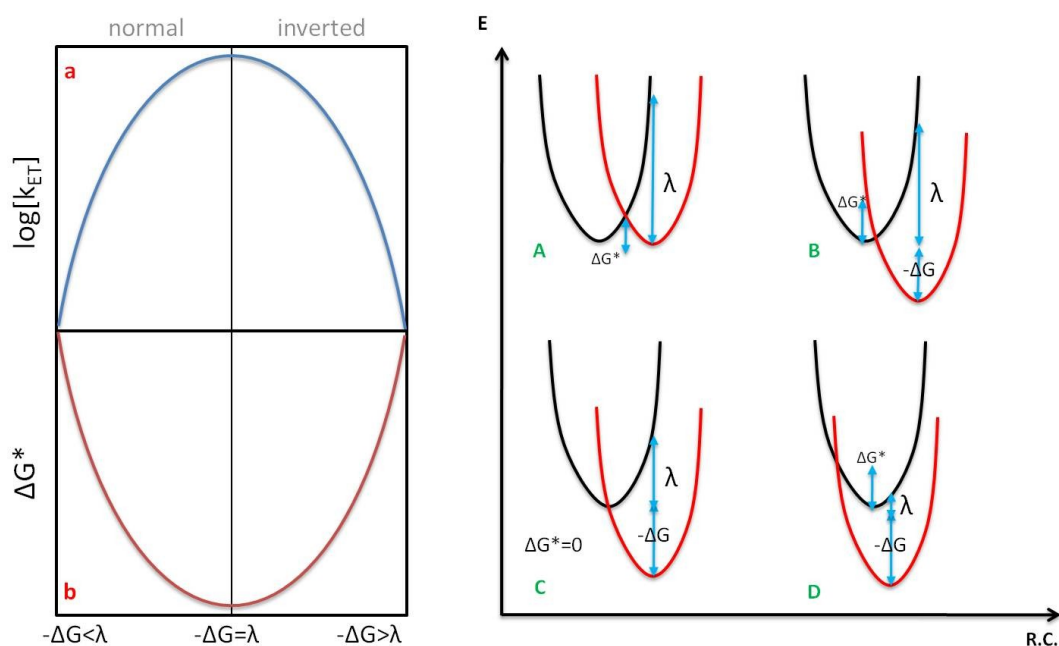


**Fig.1.6:** (left) The relationship between **a)**  $\log [k_{ET}]$  and  $\Delta G$  and **b)**  $\Delta G$  and  $\Delta G^*$ ; (right) Energy surfaces for the reactant state (black) and the product state (red): **A)**  $\Delta G=0$ , **B)** normal regime  $-\Delta G < \lambda$ , **C)** barrierless condition  $-\Delta G = \lambda$ , **D)** inverted regime  $-\Delta G > \lambda$ .

The relationship between  $\Delta G$  and  $\lambda$  results in four different situations (Fig.1.6 right). The disposition of potential energy curves for electron transfer when  $\Delta G = 0$  (self exchange) is illustrated in Fig.1.6A. An example of the normal region, where  $-\Delta G \leq \lambda$ , is shown in Fig.1.6B. From Fig.1.6C, we can see the situation of maximum overlap between potential

energy curves, which is called the barrierless condition ( $-\Delta G = \lambda$ ). The barrierless situation will exhibit the fastest kinetics since the ground state of the products is at the transition state. In the inverted region, as the free energy proceeds to more negative values, the activation energy begins to increase which is shown in Fig.1.6D ( $-\Delta G > \lambda$ ).<sup>25</sup>

### 1.2.2. Signal processing by intensity or wavelength changes<sup>28</sup>

When a molecular system contains an electron donor (D) group conjugated with an electron withdrawing, acceptor (A) group, intramolecular charge transfer occurs from D to A upon excitation by light, known as photoinduced charge transfer (PCT). This charge transfer causes a change of dipole moment of the molecules which produces changes in the Stokes shift that depends on the environment changes such as polarity and polarizability. Absorption and fluorescence spectra can shift with the effect of cation binding.

When the electron donor group (D) of the fluorophore interacts with a cation, the electron donating property reduces as a result of less available electron density for the charge transfer. This causes a blue shift on the absorption spectrum (Fig.1.7).

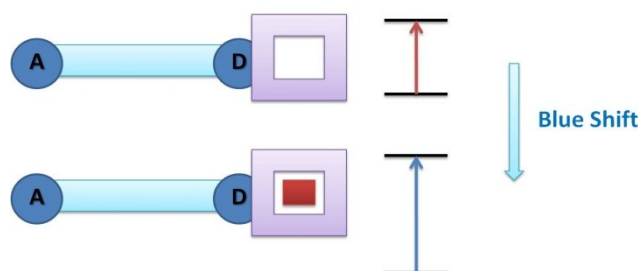


**Fig.1.7:** Spectral displacements of PCT sensors resulting from interaction of a bound cation with an electron donating group (purple hollow square: receptor, red square: ion, light blue part: fluorophore).

If the acceptor group (A) of the fluorophore interacts with the cation, this increases the electron withdrawing property. As a result, the absorption spectrum shifts to the red (Fig.1.8).

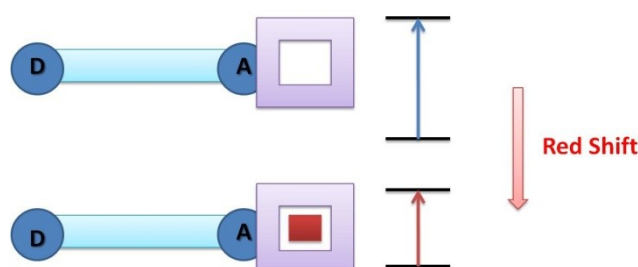


**Fig.1.8:** Spectral displacements of PCT sensors resulting from interaction of a bound cation with an electron withdrawing group (purple hollow square: receptor, red square: ion, light blue part: fluorophore).

This wavelength shift in absorption and fluorescence spectra by cation binding can be used in different applications such as logic gates. Choosing appropriate excitation and observation wavelengths, quite large changes in fluorescence intensity can be often observed<sup>29</sup>.

### 1.3. Cation Recognition Units

As a recognition unit, BAPTA (1,2-bis(o-aminophenoxy)ethane-N,N,N',N'-tetraacetic acid) is a highly selective  $\text{Ca}^{2+}$  chelator, possessing 6 possible protonation sites. It can be seen as a derivative of EGTA (ethylene glycol tetraacetic acid) in which benzene rings replace the methylene groups connecting N to O with little effect on the overall geometry of the molecule (Fig.1.9). Therefore the cavity should offer the same desirable size and shape as EGTA but with the nitrogen  $\text{pK}_a$ s lowered from 8 or 9 down to 5 or 6, making protonation less favourable in physiologic conditions. As the affinity of BAPTA to  $\text{Ca}^{2+}$  is insensitive to pH in non-acid media, it is more suitable for spectrometric studies<sup>30</sup>.

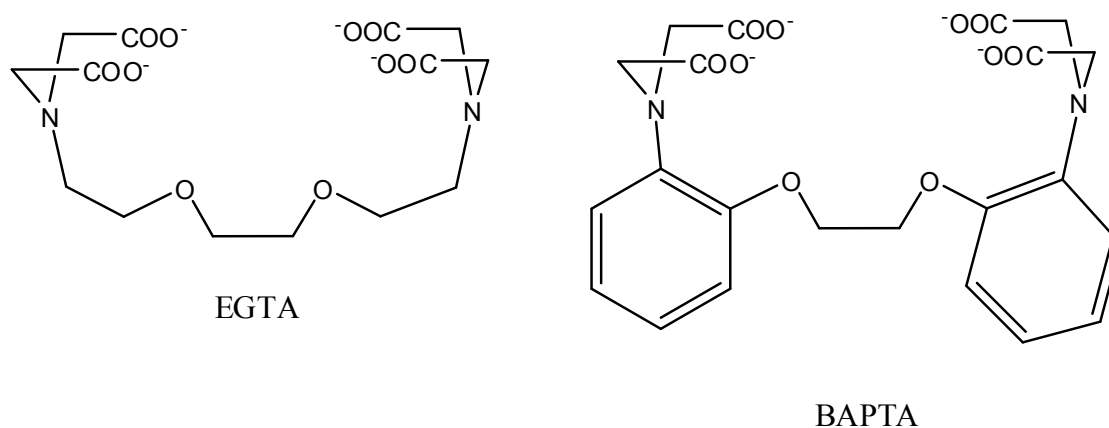


**Fig.1.9:** Structures of EGTA and BAPTA

BAPTA extinction coefficients are  $16000 \text{ cm}^{-1} \text{ M}^{-1}$  (254 nm) and  $5600 \text{ cm}^{-1} \text{ M}^{-1}$  (287 nm), while the extinction coefficient for the  $\text{Ca}^{2+}$  complex is  $4200 \text{ cm}^{-1} \text{ M}^{-1}$  (274 nm)<sup>30,31</sup>. In the former, with no special constraint on the conformation of the molecule, the normal tendency of aromatic amine lone pairs to conjugate with rings would assert itself, so that the spectrum of an ordinary dialkylaniline or anisidine would be observed. However, in the presence of  $\text{Ca}^{2+}$  cation the nitrogens, their attached acetate groups, and the ether oxygens envelop and chelate the  $\text{Ca}^{2+}$  cation, which means in the nitrogen-ring bonds twisting by nearly  $90^\circ$ , thus breaking the conjugation with the rings, giving a spectrum of a simple anisole or benzene<sup>30,32</sup>. In addition, the affinity for  $\text{Ca}^{2+}$  can be altered by aromatic ring substitution with electron withdrawing or donating groups due to their conjugation to the binding site (amine nitrogen). On the other hand this opens the door for the determination of  $\text{Ca}^{2+}$  concentration, when



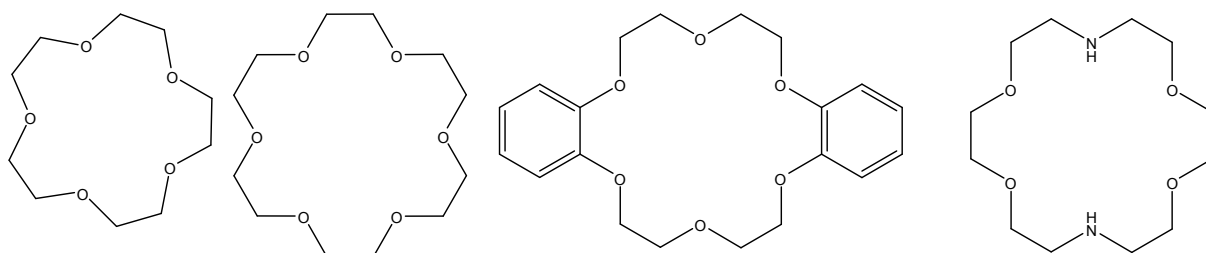


**Fig.1.11:** Structures of some crown ethers.

The main characteristic of crown ethers is the ability of the ether oxygens to complex with various ionic species. Aza-analogues of crown ethers, called azacrowns, have a nitrogen atom which is also capable to complex cations. Fig.1.12 presents azacrowns conjugated with different electron-withdrawing groups<sup>28</sup>.

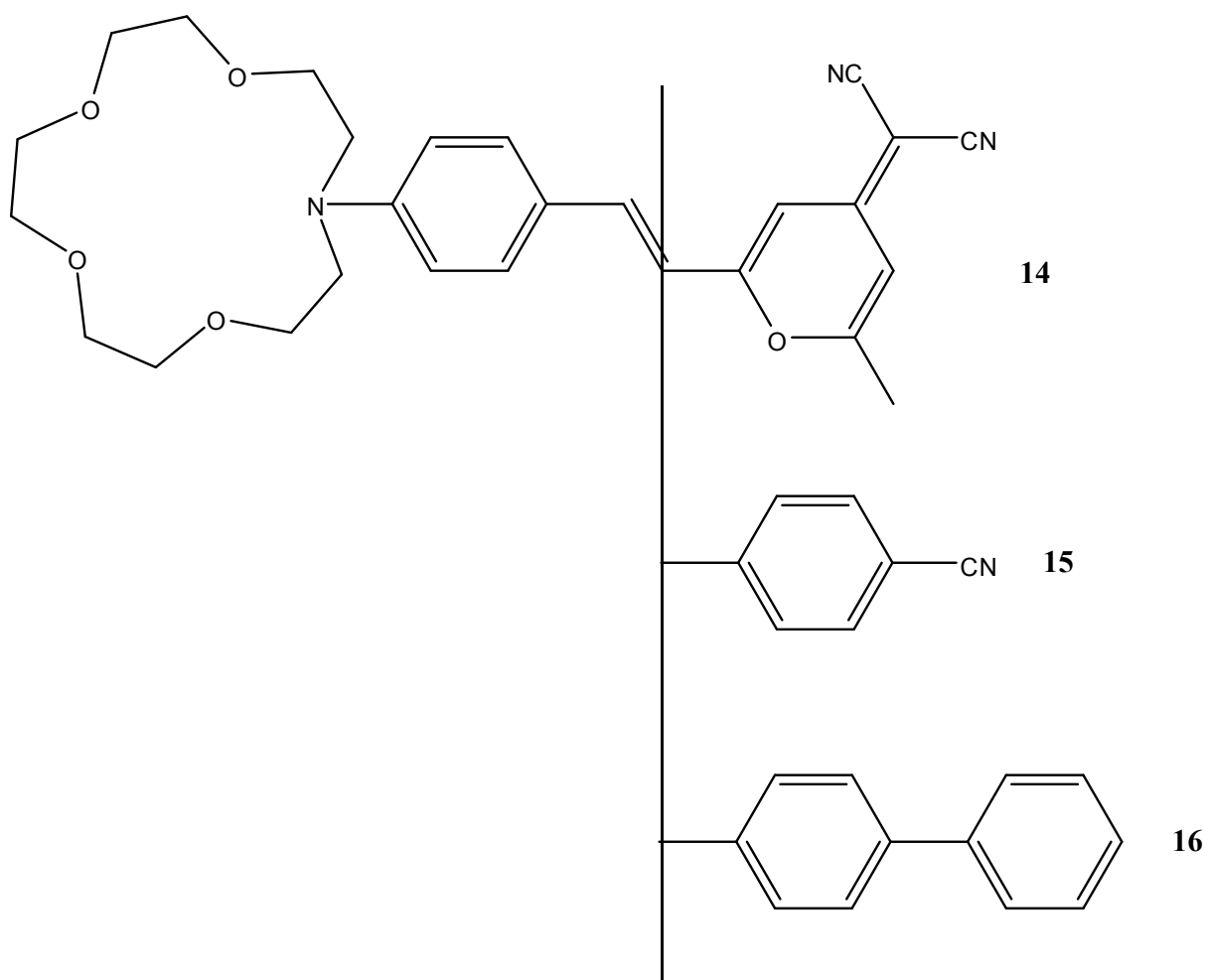


**Fig.1.12:** Chemical structures of some azacrown containing compounds.

The general behaviour of these molecules is a complexation-induced blue shift in absorption and emission spectra. The maxima of the absorption band for free **14**<sup>34</sup>, **15**<sup>35</sup> and **16**<sup>36</sup> are at 494, 392 and 372 nm, respectively. In the presence of calcium the maxima are shifted to 398, 330 and 332 nm. Meanwhile, fluorescence spectra do not show such big shifts in the case of complexation with calcium. The emission maxima for **14**, **15** and **16** are at 621, 525 and 483

nm. The maxima for complexes of **14**, **15** and **16** are at 608, 503 and 469 nm. Following the photoinduced charge transfer, the electron density on N atom of the azacrown is reduced, which causes the decoordination of cation. Subpicosecond experiments showed evidence of this decoordination. The rate of disruption of the link between **14** and calcium is found 30 ps<sup>37</sup>, for **15** it is 3 ps<sup>38</sup> and for **16** it is 20 ps.<sup>39</sup>

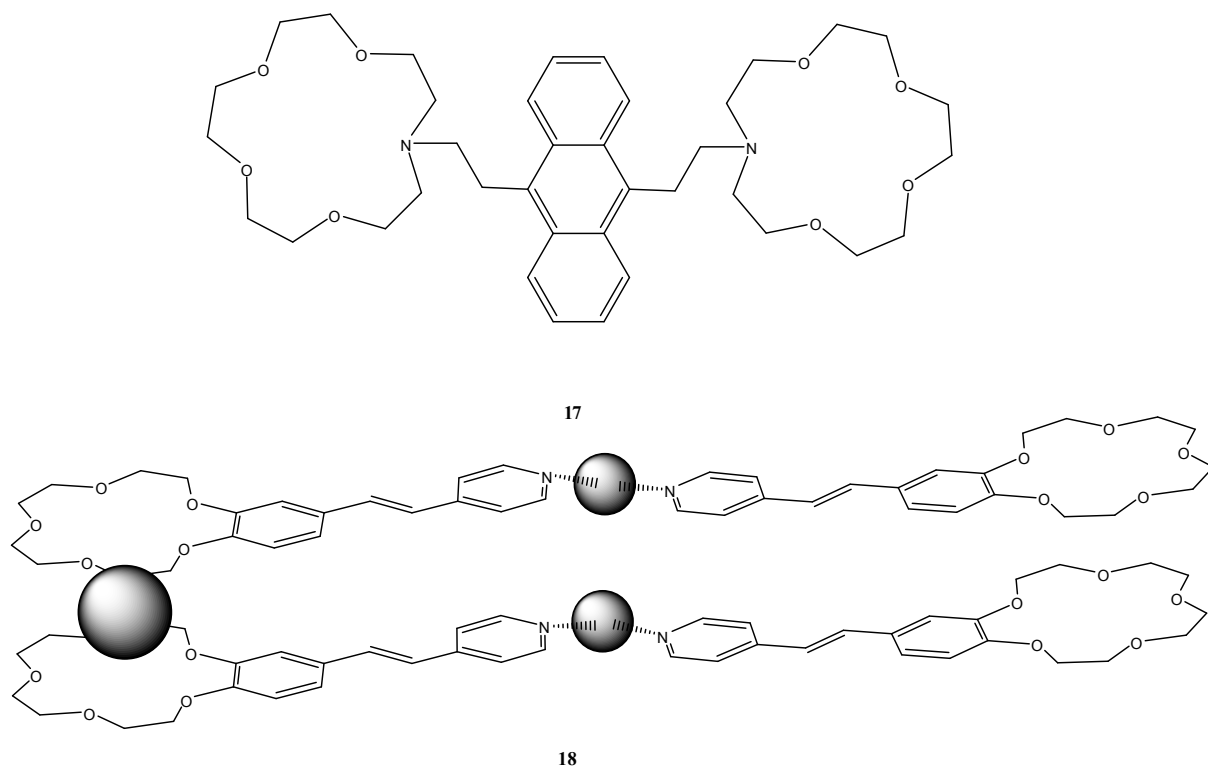


**Fig.1.13:** Some crown-containing cation sharing molecules.

Crown-containing systems can share one cation between two molecules. These kinds of complexes are called sandwich complexes<sup>40</sup>. Fig.1.13 shows molecules which make sandwich complexes in the presence of cation. The molecular system **18** exhibits a “play catch” phenomenon (intramolecular cation sharing) with mercury cation<sup>41</sup>.

In the following chapters, molecular systems based on chelators (BAPTA) and coronands (Azacrownether, lariat ether) will be considered. These systems have many potential applications due to their selective cation sensing properties. By adding a fluorophore, they can be used as subunits for more complex systems used in molecular electronics, artificial membranes, labels etc. The development in this area is limited only by the imagination.

## Chapter 2

### Experimental Methods

#### 2.1. Steady-state Spectroscopy

##### 2.1.1. Absorption

The transitions between different electronic energy levels of molecules produce electronic absorption spectrum (sometimes called UV-VIS spectrum). When a beam of light with wavelength  $\lambda$  is incident on a sample, the logarithm of the ratio of incident light intensity ( $I_0$ ) to transmitted light intensity ( $I$ ) is termed the absorbance ( $A_\lambda$ ).

$$A_\lambda = \log\left(\frac{I_0}{I}\right) = \varepsilon_\lambda \cdot c \cdot l \quad (15)$$

Where  $c$  is concentration,  $\varepsilon_\lambda$  is molar extinction coefficient at wavelength  $\lambda$  and  $l$  is the optical path-length of the sample.

All absorption spectra in this work were recorded on a spectrophotometer Cary 5G UV-Vis-NIR (Varian) in 1 cm quartz cell.

##### 2.1.2. Emission

Following light absorption an excited state of the molecule is populated. Luminescence is the radiative relaxation of the excited molecule. If the emission occurs from the lowest excited singlet it is named fluorescence and from the lowest excited triplet it state is known as phosphorescence.

Fluorescence is a spectral method of analysis where the photoactive molecule is excited by light at a certain wavelength and emits radiation at a different wavelength. Fluorescence spectra described here were recorded on a Fluorolog (Jobin Yvon) spectrofluorometer. Usually, the excitation wavelength chosen corresponds to the maximum of the absorption band of the molecule under investigation. The monochromator scans the wavelengths to measure the spectrum. The correction of the emission spectrum with respect to the spectral sensitivity of detector is established by software.

##### 2.1.2. a. Quantum Yield of Fluorescence

The fluorescence quantum yield ( $\Phi_F$ ) is the fraction of photons emitted through fluorescence relative to the number of photons absorbed by the sample. In other words the quantum yield gives the probability of the excited state being deactivated by fluorescence rather than by non-

radiative mechanism. In the fluorescence measurement, the excitation beam is sent through the sample. According to the Beer-Lambert law, intensity of transmitted beam:

$$I(\lambda) = I_0(\lambda) \cdot 10^{-A(\lambda) \cdot l} \quad (16)$$

Here  $I_0$  is the initial beam intensity,  $A$  is the absorbance at  $\lambda$  in  $\text{cm}^{-1}$  and  $l$  is the distance the beam travels through the material in cm. The intensity of the absorbed beam at the position  $l$  is given by:

$$\frac{dI(\lambda)}{dl} = I_{\text{absorbed}} = I_0(\lambda) \cdot A(\lambda) \cdot \ln 10 \cdot 10^{-A(\lambda) \cdot l} \quad (17)$$

Our used spectrofluorometer collects the fluorescence at the 5<sup>th</sup> millimetre of the cell. If we rewrite the equation, it becomes:

$$I_{\text{absorbed}} = I_0(\lambda) \cdot A(\lambda) \cdot \ln 10 \cdot 10^{-A(\lambda) \cdot 0.5} \quad (18)$$

It has to be considered the absorption of excitation beam in the sample and the fluorescence should be corrected using following formula:

$$I_{\text{fluo-corrected}} = \frac{I_{\text{fluo}}}{A(\lambda) \cdot \ln 10 \cdot 10^{-A(\lambda) \cdot 0.5}} \quad (19)$$

Here, the  $I_{\text{fluo}}$  is the data taken from the spectrofluorometer and  $I_{\text{fluo-corrected}}$  is the corrected fluorescence intensity. The quantum yield of fluorescence can be calculated by the following equation for solutions of a molecule (x) and standard (ST).

$$\phi_x = \phi_{ST} \frac{(\text{integrated fluorescence intensity})_x}{(\text{integrated fluorescence intensity})_{ST}} \left( \frac{n_x}{n_{ST}} \right)^2 \quad (20)$$

## 2.2. Time-resolved spectroscopy

### 2.2.1. Time-resolved fluorescence

Fluorescence gives information not only about the molecule itself, but also its environment. In steady-state measurements, some of information on dynamic processes such as isomerisation, solvation and anisotropy dynamics is hard to elucidate. In the current time-resolved experiments, a train of short (fs, ps) excitation pulses enters the cell normal to one of its faces. Fluorescence is collected in forward direction by the optical system consisting of spherical mirrors and a periscope. The collected light is sent then into a spectrograph coupled with a streak camera. By this method fluorescence intensity can be detected as a function of wavelength and time.

### 2.2.2. Transient Absorption

In transient absorption experiment, short pump pulse promotes the molecular system into some transient state which possesses a specific absorption spectrum. The spectrotemporal

evolution of this spectrum represents a unique fingerprint of a particular molecular system. In order to realize this, a wavelength-tunable short light pulse is used to excite the sample. The absorption of the sample can be measured with a white light probe pulse. The transient absorption of the sample is determined by the ratio of the probe light transmitted through the sample with and without excitation for each delay between pump and probe pulses and for each wavelength, and is defined as the logarithm of that ratio.

$$\Delta O.D. = -\log\left(\frac{\text{transmitted light with excitation}}{\text{transmitted light without excitation}}\right) \quad (21)$$

In a traditional (stroboscopic) pump-probe experiment, transient absorption spectra are measured in the following way. The pump pulse creates the absorption of the sample at given instant. In order to obtain the temporal trace of absorption behaviour the time delay between pump pulse and probe pulse needs to be varied. The transient spectra are recorded at each time delay and such way a 2D -wavelength vs. delay- map of absorption intensity is collected. In the pump-probe setup (Fig.2.1) where fs resolution employed to collect data for this work, this stroboscopic measurement procedure is used. The laser system (Ti:Sa laser optically pumped with Nd:YAG laser at 532 nm) generates pulses of 30 fs centered at 800 nm (800  $\mu$ J, 1 kHz repetition rate). The laser output is split in two parts, producing the pump and the probe. 80% of pulses are used to pump an optical parametric generator (TOPAS) to generate the wavelength tunable pump pulse. Following TOPAS the harmonic generation or frequency mixing in a nonlinear crystal produces the excitation pulses in the range 250 – 2600 nm. The probe is a white light continuum pulse, extending from 390 nm to 900 nm, generated by focusing the 800 nm pulses ( $\sim$ 5  $\mu$ J per pulse) into a 5 mm thick D<sub>2</sub>O cell. A part of the probe pulse is split off for reference before interaction with the sample and is directed into the spectrograph coupled with a CCD array (a simple steady-state detector with no time resolving abilities) by means of an optical fibre. The remaining part of the continuum is used as a probe pulse to monitor the transient absorption spectra of the sample at different time delays  $\Delta t$  between the pump pulse and the continuum probe pulse.

The transient absorption spectrum is determined in presence and in absence of the pump pulse, controlled by a shutter, at given time delay between the pump and the probe pulses with an error of about 0.005 for the optical density.

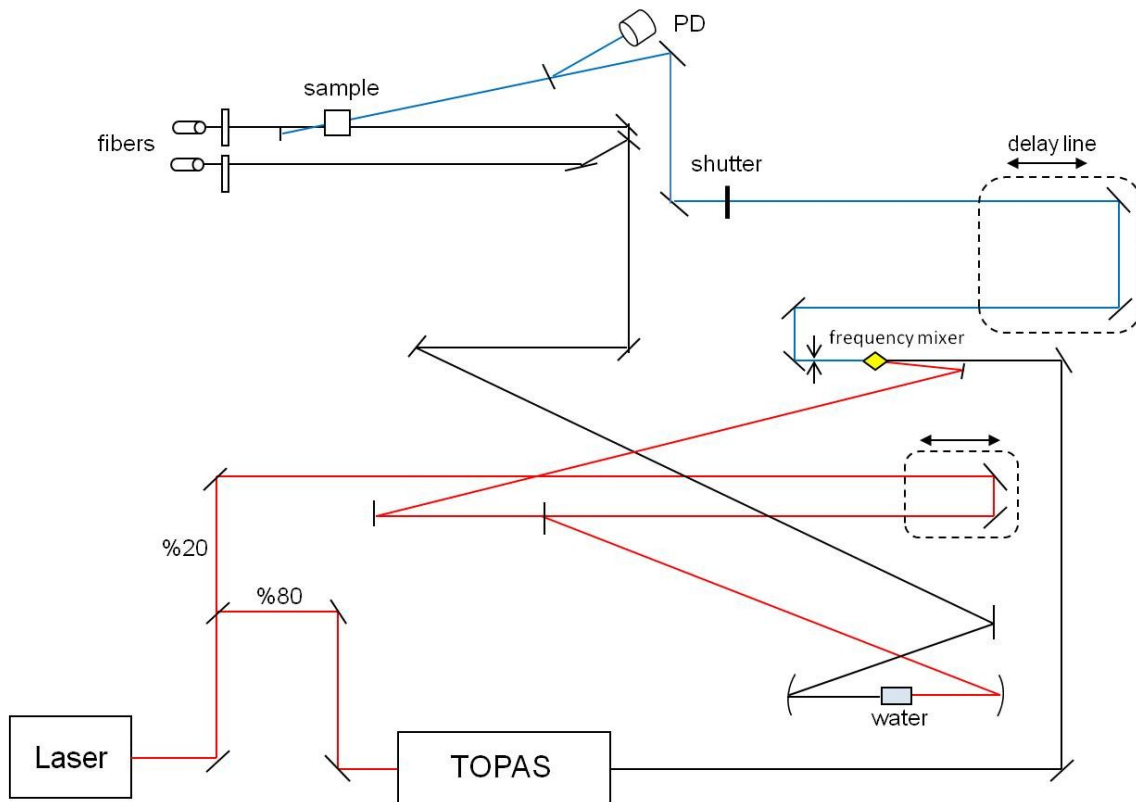


**Fig.2.1:** The pump-probe setup with fs resolution.

In our experimental setup with ps resolution, a streak camera is used in order to measure transient absorption. The principle of transient absorption measurements with a streak camera is different from the stroboscopic pump-probe method described above. The streak camera records the temporal evolution of light passed through excited sample continuously (analogically). Full transient absorption spectrotemporal map can be recorded by using a continuous white light source which is long enough to cover the length of streak camera time window. Fig.2.2 shows the schematics of ps-resolution pump-probe setup.

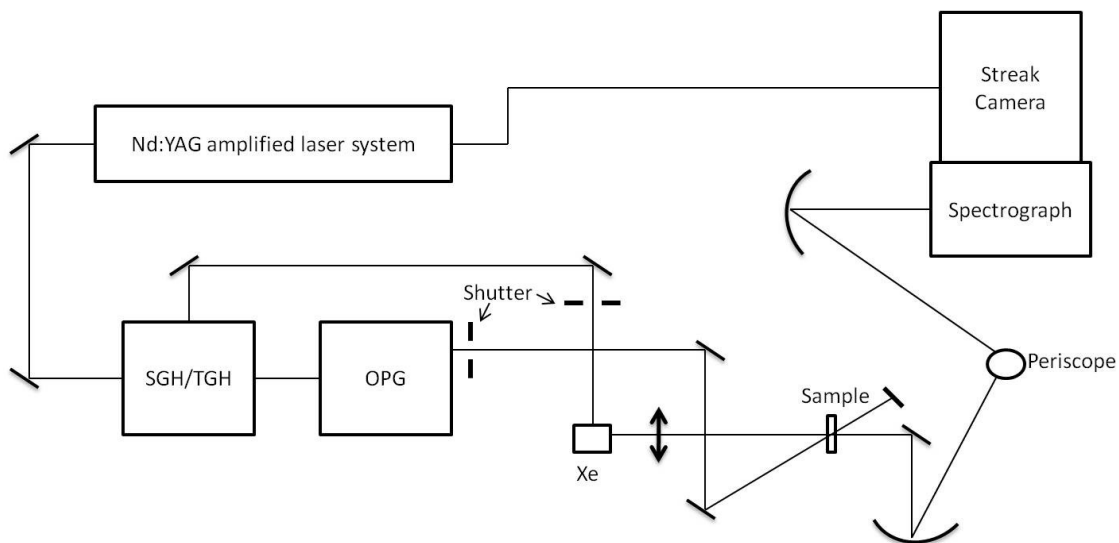


**Fig.2.2:** The pump-probe setup with ps resolution.

A frequency tripled Nd:YAG amplified laser system (30 ps, 30 mJ @1064 nm, 20 Hz, Ekspla model PL 2143) output was used to pump an optical parametric generator (Ekspla model PG 401) producing tunable excitation pulses in the range 410 – 2300 nm. The residual of fundamental laser radiation was focused in a high pressure Xe filled breakdown cell where a white light pulse (1  $\mu$ J, ~50 ns) for sample probing was produced. All light signals were analyzed by spectrograph (Acton) coupled with a high dynamic range streak camera (Hamamatsu C7700). Streak trigger signal is generated from a digital delay generator (DG535) with laser oscillator as master for longer time windows and an optical signal, via photodiode up to 50 ns delay. Accumulated sequences (sample emission, probe without and with excitation) of pulses were recorded and treated by HPDTA (Hamamatsu) software to produce two dimensional maps (wavelength vs delay) of transient absorption intensity in the range 300 – 800 nm. Typical measurement error was better than  $10^{-3}$  OD.

### 2.3. Resolution of the rate equation

Time-resolved experiments allow us to measure the dynamic evolution of population of excited states following photon absorption. In order to analyze the kinetics, the rate equations have to be solved.

The intensity of the beam, which interacts with the sample, can be described by a Gaussian function with pulse duration of  $\tau_p$ .

$$I(t) = I_0 \exp \left[ -4 \ln 2 \left( \frac{t-t_0}{\tau_p} \right)^2 \right] \quad (22)$$

Here  $I_0$  is the intensity at the centre (maximum intensity). In following, we will describe the relaxation of excited states.

#### 2.3.1. One level model

For the one level model, it is imagined that the molecules in the excited  $S_1$  state have a population of  $N_1(t)$  at time and it relax with a rate  $k_1$ . Depopulation of ground state  $S_0$  is negligible ( $N_0 \gg N$ ) and there is no excited state population before the pulse arrive ( $N(-\infty)=0$ ).  $\sigma$  is the absorption cross section between  $S_1 \leftarrow S_0$  transition.

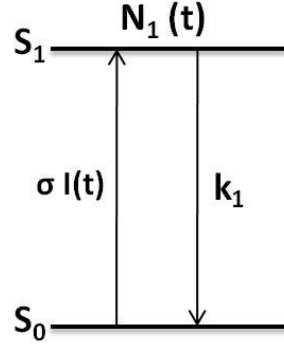


**Fig.2.3:** Scheme for one level model.

$$\frac{dN_1(t)}{dt} = \sigma I(t) - k_1 N_1(t) \quad (23)$$

$$N_1(t) = \frac{\sigma \tau_p I_0}{4} \sqrt{\frac{\pi}{\ln 2}} \exp\left(\frac{k_1^2 \tau_p^2}{16 \ln 2}\right) \left(1 + \operatorname{erf}\left(2\sqrt{\ln 2} \frac{t}{\tau_p} - \frac{k_1 \tau_p}{4\sqrt{\ln 2}}\right)\right) \exp(-k_1 t) \quad (24)$$

### 2.3.2. Two level model

If the relaxation of the excited state comprised with two levels, one level populates as another level by relaxation, the following solution can proposed:

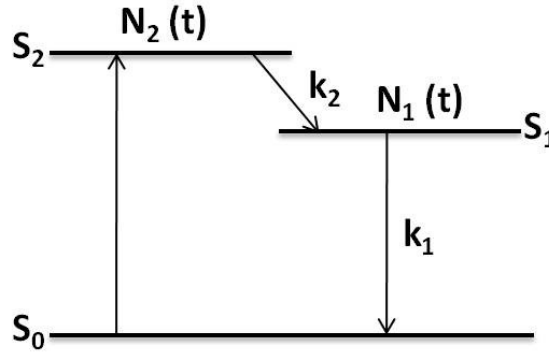


**Fig.2.4:** Scheme for two-level model.

Depopulation of ground state  $S_0$  is negligible ( $N_0 \gg N$ ) and there is no excited state population before pulse arrive ( $N(-\infty) = 0$ ).  $\sigma$  is the absorption cross section between  $S_1 \leftarrow S_0$  transition.

$$\frac{dN_2(t)}{dt} = \sigma I(t) - k_2 N_2(t) \quad (25)$$

$$\frac{dN_1(t)}{dt} = k_2 N_2(t) - k_1 N_1(t) \quad (26)$$

$$N_2(t) = \frac{\sigma \tau_p I_0}{4} \sqrt{\frac{\pi}{\ln 2}} \exp\left(\frac{k_2^2 \tau_p^2}{16 \ln 2}\right) \left(1 + \operatorname{erf}\left(2\sqrt{\ln 2} \frac{t}{\tau_p} - \frac{k_2 \tau_p}{4\sqrt{\ln 2}}\right)\right) \exp(-k_2 t) \quad (27)$$

$$\begin{aligned}
N_1(t) = & \frac{\sigma\tau_p I_0}{4} \sqrt{\frac{\pi}{\ln 2}} \exp\left(\frac{k_1^2 \tau_p^2}{16 \ln 2}\right) \frac{k_2}{k_2 - k_1} \left(1 + \operatorname{erf}\left(2\sqrt{\ln 2} \frac{t}{\tau_p} - \frac{k_1 \tau_p}{4\sqrt{\ln 2}}\right)\right) \exp(-k_1 t) - \\
& \frac{\sigma\tau_p I_0}{4} \sqrt{\frac{\pi}{\ln 2}} \exp\left(\frac{k_2^2 \tau_p^2}{16 \ln 2}\right) \frac{k_2}{k_2 - k_1} \left(1 + \operatorname{erf}\left(2\sqrt{\ln 2} \frac{t}{\tau_p} - \frac{k_2 \tau_p}{4\sqrt{\ln 2}}\right)\right) \exp(-k_2 t) \quad (28)
\end{aligned}$$

The overall temporal evolution  $N(t)$  of excited molecules can be written:

$$N(t) = A_1 N_1(t) + A_2 N_2(t) \quad (29)$$

$A_1$  and  $A_2$  represent the amplitudes for levels 1 and 2.

## Chapter 3

### Hemicyanine based artificial membranes

#### Introduction

Cyanine dyes are widely used classes of organic dyes, which have many application fields including sensors<sup>42-45</sup>, fluorescent labels<sup>40,46-48</sup>, probes<sup>49-51</sup>, laser dyes<sup>52-54</sup>. Williams<sup>55</sup> in 1859 obtained cyanine dye from corn flour. Synthetic procedures of its synthesis were reported later<sup>56, 57</sup>. Its first application field was photography due its light sensitivity. Cyanine dyes have a general formula of  $R_2N[CH=CH]_nCH=N^+R_2$  ( $n$  is a odd number) in which the charged nitrogen is conjugated usually with a heterocyclic system<sup>56</sup>. Depending on the heterocyclic unit and charges, these dyes are classified as follows: Cationic cyanine, hemicyanine dyes **19**, anionic cyanine, oxonol dyes **20**, neutral cyanine, mesocyanine dyes **21** and zwitterionic cyanine, squaraine based cyanine dyes **22** given in Fig.3.1.<sup>57</sup>

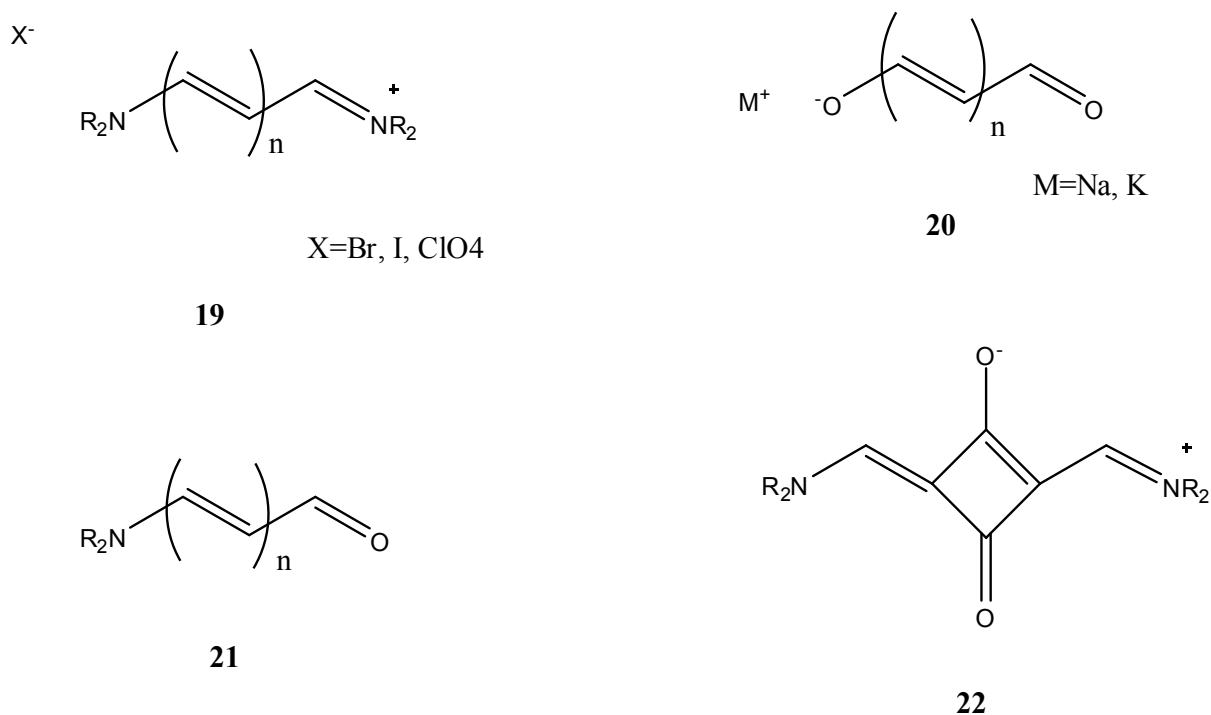


**Fig.3.1.** The general chemical structures of cyanine dyes.

Hemicyanine dyes are represented as shown in **19** and particular derivatives with shortest bridge ( $n=1$ ) are called styryl dyes. Hemicyanine dyes, depending on their substituents and the length of the bridge, can be designed with absorption and fluorescence ranging from the near-UV region (up to 400 nm) to the near-infrared region (up to 1000 nm)<sup>56</sup>. Their

absorption bands are relatively narrow with moderate extinction coefficient in the order of  $10^4$ . Fluorescence quantum yield decreases with increasing length of the bridge<sup>58</sup>.

Hemicyanine dyes, whose absorption and emission properties are sensitive to polarity of solvents, have been used as fluorescent probes. The influence of solvent on the spectral behaviour of compounds is called solvatochromism<sup>11</sup>. In Fig.3.2, some important cyanine dyes are presented.

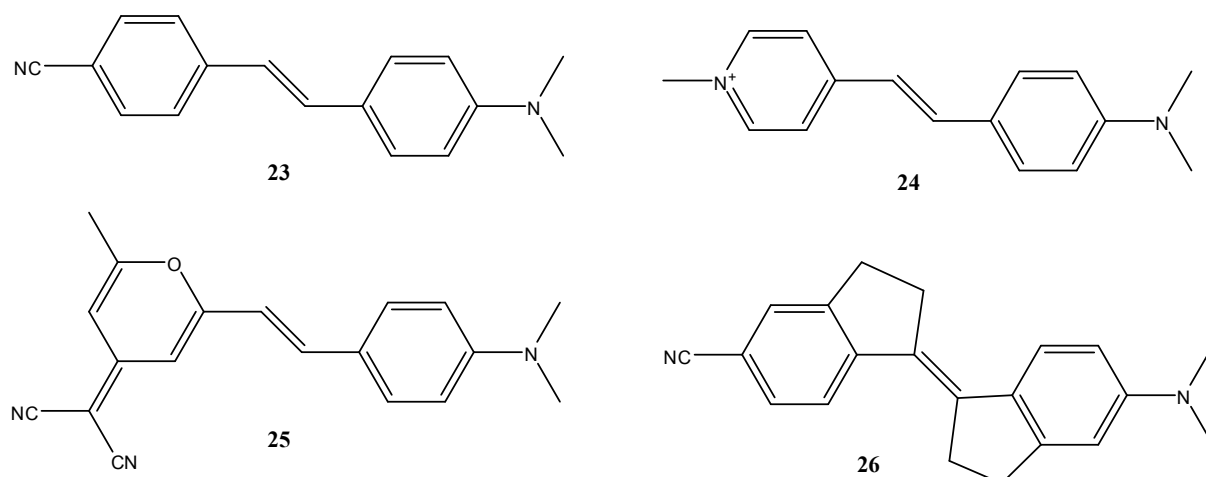


**Fig.3.2.** The chemical structures of some styryl-based cyanine dyes.

Molecule **23** (DCS) shows a shift to longer wavelengths in emission maxima depending on the increasing polarity of solvents as characterized by their dielectric constant and refractive index: 439 (Hexane), 475 (EtOEt), 499 (THF), 524 (EtOH) and 530 (ACN)<sup>59</sup>. The quantum yield of fluorescence is 0.11 in ACN. **24** (DPS), **25** (DCM) and **26** (DCS-B24) also show the same dependence to solvent polarity in their fluorescence emission maxima<sup>60,61</sup>.

This strong red shifted fluorescence with the increase of solvent polarity can be explained with solvent relaxation. When molecule is in excited state (called the Franck–Condon state or locally excited state, LE), it is not in equilibrium with the solvent molecules around it. Because of the intermolecular charge transfer (ICT) the dipole moment of the excited molecule differs from its ground state. The solvent molecules around the molecule rotate during the lifetime of the excited state until the solvation shell is in equilibrium with the molecule and a relaxed ICT state is reached.

In case of molecules in Fig.3.2, the molecules are planar in the ground state. According to the Franck–Condon principle, the locally excited state (LE) is still planar, but solvent relaxation takes place with a rotation of dimethylamino group until it is twisted at right angles and the conjugation is lost. In the resulting TICT (Twisted Intramolecular Charge Transfer) state, stabilized by polar solvent molecules, there is a total charge separation between the

dimethylamino group and the rest of the molecule (Fig.3.3). An emission band corresponding to emission from the TICT state is observed at longer wavelengths.<sup>10</sup>

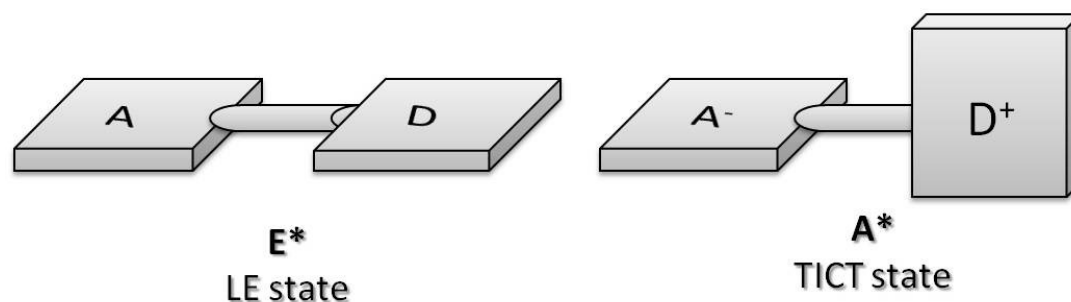


**Fig.3.3.** The model for planar LE state ( $E^*$ ) and TICT state ( $A^*$ ).

Three-state kinetic scheme is necessary to explain the photophysics of the dyes in Fig.3.2. Following the notation in Fig. 3.3,  $E^*$  is the LE state which has a planar geometry.  $A^*$  is the twisted intermolecular charge transfer state (TICT) by twisting single bond.  $P^*$  is a so called phantom state which acts as a funnel towards the ground state by twisting a double bond which causes photoisomerization<sup>60,61</sup>.

For molecule **23** (DCS), the  $A^*$  state is luminescent (quantum yield 0.11 in ACN) and competes with the non-radiative deactivation through double-bond twisting. Intramolecular bridging of **26** (DCS-B24) suppresses formation of  $A^*$  state.<sup>60</sup> **26** shows 0.8 quantum yield of fluorescence, which means that relaxation through TICT states was present in nonbridged compound. It can be concluded also from increase of quantum yield of **23** at  $-90^\circ\text{C}$  in frozen EtOH.<sup>61</sup>

Cyanine dyes linked with crown ether moieties due to their photocontrollable cation binding properties, can be used as ion sensors and have potential application in detecting metal ions in biological systems as well as for molecular data processing. Intramolecular charge-transfer can be affected during complexation with metal cations depending on the size and charge density of the ionophore. Thomas et al. studied the photophysical properties of cyanine dyes containing an azacrown ether moiety and their complexation behavior with  $\text{Li}^+$  and  $\text{Na}^+$  cations.<sup>62</sup>

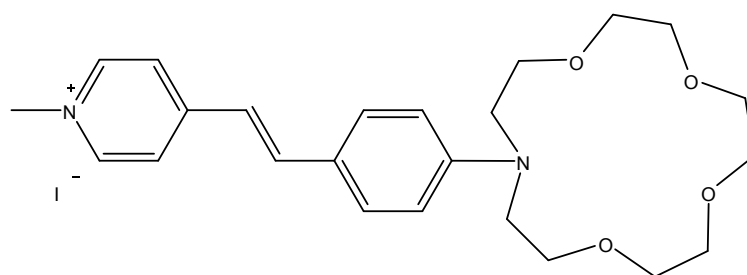


**Fig.3.4:** Crown containing hemicyanine dye.

**27** (Fig.3.4) shows absorption maximum in acetonitrile at 474 nm and emission maximum at 615 nm with a quantum yield of 0.014.<sup>62</sup> Decrease in the absorption maximum with increase in solvent polarity suggests that the molecule has a higher ground state dipole moment compared to its excited state dipole moment. Complexation with  $\text{Li}^+$  and  $\text{Na}^+$ , due to the suppression of its intramolecular charge-transfer transition, causes a shift to shorter wavelengths (602 nm for  $\text{Li}^+$  and 603 nm for  $\text{Na}^+$ ) whereas the quantum yield increases slightly.<sup>62</sup>

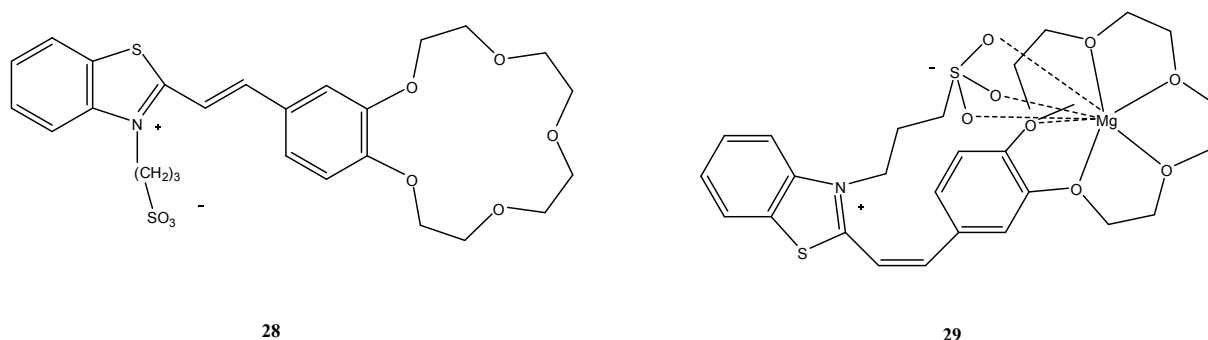


**Fig.3.5:** *Cis-trans isomers of crown-containing dye and its complexation.*

Dyes **28** and **29** in Fig.3.5 are examples of styryl dyes which show complexation induced cis-trans isomerisation<sup>63</sup>. **29** is the cis isomer of **28**. Intramolecular coordination between  $\text{SO}_3^-$  group and the crown ether ring entraps the  $\text{Mg}^{2+}$  cation. Absorption maximum of **29** shifts to shorter wavelengths compare to **28**. If  $\text{Mg}^{2+}$  concentration becomes higher than  $10^{-3}\text{M}$ , the molecule starts to bind a second  $\text{Mg}^{2+}$  cation by  $\text{SO}_3^-$  fragment separately<sup>64</sup>.

**30**, **31** and **32**<sup>65</sup> in Fig.3.6 show similar absorption maxima at around 430 nm. **30** can only complex with  $\text{Hg}^{2+}$  which causes a 10 nm shift to longer wavelengths. **31** and **32** shows also hypsochromic shift of 8 and 18 nm on complexation with  $\text{Ag}^+$  and  $\text{Hg}^{2+}$  cations, respectively. Cis isomer of **30** and **32** on complexation with  $\text{Ag}^+$  and  $\text{Hg}^{2+}$  show smaller hypsochromic shift than their trans isomer, because intramolecular coordination between the  $\text{COOH}$  group and metal cations becomes weaker in the trans form.

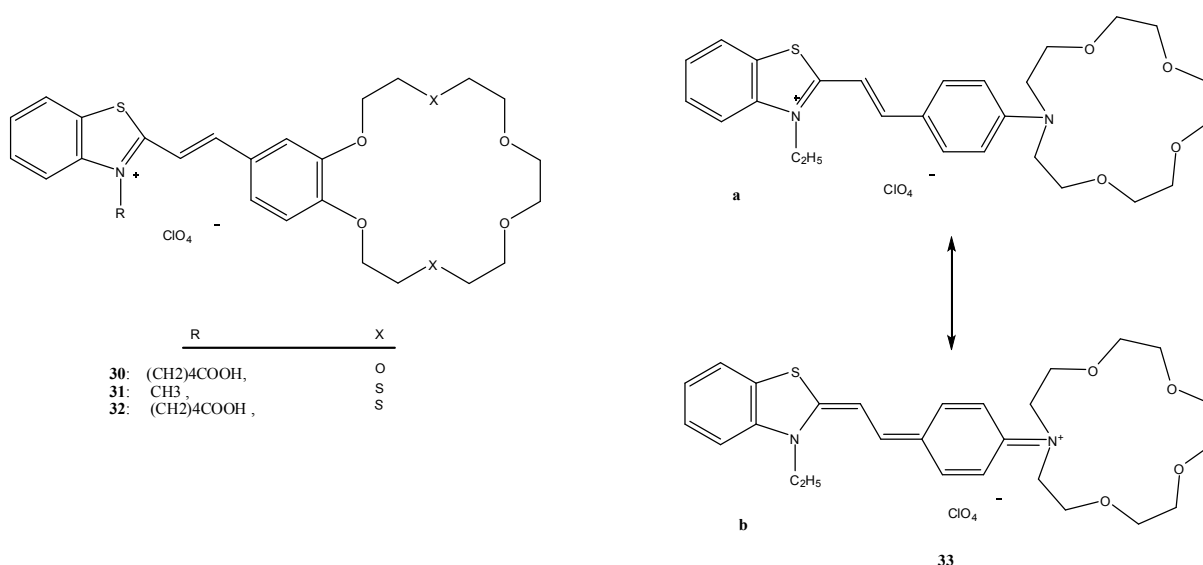


**Fig.3.6:** The structures of some crown-containing cyanine dyes.

The aza-15-crown ether containing **33**<sup>66</sup> tends to make complexation with Ba<sup>2+</sup> and Ag<sup>+</sup> in acetonitrile solution. From X-ray diffraction studies, it is proposed that the dye exists in equilibrium with the quinoid form (**33b**). This is due to intramolecular charge transfer between both the nitrogen atoms of molecule. Dye **33** forms a complex with Ba<sup>2+</sup> which causes a hypsochromic shift which is due to redistribution of charge within the extended chromophore.

The aggregation of dyes exhibit changes in absorption bands as compared to monomeric species. According to exciton theory, the dye is regarded as a dipole. Since the dye interacts with other dye molecules in the aggregate, the energy level splits in to two. If the dye molecules aggregate in a parallel way, a transition to the upper energy level occurs. This causes a bathochromic H-aggregate absorption band. If the dye molecules aggregate in head-to-tail arrangement, transition occurs to lower energy state and results a hypsochromic J-aggregate<sup>57</sup>. Cyanine dyes are the best known self aggregating dyes. The aggregation process depends on the structure of the dye and the environmental factors such as pH, temperature, solvent polarity, concentration, ionic strength.

Molecule **34** (Fig.3.7) shows hypsochromic shift due to H-aggregates formation in aqueous solution<sup>67</sup>. It forms J-aggregate formation in hexane-methanol-chloroform medium which is concluded from the bathochromic shift<sup>68</sup>.

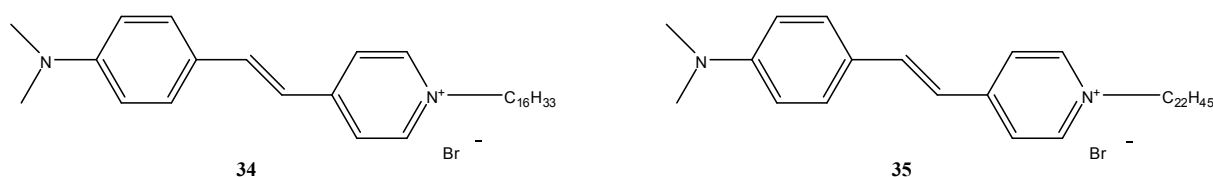
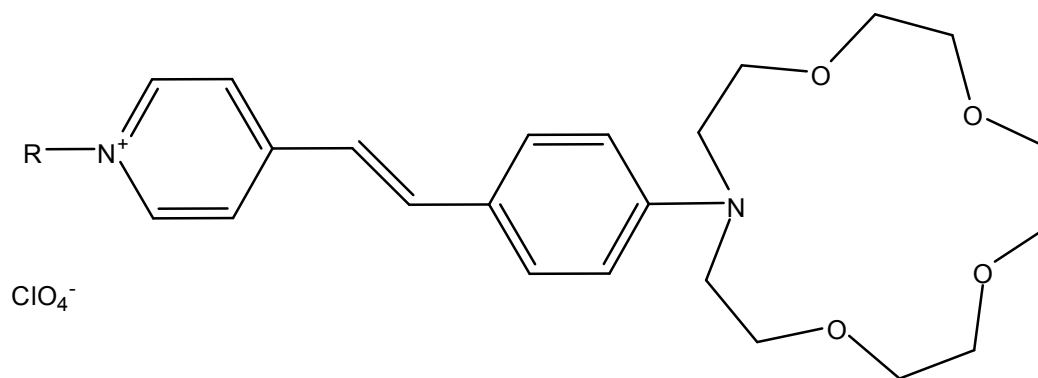


**Fig.3.7:** Hemicyanine dyes with alkyl chain.

Dye **35** in LB film deposited on silica exhibits four absorption bands<sup>69</sup>. The highest energy band remains unperturbed with concentration change. The lowest energy band is due to monomer absorption and the other two bands are due to aggregation. Carpenter et al. studied second harmonic generation on these LB films. They observed that the monomer has a much higher hyperpolarizability than their aggregates. The monomer also displays increased second order susceptibility. Li et al<sup>70</sup>. worked on **34** complexed with a zinc cation. They have reported enhancement of second-order susceptibility as a result of perturbation of aggregation in the presence of zinc cations. There are several works on their nonlinear optical properties and the relationship between the chromophore organization and structure<sup>71-73</sup>.

In this chapter, the results of the study on hemicyanin derivative molecules **C1** and **C2** (see Fig.3.8) are presented. The donor and the acceptor parts of the molecule can be functionalized with various chemical groups to instil different properties in the molecule.



**C1:** R=CH<sub>3</sub>  
**C2:** R=C<sub>22</sub>H<sub>45</sub>

**Fig.3.8:** Structure and formula of **C1** and **C2**.

Molecules **C1** and **C2** have been functionalized the molecule with an azacrown. The azacrown moiety can coordinate cations such as Ca<sup>2+</sup> with binding constants in the range 3.75 to 6.78<sup>33</sup>. Ca<sup>2+</sup> is one of the most important cations for living organisms. Not just controlling the concentration of Ca<sup>2+</sup> is very important, but also determining precisely their coordination in space and time is important also.

Another modification is made on the acceptor part of the molecule. Functionalizing with long amphiphilic chains allows us to work at the air-water interface. Indeed, these molecules can be organized into Langmuir monolayers or self-assembled films<sup>74</sup>.

Hemicyanine Langmuir-Blodgett (LB) films can be employed to conceive functionalized artificial membranes by incorporating light-sensitive molecular units designed to introduce

specific membrane functionalities such as light harvesting, information processing and sensing. Additionally, their inherent biocompatibility opens prospects in medicine and environmental monitoring. For example, hemicyanine dyes are powerful molecular probes to follow fast changes the membrane voltage of neurons. Work of Lambacher also shows amphiphilic hemicyanine dyes can be used for optical recording of electrical activity on neurons<sup>75</sup>.

In this chapter, two complementary approaches have been used. First, molecules were investigated in solution. Their behaviour in different solvents, their ground state absorption and fluorescence, their complexation with various cations were studied. Their behaviour in the excited state was also studied by time-resolved methods.

The second part focuses on LB films. The organization and aggregation properties of molecules were studied and isotherms and ground state absorption and fluorescence spectra were used to elucidate the behaviour of the molecules at the air-water interface and in LB monolayer form.

## PART I

### 3.1.1. Absorption and Fluorescence Spectra

The incorporation of an alkyl chain combined with charged head group makes the molecule **C2** amphiphilic and poorly soluble in most solvents. In order to get more information of the behaviour in solution, molecule **C1** was used where a methyl group replaces the long chain.

The electronic absorption spectra of both molecules **C1** and **C2**, as well as the fluorescence are shown in Fig.3.9. Concerning the lowest energy absorption band, a 6 nm ( $264\text{ cm}^{-1}$ ) shift is observed between the spectra maxima due to the presence of 10% in volume of  $\text{CHCl}_3$  in solution of **C2**. (**C2** is not soluble in  $\text{CH}_3\text{CN}$ ).

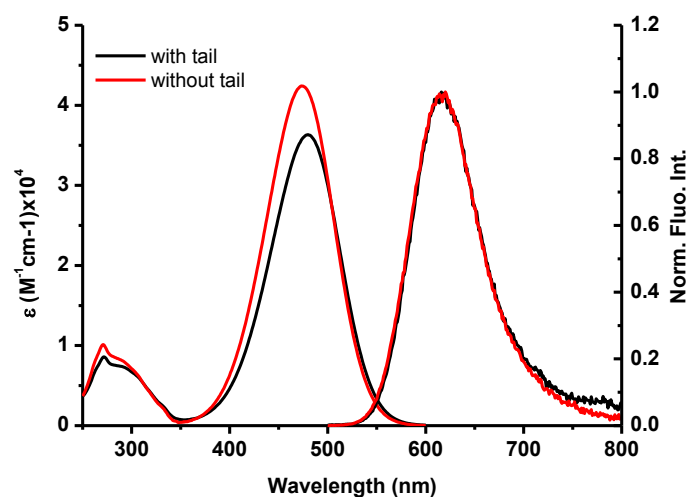


**Fig.3.9:** Absorption and emission spectra of **C1** (in  $\text{CH}_3\text{CN}$ ) and **C2** (in  $\text{CH}_3\text{CN}:\text{CHCl}_3$ , 90:10, v/v) ( $\lambda_{\text{exc}}=474\text{ nm}$ ).

The electronic absorption spectra show broad structureless absorption bands which are typical for conjugated push-pull systems with an aniline-like donor and pyridinium acceptor with a bridge<sup>76</sup>. The main band at 474 nm is related to the charge transfer from the aniline moiety to the pyridinium part. Fluorescence emission maxima for both molecules are at 617 nm. Quantum yield of fluorescence for **C1** is 0.016 and **C2** is 0.025 in acetonitrile.

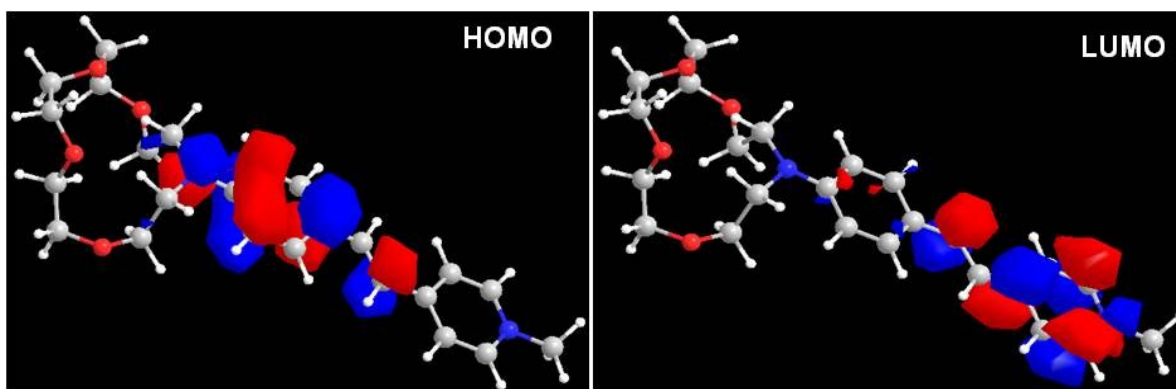


**Fig.3.10:** *HOMO and LUMO orbitals of C1.*

The negative charge of the chromophore is displaced from the amine moiety towards the pyridinium moiety upon excitation. This displacement of charge is calculated with quantum chemical methods. Fig.3.10 shows that the molecular orbital is placed on the amine moiety in the ground state and moves to the pyridinium moiety on excitation. The transition from HOMO to LUMO corresponds to absorption and this displacement of orbitals on the molecule shows the charge transfer induced by excitation.

### 3.1.2. Solvent Effects

While the solvent polarity changes, the maxima of absorption and emission bands change also. Here, we consider the solvatochromic behaviour of **C1** in more detail.

All results, molecular absorption, fluorescence quantum yield, Stokes shifts, maxima of absorption and fluorescence wavelengths for different solvents, are shown in Table-3.1.

**Table-3.1:** *Properties of C1 in different solvents*

Solvent	$\lambda_{\text{abs}}$	$\lambda_{\text{fluo}}$	$\epsilon$	Stokes Shift ( $\text{cm}^{-1}$ )	$\epsilon$ ( $\text{M}^{-1}\text{L}^{-1}$ )	$\phi_{\text{fluo}}$ (%)
Benzene ( $\text{C}_6\text{H}_6$ )	474	601	2.3	4022	24110	7.6
Ethyl Acetate (EA)	470	602	6.02	4665	23000	8.2
Ethylene glycol dimethyl ether (EGDME)	478	616	7.2	4686	45074	4.8
Methylisobutylketone (MIBK)	487	615	13.11	4273	46292	3.6
Acetone (AC)	479	618	20.56	4695	50288	1.3
Acetonitrile (ACN)	474	617	35.92	4783	42496	1.4
Dimethyl sulfoxide (DMSO)	474	616	46.45	4863	41956	7.2
Propylene carbonate (PC)	475	616	64.92	4818	40370	4.3
Water ( $\text{H}_2\text{O}$ )	454	600	80	5359	20336	1.2

The positions, intensities and shapes of absorption and emission spectra can show changes under the influence of the solvent surrounding the solute. Looking to Table-3.1, by increasing the polarity of the solvent, red shifting of the emission wavelength is observed from the 601 nm to 618 nm and the shift on absorption maxima does not show a dependence on just solvent polarity, the maxima vary between 454 nm and 487 nm. Molecule shows solvatochromism in emission spectra while absorption spectra show slight shifts. The first excited state for this molecule is the locally excited state (or Frank-Condon (FC) state). Afterwards, the molecule finds itself in a charge transfer (CT) state. The dipole moment of the excited state changes after charge transfer compared to the ground state dipole moment. The solvent molecules around the molecule reorient themselves and stabilize the CT state<sup>77</sup>. This situation causes the shifts on emission spectra.

The dipole moment of the molecules can be affected by the dipole moment of the solvents with various dielectric constants and refractive index<sup>77</sup>. Different theories were developed to explain the interaction between solute and solvent dipole moments. There are lots of parameters to affect this interaction. These theories mostly differ in the way of their approximations.

Taking into account the Onsager reaction<sup>78</sup> field approximation, the Ooshika formula was developed<sup>79</sup> to the following two equations for the  $\nu_A$  and  $\nu_F$  band shifts different any solvent, where  $\mu_E$  and  $\mu_G$  are the excited and ground state dipole moments, respectively,  $F(n,\varepsilon)$  and  $F'(n,\varepsilon)$  are the so-called reaction field factors depending on the shape and the Onsager cavity radius of the solute and on the dielectric constant  $\varepsilon$  and the refractive index  $n$  of the solvent.

$$hc\Delta\nu_A = -\mu_G(\mu_E - \mu_G)F(n, \varepsilon) - \frac{(\mu_E^2 - \mu_G^2)}{2}F'(n, \varepsilon) \quad (30)$$

$$hc\Delta\nu_F = -\mu_E(\mu_E - \mu_G)F(n, \varepsilon) - \frac{(\mu_E^2 - \mu_G^2)}{2}F'(n, \varepsilon) \quad (31)$$

Shifts on emission spectra can be interpreted in terms of Lippert equation<sup>80</sup> which gives the relationship between the Stokes shifts and the changes of the dipole moment of the molecule.

$$\Delta\nu = \nu_A - \nu_F = \frac{2}{hc a^3} \left[ \left( \frac{\varepsilon-1}{2\varepsilon+1} \right) - \left( \frac{n^2-1}{2n^2+1} \right) \right] (\mu_E - \mu_G)^2 \quad (32)$$

According to Lippert theory<sup>80</sup>, in the ground state, there is no reaction field (no oriented solvent molecules surrounding the solute), but upon excitation a charge transfer is created and usually molecule becomes more polar. If solvent is polar, solvent molecules are reorganized around the solute molecule and this decreases the potential energy of the solute. Charge transfer state becomes the lowest state. If the solvent is nonpolar, the initially created charge transfer state, which is called locally excited state (LE), is the lowest state.

In equation (32), the term  $\left(\frac{\epsilon-1}{2\epsilon+1}\right) - \left(\frac{n^2-1}{2n^2+1}\right)$  is called orientation polarizability. The polarizability is a result of both the electronic polarizability of the solvent molecules and the dielectric permittivity of the solvent. The term  $\left(\frac{n^2-1}{2n^2+1}\right)$  is called high-frequency polarizability or electronic polarizability and is due to property of solvent molecule electrons to interact with electric field of the light. The term  $\left(\frac{\epsilon-1}{2\epsilon+1}\right)$  is called low-frequency polarizability, which is due to orientation of solvent molecules.  $\epsilon$  is a static property for the reason that reorientation of molecules takes much longer time than light electric field oscillation period.

We obtain the difference of high-frequency polarizability and low-frequency polarizability; spectral shifts are proportional to the adaption of the solvent molecules, which is the orientation polarizability of the solvent.

Lippert theory assumes that the excited state dipole moment for Franck-Condon state and relaxed state is same. This assumption is not as drastic as it may seem, because it is basically equivalent to assume that the initial and the final state molecular geometries are similar. However if the molecule is flexible and undergoes evolves to a twisted intramolecular charge transfer state (TICT), initial and final states do not have a similar geometry anymore. It is important also to note that Lippert equation ignores the polarizability of fluorophore (solute) and the direction of dipole moments in the excited and ground state. Theory assumes that the polarizability of the solute is zero and the direction of dipole moments is collinear.

Fig.3.11 gives the plot of  $\nu_A - \nu_F$  versus  $\Delta f_{LM}$ . From the slope the relationship between excited and ground state dipole moments can be calculated. Calculation steps are given below in equations (33) and (34).

$$m = \frac{2(\mu_E - \mu_G)^2}{hca^3} \quad (33)$$

$$\mu_E = \mu_G \pm 0.010\sqrt{ma^3} \quad (34)$$

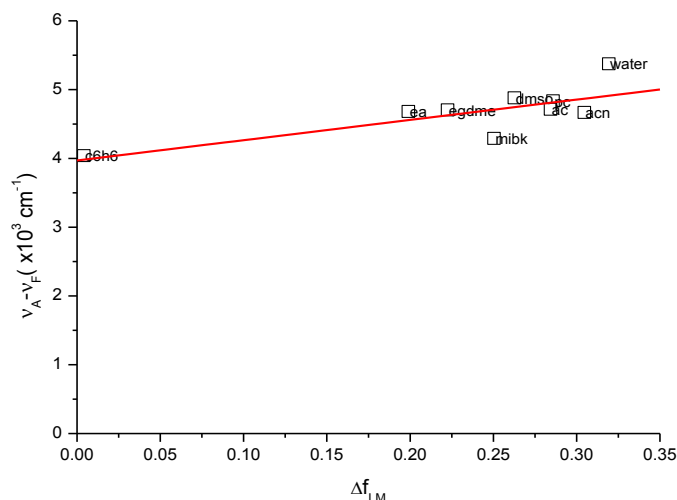


**Fig.3.11:** The plot of  $v_A - v_F$  versus  $\Delta f_{LM}$ .

According to Lippert equations from the slope of the graph in Fig.3.11, the difference of excited and ground state dipole moments is found as 11.15 D. The difference is expected due to the reason that the dipole moment in ground state and in the excited state of **C1** is not same. The positive charge of the chromophore is displaced upon excitation from the pyridinium moiety toward the amine moiety. The dipole moments were obtained from quantum chemical computations by using MOPAC (Molecular Orbital PACKage)<sup>81</sup> which is a semiempirical quantum chemistry software. The ground and excited state dipole moments are calculated, 17.7D and 2.3D respectively. The calculated value and experimental values are mismatched. It should be noted that Lippert made some assumption on the theory of solvatochromism. As mentioned before, one of these assumptions of Lippert theory is taking the molecular polarizability of the solute zero.

For an isotropic polarizability of the solute, the following equations can be obtained from eq.(30) and (31)<sup>82</sup>.

$$v_A - v_F = m_1 \Delta f(\epsilon, n) + const \quad (35)$$

$$v_A + v_F = -m_2 \varphi(\epsilon, n) + const \quad (36)$$

$$\varphi(\epsilon, n) = f(\epsilon, n) + 2g(n) \quad (37)$$

Here are the  $f(\epsilon, n)$  and  $g(n)$  are the polarizability functions of solvent. Their relation with dielectric constant and refractive index are given below.

$$\Delta f_{BK} = \frac{2n^2+1}{n^2+2} \left[ \left( \frac{\epsilon-1}{\epsilon+2} \right) - \left( \frac{n^2-1}{n^2+2} \right) \right] \quad (38)$$

$$g(n) = \frac{3}{2} \frac{n^4-1}{(n^2+3)^2} \quad (39)$$

The following graphs (Fig.3.12) are drawn due to eq. (35) and (36).

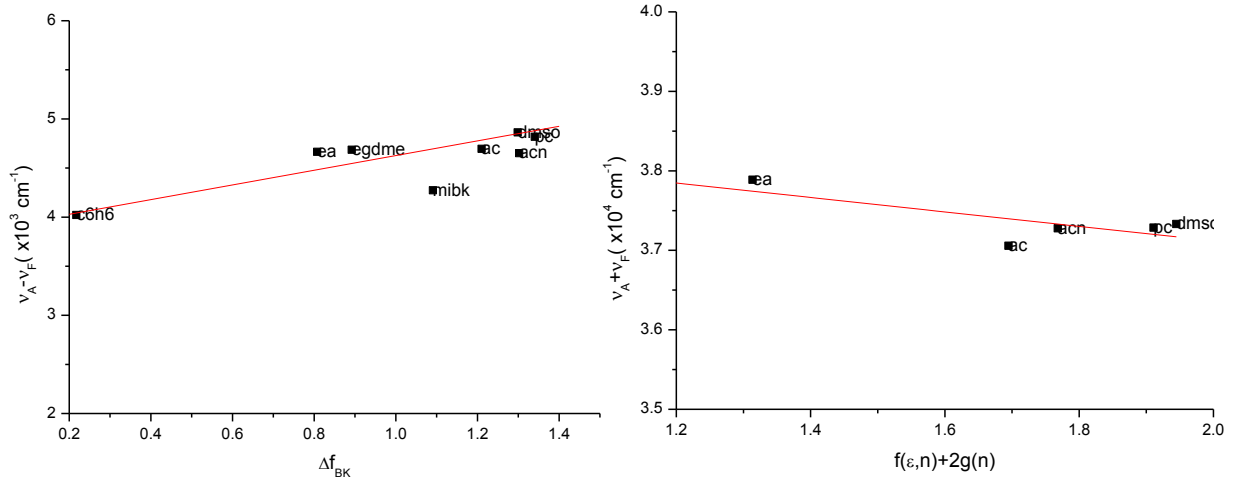


**Fig.3.12:** The plot of  $\nu_A - \nu_F$  and  $\nu_A + \nu_F$  versus  $\Delta f_{BK}$  and  $\Delta f_{BK} + g(n)$ .

From the slope of fits of experimental data, the ratio of dipole moments can be obtained as following:

$$\frac{\mu_E}{\mu_G} = \frac{m_1 + m_2}{m_2 - m_1} = 10.16 \quad (40)$$

In general, excited and ground state dipole moments are not parallel. The angle between them can be calculated using eq. (41).

$$\cos\varphi = \frac{1}{2\mu_G\mu_E} \left[ (\mu_G^2 + \mu_E^2) - \frac{m_1}{m_2} (\mu_E^2 - \mu_G^2) \right] \quad (41)$$

Using  $m_1$  and  $m_2$  from the slopes of graphs above, it is obtained that  $\varphi$  is closed to  $0^\circ$ .

Until now, we consider that solute has a spherical shape. For an ellipsoidal molecule of isotropic polarizability it follows from the general theory of Liptay<sup>83</sup> that the solvent polarizability functions are as follows:

$$f_L = \left( \frac{\epsilon - 1}{\epsilon + 2} - \frac{n^2 - 1}{n^2 + 2} \right) \quad (42)$$

$$\varphi_L = \frac{\epsilon - 1}{\epsilon + 2} \quad (43)$$

Using these functions on equations (35) and (36), the plot of  $\nu_A - \nu_F$  versus  $\Delta f_L$  and  $\nu_A + \nu_F$  versus  $\varphi_L$  are drawn in Fig.3.13.

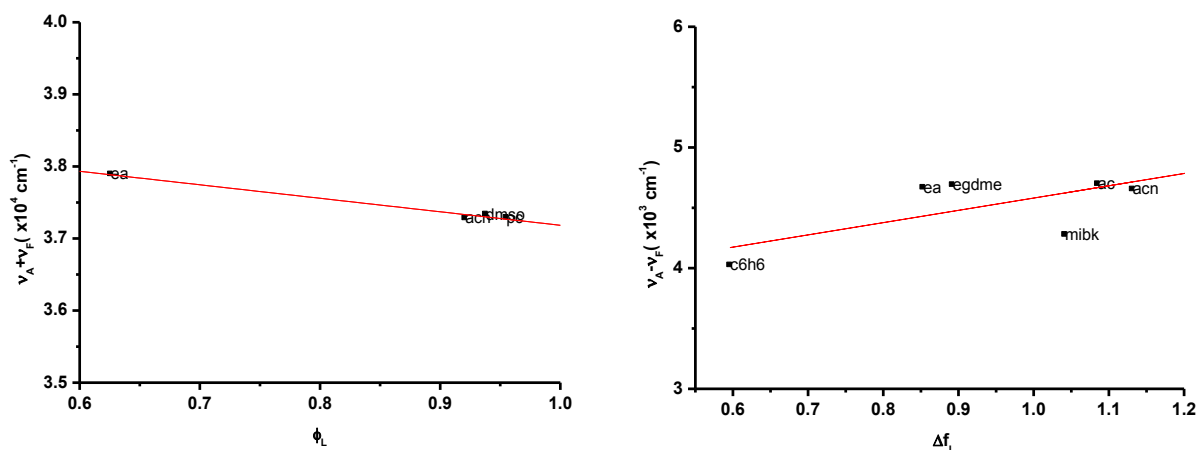


**Fig.3.13:** The plot of  $\nu_A - \nu_F$  and  $\nu_A + \nu_F$  versus  $\Delta f_L$  and  $\phi_L$ .

From the slopes of these graphs, the ratio was calculated as follows:

$$\frac{\mu_E}{\mu_G} = \frac{m_1 + m_2}{m_2 - m_1} = 3.8 \quad (44)$$

The angle between excited and ground state dipole moments is found  $\sim 0^\circ$  by using eq. (41).

By comparison all the results, among all theories we applied the results of Lippert theory predicts more closely the experimental data, in spite of its limitations. Failure of the other theories can be explained as follows. First point, **C1** is a charged molecule. It has high dipole moment in ground state. All these theories make their assumption for an inverse situation. By excitation of the molecule charge transfer occurs. A molecule which was apolar or less polar in ground state becomes more polar by excitation. All theories are based on this situation. In our case by excitation a highly polar molecule becomes less polar. Second point, according to general theory of Ooshika, the molecule is affected only in excited state. The solute-solvent interaction in the ground state is ignored. On the other hand, shifts on absorption wavelengths show that molecule and solute have interactions in the ground state also. As a third point the quantum chemical estimations were made taking the fixed dielectric constant of environment to be 20. Theories consider many different solvents with different dielectric constants. As a last point, all theories fail in the case of aggregation. In water, we have observed more likely aggregation. **C1** is a polar molecule it is soluble in water which is a polar solvent and the extinction coefficient in water is low. The low extinction coefficient in certain solvents can be explained by the presence of the aggregation.

In the following section a model considering the aggregation situation is proposed. The experimental results will be discussed also to take into account the proposed model.

### 3.1.3. Ion Complexation

The cavity size of the azacrown ether and nature, number and orientation of coordinating nitrogen and oxygen atoms provides selectivity for binding  $\text{Ca}^{2+}$  and  $\text{Ba}^{2+}$  cations (ion radius 1.2 Å and 1.4 Å, respectively). In this chapter we will present the results of complexometric titrations are given and the stoichiometry of complexes is discussed. As mentioned above, the main absorption band of the chromophore located at 474 nm corresponds to the charge transfer band. The emission of this compound is at 617 nm. Acetonitrile is used for all experiments. The addition of  $\text{HClO}_4$  or solutions of perchlorates of  $\text{Ca}^{2+}$  and  $\text{Ba}^{2+}$  results in a hypsochromic shift of the main band is due to the coordination of cations (or protonation) by nitrogen of azacrown ether. This coordination reduces the charge transfer and causes a decrease of intensity of the band at 474 nm and a rise of a new band due to complex starts to be observed. In Fig.3.14, it is shown the titration of **C1** with  $\text{Ca}(\text{ClO}_4)_2$ . The spectrum related to complex absorption (cyan curve) possesses two main bands located at 370 nm and 474 nm. The emission by exciting the band at 370 nm occurs at 604 nm.

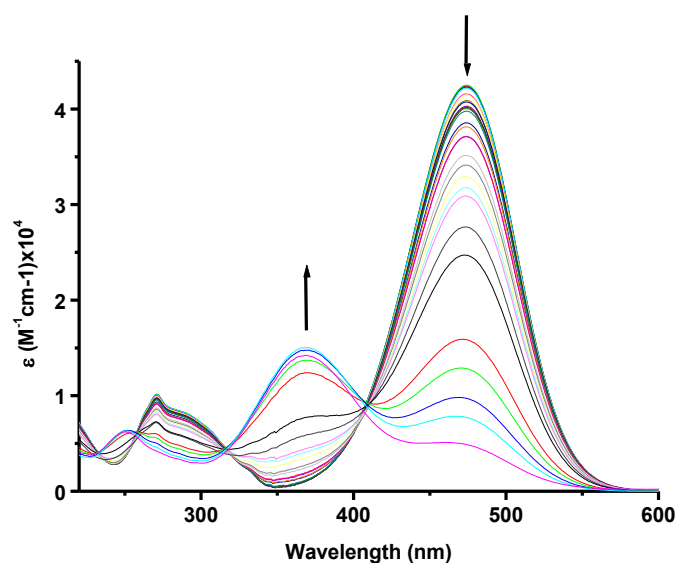


**Fig.3.14:** *The changes of absorption in the presence of  $\text{Ca}(\text{ClO}_4)_2$  in  $\text{CH}_3\text{CN}$  solution.*

Complexometric study is shown in Fig.3.15 by titration of **C1** with  $\text{Ba}(\text{ClO}_4)_2$ . The complex spectrum (which is shown in green curve) has two absorption bands, at 390nm and 474 nm. The emission by excitation of the band at 390 nm is located at 606 nm.

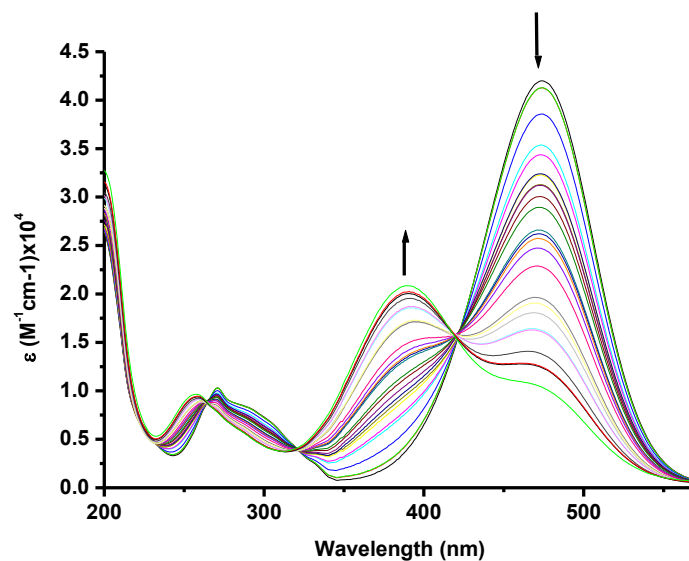


**Fig.3.15:** *The changes of absorption in the presence of  $Ba(ClO_4)_2$  in  $CH_3CN$  solution.*

Complexometric study is shown in Fig.3.16 by titration of **C1** with  $HClO_4$ . The complex spectrum (which is shown in dark blue curve) has an absorption band at 330 nm. The emission by excitation of the band at 330 nm is located at 402 nm. The nitrogen atom in the crown has been protonated. This blue-shifted emission is the emission from the chromophore without the influence of azacrown. The equilibrium constant of  $H^+$  is high ( $\log K_{11} > 7$ ) for stoichiometry of 1:1.

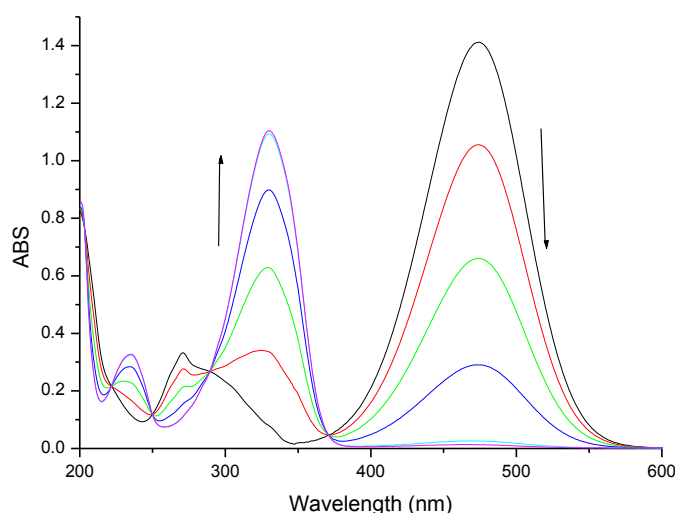


**Fig.3.16:** *The changes of absorption in the presence of  $HClO_4$  in  $CH_3CN$  solution.*

Complexometric studies were performed for determination of stoichiometry of the complexes. The ratio of molecule **C1** to  $Ba^{2+}$  or  $Ca^{2+}$  cations is varied by adding aliquots of a solution of corresponding salt of known concentration to a solution of **C1** of known concentration. The

absorption spectrum of each solution is recorded. The stability constants of the complexes are determined using the SPECFIT/32 program<sup>84</sup>.

The equilibrium is considered for complex formation with cations:



The absorption spectral shapes of free ligand and their complexes  $L_2M$  with  $Ca^{2+}$  and  $Ba^{2+}$  cations are also calculated using SPECFIT/32 program. Fig.3.17 shows the calculated spectra of **C1** and its 2:1 complex with  $Ca^{2+}$ . The binding constant is calculated as  $K_{21}=7.3$ .

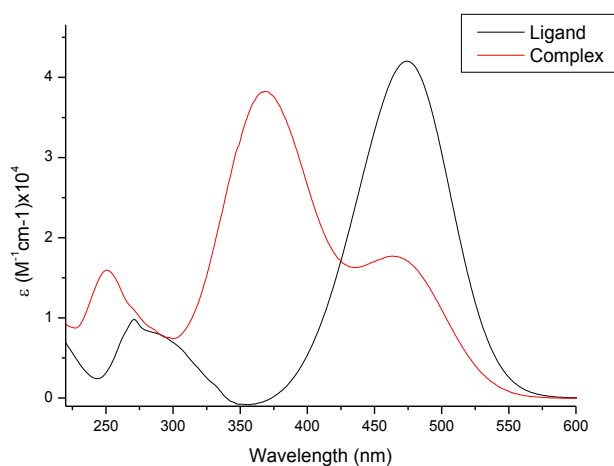


**Fig.3.17:** The calculated absorption spectra of **C1** and 2:1 complex of **C1** with  $Ca^{+2}$ .

The treatment for the complexometric titration data for  $Ba^{2+}$  was done in the same way. The calculated spectrum of free **C1** and its 2:1 complex with  $Ba^{2+}$  is given in Fig.3.18. The binding constant is calculated as  $\log K_{21}=7.5$ .

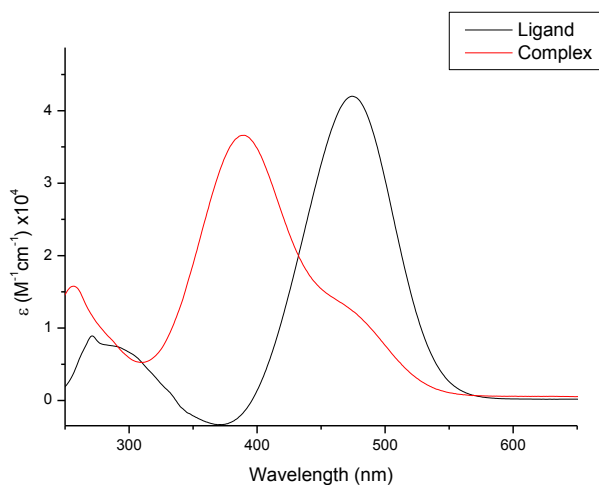


**Fig.3.18:** The calculated absorption spectra of free ligand and 2:1 complex of **C1** with  $Ba^{2+}$ .

Influence of  $\text{Ca}^{2+}$  and  $\text{Ba}^{2+}$  is also seen on the fluorescence emission. In Fig.3.19, the fluorescence spectra of **C1** and its complexes with cations are given.

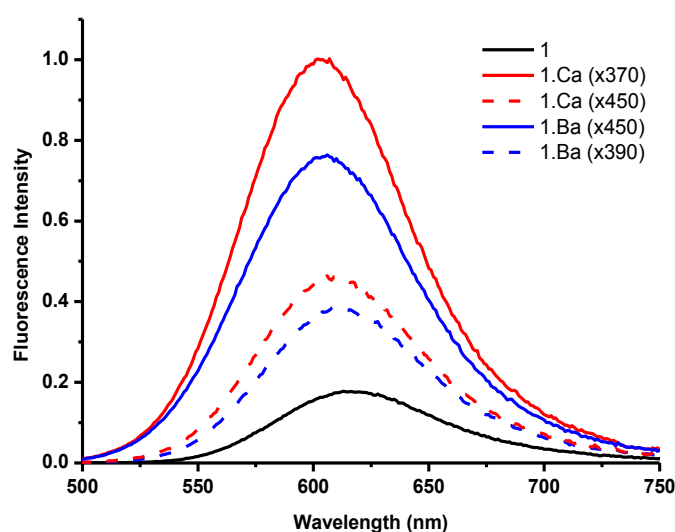


**Fig.3.19:** The emission spectra of **C1** and its complexes with cation by different excitation wavelengths.

**Table-3.2:** The quantum yield of fluorescence of **C1** and its complexes

	Emission (nm)	Quantum yield (%)
<b>C1</b>	617	<b>1.4</b> (exc 450)
<b>C1.Ca</b>	610	<b>3.4</b> (exc 450)
	604	<b>4.7</b> (exc 370)
<b>C1.Ba</b>	612	<b>3.4</b> (exc 450)
	606	<b>4.1</b> (exc 390)
<b>C1.H</b>	402	<b>0.2</b> (exc 330)

Excitation of both UV and visible bands causes a slightly blue shifted emission with an increase in quantum yield of fluorescence in comparison with noncomplexed dye. In the presence of  $\text{Ca}^{2+}$  and  $\text{Ba}^{2+}$ , very likely a stacking dimer complex, in other words, a sandwich complex forms as shown in Fig.3.20. Looking to their spectra, it is seen an absorption band at the similar position of main absorption band of free **C1**. This can be explained in such way:

One of the molecules (**C1a**) of the sandwich is shifted with respect to other molecule (**C1b**). The nitrogen of the azacrown of this shifted-**C1a**- molecule is closer to cation than **C1b**. This means that the donor part of **C1b** molecule is less affected. This geometry of sandwich causes two absorption bands in the complex spectrum, one is at UV which corresponds to **C1** with closer to cation lying nitrogen and the second band corresponds to **C1** with less affected donor.

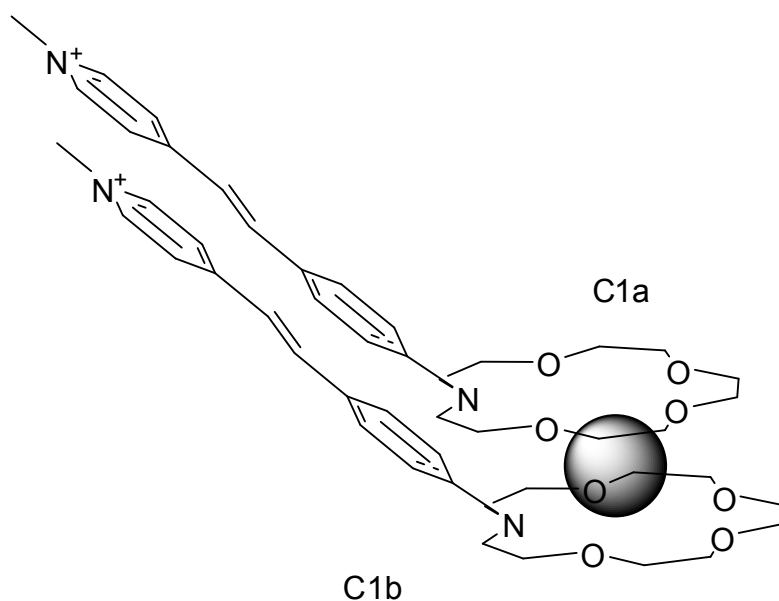


**Fig.3.20.** *The model of complex of C1 with cation.*

Equally, the environment of molecules in the dimer is not the same as that of the free molecules. Complexation with cations affects the electronic structure of the molecules. The shifts can be seen on fluorescence emission due to these reasons. The cause of shifts will be discussed on following parts in detail.

### 3.1.4. Fluorescence Anisotropy<sup>11,10</sup>

When a population of fluorophores is illuminated by a polarized light, those, which have the transition moment parallel to the electric field vector of polarized light, have the highest probability of excitation. The transition moment of a fluorophore need not necessarily be precisely aligned with the z-axis to absorb light polarized along this axis. The probability of absorption is proportional to the  $\cos^2\theta$ , where  $\theta$  is the angle the absorption dipole makes with the z-axis. As a result of excitation with polarized light, the fluorophores that are partially oriented along the z-axis are also excited. This phenomenon is called photoselection. In solution, the distribution of excited fluorophores is anisotropic immediately after excitation. As a result of this, their emission is anisotropic (polarized) too. Later, the emission can become depolarized by a number of processes like Brownian motion. When the emission is parallel ( $\parallel$ ) to the direction of the polarized excitation the observed intensity is called  $I_{\parallel}$ . Likewise, when the emission is perpendicular ( $\perp$ ), the intensity is called  $I_{\perp}$ . These intensity values are used to calculate the anisotropy:

$$r = \frac{I_{\parallel} - I_{\perp}}{I_{\parallel} + 2I_{\perp}} \quad (45)$$

The theory for fluorescence anisotropy can be derived by consideration of absorption and emission dipoles orientation of a molecule, assuming that the absorption and emission

transition moments are parallel. Figure shows  $I_{\parallel}$  and  $I_{\perp}$  being proportional to the projection of the transition moment onto the axes.

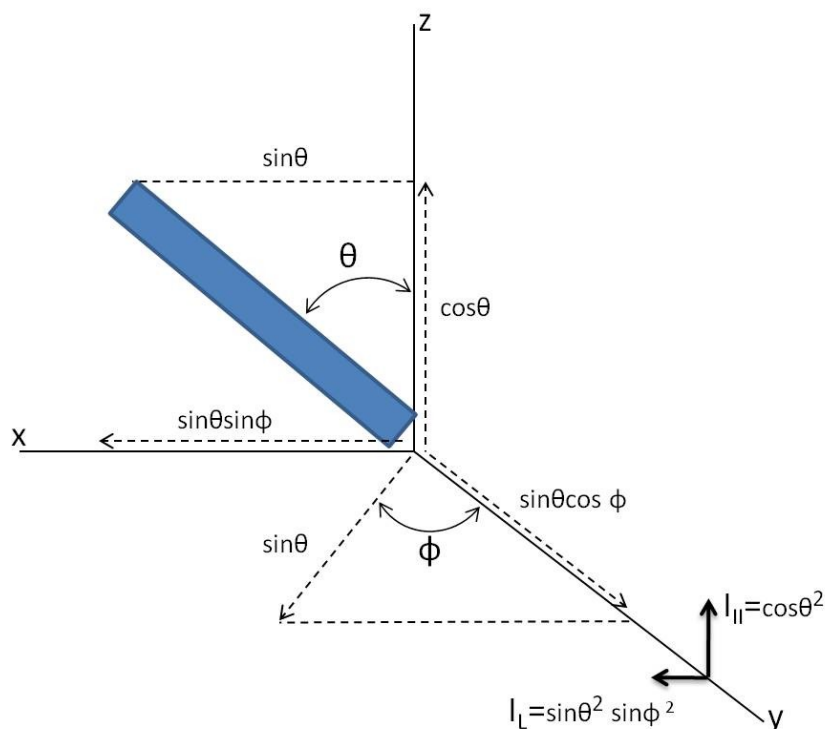


**Fig.3.21:** Emission intensities for a single fluorophore in a coordinate system (blue rectangle represents molecule).

The projection of the field onto the z-axis is proportional to  $\cos\theta$  and the intensity is proportional to  $\cos^2\theta$ . Similarly, the field along the x-axis is proportional to  $\sin\theta\sin\phi$ . The average value of  $\sin^2\phi$  is  $\frac{1}{2}$ . The intensities are given by  $I_{\parallel} = \cos^2\theta$ ,  $I_{\perp} = \sin^2\theta$ . Substituting these expressions into (45), anisotropy becomes:

$$r = \frac{3\cos^2\theta - 1}{2} \quad (46)$$

The maximum possible value of this quantity, assuming that the molecules are randomly oriented at excitation, have not rotated at all during the interval between excitation and fluorescence, and that the absorption and emission transition dipoles are parallel, is calculated as  $r_0 = 2/5$ .

While the dipole moments of emission and absorption are not always parallel, the anisotropy can be written:

$$r_0 = \frac{3\cos^2\beta - 1}{2} \times \frac{3\cos^2\alpha - 1}{2} \quad (47)$$

Here,  $\beta$  is the angle of dipole moment of absorption and  $\alpha$  is the angle between emission and absorption dipole moments. By averaging the equation (47) by time, the equation becomes:

$$r_0 = \frac{2}{5} \left( \frac{3\cos^2\alpha - 1}{2} \right) \quad (48)$$

$r_0$  is called fundamental anisotropy. It is a theoretical value in the absence of motion. Experimental value should be smaller than this value ( $-0.2 < r_0 < 0.4$ ).

To explain the change of anisotropy in time, we should consider the case in which the molecules are dissolved in a solvent and undergo Brownian rotational movement due to solvent-solute shocks. The orientations of the molecules change as they rotate, so the fluorescence anisotropy will change.  $r_0$  will decay to zero.

$$r(t) = r_0 \cdot f(t) \quad (49)$$

where  $f(t)$  characterizes the dynamics of rotational motions and whose value is 1 at time zero. During the excited state life time, the fluorescence of the molecules is depolarized by effect of following factors:

- Orientation changes between absorption and emission transition moments
- Brownian motion
- Transfer of excitation energy to another system/molecule
- Torsional vibration

Since all these factors cause fluorescence anisotropy changes (decay), the fluorescence anisotropy experiment is a useful tool to get information about the dynamics of molecular systems. Information about the size and shape of a molecule, as well as its interaction with the surrounding solvent and with other molecules, can be obtained. The reorientational motion of a solute molecule in fluids may be treated as a form of rotational Brownian motion. It can be described by the Langevin equation. In this model, the total torque acting on the molecule is separated into the frictional torque, which is proportional to the angular velocity of the molecule, and a random torque<sup>85,86</sup>.

$$I \frac{\partial}{\partial t} \vec{\omega}(t) = \zeta I \vec{\omega}(t) + \vec{T} \quad (50)$$

Here,  $\vec{\omega}(t)$  angular velocity,  $\zeta$  is the microscopic friction of solvent,  $I$  moment of inertia of solute and  $\vec{T}$  is the torque. After some assumptions, finally the equation for anisotropy decay can be simplified as follows:

$$r(t) = C \exp\left(-\frac{6kT\tau}{I\xi}\right) \quad (51)$$

and anisotropy decay time can be expressed:

$$\tau = \frac{I\xi}{6kT} \quad (52)$$

In our time resolved fluorescence experiment, we have measured the anisotropy decay times for **C1** and its complexes with  $\text{Ca}^{2+}$  and  $\text{Ba}^{2+}$  cations and different kind of dyes for

comparison. All solutions were prepared in acetonitrile. Moments of inertia for all molecules were calculated by CHEMOffice software<sup>87</sup>. We proposed a sandwich-dimer model for the complexes of C1 with cations. In Fig.3.22, it is shown on the graph; the anisotropy decay time versus moment of inertia of molecules.

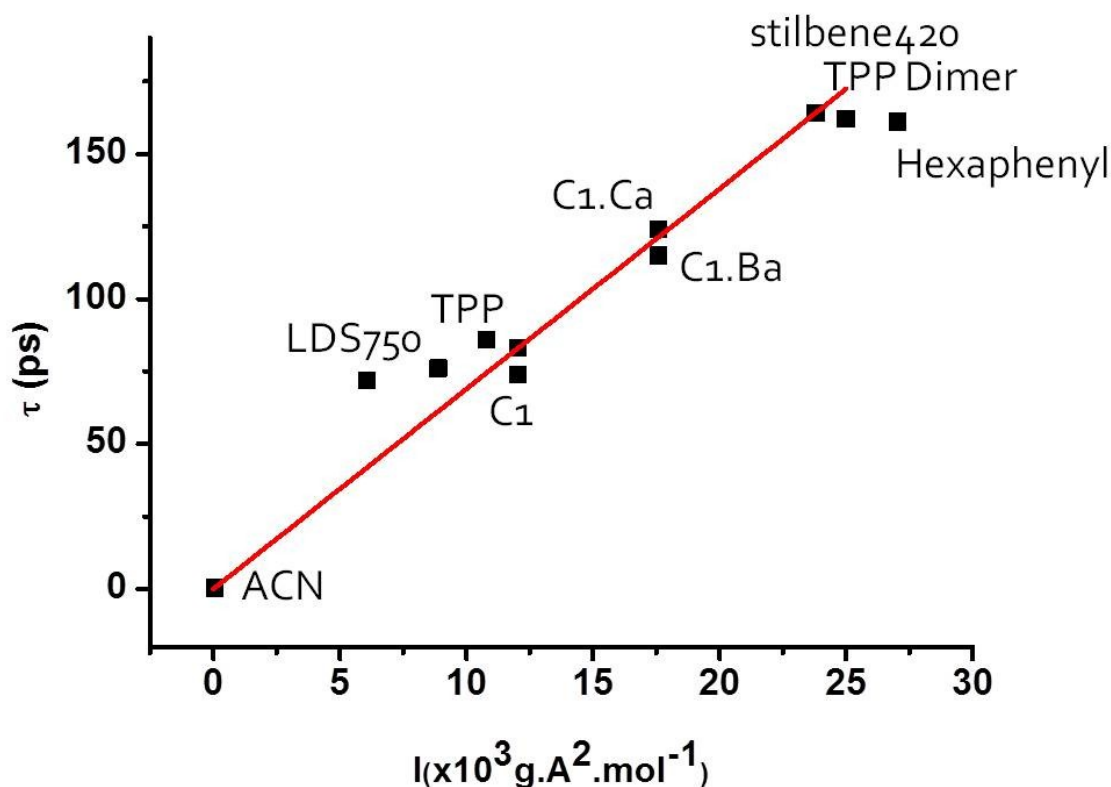


**Fig.3.22:** The anisotropy decay time versus moment of inertia of molecules.

According to equation (52), the slope should give the microscopic friction of acetonitrile. This value found in the literature<sup>88,89</sup>  $4.10^{-12}\text{s}^{-1}$ . From the slope, microscopic friction of acetonitrile is calculated  $10^{-13} \text{ s}^{-1}$ . The inconsistency of results can be explained in few ways. First, calculation of moment of inertia is done just for the molecule. But in real world, some of the solvent molecule can be attached on molecules. This increases the values of moment of inertia. Secondly, Hubbart<sup>90,91</sup> is proposed a factor  $p$  for correcting the equation (52). The  $p$  factor is added to account for the fact that not every interaction that leads to molecular reorientation will necessarily coincide with the rotational motion along the reaction coordinate. Taking into account this factor explains the difference between calculated value and the real value.

In summary, we worked with different molecules with different fluorescence anisotropy decay times. The moment of inertia of each molecule was calculated. For the calculation of moment of inertia of the complexes of **C1** with  $\text{Ca}^{2+}$  and  $\text{Ba}^{2+}$ , we used sandwich dimer model we proposed in previous chapter. By using the relationship between decay times and moment of inertia given in equation (52), a graph can be drawn, that its slope should give a certain number ( $\frac{\xi}{6kT}$ ). Looking to Fig.3.22, It should be noted that all data are on the same slope. Due this fact we can say that our proposed model is true for **C1** and its complexes.

### 3.1.5 Time-Resolved Study

In previous parts, it is mentioned that the absorption spectra of complexes show two bands; one band is at 474 nm which is the same wavelength with free molecule and the other is at the UV. Looking to these complex spectra a sandwich dimer model is proposed which consists of two molecules that the nitrogen of crown of one molecule is less affected by cation compare to other. When the band at 474 nm is illuminated, an emission at 610 nm is observed, which is close to free molecule emission at 617 nm. The Stokes shift is  $4703 \text{ cm}^{-1}$ . Emission by excitation the UV band is observed at 606 nm. The Stokes shift is  $10526 \text{ cm}^{-1}$ . This enormous shift is caused from the drop of the energy level of complex to the free ligand energy level. The reason of this drop can be explained in two ways: the decomplexation of cation or the energy transfer between the molecules of sandwich. To get a deeper comprehension, pump-probe experiments in ps scale were done. Fig.3.23 shows the 2D transient absorption image of the complex with  $\text{Ca}^{2+}$ .

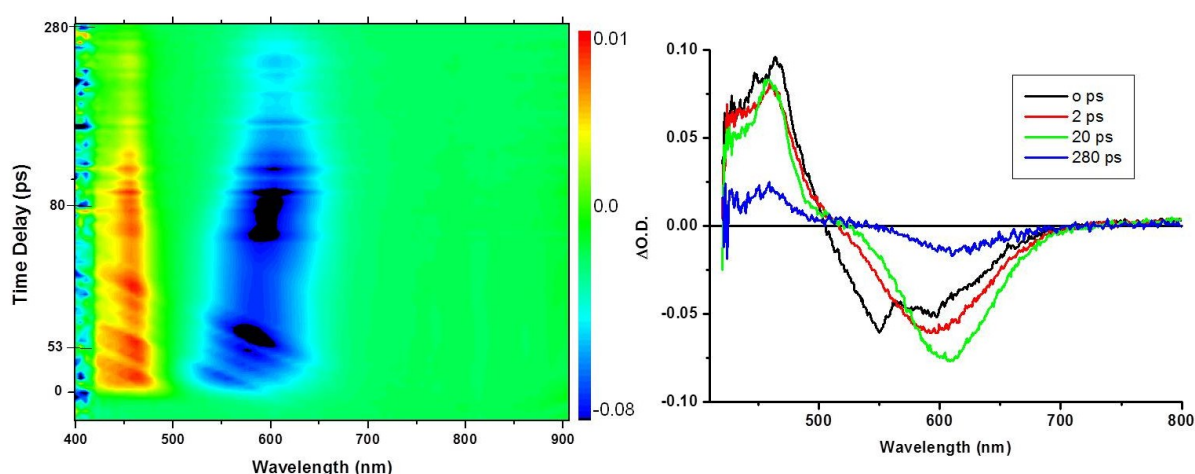


**Fig.3.23:** *Transient absorption of  $\text{C1.Ca}^{2+}$  ( $\lambda_{exc}=360 \text{ nm}$ ).*

A positive band with a maximum at 450 nm and a negative band between 500 and 650 nm, which have same decay time of 270 ps, are observed. No other transient features are observed. The positive band is attributed to excited singlet state absorption band and the negative band is the stimulated emission band. The stimulated emission is shifting to red in time.

Mathevet *et al.*<sup>92</sup>, described the decomplexation process of a similar hemicyanine dye as taking 4 ps. Martin *et al.*<sup>37</sup> were found the decomplexation time of 30 ps for another hemicyanine dye. However, we could not observe any changes on the transient spectra which can support the decomplexation of the molecule. Mukamel *et al.*<sup>93</sup> reported the energy transfer between different chlorophyll dimers ranging 150 fs to 500 fs.

No transient signatures corresponding to neither decomplexation nor the energy transfer were found.

Considering that a probable decomplexation process takes 4 ps and the energy transfer is faster (it can be supposed that it is much faster between same types of monomers) the typical decomplexation signatures will not be seen in the transient absorption signal. It can be even supposed that the energy transfer occurs in few tens of fs (having in mind a favourable disposition of ligands, see Fig. 3.20), which is shorter than our resolution, making impossible the observation of the first step of de-excitation occurring with such process rate.

The quantum chemical calculations done by MOPAC by using PM6 method are given on Fig.3.24. The HOMO orbital is located on one molecule and LUMO is located on other.

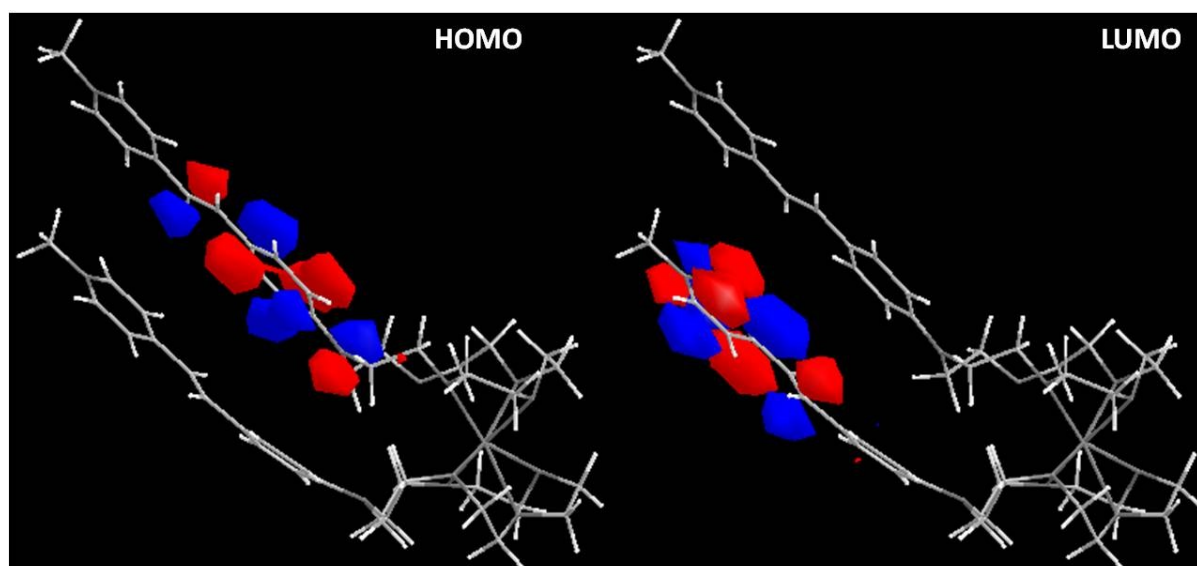


**Fig.3.24:** *HOMO and LUMO of C1 complex.*

When the molecule (**C1a**), which is more affected by cation in sandwich dimer and causes the absorption band at UV, is excited, it transfers its energy to the molecule (**C1b**), which is less

affected by cation. **C1b** is relaxing by emission at 604 nm in the case of  $\text{Ca}^{2+}$  and 606 nm in the case of  $\text{Ba}^{2+}$ . When **C1b**, which causes the absorption band at 474 nm, is excited, the emission is observed at 610 nm in the case of  $\text{Ca}^{2+}$  and 612 nm in the case of  $\text{Ba}^{2+}$ .

In transient absorption spectrum, a shift to longer wavelengths on gain band was observed. Fig.3.25 presents the maxima of the gain band in time delays. The lifetime of this shift is determined to be 116 ps.

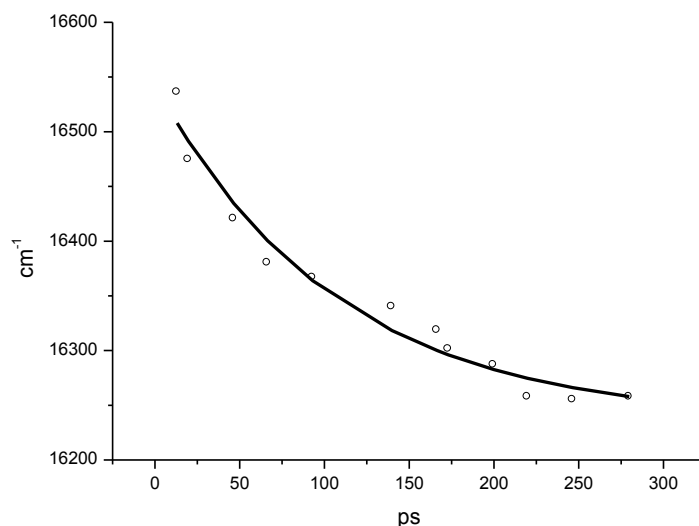


**Fig.3.25:** *The temporal and spectral shift of emission maxima of C1.Ca<sup>2+</sup>.*

The similar shift is also observed on time resolved fluorescence spectra of complexes. Fig.3.26 shows the shifts on fluorescence decays of **C1.Ca<sup>2+</sup>** and **C1.Ba<sup>2+</sup>**. The fluorescence lifetimes are given in Table-3.3.

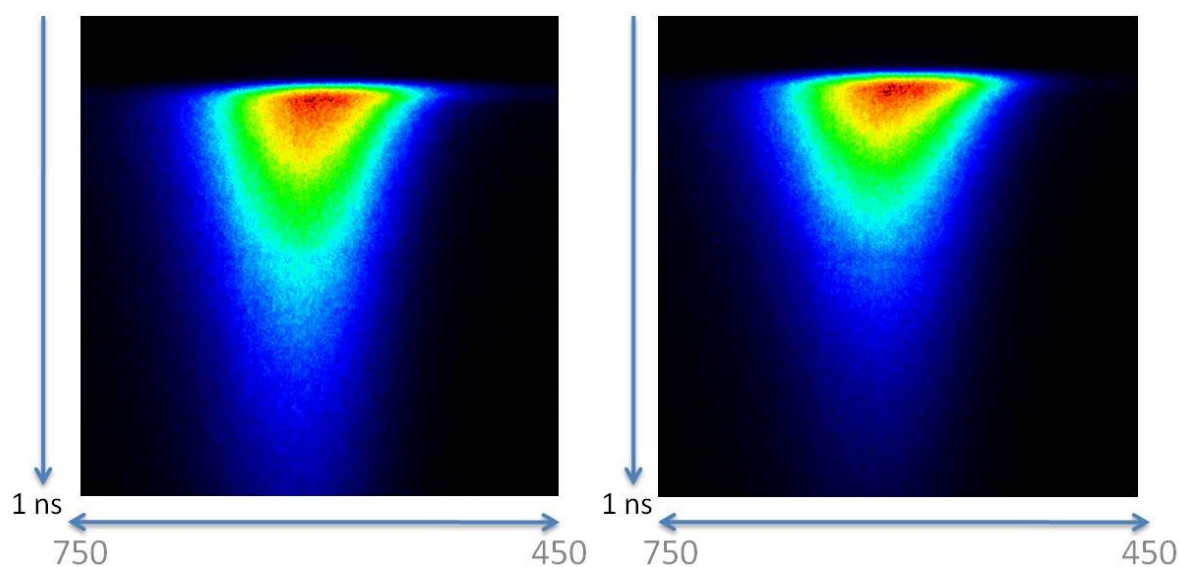


**Fig.3.26:** *Time resolved fluorescence of the C1 complexes, Ca<sup>2+</sup> (left), Ba<sup>2+</sup> (right)*

For these experiments acetonitrile was used as solvent, in which solvation occurs within 200 fs<sup>94</sup>. The duration of the shifting is around 120 ps. This time is too long to be solvation of molecules.

**Table-3.3:** Fluorescence lifetime of **C1** and its complexes in  $CH_3CN$

	$\tau_F$ (ps)
<b>C1</b>	73
<b>C1.Ca<sup>2+</sup></b>	257
<b>C1.Ba<sup>2+</sup></b>	185

If we recall the fluorescence anisotropy experiments, in Fig.22, it can be figured out that the anisotropy decay time for **C1.Ca<sup>2+</sup>** is 115 ps and **C1.Ba<sup>2+</sup>** is 124 ps. The similarity of these two numbers with the duration of fluorescence (stimulated emission) band shifts is not a coincident. When the molecule **C1a** is excited, it quickly transfers energy to **C1b**. **C1b** takes apart from **C1a** while relaxing. The moment of inertia is calculated for the molecule **C1** that can rotate only around its crown end. The moment of inertia calculations, which were presented in section 3.1.4, were corrected considering this one-end fixed dimer model. Looking in Fig.3.22, the results are compatible with reference data after correction.

According to the theory of fluorescence anisotropy, using  $r_0$  values of **C1.Ca<sup>2+</sup>** and **C1.Ba<sup>2+</sup>** into eq.48,  $\alpha$  is found 30°. It can be concluded that **C1b** after energy transfer takes apart 30° from **C1a**.

## Conclusion

Molecule **C1** was studied in solution in different solvents and with different cations. A model was proposed to explain the results: **C1** molecules built a sandwich dimer. This sandwich dimer model is also confirmed by comparison fluorescence anisotropy decay times. Transient absorption experiments show that there is no decomplexation in excited state but an energy transfer between molecules of dimer is possible. Due to fluorescence anisotropy experiments and transient absorption experiments it is found that after energy transfer molecule is relaxing by turning 30°.

## *PART II*

### 3.2.1. Langmuir-Blodgett films (LB films)<sup>95-98</sup>

Langmuir-Blodgett films (LB films) are monolayers transferred from the water-air interface onto a planar substrate, which is silica plate in this study. Molecules solubilised in a volatile solvent are first spread at the air-water interface of a Langmuir trough equipped with two compression barriers (Fig.3.27). After evaporation of the solvent, molecules are compressed, whereas the changes of surface tension of the interface (due to the formation of a two dimensional molecular system) is measured, thanks to a Wilhelmy plate partially immersed into the aqueous subphase. Monolayers are formed on the surface of the water by molecules called amphiphiles, which consist of two parts. One part is hydrophilic (usually polar) and usually referred to the “head” group. The second part is hydrophobic- for example one or more saturated alkyl chains, so called “tails”. If the tail is hydrophobic enough, this makes the molecule insoluble in water. These molecules form a two dimensional system on the surface of water. By changing the surface pressure ordered molecular assemblies can be constructed. Applications of monolayers are various. They are excellent model systems for biological membranes, since those can be considered as two weakly coupled monolayers.

Phase transitions of monolayers from liquid like to crystalline give the opportunity to study the structure changes related with intermolecular interactions.

The most important indicator of the monolayer properties of a material is given by a plot of surface pressure as a function of the area of water surface available to each molecule. This experiment is carried at constant temperature and is called as a surface pressure/area isotherm,  $\pi$ -A isotherms. Fig.3.27 shows the relationship between the variations of surface pressure and mean molecular area changes of molecules due to their reorganization in monolayer.  $\pi$ -A isotherm, that is to say a plot of the surface pressure  $\pi$  as a function of mean molecular area A, carried out at a constant temperature. Surface pressure is defined as  $\pi = \gamma_0 - \gamma$ , where  $\gamma_0$  and  $\gamma$  are the surface tension of pure water or water covered with a monolayer. Mean molecular area is defined as  $A = \frac{S}{N}$ , where S is the surface between the two barriers and N the total number of molecules spread at the air-water interface.

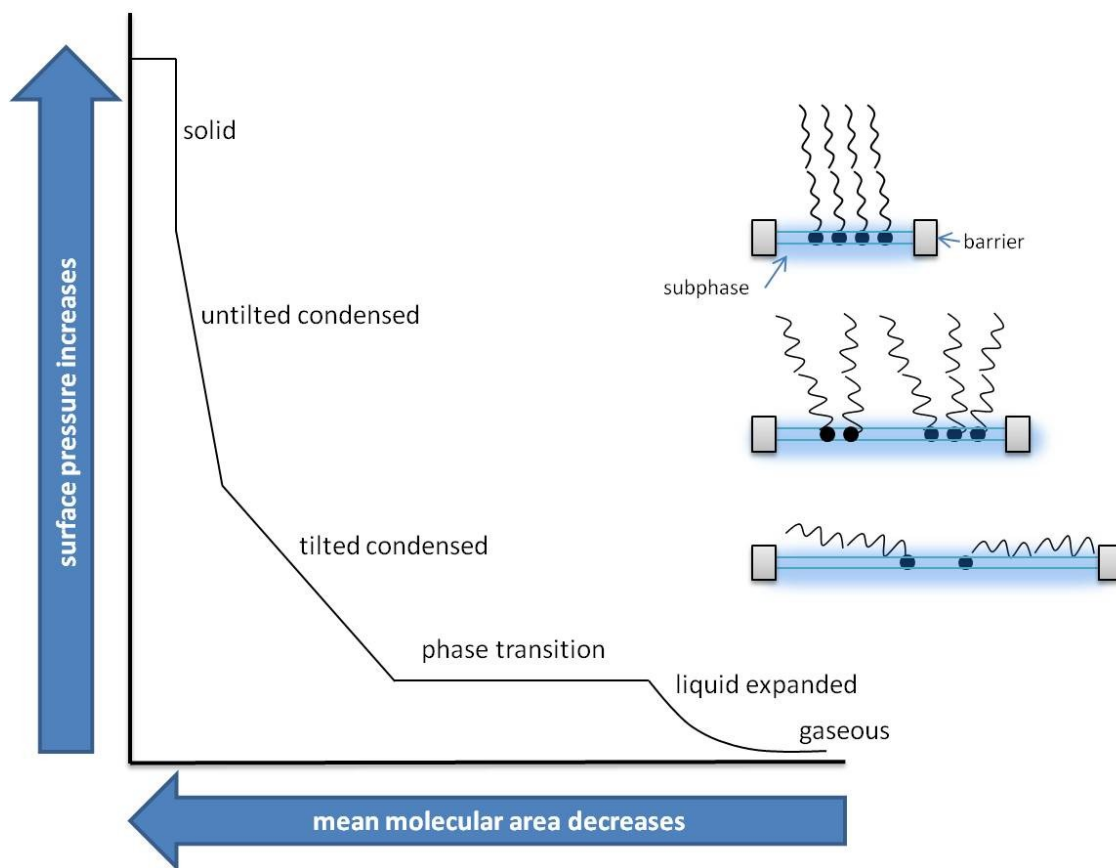


**Fig.3.27:** A schematic diagram of a Langmuir trough (top) and a generalized isotherm of a Langmuir monolayer.

The very dilute monolayer, characterized by a mean molecular area in the range of hundreds of square angstroms, is well described as a two-dimensional gas. By compressing the monolayer, surface pressure increases whereas mean molecular area decreases. The monolayer proceeds into what has traditionally been called the liquid expanded phase. In this phase, molecules are in a fluid and disordered state. Further compression of the monolayer gives rise to a transition from liquid expanded phase to a condensed phase with (usually) a plateau indicating a first-order phase transition between these two phases. The monolayer is less compressible in the condensed state than in the liquid expanded state. Upon further compression one typically observes a kink on the isotherm, with the compressibility decreasing further after the kink. The two regions of the isotherm possessing different compressibility are frequently referred to as “liquid condensed” and “solid” states. A compression beyond the solid state leads to the collapse: the monolayer breaks and multilayers form at the air-water interface. Thus the isotherm is crucial in order to obtain at least partial information on the processes occurring at the molecular level. Moreover, the shape of the isotherm depends strongly on many experimental parameters such as subphase

temperature, speed of compression, molecules intentionally dissolved into the subphase interacting with the monolayer or eventual impurities.

In our experiments, surface pressure measurements were carried out in air by using a 601M Nima Langmuir trough (approximately 19 cm x 12 cm x 0.5 cm) equipped with a Wilhelmy balance (Nima). Pure Millipore water or aqueous solutions of barium or calcium perchlorates (0-10mM) were used as subphase. Hemicyanine molecules were dissolved in chloroform at a concentration in the 0.5-1 mM range and spread at the air-water interface. After of the evaporation of chloroform (15 min), molecules were compressed continuously at a rate of 15 cm<sup>2</sup>/min. The temperature of the subphase was kept constant to 20 ± 1°C.

In the case of a LB transfer, a silica plate was immersed into the trough, perpendicular to the interface, before the molecules were spreading. After compression of the monolayer to the suitable surface pressure, this pressure between the two barriers was kept constant via surface pressure controlling system. In the case of hemicyanine monolayers, the surface pressure decreased slightly during 10 to 15 minutes, likely due to a reorganisation of molecules on the air-water interface. After this time of stabilization, the silica plate was removed from water at a constant speed of 20 mm/min, a hemicyanine monolayer being transferred on both sides of the plate.

All these experiments were performed under red light, in order to limit non desired photoreactions.

### 3.2.2. Isotherms

As mentioned above, the shapes of isotherms depend on many variations including temperature, impurities and speed of compression. By simply analyzing the  $\pi$ -A isotherms, the process of monolayer formation and physical properties of the molecular organization can be inferred from the shape of the  $\pi$ -A isotherms.

Fig. 3.28 and 3.29 show the  $\pi$ -A isotherms of **C2** spreading on pure water or on subphase containing different concentrations of Ca(ClO<sub>4</sub>)<sub>2</sub> and Ba(ClO<sub>4</sub>)<sub>2</sub>. The other experimental conditions (temperature and pH of the subphase) were kept at the same value for all experiments.

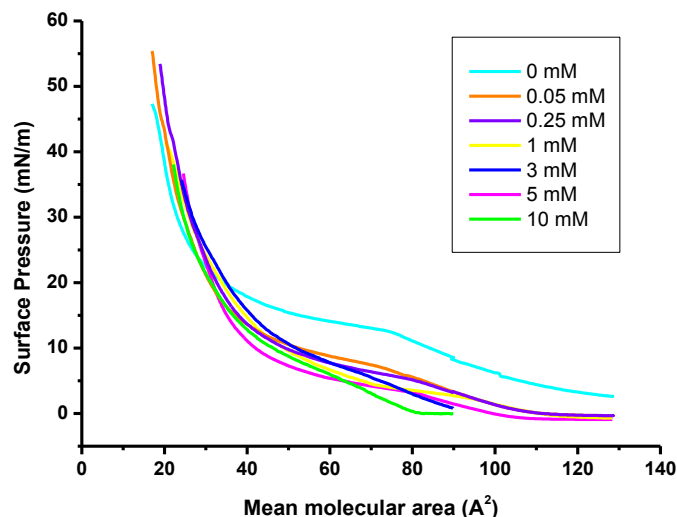


**Fig.3.28.** Isotherms of monolayers of **C2** on water subphase with different calcium perchlorate concentrations.

**C2** molecules form stable monolayers at the air-water interface.  $\pi$ -A isotherm (Fig.3.28, cyan curve (0 mM)) of the monolayer spread on pure water shows first a regular and monotonous increase of the surface pressure with compression at mean molecular areas between 130  $\text{\AA}^2/\text{molecule}$  ( $\text{\AA}^2/\text{m}$ ) and 75  $\text{\AA}^2/\text{m}$ . The surface pressure is not equal to zero at the beginning of the compression, because it was necessary to spread a rather high number of molecules to observe a complete isotherm, taking into account the size of the trough. An extrapolation gives an estimation of the onset mean molecular area around 160  $\text{\AA}^2/\text{m}$ . At the mean molecular area of 75  $\text{\AA}^2/\text{m}$ , an inflection of the isotherm followed by a well-defined plateau is observed: surface pressure remains almost constant around 15 mN/m until a mean molecular area of 40  $\text{\AA}^2/\text{m}$ . A further compression induces a steeper increase of surface pressure as compared to the first part of the isotherm, the final mean molecular area being around 20  $\text{\AA}^2/\text{m}$ .

The presence of  $\text{Ca}^{2+}$  or  $\text{Ba}^{2+}$  cations into the subphase (0.05-10 mM) induces changes on the isotherm, as shown in Fig.3.28 and Fig.3.29, respectively. By increasing the concentration of  $\text{Ca}(\text{ClO}_4)_2$  on subphase, the onset is shifting towards lower area per molecule. For example it is 110  $\text{\AA}^2/\text{m}$  for 0.05mM, 90  $\text{\AA}^2/\text{m}$  for 3mM and 82  $\text{\AA}^2/\text{m}$  for 10 mM of  $\text{Ca}(\text{ClO}_4)_2$  salt. This shift is not linearly dependent on the salt concentration.

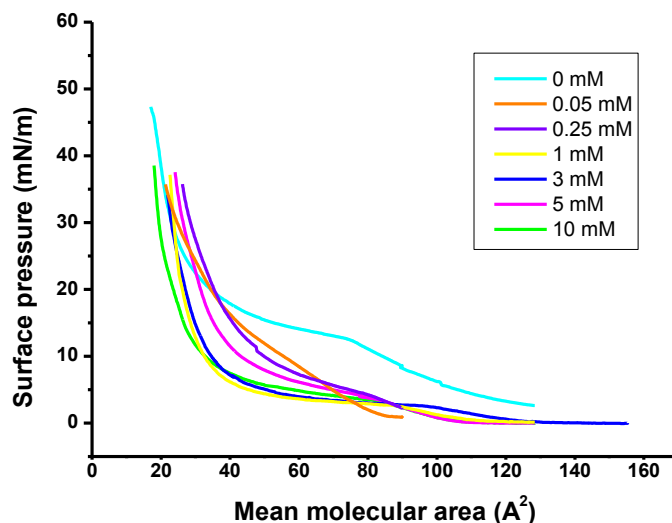


**Fig.3.29.** Isotherms of monolayers of C2 on water subphase with different barium perchlorate salt concentrations.

By increasing the  $\text{Ba}(\text{ClO}_4)_2$  concentration in the subphase, we observed a similar effect in the  $\text{Ca}(\text{ClO}_4)_2$  case. The onset value shifts to lower area per molecule. This shift is not regularly dependent on  $\text{Ba}^{2+}$  concentration. For example mean molecular area is  $114 \text{ \AA}^2/\text{m}$  for 10mM,  $130 \text{ \AA}^2/\text{m}$  for 3mM and  $104 \text{ \AA}^2/\text{m}$  for 0.5 mM of  $\text{Ba}(\text{ClO}_4)_2$ .

Another change concerning isotherms is the changes of the slopes of isotherms. By increasing the cation concentration, the smooth increase of isotherms becomes steeper. The smooth increase of isotherms is a sign of fluidity of monolayer. In pure water case, we observed a plateau at 12mN/m which means a new organization on the monolayer starts. After the plateau, the slope starts to become steeper when surface pressure increases. This steep slope means that molecules start to become organized, or in other words the monolayer becomes more solid. The slopes become steeper because of the decreasing on the compressibility of surface. This shows the mean molecular area between molecules is more rigid.

If we analyse now the isotherms in the presence of cations, for  $\text{Ca}^{2+}$  concentrations higher than 1 mM and for  $\text{Ba}^{2+}$  for already very low concentrations (less than 0.05 mM), the plateau still can be seen around 5 mN/m. For higher concentrations, a first order transition can no longer be observed. By increasing surface pressure, a steep increase of the slope of  $\pi$ -A isotherms is observed immediately, which means molecules interact with cations and organize already before compression starts. This is not a cation concentration dependent phenomenon. We also observed irregularity on the limiting area (area at high pressure when the

compressibility is lowest before monolayer isotherm breaks) of the isotherm curves. Mean molecular limiting area is approximately  $20 \text{ \AA}^2$  at  $40 \text{ mN/m}$  for all cases.

It can be clearly noted that the cation presence causes an onset shifting to lower areas and change on the steepness of the slope. This can be explained with a new organization of molecules at air-water interface by help of a cation.

Dye molecules when they are first spread onto the water are covered by a solvation shell consisting of water molecules. Strong H-bonding is observed between dye molecule and the water molecules. By decreasing the mean molecular area, molecules get closer to each other and their solvation shells superpose. When the density of molecules reaches a certain number, the available volume for water molecules becomes insufficient to form complete solvation shell for each solute. The water molecules between the molecules start to displace and intermolecular interaction between molecules become more pronounced which causes aggregation. When a cation is inserted into water, water molecules orient themselves towards cations. This reorientation affects hydrogen bonding in solvent shell. While the solvation shell is affected by the presence of cations, the aggregation procedure becomes also affected. The molecules are more eligible to make complexation and concerning the results from previous part, more likely they form sandwich dimers.

However, surface pressure measurements are not sufficient to precisely describe the behaviour of C1 molecules at the air-water interface. Our previous study in solution showed that absorption and fluorescence spectroscopies are useful to get information about their organization. Therefore, we transferred monolayers from the air-water interface onto planar supports for a complementary spectroscopic study.

### 3.2.3. Absorption of LB films

UV-visible absorption spectra of LB films were collected on a CARY 5G spectrophotometer (Varian), at normal incidence and at room temperature. Uncoated silica plate was used as absorption reference for LB films.

In Fig.3.30 and Fig.3.31 are shown the absorption spectra of monolayers transferred on silica plates at constant surface pressure of  $30 \text{ mN/m}$ . A sufficiently high surface pressure is necessary during the transfer to maintain the molecular cohesion from the air-water interface to the substrate.

In the case of monolayers transferred from a pure water subphase, two bands are observed in absorption spectrum which correspond  $S_1 \leftarrow S_0$  transition at 458 nm and  $S_2 \leftarrow S_0$  transition at 272 nm. In the presence of cations, important changes are observed.

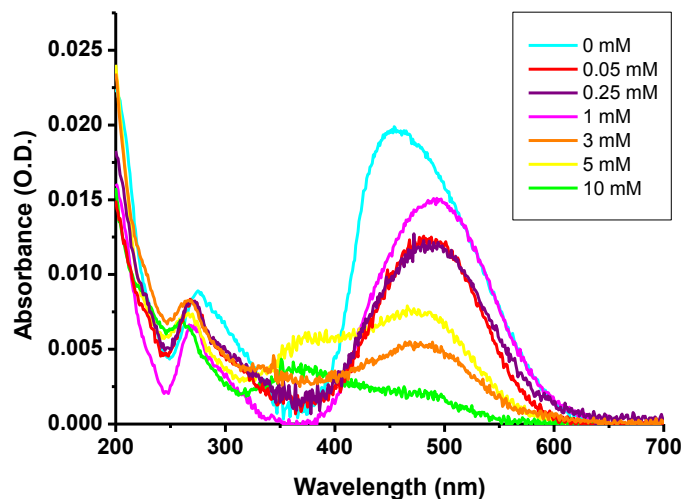


**Fig.3.30.** Absorption spectra of LB films of **C2** on silica obtained from subphases with different calcium perchlorate salt concentrations.

In the presence of cations, important changes are observed, even at the lowest concentrations. The absorbance changes manifest themselves as follows: 1) it can be strongly supposed that in the absorption spectrum of LB film obtained from pure water subphase the dominant feature could be attributed to the absorption of H-aggregates. This blue shifted absorption maximum as compared with the solution spectrum indicates the possibility of such an aggregation. In solution case, we have already observed aggregates formed due to low solubility. In the presence of cations, the main absorption band shifts to red until 500 nm, which can be explained by the same arguments proposed in the isotherm section. 2) Absorbance intensity is decreasing with increasing the cation concentration. The main absorption band is related to the charge transfer along **C2**. When cation concentration increases in the subphase, the complexation probability between cation and **C2** increases too. Coordination of cation by nitrogen of **C2** causes a decrease of the absorbance of the main band. At the same time, as a sign of complexation we start to observe a new band at 370nm.

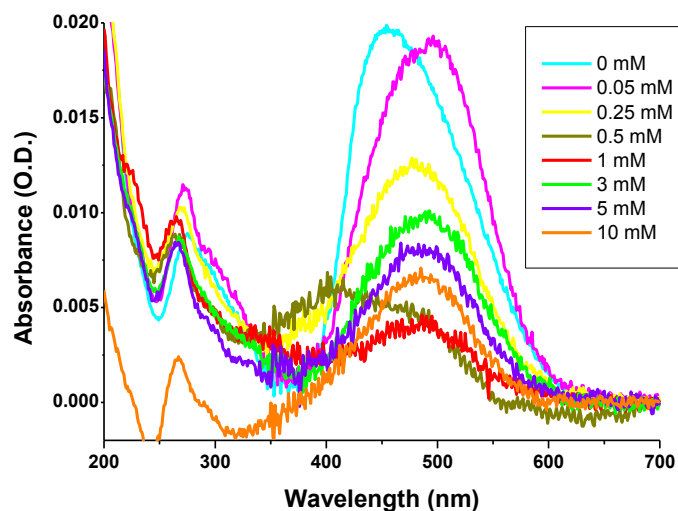


**Fig.3.31.** Absorption spectrum of LB films of C2 on silica obtained from subphases with different barium perchlorate salt concentrations.

$\text{Ba}^{2+}$  is more voluminous cation with respect to  $\text{Ca}^{2+}$ . Due to this fact, we expected differently affected monolayers in the presence of the barium cation. However, we could not observe notable disparities neither in isotherms nor in absorption spectra. Even a low concentration of  $\text{Ba}^{2+}$  causes a great change in the absorption spectra. The behaviour is similar to the case of the calcium cation: First, a shift to longer wavelength which means aggregate destruction followed by the decrease in absorbance by increase of cation concentration. Surprisingly, we observed a new absorption band due to complexation for lower  $\text{Ba}^{2+}$  concentrations in the subphase. The absorption spectra illustrate the formation of new organization step by step. The details of this new organization will be discussed in discussion section.

### 3.2.4. Fluorescence Emission of LB Films

Fluorescence emission spectra were recorded in a  $45^\circ$  degree configuration with a Fluoromax-3 spectrofluorometer (Jobin Yvon). An excitation wavelength of 500 nm was used for all samples. Spectra were corrected with respect to the absorption of each film at this wavelength.

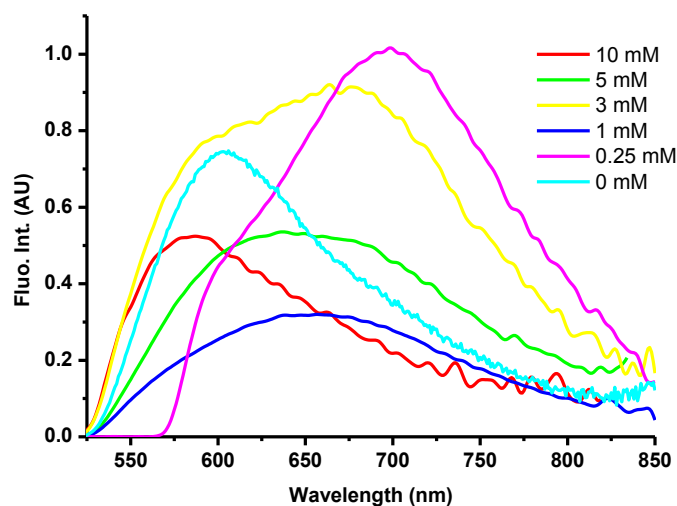


**Fig.3.32.** Smoothed fluorescence spectrum of LB films of **C2** on silica obtained from subphases with different calcium perchlorate concentrations.

Fig.3.32 shows the fluorescence spectra of LB films obtained from pure water and subphase with different  $\text{Ca}^{2+}$  concentrations. We observed a blue shifted aggregate emission at 600 nm on pure water. At 0.25 mM  $\text{Ca}^{2+}$  concentration, the fluorescence emission spectrum changes its shape. Now it has two bands at 600 nm and at 700 nm; the band at 600 nm still corresponds to the aggregate band. The band at 700 nm is due to the effect of complexation with calcium cation. As mentioned before, cations perturb the aggregation behaviour. Considering the behaviour of molecules in solution in case of complexation, we can conclude molecules can make sandwich dimers. By excitation of the molecule in the dimer can form an excimer, which causes a red shifted fluorescence as we observed in this situation. On 1mM, 3mM and 5mM concentration these two bands due to excimers and aggregates are still observed with different intensity ratios. On 10mM concentration, the shape of spectra changes again. A blue shifted emission band is observed at 575 nm. It can be concluded that with high concentration of cations causes a different formation on the films. Looking to its blue shift, this new formation can be thought as an aggregation including cations.

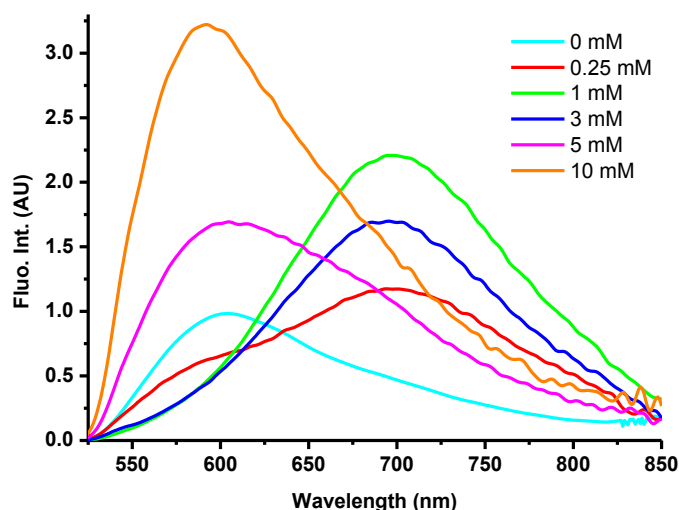


**Fig.3.33.** Smoothed fluorescence spectrum of LB films of C2 on silica fabricated on subphases with different barium perchlorate salt concentration.

The fluorescence spectra of LB films fabricated on  $Ba^{2+}$  solution is seen on Fig.3.33. Similar behaviour as in calcium case was observed for the case of barium. The transition between species can be seen more clearly for  $Ba^{2+}$  case. At 0.25 mM concentration, excimer emission at 700 nm starts to be seen instead of aggregates. On 1 mM concentration subphase we have observed just excimer emission spectrum and excimer intensity decrease by addition of  $Ba^{2+}$  as seen on spectrum of 3 mM. On 5 mM two bands start to be seen which belong to excimer and aggregates. At 10 mM blue shifted aggregate emission is seen at 575 nm.

Surface pressure and spectroscopic measurements give information on the organization of molecules into the LB films (monomer, aggregate, excimer). However, it is useful to complete this information by observing directly their morphology. Hemicyanines being intrinsically fluorescent, fluorescence microscopy is particularly suitable since no additional fluorescent probe is needed.

#### 3.2.4. Fluorescence Microscopy on LB Films

The silica plate covered with the monolayer was placed on the stage of a fixed-stage upright microscope (BX51WI from Olympus) equipped with a 100 W mercury lamp (U-LH100HG), a BX-RFA illuminator, and an U-MWBV2 (excitation at 400-440 nm, emission above 475 nm) or U-MNB2 (excitation at 470-490 nm, emission above 520 nm) filter cube. LMPF1 x10, x20, x50 objectives were used for imaging. Images were recorded with a Color View II CCD camera from SIS (Germany). Acquisition times were on the whole in the 1-5 s range. At least

3 images were taken at different points of the monolayer. The lateral resolution of our setup was in the 0.4-0.6  $\mu\text{m}$  range according to the numerical aperture of the objectives. Images of LB films are presented in Fig.3.34.

Images 1 and 2 correspond to LB films transferred at 30 mN/m from pure water. These images show that these films are rather homogenous, which could support the hypothesis of aggregated molecules forming a homogenous phase (the dark part on the right side of the image 1 is the non-covered silica plate). However, on image 2, we observe also a dark island on the right side. This island can be due to differently organized molecules (affected for instance in a different way by pH or temperature), or the presence of local defects or dusts on the silica plate.

Images 3, 4 and 5 belong to LB films prepared varying concentrations of cations (0.25-5 mM  $\text{Ca}^{2+}$  or  $\text{Ba}^{2+}$ ). They show different formations on the same film. There are bright fluorescent spots and also some less/non fluorescent structures on films. This means both aggregates and excimers can be seen at same time in a film. The last image, 6 is prepared on 10 mM concentration of  $\text{Ca}^{2+}$ ), shows a homogenous film. This homogeneity can be due to aggregation.

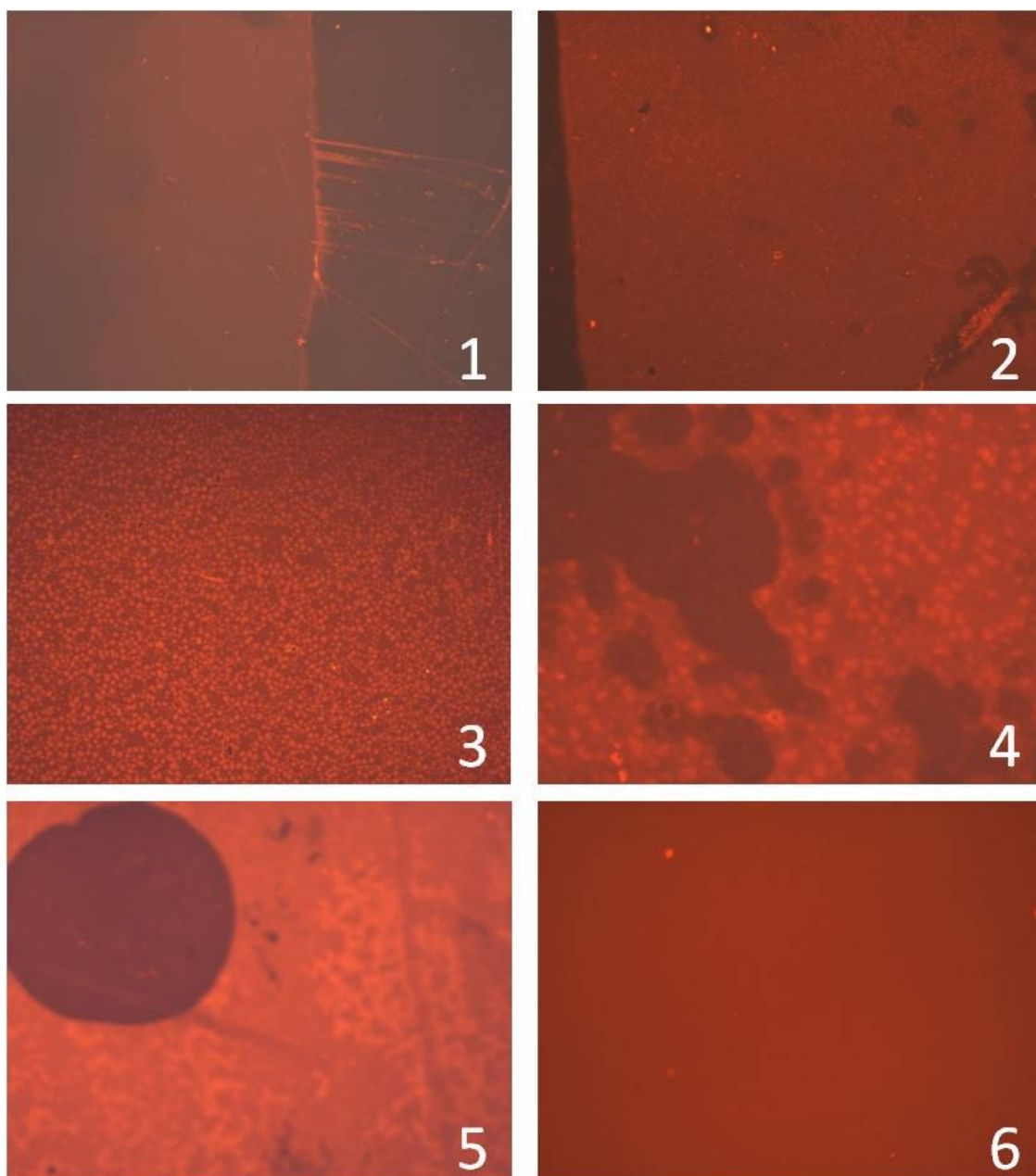


**Fig.3.34:** *The fluorescence microscopy images of LB films (For all images, U\_MNB2 (excitation at 470-490 nm, emission above 520 nm) is used as filter. x10 objective is used for the images 3 and 4, x20 objective is used for the rest. 1 and 2 are the images of the films of pure water subphase. 3, 4, 5 and 6 belong to films of varying concentrations of cations.).*

### 3.2.6. Discussion

When we spread the molecules on air-water interface, the molecules start to aggregate at relatively low surface pressure (12 mN/m) and to form H-aggregates. One of the important factors influencing the aggregation is the hydrogen bonding between water molecules and the amino group and the ethers of the crown. Thus, the solvent (water) shell is around the solute and this makes spontaneous aggregation impossible. One needs to apply some initial pressure in order to disturb the solvent shell and to start the aggregation as explained in 3.2.2.

On the other hand, introducing even low concentrations of cations (e.g. changes on pH) in water or small temperature changes will spectacularly affect this shell stability. The solvation shell around molecules in water, principally produced by hydrogen bonding, is broken when ions are present (for example cations coordinated by N atom of the crown) and the solvation shell can be easily removed even by the Van der Waals interaction forces between two dye molecules forming the sandwich. Then, if the complexation occurs, involving two molecules, they can spontaneously form sandwich dimer maintained in head-to-head geometry by Van der Waals interaction. The sandwich geometry thus reduces overall concentration of molecular units involved in film formation twice, and this reduces the mean molecular possible area without applying any force (barrier moving) approximately two times with respect to the situation we observed on pure water subphase. On further area decrease, we observe the change of slope meaning that the interaction between sandwiches in film begins, i.e. the sandwiches begin to aggregate. We can strongly suppose that the monolayer formation up to higher pressure is simply making aggregate denser; the transfer to silica plate is not further affecting the aggregate (of sandwiches) structure. By excitation these aggregates we can see the emission of the excimer. Quite probably, this excimer is formed from two molecules belonging to two different sandwiches. We have observed also the photoreaction between molecules in aggregates which is still one more evidence supporting our hypothesis about film in the form of aggregates of sandwiches.

The aggregates of sandwiches (Fig.3.35) behave in different way with respect to the cation (Fig.3.36). Since the  $\text{Ca}^{2+}$  is small, it can move easily between two molecules of the sandwich thus these molecules are affected similarly by the cation. As a result of that we observed one band in absorption spectra of the films for low concentration subphase.

Barium cations have larger size respect to calcium cations while they cannot move easily like calcium cations.  $\text{Ba}^{2+}$  is coordinated by the molecules of sandwich; however the crowns of the sandwiches are tilted like the sandwich dimer in solution. As a result,  $\text{Ba}^{2+}$  is closer to the

amine group of one molecule than the other. Finally, we observed more easily two bands in absorption spectra of the films for low concentration subphase.

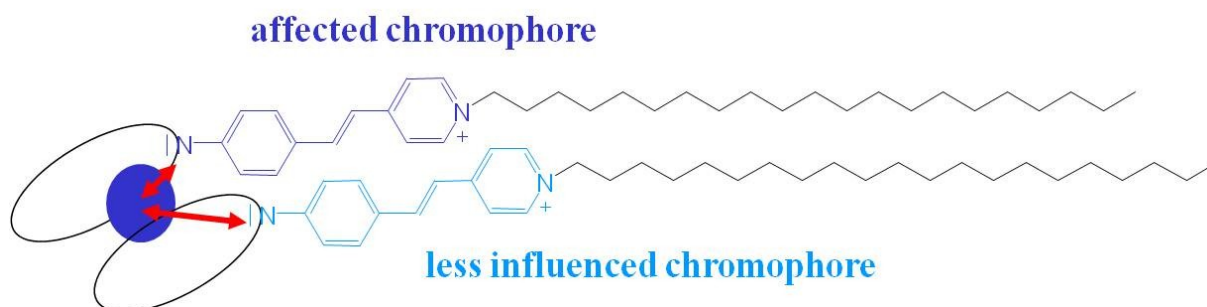


**Fig.3.35:** The model for the case of low concentration of cations.

When the concentration of cations in the subphase increases, the cations start to enter between sandwiches. The aggregation of sandwiches is not mentioned elsewhere. The new aggregates consist of ordered molecules and cations between them.  $\text{Ca}^{2+}$ , because of its smaller size, can enter into the crown. As cation concentration becomes higher, two bands start to be observed on the absorption spectra of the films. It is consistent with molecules forming a ladder-type arrangement. This situation leads to separation of molecules in to two. One kind of molecule can be affected by the cation of their crown; the other kind of molecule is affected not only by  $\text{Ca}^{2+}$  cations in their own crowns but also they can be affected by the cations of the neighbour molecules. As a cause of this situation the absorption spectra of films for high concentration subphase have two bands.

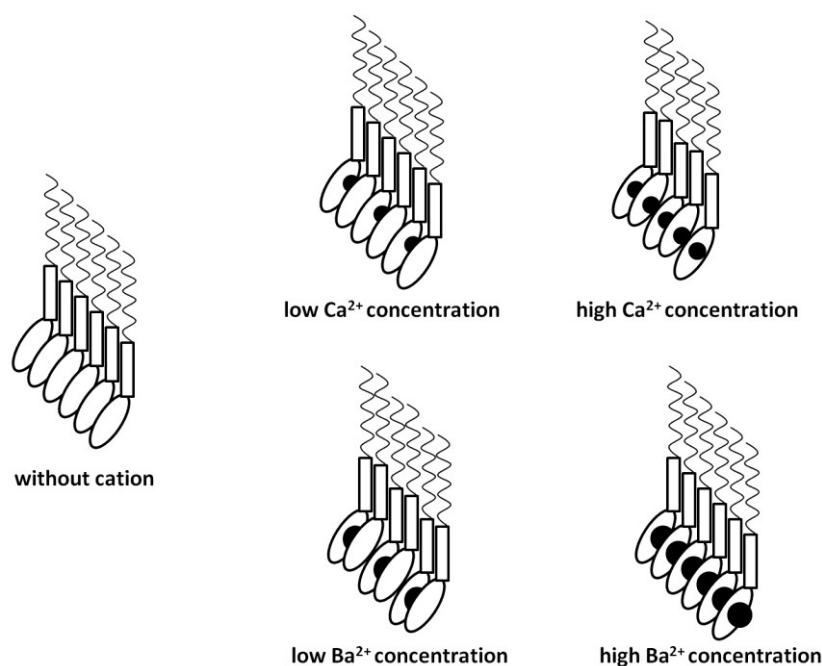


**Fig.3.36:** The behaviour of molecules on monolayer in the presence and absence of cations.

We have observed another phenomenon on the absorption spectrum of the film on the high concentration subphase. In Fig.3.37, the black curve is the absorption spectrum of the film on 10mM  $\text{Ca}^{2+}$  subphase. When the film was kept in 80°C during few hours, the absorption spectrum becomes the spectrum shown in the red curve. A new absorption band is seen at 230 nm and intensity ratio of the bands at 370 nm and 450 nm is changed. Molecules in the aggregates make photoreaction with neighbour molecules: the double bond of the chromophore opens and forms bond with neighbour molecules, which can be the cause of new band at deep UV. This photoreaction causes a more ordered ladder type organization in aggregation.

Once, the band at 230 nm is illuminated, the absorption spectrum turns out to be the spectrum shown in the green curve. The band at 230 nm vanishes, but the ratio of the bands (370 nm/450 nm) still remains, which shows the more ordered organization still remains.

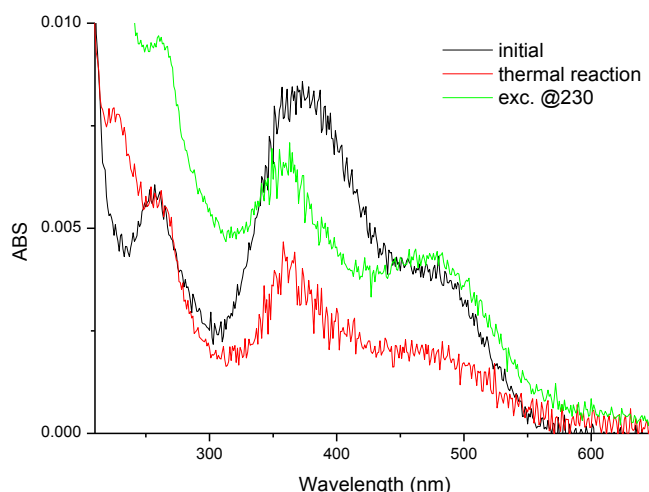


**Fig.3.37:** The absorption spectrum of the film on 10mM  $\text{Ca}^{2+}$  solution subphase in different conditions.

For higher concentrations,  $\text{Ba}^{2+}$  does not show the same results as calcium (Fig.3.36). Due to their relatively large size,  $\text{Ba}^{2+}$  cations cannot enter the crowns. The cations are coordinated by two adjacent molecules. The tilt of the crown is still valid for this situation also. In this aggregation with cations, each molecule is affected by two cations that one is closer to molecule with respect to the other.

Since this situation is repeated along all aggregate, each molecule of the aggregate has the same distribution by cations. As a cause of this, the absorption spectra of films for high concentration subphase have one absorption band. The aggregates of these ordered molecules

with cations between them can be described as an H-aggregate too. The emission spectra of these are even more blue shifted compared to H-aggregates formed on a pure water subphase. In both of cases, as seen by fluorescence microscopy images, aggregates, dimers, excimers can be seen on a film at the same time. Temperature, pH of water, the quality of silica plate can affect these formations. The effect of pH was already worked, while the effect of temperature on the formation of films can be a goal of future research. A homogenous cation responsive film has been formed and studies show encouraging results for artificial membrane development.

## Chapter 4

# Fast Processes in BF<sub>2</sub>-dipyrromethene (BODIPY) - type dyes

### Introduction

BF<sub>2</sub>-dipyrromethene dyes, commonly referred BODIPY dyes, were first described by Treibs and Kreuzer in 1968<sup>99</sup>. Since then, the BODIPY dyes have been widely used for monitoring biomolecules in living cells<sup>100</sup>, attaching to proteins<sup>101</sup>, viruses<sup>102</sup>, etc. Their high emission quantum yield, high extinction coefficient<sup>103, 104</sup> and high photostability allow them to be used as laser dyes<sup>105</sup>, nanocrystals<sup>106</sup>, fluorescent switches<sup>107, 104, 108</sup>, chemosensors<sup>109</sup>. In fig.4.1, the IUPAC numbering system and the terms  $\alpha$ -,  $\beta$ -positions, and meso- are given for basic core of a BF<sub>2</sub>-dipyrromethene.

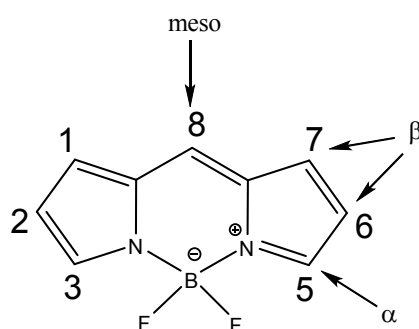


**Fig.4.1:** The basic core of BF<sub>2</sub>-dipyrromethene (BODIPY).

The boron bridge introduces rigidity to the system and prevents cis-trans isomerisation and twisting, which yields highly fluorescent and photostable dyes, such as compound **36**<sup>110</sup> and **37**<sup>110,111</sup> in Fig.4.2. **36** and **37** shows absorption maxima at 507, 505 nm and emission maximum at 520, 516 nm with a quantum yield of 0.81 and 0.8 in EtOH, respectively.

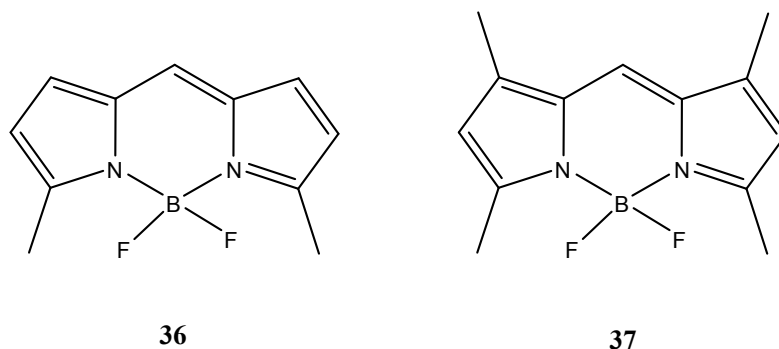


**Fig.4.2:** The structure of some BODIPY dyes.

Various substitutions can be envisaged which affect different way on their photophysical properties<sup>112, 113</sup>. Meso-phenyl substitution does not affect wavelength range, however it reduces quantum yield of fluorescence in certain cases.

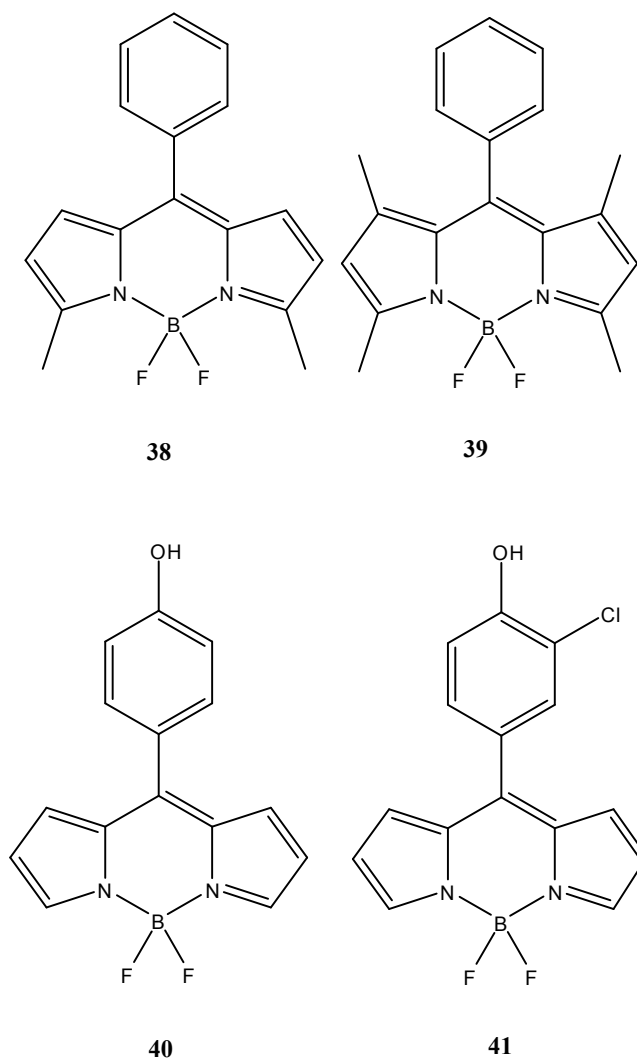


**Fig.4.3:** The structure of some meso substituted BODIPY dyes.

Compounds **38**, **40**, **41** (Fig.4.3) have absorption maxima at 508, 505, 507 nm and their emission maxima with the quantum yield in MeOH are 521 (0.19), 517 (0.28) and 520 (0.16) respectively<sup>114, 112</sup>. **39** shows absorption maximum at 498 nm and emission maximum at 505 nm with a quantum yield of 0.6 in acetonitrile. Emission maximum in MeOH is at 508 nm with a quantum yield of fluorescence 0.65. This difference is due to the 1,7 substituents prevent the loss of energy by free rotation of phenyl group<sup>115, 111</sup>

Substitutions at the 3,5-position such as compounds **42**, **43** in Fig.4.4 can cause shifting of absorption and emission maxima depending on the nature of linkage of substituent<sup>116</sup>. **42** with ethynylphenyl substitution has absorption at 605 nm and emission at 622 nm with a quantum

yield of 1 in MeOH<sup>117</sup>. **43** with steryl substitution absorbs at 628 nm and emits at 642 nm with a quantum yield of 0.84<sup>118</sup>.

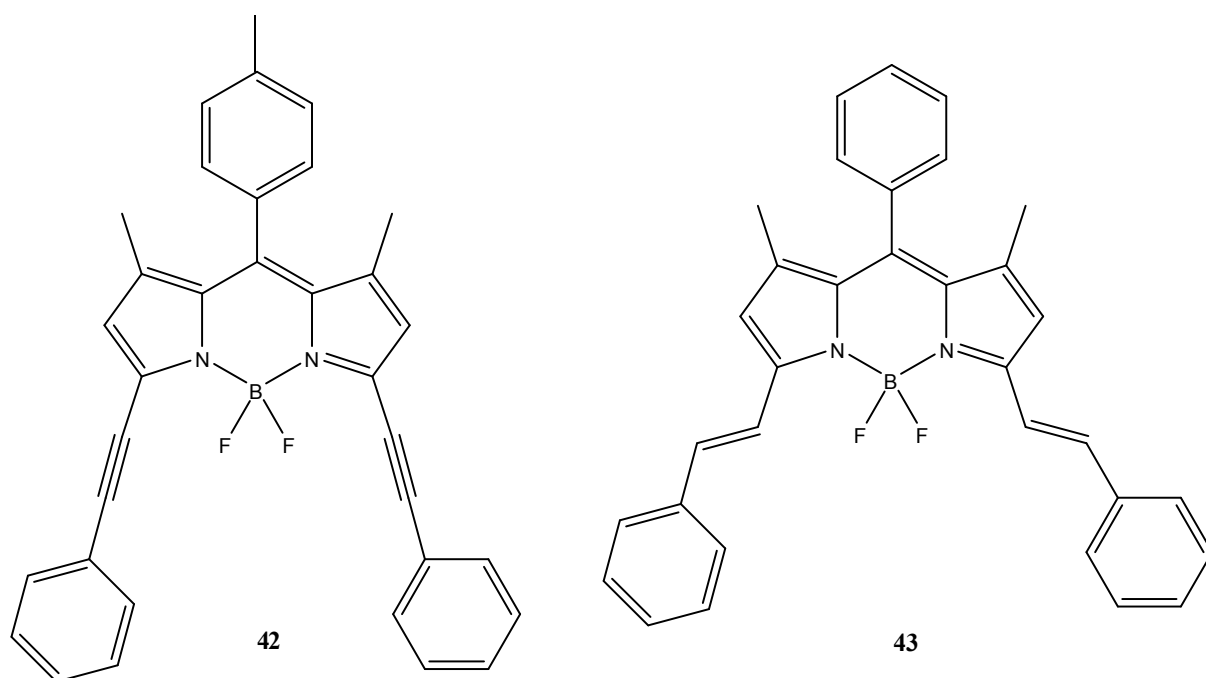


**Fig.4.4:** The structure of some 3,5-position substituted BODIPY dyes.

Substitutions at the 2,6-position such as compounds **44** and **45** in Fig.5 can lead to lower quantum yield but with longer absorption and emission wavelengths. The absorption maximum of **44** and **45** are at 528 and 559 nm and emission maximum at 535 and 580 nm with a quantum yield of 0.56 and 0.5 in EtOH<sup>114</sup> respectively. Comparing the given information for compound **44** and **45**, its 2,6-position substituents cause an effect on absorption and emission wavelength.

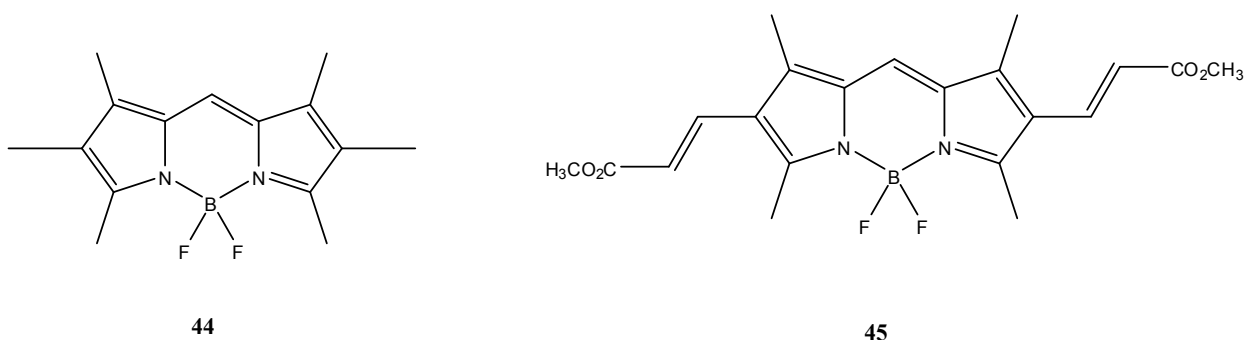


**Fig.4.5:** The structure of some 2,6-position substituted BODIPY dyes.

Steric constraints of molecular structure increase the fluorescence quantum yield. For example methyl substitution at 1 and 7 position entails an increase from **46a** to **46b** (Fig.4.6) from 0.38 to 0.72<sup>119</sup>. In other case, by replacing H atoms of the *meso* substituent of **47a** with a methyl group in **47b**, increases the quantum yield of fluorescence from 0.21 to 0.68<sup>120, 121</sup>. To force aryl substituent into the plane of BODIPY core by introducing alkyl bridges like in **46a** results in a red shift in absorption and emission maxima. When the absorption is at 547 nm and emission is at 582 nm for **47a** in MeOH, whereas absorption and emission maxima shift to 634 and 647 nm respectively for **46a**.

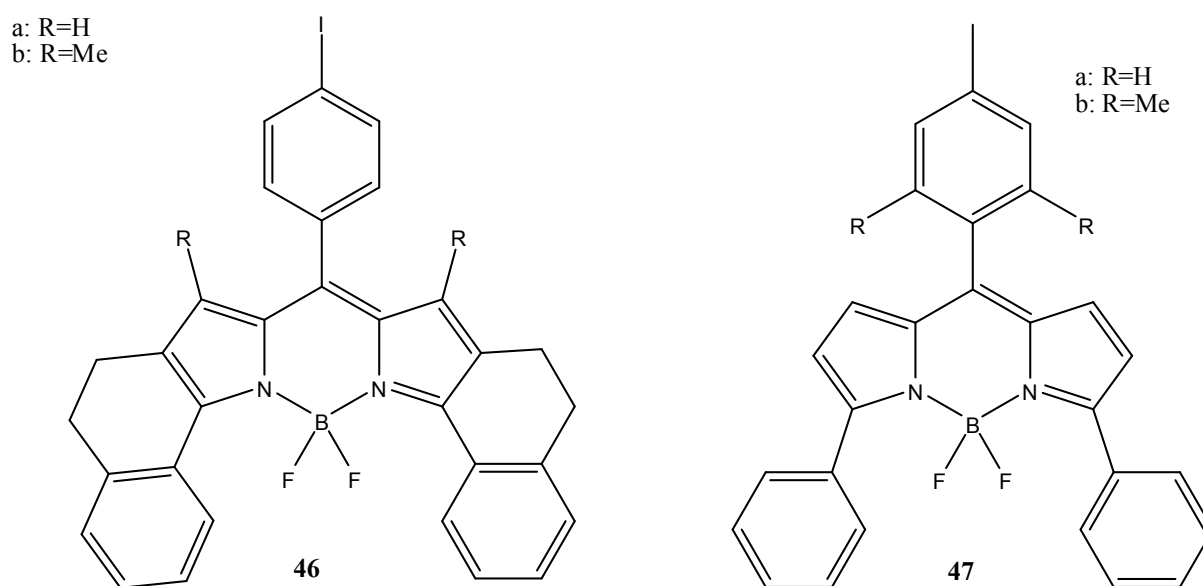


**Fig.4.6:** The structure of some sterically constrained BODIPY dyes.

A diversity of aromatic groups can be introduced to *meso*-position for appropriate functionalizations of BODIPY dyes. Dyes with special *meso*-groups can be used for many different applications. Some derivatives of this type of molecules are shown in Fig.4.7.

**48**<sup>122</sup>, **49**<sup>123</sup> and **50**<sup>124</sup> are used as redox active molecules. **50** can be used as nitric oxide probe. Low fluorescence intensity of this molecule increases when nitric oxide converts diamine into benzotriazole.

**51**<sup>125</sup> and **52**<sup>126</sup> can be used as pH probes. **53**<sup>127</sup>, **54**<sup>125</sup>, **55**<sup>128</sup>, **56**<sup>129</sup> and **57**<sup>130</sup> are metal chelators. **53**, **54** are selective for Fe<sup>3+</sup> Zn<sup>2+</sup>. **55** and **57** have good cavities for Ca<sup>2+</sup>. **56** can bind Hg<sup>2+</sup>, Ag<sup>2+</sup> and Cu<sup>2+</sup>. There are many examples for BODIPY based metal chelators. For instance, there are few examples can be soluble in water which can be used in biological applications. Fluorescence properties of these *meso*-modified BODIPY dyes can be operated by perturbing the reduction potential of *meso*-substituent. Substituents, depending on their reduction potentials relative to the excited state of BODIPY core, can act as electron donor or

acceptor. When electron transfer occurs, fluorescence cannot be observed. Chelation makes the reduction potential more negative compared to the BODIPY core. In such cases, electron transfer is switched off and the probe becomes fluorescent.

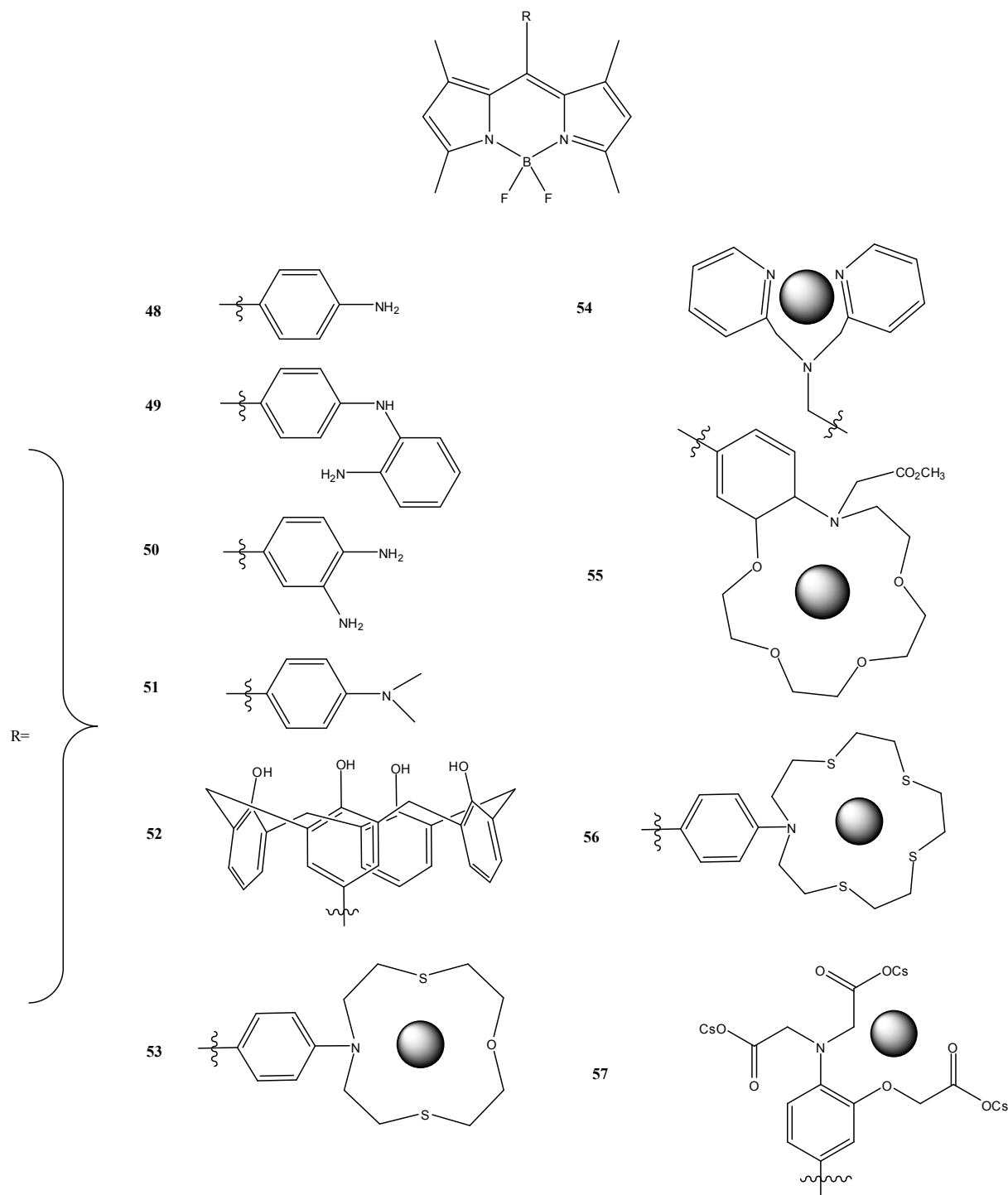


**Fig.4.7:** The BODIPY dyes with special meso-groups.

Exchange of *meso*-(8)-carbon for a nitrogen atom causes red shifts in optical transitions. The main core with *meso* N is called azadipyrromethenes (aza-BODIPY) which were first reported

in the 1940s<sup>131</sup>. Azadipyromethenes are NIR fluorophores which are amenable to structural modification, and exhibit excellent spectral properties<sup>132</sup>.

Research on these molecules has started with O'Shea's group from 2002 and has resulted with synthesis of dyes **58-65**<sup>113,133,134</sup> (Fig.4.8). UV-absorption maxima are strongly depended to *para*-substituted electron donating group (**58** versus **59**). Dimethylamino substitution of **62**<sup>134</sup> causes 149 nm bathochromic shifts. Absorption maxima of aza-BODIPY dyes are dependent on solvent polarity, but no dependence was reported for fluorescence emission maxima. FWHM of absorption bands vary from 51 nm to 67 nm. Extinction coefficient in CH<sub>3</sub>Cl ranges from 75000 M<sup>-1</sup>cm<sup>-1</sup> to 85000 M<sup>-1</sup>cm<sup>-1</sup>. Compounds **58-61** show moderate quantum yields. Bromine substitution of **61** does not affect the quantum yield of fluorescence significantly<sup>113</sup>. **63-65** have bromine atoms directly attached to the BODIPY core, which results in a significant decrease in fluorescence quantum yield. Singlet oxygen generation is increasing with bromine substitution that makes these molecules potentially useful as photodynamic therapy agents<sup>135-138</sup>. Compound **66**<sup>139</sup> is highly selective for the mercury ion which makes the molecule a good chelator. Red-shifts are observed for both the UV-absorption and fluorescence emission maxima. Compounds **67a** and **67b**<sup>140</sup> are used as visible chemosensors for the paralytic shellfish toxin Saxitoxin based on aza-BODIPY chromophore. Functional groups of Saxitoxin interact with the crown ether part. PET is observed from the crown ether to the fluorophore in the absence of toxin, which quenches the fluorescence. By complexation fluorescence is turned on.

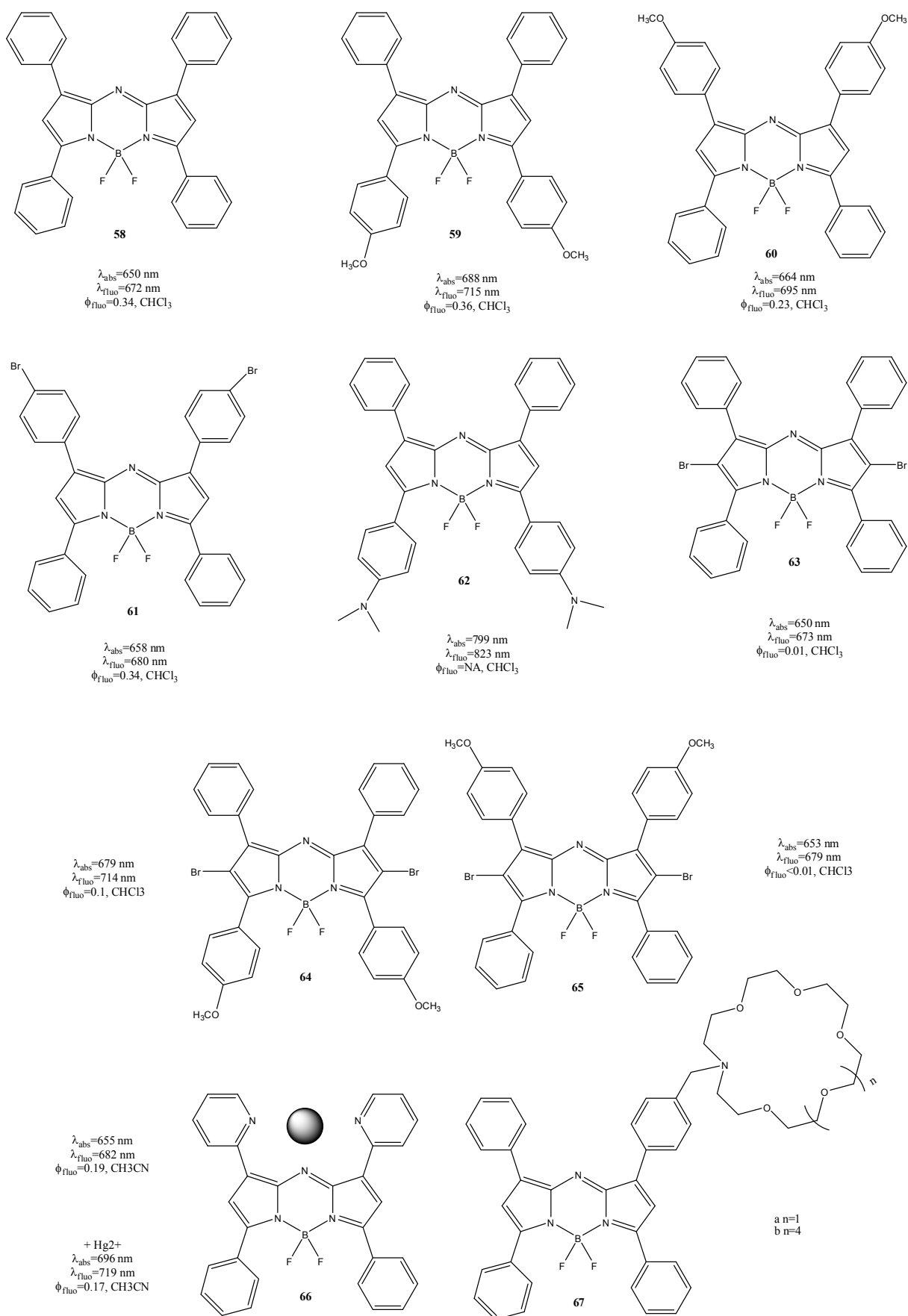


**Fig.4.8:** Structures of some aza-BODIPY based molecules.

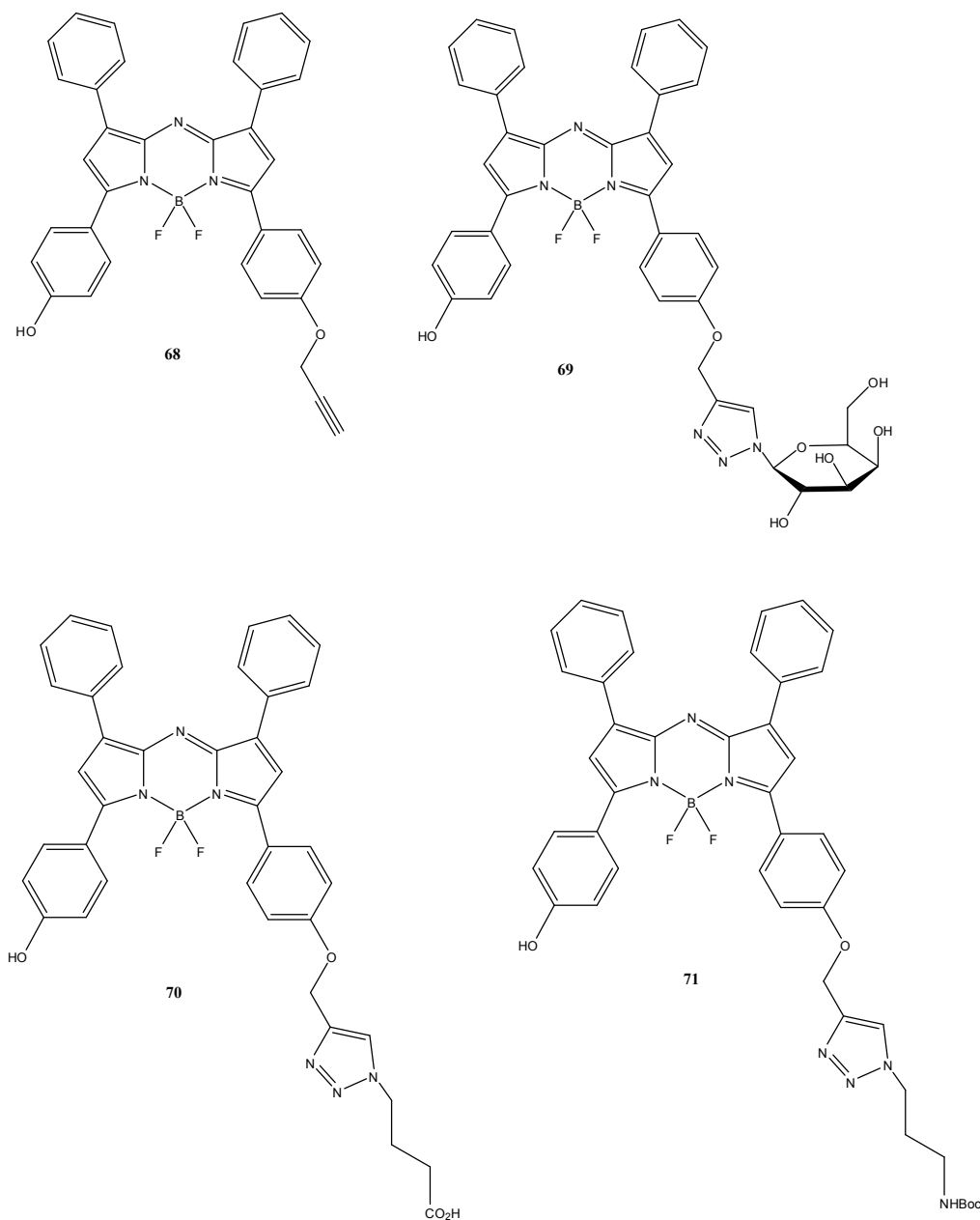


**Fig.4.9:** The structures of aza-BODIPY based functionalised molecules.

Since azadipyrrromethene based fluorophores have excellent absorption and emission properties in NIR region, these photophysical characteristic make them useful as fluorescent sensors. In Fig.4.9, series of pH responsive molecules synthesized by D.F. O'Shea's group are presented<sup>141</sup>. The absorption maxima of **68**, **69**, **70** and **71** in MeOH are at 688, 687, 687 and 687 nm, respectively. Fluorescence maxima are at 716 nm. The fluorescence intensity of **68** increases 15-fold from pH 6 to 8 ( $pK_a=6.9$ ). The comparison of the measured fluorescence intensity from pH 6.6 to 8 is greater than 6-fold for **69**. Similar as BODIPY dyes, rigidifying the molecular structure also results red shifts in absorption and emission spectra of aza-BODIPYs. The conformationally restricted aza-BODIPY dyes<sup>142, 143</sup> are presented in Fig.4.10.

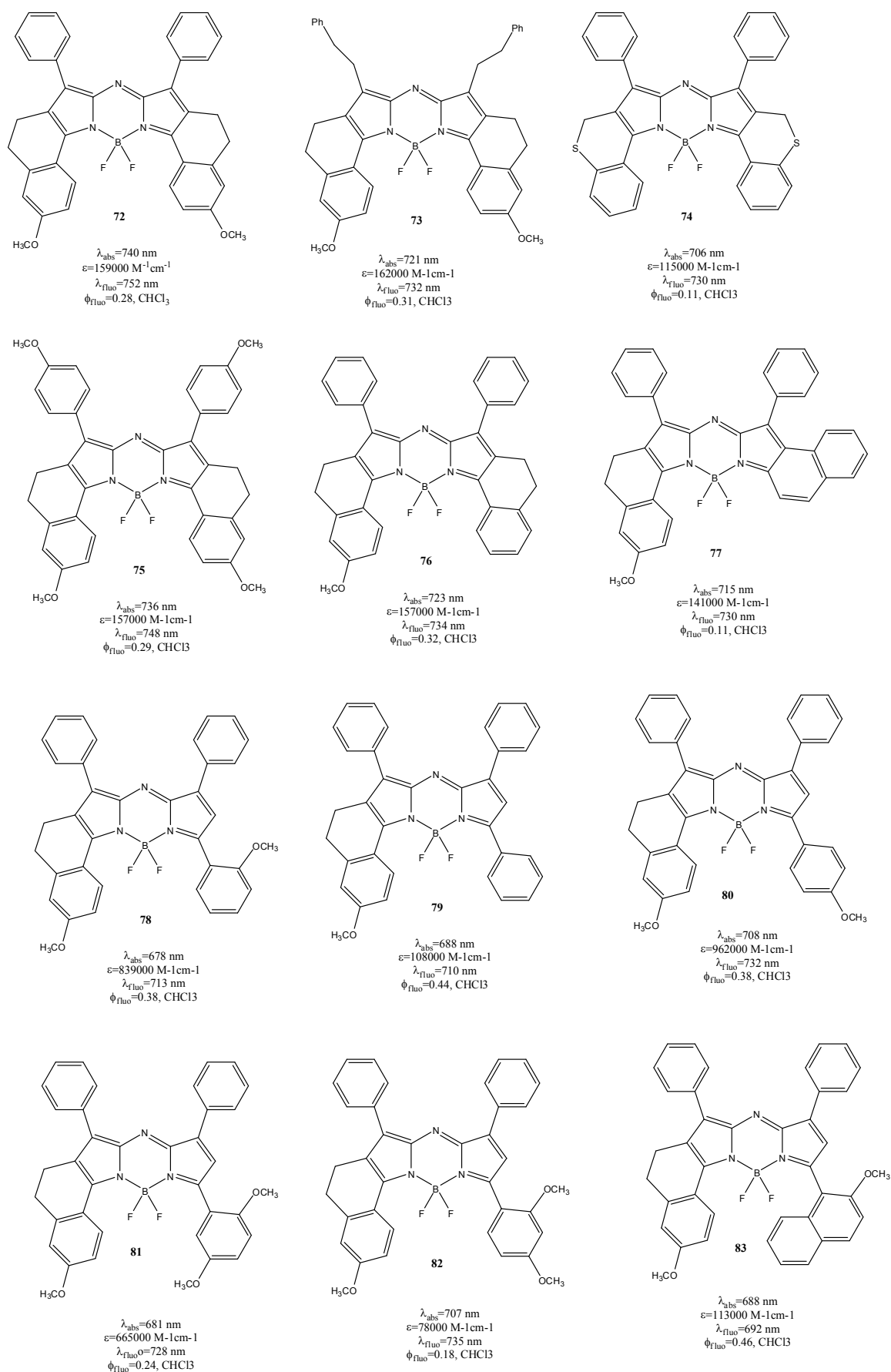


**Fig.4.10:** The structure of some sterically constrained aza-BODIPY dyes.

In comparison to the “non-constrained” azaBODIPY dyes, compounds **72**, **73** and **75** have narrow, high absorption bands at longer wavelengths. Their polarity dependent fluorescence intensity and excellent chemical-photo stability were reported<sup>142,143</sup>. Introduction of electron-donating groups results in a small blue shift and a slightly higher fluorescence quantum yield (**72** vs **75**). Sulfur-containing dye **74** has more blue shifted absorption maximum and lower fluorescence quantum yield. The restricted ring in system **77** decreases its quantum yield relative to **72**. Aza-BODIPYs with only one side restricted have much lower extinction coefficients (**79-83** vs **72**). The quantum yields of these non-symmetric aza-BODIPY dyes are highly dependent on the substituents on the aromatic ring. Electron donating *para*-substituents give higher quantum yields (**79** and **80**), with blue shifted absorption wavelengths. Ortho-Electron donating groups (e.g., in **78**) result in blue shifted absorption wavelengths also. Same effect in absorption wavelengths and lower quantum yields were observed when two methoxy groups were present (**81** and **82**). The sharp and intense absorption, higher quantum yield obtained in the special case of **83**<sup>142,143</sup>.

In this chapter the photophysical and chemical studies on various BODIPY dyes (see Fig.4.11) will be presented. These molecules can be divided into categories at an application level. Derivatives of aza-BODIPY dyes (**B1-B6**) which offer a role as molecular oxygen sensitizers can be used as Photodynamic Therapy (PDT) agents. Derivatives of BODIPY dyes (**B7-B10**) are suitable for applications that exploit their high fluorescence quantum yields such as fluorochromes<sup>144, 141</sup>, sensors<sup>108, 137, 145</sup> and donor/acceptor conjugates<sup>132</sup>. Due to their photostability and NIR emitting properties, they can be used as fluorescent dyes, labels in imaging for microscopy. The BODIPYs (**B7-B8**) conjugated with an ionophore can be used as cation sensors.

Fundamental photophysical and chemical data reported for earlier works of following dyes were mentioned until now. However, the excited state behaviour of aza-BODIPY dyes and fast processes in BODIPY-containing fluoroionophores are still largely untouched. In the following parts of this chapter via time-resolved studies, we will present an insight into excited-state dynamics and properties from the picosecond to microsecond time domains of following BODIPY and aza-BODIPY derivatives.

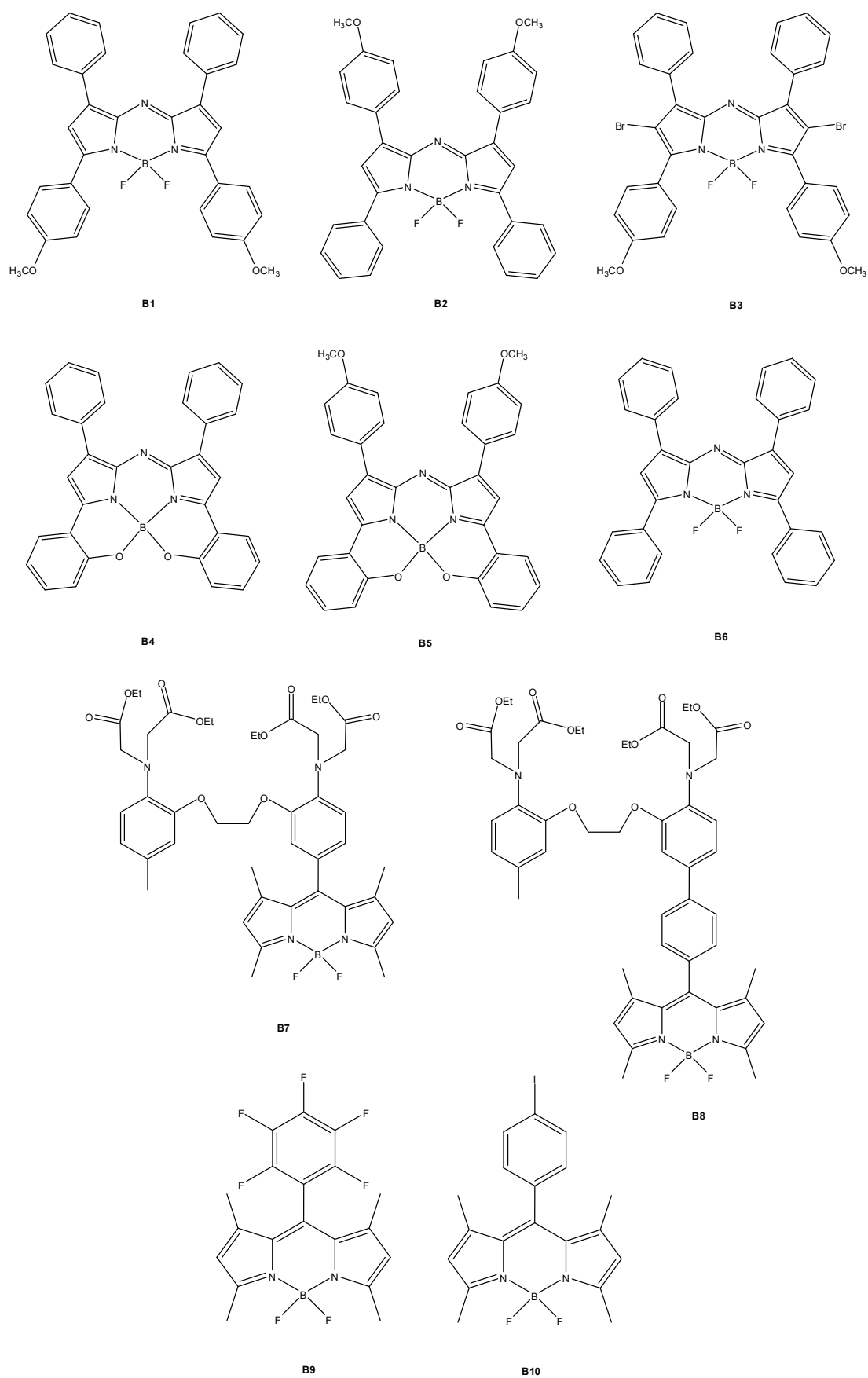


**Fig.4.11.** The structures of studied BF<sub>2</sub>-Azadipyrromethenes and BF<sub>2</sub>-Dipyrromethenes studied in this work.

## PART I

### *Photophysics of Aza-BODIPYs (BF<sub>2</sub>-Azadipyrromethenes): NIR Fluorophores and Photodynamic Therapy Agent*

#### 4.1.1. Introduction

In this part, BF<sub>2</sub>-azadipyrromethene molecules (Fig.4.12) will be presented. They all have useful properties in terms of NIR-emitting fluorophores<sup>144, 146</sup>. However, here we will also discuss their potential applications as a photodynamic therapy (PDT) agent and singlet oxygen sensitizers. Herein studies of two analogues (**B1** and **B3**, Fig.4.12) differing only by the substituent at the 2, 6 position (H or Br) will be compared. Time-resolved fluorescence and transient absorption spectroscopy offer an unprecedented insight into excited-state dynamics and properties from the picosecond to microsecond time domains, including fluorescence, intersystem crossing in heavy bromine atom containing **B3**, and singlet and triplet lifetimes. The latter parameters describe applicability as photodynamic therapy (PDT) agents.

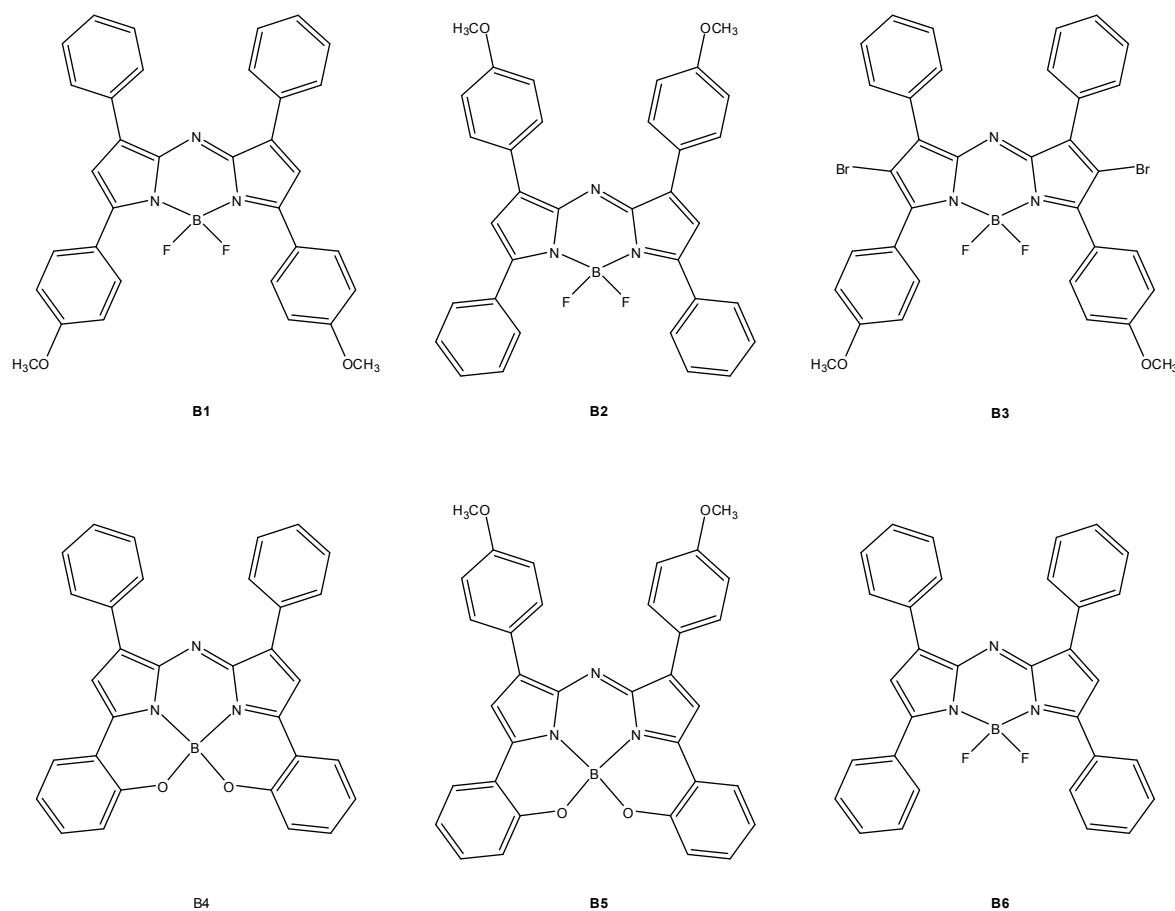


**Fig.4.12.** Structures of studied halogenated and non-halogenated BF<sub>2</sub> Azadipyrromethenes.

PDT is a method for killing cancer cells. For this method molecular photosensitizers, which have NIR absorption are used. Drugs, which contain these photosensitizers are injected to patient's body. These photosensitizers will be absorbed by all cells in the body. Due to their different metabolism, tumour cells can keep the photosensitizer drug up to 72 hours. In this time interval, the patient's body is irradiated by light. This light activates the photosensitizer and excites it to the singlet excited state (Fig.4.13b). Subsequently, relaxation to the triplet states of the molecules by intersystem crossing occurs (Fig.4.13c). Energy transfer from triplet state of photosensitizer to molecular oxygen causes singlet oxygen generation (Fig.4.13e). Singlet oxygen can destroy (with a reaction efficiency of 1 micron) the lipophilicity of cell membrane. Singlet oxygen relaxes to ground state (triplet) by luminescence at 1270 nm.

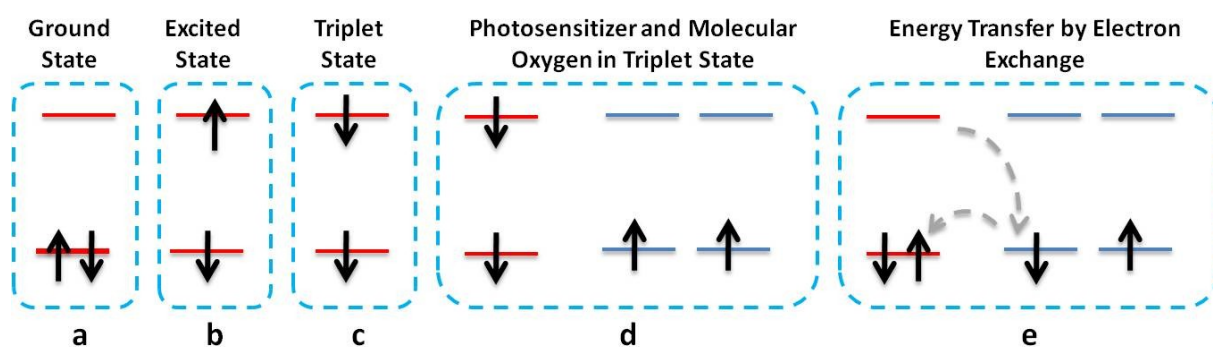


**Fig.4.13:** Singlet oxygen generation scheme.

The key limitation for clinical applications is optical absorption and scattering by tissue. At near-IR wavelengths (2000–3000 nm), water is the dominant absorber, so light penetration depth is limited to 0.1–1 mm. In the UV region near 300 nm, light scattering is very high as well as the absorption depth by cellular macromolecules is high. Between 650 nm and 1300 nm, absorption by water, haemoglobin, and lipids is lowest and light scattering is also low (according to the Mie's law, light scattering is proportional to the  $\lambda^{-4}$ ). As a cause of that light can penetrate to several centimetres, and contrast between tissue components remains high. That wavelength range is often referred to as the “therapeutic window” or “diagnostic window.”

Photofrin is the first and the most commonly used PDT agent. Although it has been used in treatment of oesophageal, endobroncheal, bladder, lung, stomach, cervical and skin cancers, it is not an ideal drug for PDT. It is a mixture of dimeric and oligomeric compounds derived from hematoporphyrin **84**. Poly-pyrrole macrocycles such as porphyrins and phtalocyanins are the second generation photosensitizers. Some porphyrin based PDT agents are shown in Fig.4.14. Protoporphyrin IX **85**, which is developed therapeutically compared to its

biosynthetic precursor, used for the treatment of Barrett's oesophagus and skin cancers. The benzoporphyrin derivative **86** (Visudyne) is widely used for the treatment of AMD (age-related muscular degeneration). The dihydroporphyrin or chlorin based PDT agent, *m*-tetrahydroxyphenyl-chlorin **87** (Foscan), is commonly used in Europe for the treatment of head and neck cancer. Tin etiopurpurin (Purlytin) **88** is used in clinical testing for the treatment of AMD. The palladium-bacteriopheophorbide **89** (TOOKAD), the expanded porphyrin **90** (Motexafin Lutetium), and the phthalocyanines **91** are all in various stages of clinical testing for different cancerous tissue targets.

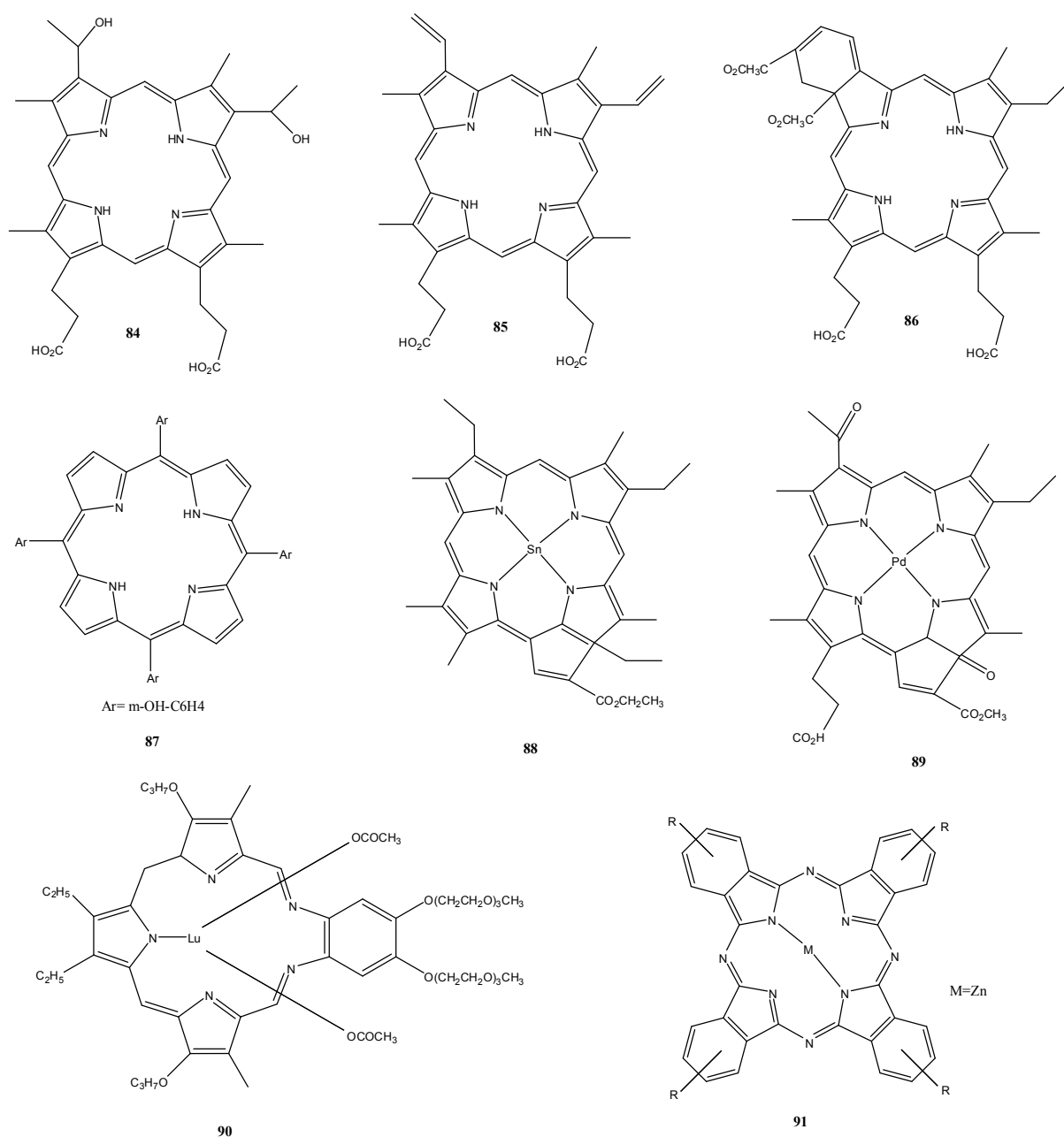


**Fig.4.14:** Polypyrrole macrocyclic PDT agents.

Developments for PDT agents based on non-porphyrin photosensitizers are less extensive. The pioneers of these class are the cationic photosensitizers such as methylene blue **92**, Nile blue analogue **93**, and the chalcogenopyrylium class of sensitizer **94** (Fig.4.15). Toxicity due to nuclear localization of these cationic compounds, and their relatively short absorption maxima of less than 650 nm in aqueous solutions are the disadvantages for these class, which make them not available for in vivo applications.

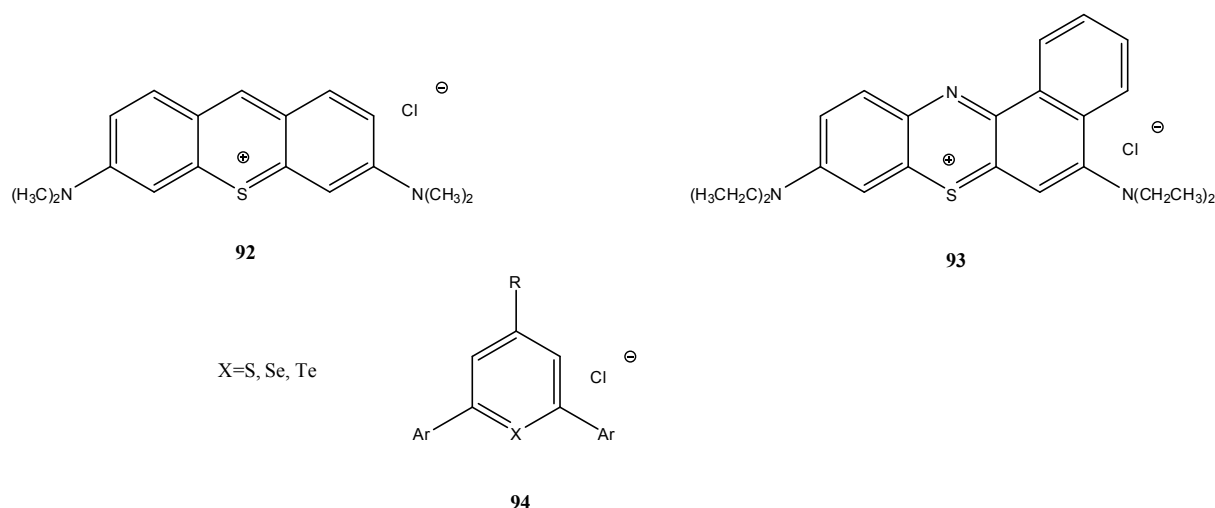


**Fig.4.15:** *Non-porphyrin PDT agents.*

For further development, necessity of new PDT agents has become apparent. Due to their amenability to modification around the periphery of the chromophore, which could allow for optimization of all aspects of their photophysical and therapeutic properties, BF<sub>2</sub>-azadipyrromethenes based dyes can be used as potential PDT agents. The first study on **58-65** was reported as PDT agents in 2002<sup>133</sup>. Requirements for a successful PDT agent, such as therapeutic window absorption, and capacity for singlet-oxygen generation play the biggest role for designing a PDT agent. Their absorption maxima vary within the therapeutic window between 650 and 700 nm, with high extinction coefficients ranging from 75000 to 85000 M<sup>-1</sup> cm<sup>-1</sup>. This relatively high extinction coefficient is an advantage over other PDT agent such as Photofrin or protoporphrin IX **85** and one of the factors that can facilitate singlet oxygen generation. A comparative singlet oxygen generation analysis had been done to measure the ability of singlet oxygen generation of these compounds. As a result of these analyses, writers concluded that the bromine substituent due to heavy atom effect is more effective in singlet oxygen generation. However the bromine substituent distant from the main core does not show a significant effect. Dye **64** is more effective in generation singlet oxygen than **63** even at a 100-fold lower concentration.

In the following, we will present the fundamental photophysical properties of **B1-B6** molecules, which are already given in literature. After, we will give more detailed results about their excited state dynamics and non-linear optical behavior.

#### 4.1.2. Steady State studies

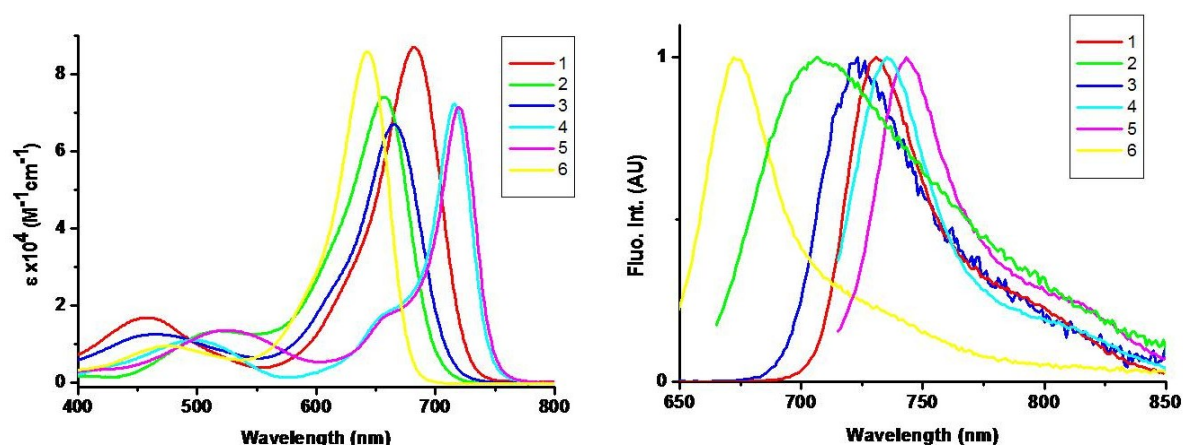


**Fig.4.16:** Absorption and Emission spectra in acetonitrile ( $\lambda_{exc}(nm)$ = **B1**(650), **B2**(657), **B3**(650), **B4**(716), **B5**(719), **B6**(642)).

All compounds show a strong  $S_1 \leftarrow S_0$  transition with maximum of absorption centred between 642 and 719 nm. **B4** and **B5** are the most red-shifted, due to the presence of the constrained B-O bonds<sup>145</sup>.

Fluorescence and phosphorescence studies have been conducted on these compounds, at room and liquid nitrogen temperature, in order to assess the energy levels of the singlet and triplet states. Emission arising from the  $S_1$  excited state was detected in all cases, whatever the solvent and temperature. At room temperature, the maxima of emission are centred between 672 and 740 nm.

Whatever the conditions used, we were unable to detect the phosphorescence from the triplet state, even at 77K and in the presence of 10-30 % v/v of ethyl iodide, which favours intersystem crossing and the population of the triplet state. Nevertheless, the absence of phosphorescence does not preclude the population of the triplet state, as is shown with **B3**, which is able to sensitize the luminescence from  $^1O_2$  (Fig.4.17).

The singlet oxygen generation capacity was compared to  $C_{60}$ , a popular standard in the same solvent (toluene), whose singlet oxygen producing efficiency was established to be 0.96 on

visible excitation<sup>147</sup>. Relative measured  $^1\text{O}_2$  emission was around 0.77 using **B3**, giving an absolute value of around 74% for  $^1\text{O}_2$ .

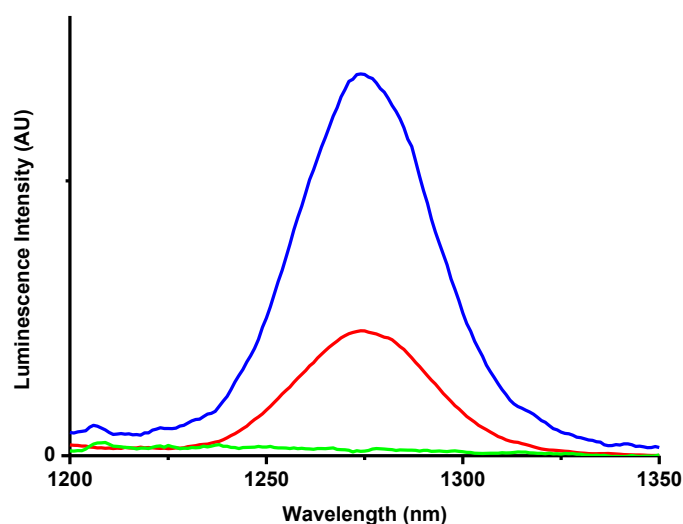


**Fig.4.17** Singlet oxygen emission sensitized by isosbestic solutions of  $\text{C}_{60}$  (blue) in air-equilibrated toluene ( $\lambda_{\text{exc}}=399$  nm); **B1** ( $\lambda_{\text{exc}}=663$  nm; green) and **B3** ( $\lambda_{\text{exc}}=666$  nm; red) in air-equilibrated acetonitrile (Note: residual fluorescence of **B1** and **B3** subtracted).

The dynamic behaviour of **B1-B6** reveals some variations depending on the substituents on the tetraphenylazaborondipyrromethene core (see Table-4.1). Firstly,  $\text{BF}_2$ -chelated azadipyrromethenes (**B1-B3**, **B6**) have shorter lifetimes compared to B-O chelated molecules (**B4**, **B5**), a fact that can be attributed to the more constrained bonds in **B4** and **B5**. Secondly, the methoxy substitution onto the aryl rings in the  $\beta$ -pyrrole positions tends to decrease the lifetime (see for example **B5** compared to **B4**), while the same substitution on the aryl rings of the  $\beta$ -pyrrole positions yields to a longer lifetime (in **B1**). In the molecular design, the electron donor group was introduced to push the absorption and emission envelope further to the red. Thirdly, the bromine substitution in **B3** decreases the lifetime compared to **B1**, as expected by the heavy atom effect. At 77K, a general increase of the lifetimes is observed, a less pronounced effect in **B4** and **B5**, whose structures are already more constrained than in **B1-B3** and **B6**. (see Table-4.1)

**Table-4.1 :** Spectroscopic properties of **B1-B6** in acetonitrile (r.t.) or butyronitrile (77 K).  $\lambda_{exc} = 650 \text{ nm}$  (B1-B5) or  $625 \text{ nm}$  (B6) (single photon counting data).

	absorption	emission r.t.		emission 77 K	
compound	$\lambda_{max} / \text{nm}$ ( $\epsilon / \text{M}^{-1} \cdot \text{cm}^{-1}$ )	$\lambda_{max} / \text{nm}$	$\tau / \text{ns}$	$\lambda_{max} / \text{nm}$	$\tau / \text{ns}$
<b>B1</b>	682 (87000)	721	2.3	722	5.3
<b>B2</b>	657 (73000)	715	1.1	696	4.9
<b>B3</b>	665 (67000)	716	0.7	703	3.6
<b>B4</b>	716 (72000)	739	4.5	730	6.3
<b>B5</b>	719 (71000)	740	3.3	737	5.4
<b>B6</b>	642 (85000)	672	0.6	672	6.5

#### 4.1.3. Time resolved Fluorescence

Time resolved fluorescence experiments were carried out in deaerated acetonitrile solutions, where temporal behaviour is recorded by a streak camera. The results of experiments are also listed in Table 2 and correspond well with single photon counting data. The kinetics are monoexponential and are shown on Fig.4.18. The fluorescence intensities are normalized and corrected by eliminating anisotropy effects (see section 4.1.4).

**Table-4.2:** The results of time-resolved fluorescence of 1-6 in deaerated acetonitrile (streak camera measurements)

	excitation	emission	
compound	$\lambda / \text{nm}$	$\lambda_{max} / \text{nm}$	$\tau / \text{ns}$
<b>B1</b>	635	721	2.2
<b>B2</b>	630	712	0.98
<b>B3</b>	635	716	0.55
<b>B4</b>	680	736	4.2
<b>B5</b>	680	738	3.2
<b>B6</b>	630	675	0.58

**B4** and **B5** have longer lifetimes as a reason of constrained B-O bonds. **B2**, **B3** and **B6** have the shortest lifetimes. As we mentioned before, methoxy substitution onto the aryl rings in the  $\beta$ - pyrrole positions tends to decrease the lifetime (see **B2**, **B3** as compared with **B6**). Although, **B1** and **B3** have similar structures, the fluorescence lifetime of **B3** is expected to be shorter as a result of efficient intersystem crossing due to the heavy atom (bromine) substitution.

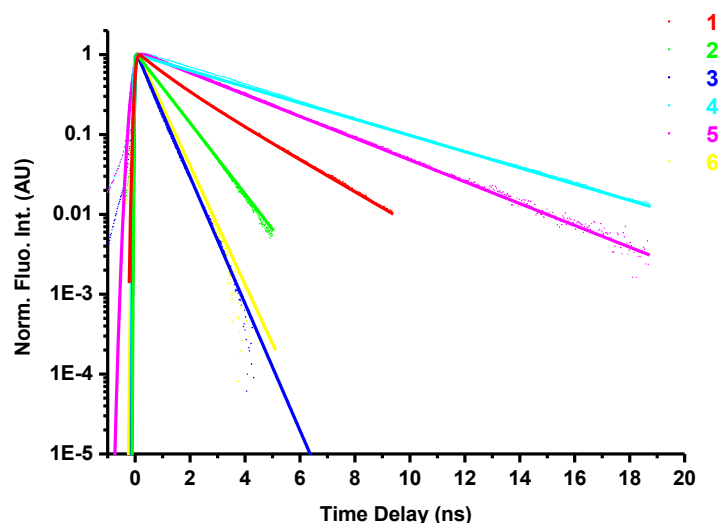


**Fig.4.18:** The kinetics of fluorescence decay of **B1-B6** in deaerated acetonitrile.

NIR-emitting compounds **B1** and **B3** have fluorescence quantum yields ( $\Phi_f$ ) of 0.36 and 0.1, respectively in chloroform. This value was equally measured in acetonitrile both by an absolute measurement and comparison to an optically dilute standard at various concentrations and extrapolations to infinite dilution. Similar values were obtained for **B1** and **B3** in both cases in acetonitrile. Their fluorescence lifetimes ( $\tau_0$ ) are 2.2 ns (**B1**) and 0.55 ns (**B3**) given in Table-4.2. Applying eq. 53 allows determination of the radiative rate constant for compound **B1**, which was determined to be  $1.6 \times 10^8 \text{ s}^{-1}$ , a value for  $k_r$  of similar magnitude to those observed for BODIPY chromophores<sup>104, 112</sup>.

$$k_r = \frac{\phi_f}{\tau_0} \quad (53)$$

#### 4.1.4. Fluorescence Anisotropy

In Fig.4.19, the anisotropy decay of **B1** is shown on the left graph and of **B3** on the right graph.

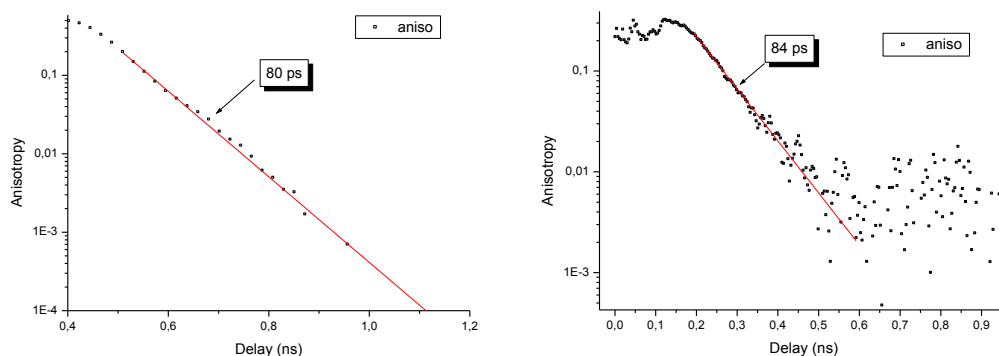


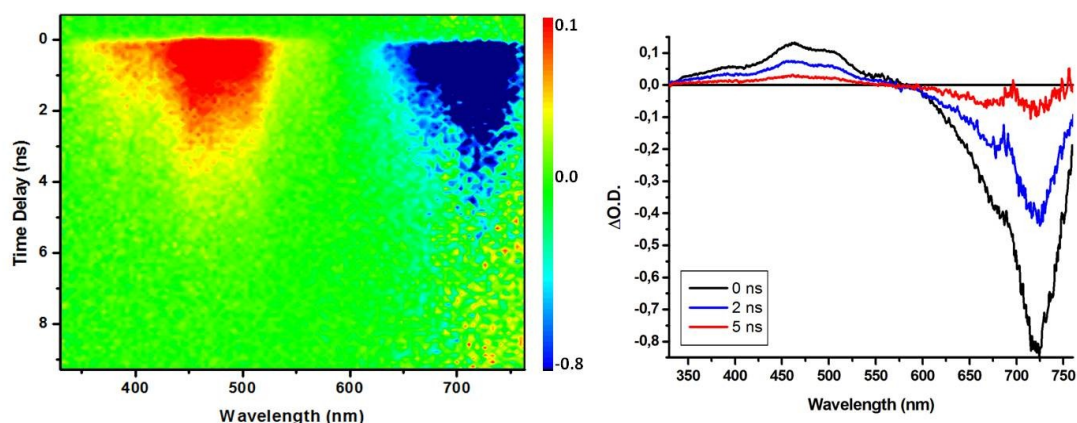
**Fig.4.19:** The anisotropy decay of **B1** (left) and **B3** (right).

As discussed in section 2.1.4, fluorescence anisotropy changes when the orientations of the molecules change, for example while they are rotating by Brownian rotational movement due to solvent-solute shocks. As a result of Langevin equation it was concluded that the anisotropy decay time is dependent on  $\zeta$ , the microscopic friction of solvent, I the moment of inertia of solute. Anisotropy decay time for **B1** is 80 ps and for **B3** is 84 ps. As halogenated molecule **B3** is slightly heavier than non-halogenated molecule **B1**, that **B3** may be expected to have longer anisotropy decay.

#### 4.1.5. Transient Absorption

In this section, we will present the results of transient absorption studies on all BF<sub>2</sub>-Azadipyrromethenes **B1-B6** complementary to time-resolved fluorescence. After giving the results for all the series of azadipyrromethenes, we will discuss in detail the photophysical processes involved in excited state relaxation for Br substituted molecule with a comparison of the analogue bearing protons instead of Br.

##### 4.1.5.a.B1



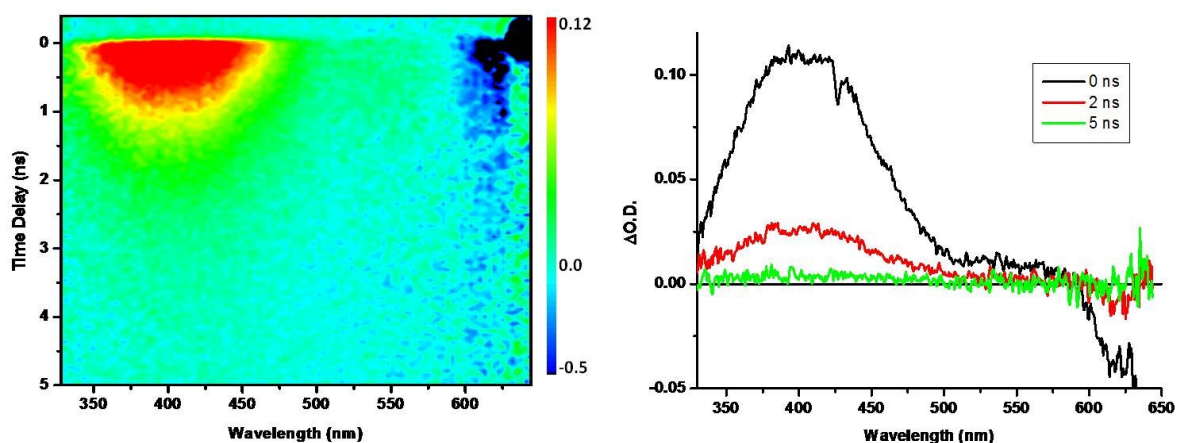
**Fig.4.20:** *Transient Absorption of of **B1** at different wavelengths as a function of time delay (Each spectrum is constructed from two spectra:  $\lambda_{exc} = 460$  nm and  $\lambda_{exc} = 650$  nm).*

Fig.4.20 shows the transient absorption spectrum of **B1** as a function of time delay. The intensity of the signal is given by the colour chat. There are positive bands at 400 nm and 460 nm which relax in 2.2 ns. Wide negative band is located at between 600 nm and 750 nm and relaxes with the same time constant. Fluorescence lifetime for this molecule is found to be 2.2 ns and the maximum of emission is at 721nm. Considering these results, these positive bands can be the excited singlet state absorption bands and the negative band is the superposition of

ground state bleaching and stimulated emission signals. Thus it is ascribed de-excitation of  $S_1$  state. No triplet formation was observed.

#### 4.1.5.b.B2

On the transient absorption image of **B2** in Fig.4.21, the positive band is located between 350 and 450nm with a decay time of 1 ns. A negative band can be seen around 600 nm. Kinetics taken at 620 nm has a lifetime of 0.9 ns. Spectra are perturbed by the pump scattering. Fluorescence lifetime of the molecule is found 0.9 ns and the maximum of emission is at 712 nm. As a conclusion, the positive band is the excited singlet state absorption band and the negative band is the ground state bleaching. Stimulated emission band is out of our measurable spectral range. Only singlet state relaxation is involved in the de-excitation process for **B2**. No triplet formation is observed.



**Fig.4.21:** Transient Absorption of of **B2** at different wavelengths as a function of time delays ( $\lambda_{exc} = 630 \text{ nm.}$ )

#### 4.1.5.c.B3

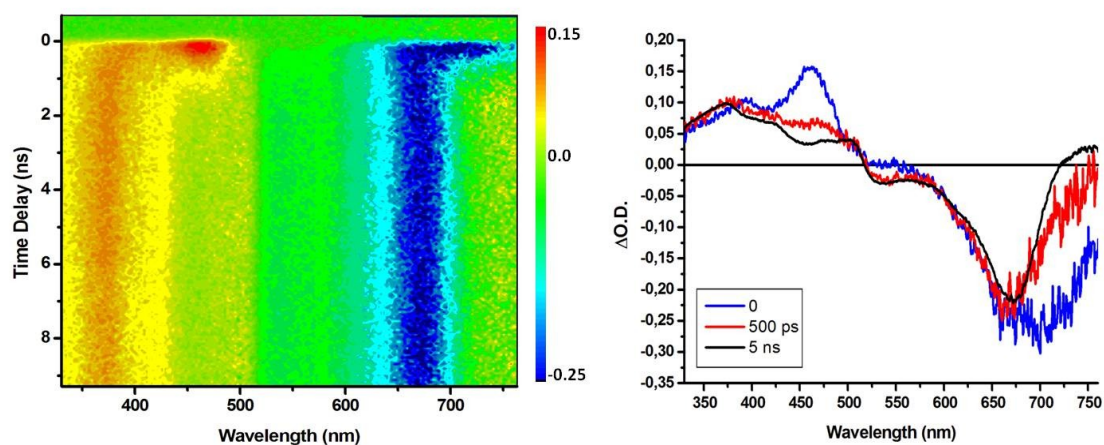


**Fig.4.22:** Transient Absorption of of **B3** at different wavelengths as a function of time delays (Each spectrum is constructed from two spectra:  $\lambda_{exc} = 460 \text{ nm}$  and  $\lambda_{exc} = 650 \text{ nm.}$ )

The transient absorption image of molecule **B3** is different from **B1** and **B2** (Fig.4.22). There are positive bands, one is at 460 nm with a relaxation time of 0.5 ns and another positive band is at 370 nm, which is forming in 0.5 ns and shows no decay in a 10 ns window. The decay time of this band is found 6  $\mu$ s. The negative band at 720 nm decays in 0.5 ns. The negative band at 620 nm shows two components decay with 0.5 ns and 6  $\mu$ s. Fluorescence lifetime of the molecule is 0.5 ns with emission maximum at 716 nm. Considering these results, the band at 460 nm band is the excited singlet state absorption. Its relaxation time is concomitant with the grow-in of the band at 370 nm, which can be attributed a triplet-triplet absorption band. The negative band at 720 nm is the stimulated emission band and the band at 620 nm is the ground state bleaching band. The decay kinetics of these bands supports the existence of singlet and triplet states.

#### 4.1.5.d.B4

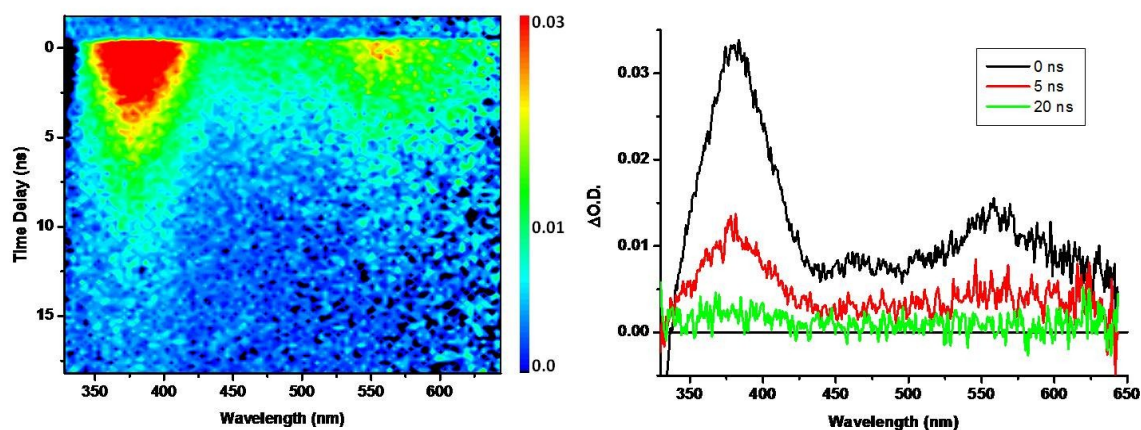


**Fig.4.23:** Transient Absorption of of **B4** at different wavelengths as a function of time delays ( $\lambda_{exc} = 680$  nm).

**B4**, has the similar spectrum (see Fig.4.23) as **B1** and **B2**. Positive bands are placed at 380 nm and 565 nm with relatively long decay time of 4.3 ns. No negative bands can be observed in our measurement range. Fluorescence lifetime of this molecule is 4.2 ns with the maximum of emission at 736 nm. Taking into account the consistency of lifetimes, it can be concluded that the positive bands are excited singlet state absorption bands and only  $S_1$  state is involved in relaxation process. No triplet formation is observed for **B4**.

#### 4.1.5.e.B5

In transient absorption spectrum of **B5** shown in Fig.4.24, the positive bands, placed at 384, 475 and 610 nm, decay in 3.2 ns. No negative band is observed. The fluorescence lifetime of

this sample is 3 ns with the emission maximum at 738 nm. These positive bands correspond to excited singlet state absorption bands. No triplet-triplet absorption is observed.

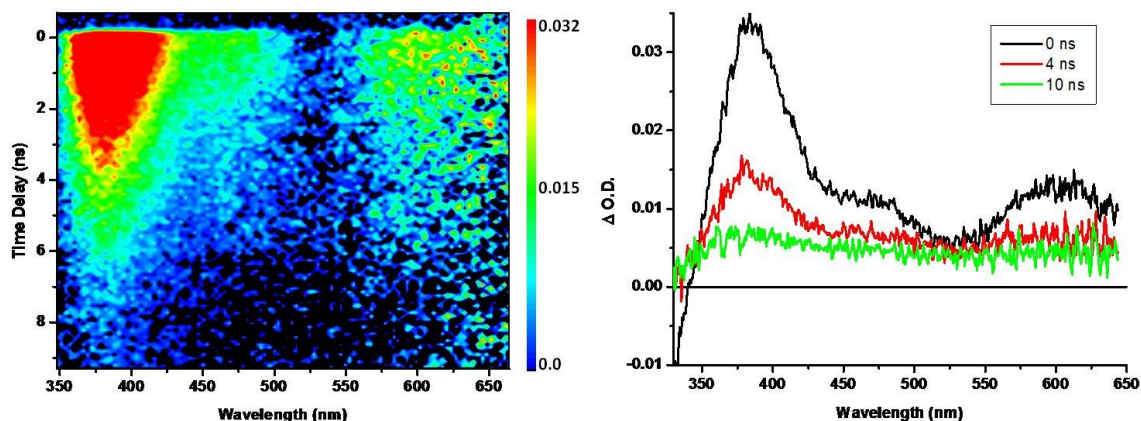


**Fig.4.24:** *Transient Absorption of B5 at different wavelengths as a function of time delays ( $\lambda_{exc}=680$  nm).*

#### 4.1.5.f.B6

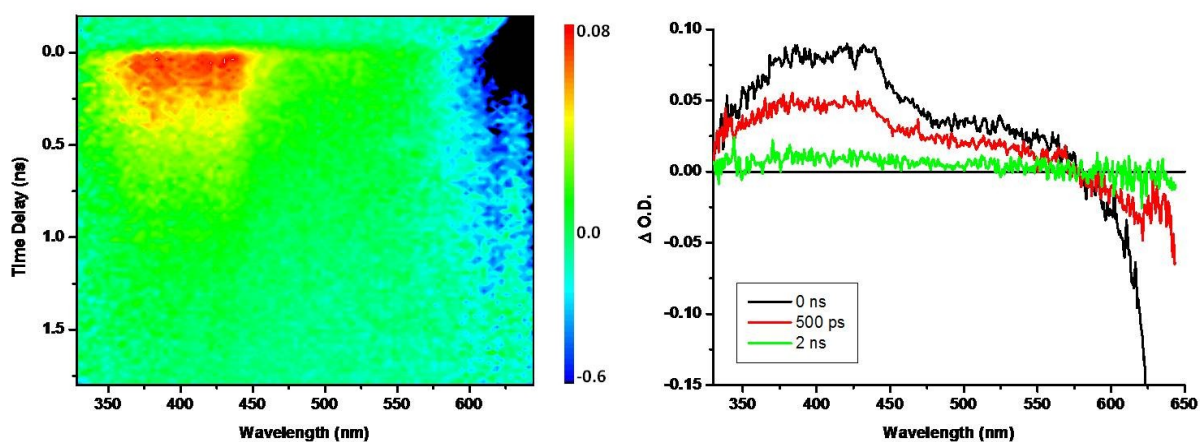


**Fig.4.25:** *Transient Absorption of B6 at different wavelengths as a function of time delays ( $\lambda_{exc}=630$  nm).*

Fig.4.25 presents transient absorption spectrum of B6. The positive bands located 360, 420 and 500 nm decay in 650 ps. Negative band at 610 nm has a decay time of 600 ps. Fluorescence lifetime of the molecule B6 is 600 ps with a maximum of emission at 675 nm. According to these results, positive singlet excited state absorption bands have a concomitant decay with the decay of negative ground state bleaching band and fluorescence emission lifetime. Stimulated emission band is out of the measurable spectral range. No triplet formation is observed.

Now, we can compare halogenated **B3** and non-halogenated **B1** molecules in detail. The transient absorption spectra of **B1** at different time delays are shown in Fig.4.26. Each spectrum is constructed from two spectra obtained by excitation 460 nm and 650 nm. This spectrum construction method was chosen in order to avoid the artefact related to pump scattering as well as to cover a large wavelength range (more than 400 nanometers). The decay time of all spectral bands in transient absorption spectrum is 2.2 ns which is the same as the fluorescence lifetime. As a conclusion, we can say that the singlet excited state relaxation is the only transition involved in de-excitation process and no other transient states were created.

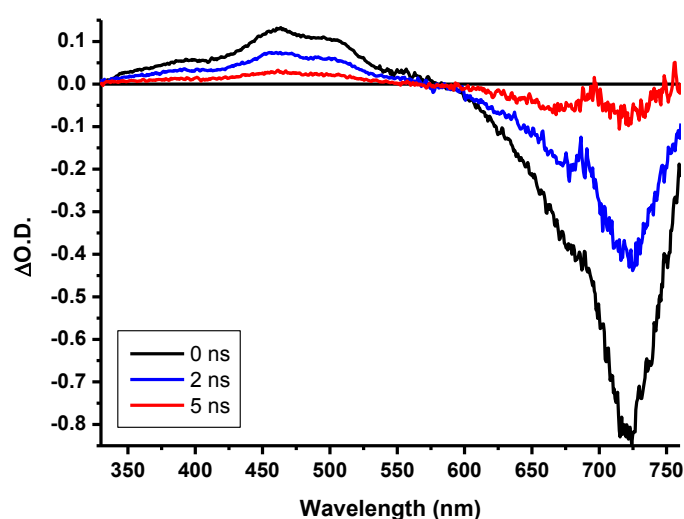


**Fig.4.26:** Transient absorption spectra after different time delays following excitation of **B1** in  $CH_3CN$ . Each spectrum is constructed from two spectra: excitation 650 nm and 460 nm.

For the halogenated molecule **B3**, the temporal evolution of transient absorption spectrum is given in Fig.4.27. The blue curve is the spectrum of singlet excited state absorption obtained immediately after excitation. The band at 460 nm, which is due to singlets decays in 500 ps. The stimulated emission band at 720 nm relaxes in 500 ps. The spectrum in black, taken after a 5 ns delay, shows the triplet-triplet absorption band at 370 nm. After excitation, the molecule is promoted to an excited singlet state. The excited singlet state mainly relaxes by intersystem crossing towards the triplet state. This later state relaxes by non-radiative pathway in 6  $\mu$ s. No phosphorescence was observed. The experiment was performed on a deaerated sample to eliminate the excited state quenching by oxygen.

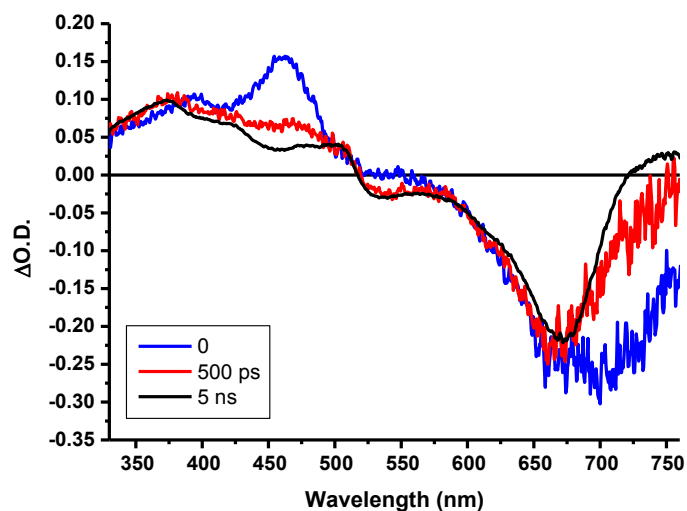


**Fig.4.27:** Transient absorption spectra after different time delays following excitation for **B3** in  $\text{CH}_3\text{CN}$ . Each spectrum is constructed from two spectra: excitation 650 nm and 460 nm.

Evolution of the transient absorption signal corresponding to the ground state bleaching at 660 nm of **B3** in degassed  $\text{CH}_3\text{CN}$  is presented in Fig.4.28. The quantum yield of intersystem crossing can be directly determined from Fig.28 to be 0.72 in **B3**, based on prompt changes in the absorption band corresponding to ground state bleaching, on going from the initial photogenerated value to the metastable triplet population after a few nanoseconds. Singlet-to-triplet intersystem crossing rate is also found as  $1.5 \times 10^9 \text{ s}^{-1}$ . Assuming , the radiative rate constant remains comparable to structurally similar compound **B1**, the rate of intersystem crossing ( $k_{ISC}$ ) in **B3** can be estimated according to equation 54, where  $\tau_f$  is the lifetime of the quenched fluorescence and  $1/\tau_0$  is the rate of the unquenched fluorescence, giving an intersystem crossing rate of  $1.4 \times 10^9 \text{ s}^{-1}$  in **B3**.

$$k_{ISC} = \frac{1}{\tau_f} - \frac{1}{\tau_0} \quad (54)$$

This value is extremely similar to the value obtained from ground state bleaching kinetics, which is a sufficiently high value for applications in photodynamic therapy<sup>148, 149</sup>.

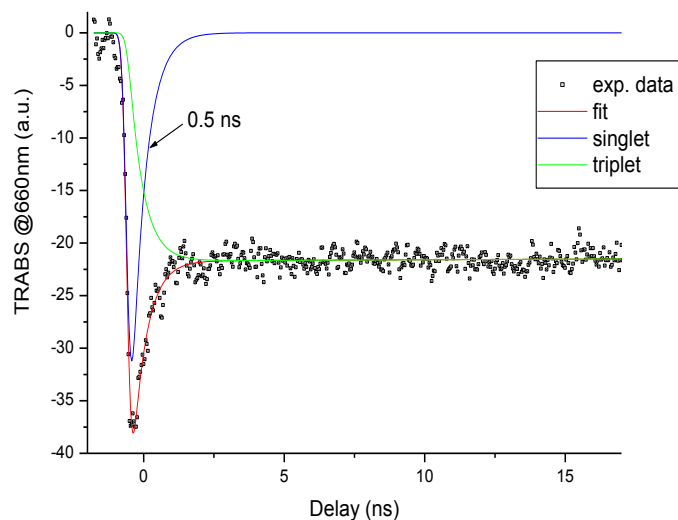


**Fig.4.28:** Evolution of transient absorption signal (TRABS) at 660 nm of **B3** in degassed  $CH_3CN$  ( $\lambda_{ex} = 635$  nm). Blue trace shows singlet state decaying and the red trace shows triplet state grow-in.

The effect of self-quenching was estimated by varying the concentration of **B3**. In Fig.4.29, it is shown the triplet lifetime versus the concentration.

The lifetime of this newly formed absorption band was recorded at different concentrations in deaerated solution in order to eliminate potential quenching with oxygen.

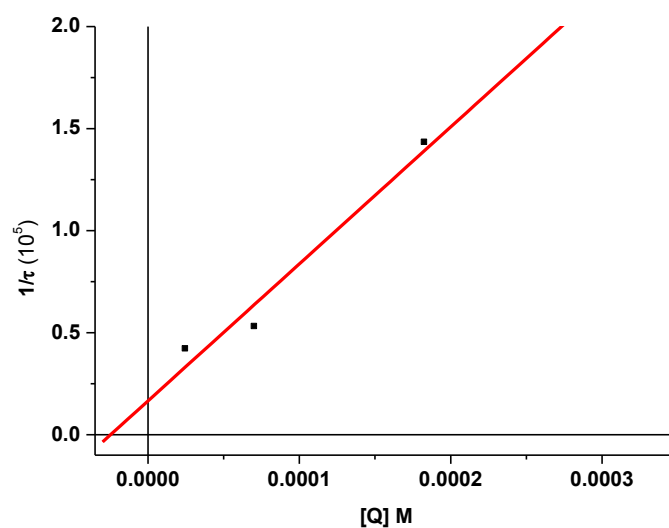


**Fig.4.29:** Deexcitation rate as a function of concentration of **B3** in  $CH_3CN$  (degassed samples).

Extrapolating a plot of  $1/\tau$  vs concentration to infinite dilution allowed estimation of the unquenched triplet lifetime to be 21  $\mu$ s. At comparable concentrations similar room temperature triplet lifetimes were reported for ruthenium-BODIPY compounds shown in Fig.4.30 (8  $\mu$ s for **95** and 30  $\mu$ s for **96**)<sup>148-150</sup>.

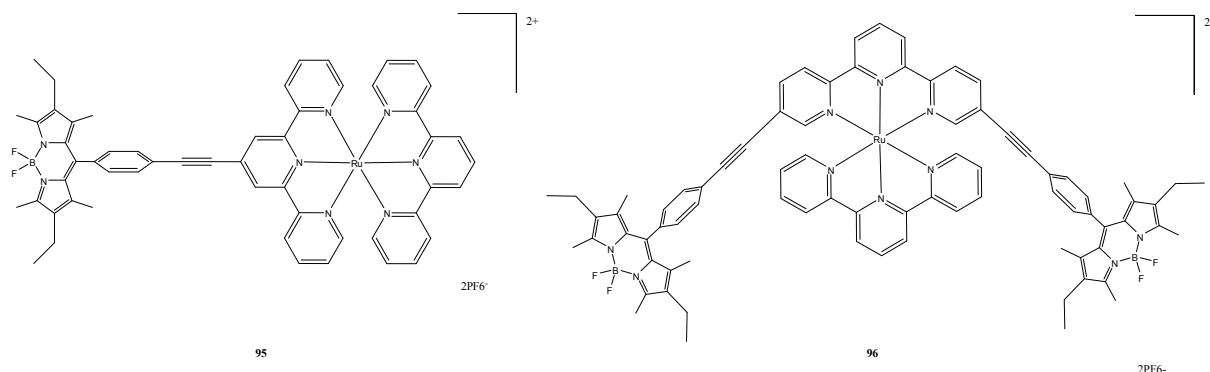


**Fig.4.30:** The structural formula of Ru-BODIPY compounds.

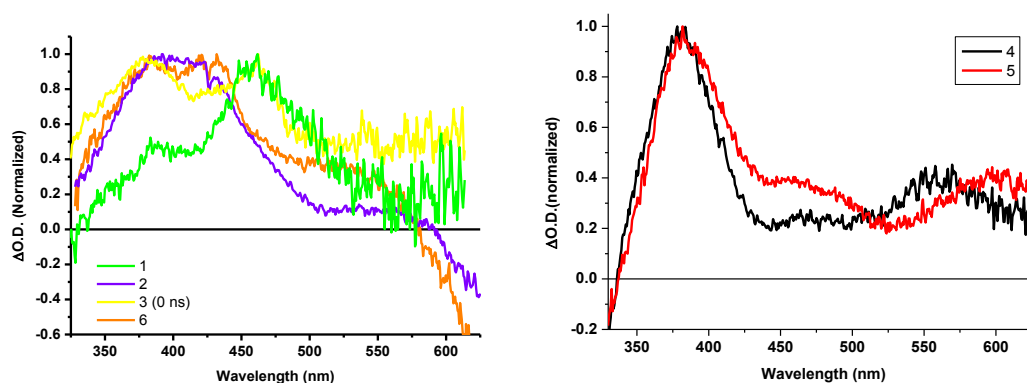


**Fig.4.31:** The transient absorption spectra of **B1**, **B2**, **B3**, **B6** (left) and **B4**, **B5** (right).

It is shown on Fig.4.31 the transient absorption signal of **B1**, **B2**, **B3** and **B6** on the left and **B4**, **B5** on the right. They are grouped according to their structural similarities. The spectrum for **B3** is taken before the triplet rises. All spectra have a band at around 370nm, which can be related to the  $\pi$ - $\pi^*$  transitions involving the  $\text{BF}_2$ -pyrromethene core. Comparing structure and spectra, it can be said that aryl substitution produces an absorption band at 430 nm and following methoxy substitution onto the aryl rings in the  $\alpha$ - pyrrole position causes the subsequent shift of this band to 460 nm.

We made an attempt to obtain  $S_n \leftarrow S_1$  absorption by eliminating spectral features related to the ground state bleaching and stimulated emission for **B1** and **B3** (see Fig.4.32, 4.33 and 4.34). To do that, the steady state absorption and fluorescence spectral shapes were subtracted from the transient spectra. Excited singlet state absorption spectra of **B1** and **B3** are similar

with bands at 700 nm and 440 nm. Excited triplet state absorption spectrum has bands at 650 nm and 360 nm. This more accurate analysis of TRABS spectra reveals the presence of a relatively narrow excited state absorption feature close to the ground state absorption wavelength.

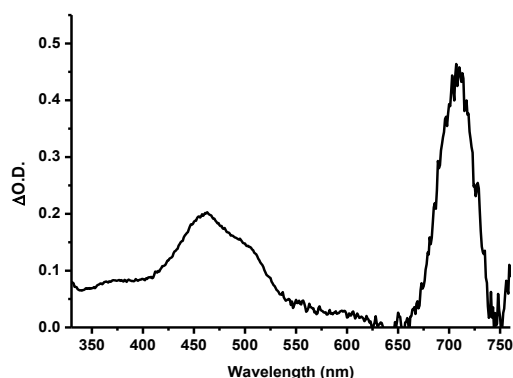


**Fig.4.32:** Absorption spectra of excited singlet state of **B1** in  $CH_3CN$ . Spectrum is constructed from two spectra: excitation 650 nm and 460 nm.

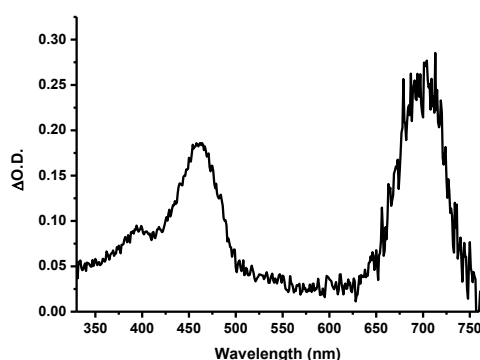


**Fig.4.33:** Absorption spectra of excited singlet state of **B3** in  $CH_3CN$ . Spectrum is constructed from two spectra: excitation 650 nm and 460 nm.

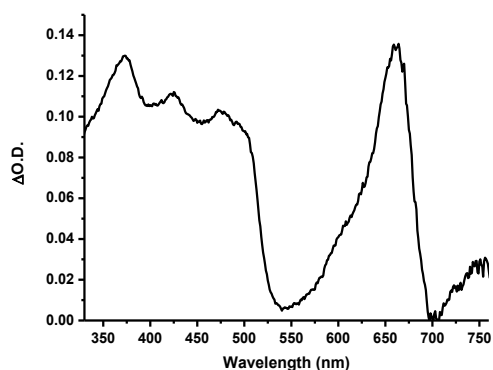


**Fig.4.34:** Absorption spectra of excited triplet state of **B3** in  $CH_3CN$ . Spectrum is constructed from two spectra: excitation 650 nm and 460 nm.

#### 4.1.6. Two Photon Absorption

In this part, we will discuss the two photon absorption properties of aza-BODIPY dyes. As mentioned before, aza-BODIPY dyes **68-70** are used for imaging application due their high NIR fluorescent properties.

If we consider also that they have main absorption band at around 650 nm, their two photon absorption (2PA) wavelength should be around 1.3  $\mu\text{m}$ , which is convenient for many applications. For example, dispersion in silica vanishes at these IR wavelengths that allow light pulse propagation without spreading. The expected 2PA at these IR wavelengths makes the aza-BODIPY dyes practical for telecommunication applications. Since BODIPY dyes (BODIPY-FL, BODIPY-TR) are widely used for two-photon microscopy imaging<sup>151, 152</sup>, it can be expected that aza-BODIPYs can be used for two-photon microscopy applications considering their NIR emission is an advantage for silicon based detectors in two-photon microscopy.

The measurements of the spectra were done by monitoring the wavelength–dependent two photon excited fluorescence normalized by the square of the excitation laser power. Carbon tetrachloride ( $\text{CCl}_4$ ) was used as solvent for experiments. The choice of the solvent ensures the absence of artefacts due to solvent absorption in wavelength range between 1000-1600nm, where most solvents absorb the light.

To obtain the unknown 2PA cross section, we measure in exactly same conditions two photon excited fluorescence intensities of sample and reference. We use Rhodamine 6G as a reference<sup>153</sup>.

The 2PA cross-section is evaluated as follows<sup>154</sup>:

$$\beta_x(\lambda) = \frac{F_x(\lambda).w_R^2(\lambda).\varphi_R.c_R.S_R}{F_x(\lambda).w_x^2(\lambda).\varphi_x.c_x.S_x} \cdot \left(\frac{\nu_x}{\nu_R}\right)^2 \cdot \beta_R \quad (55)$$

In this equation, F is the fluorescence intensity; w is the power of the laser excitation.  $\varphi$  is the quantum yield of fluorescence, c is the concentration of solution. S is the sensitivity of camera at detection wavelength of fluorescence.  $\nu$  is the laser light frequency.  $\beta$  is the cross section value of Rhodamine 6G taken from literature ( $\beta=9.5$  at 1050 nm).

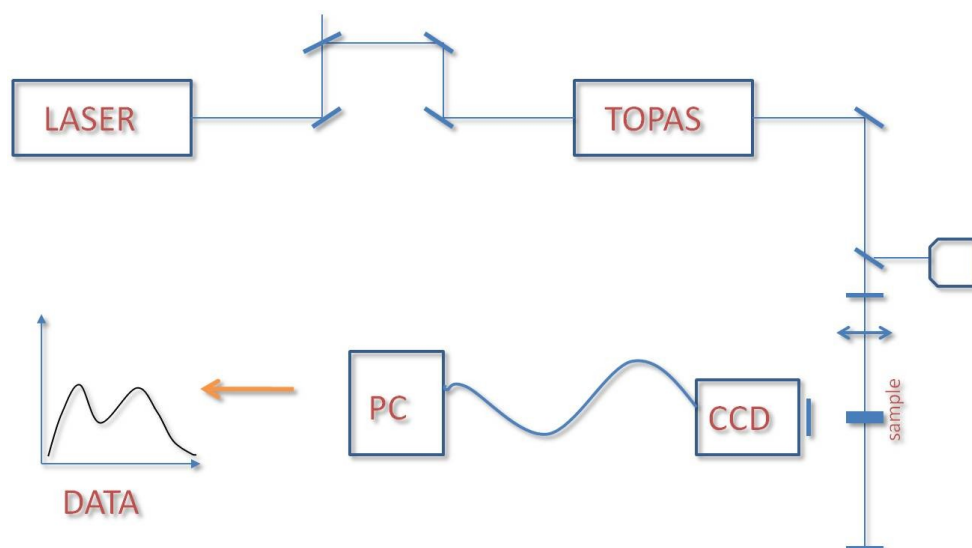


**Fig.4.35:** *The experimental setup for 2PA measurements.*

Two Photon Absorption cross sections were measured using an Optical Parametric Generator (OPG) Topas-C (Light Conversion) pumped by a femtosecond laser system Femtopower Compact Pro (Femtolasers) output. The OPG output, after necessary attenuation, was focussed with a 50 cm focal length lens. The sample and reference solutions, placed in 1 cm synthetic silica cells, were installed at 30 cm from the lens thereby ensuring a constant beam size in the sample at all wavelengths. The OPG pulse duration in the sample (circa 40 fs) was fixed for all wavelengths used. Two photon excited fluorescence was observed by a XC-75 (Sony) video camera through an appropriate pump wavelength cutting filter. The images of fluorescence pattern for sample and reference solutions were integrated and the obtained fluorescence intensities were corrected with respect to the video camera spectral sensitivity curve. Carbon tetrachloride, which is transparent to at least 1600 nm, was used to dissolve samples. Beam size and pulse duration are not taken into account explicitly in equation 1 since the pulse duration was fixed at the same value (40 fs) and optical setup (Fig.4.35) was built in such way that the beam size did not change noticeably for all used wavelengths.

2PA spectra for **B1** and **B3** together with their steady state absorption are presented in Fig.4.36 and 4.37. As **B1** and **B3** are noncentrosymmetric dyes, we observe a good matching between 1PA and 2PA curves. In a centrosymmetric dye, the allowed transitions are different for 1P and 2P excitations<sup>155</sup>.

In the absence of additional push-pull chromophores the NIR two photon absorption cross section of BF<sub>2</sub>-azadipyromethenes is modest<sup>156</sup>. However it is instructive to observe the TPA

behaviour of **B1** and **B3** due to their high potentials in TPA-related applications in the telecommunications spectral range.

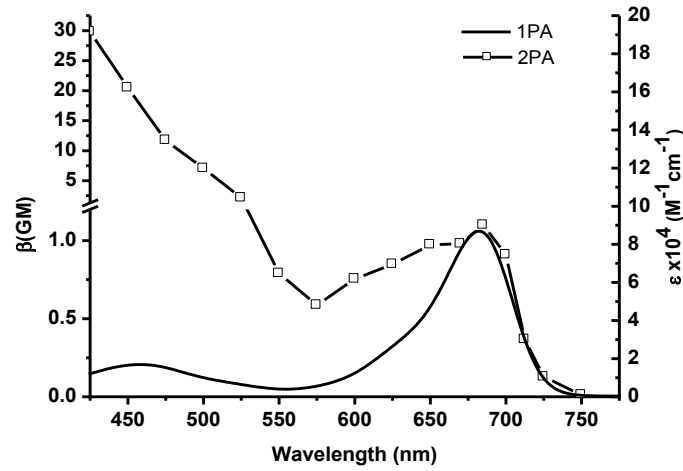


**Fig.4.36:** Comparative one and two photon absorption spectra of **B1**.

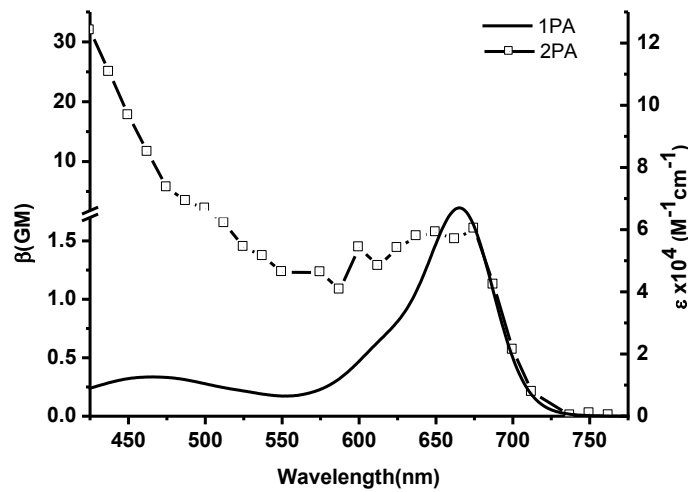


**Fig.4.37:** Comparative one and two photon absorption spectra of **B3**.

#### 4.1.7. Photostability

An important consideration for new fluorophores is the photostability, which can ultimately define the scope of usage for example down to the single molecule regime. Indeed, excited molecules have several deexcitation pathways, including photodegradation, changing the chemical composition of molecules. The quantum yield of photodegradation is a sign of photostability of fluorescent dye. It is calculated by making some assumptions. Quantum yield of photodegradation ( $Q_{\text{photodegradation}}$ ) can be given as:

$$Q_{\text{photodegradation}} = \frac{\text{No. of molecules degraded}}{\text{No. of molecules excited}} = \frac{h\nu V}{W\epsilon \ln 10\tau} \quad (56)$$

where  $W$  is the power of the excitation beam,  $V$  is the volume of the solution sample,  $\epsilon$  is extinction coefficient and  $\tau$  is the time for degradation of all molecules.

The details of calculation are given in the Appendix. Fluorescein, which is known as a dye for laser induced fluorescence applications, is used as reference. The photodegradation quantum yield value of fluorescein in methanol was reported in order of  $10^{-5}$  in literature<sup>157</sup>. We estimated the value of  $Q_{\text{photodegradation}}$  as  $7.5 \times 10^{-5}$ . In Table-4.3, the quantum yield of photodegradation of all considered AZABODIPY dyes are presented.

**Table-4.3:** *The quantum yield of photodegradation of AZABODIPY dyes and fluorescein*

<b>Molecule</b>	<b><math>\Phi_{\text{photodegradation}}</math></b>	<b>Power (mW)</b>
Fluorescein in ethanol	$7.5 \cdot 10^{-5}$	3.5
<b>B1</b> in ACN	too low to estimate	51
<b>B1</b> in DMSO	$9.6 \cdot 10^{-8}$	51
<b>B2</b> in ACN	too low to estimate	61
<b>B3</b> in ACN	$7 \cdot 10^{-8}$	41.5
<b>B4</b> in ACN	too low to estimate	25
<b>B5</b> in ACN	too low to estimate	34
<b>B6</b> in ACN	too low to estimate	62

**B1-B6** molecules were excited at 640 nm with a semiconductor laser source. Fluorescein was excited at 504 nm. The quantum yield of photodegradation of aza-BODIPY dyes shows that these dyes are few orders more stable than fluorescein, which is considered a stable dye. Fig.4.38 presents the number of photodegraded of **B1**, **B3** and fluorescein molecules as a function of number of absorbed photons.

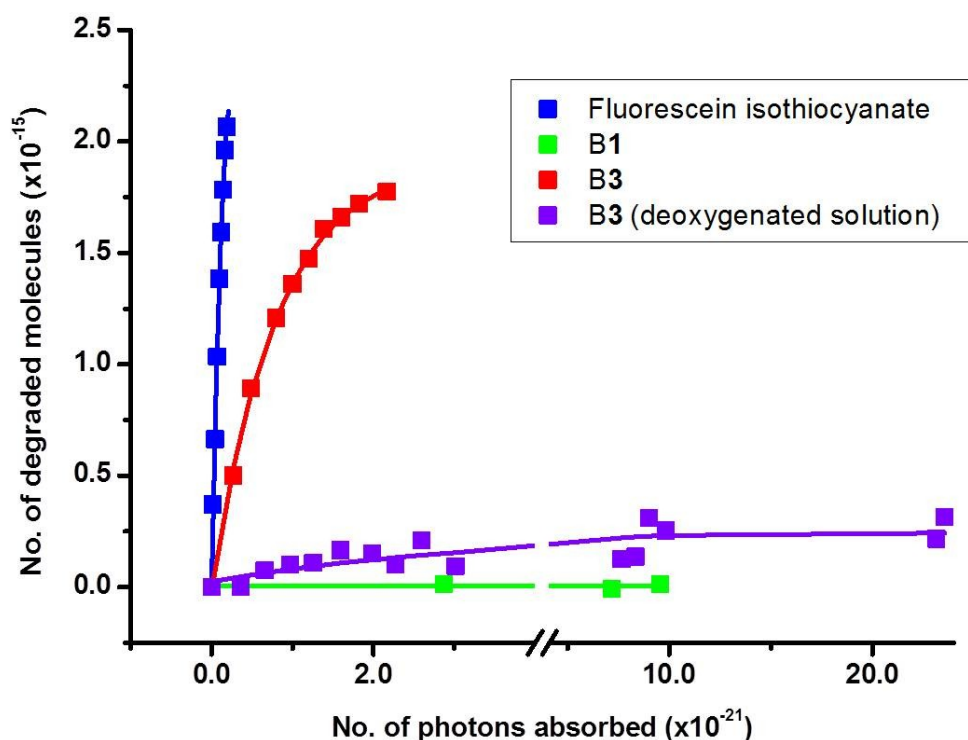


**Fig.4.38:** The photodegradation of **B1**, **B3** and fluorescein dyes.

#### 4.1.8. Conclusion

In conclusion, Br substituted  $\text{BF}_2$ -azadipyrromethene **B3** is a therapeutically interesting red-light absorbing photosensitizer. Evolution of the singlet ( $S_n \leftarrow S_1$ ) and triplet ( $T_n \leftarrow T_1$ ) transient absorption signatures of compounds **B1-B6** allows direct spectroscopic determination of the intersystem crossing efficiency and rate to the non-emissive triplet state of **B3** and lifetime of this PDT-active excited state. An intersystem crossing efficiency of 72% was determined with a triplet lifetime of 21  $\mu\text{s}$ . Singlet oxygen generation quantum yield of **B3** is estimates 74 %, or 0.77 compared to  $\text{C}_{60}$ . These photophysical properties make **B3** molecule a good candidate as a PDT agent. Clinical trials are ongoing. Their NIR absorption and emission properties, TPA cross sections and photodegradation properties make them suitable for different applications such as imaging.



Importantly for high fluorescence, the phenyl ring presents a  $90.0^\circ$  dihedral angle to the BODIPY plane in the solid state. On comparing with a related hydrocarbon analogue, the fluorine atoms can be seen to be responsible for this behaviour. For example replacing the pentafluorophenyl ring with a para-bromophenyl<sup>158</sup> (Fig.4.40a), such that ortho protons replace protons is resulted in a decreased angle of  $78.9^\circ$  between planes; while that comprising a dimethylamino group<sup>159</sup> (Fig.4.40b) was  $87.6^\circ$ .

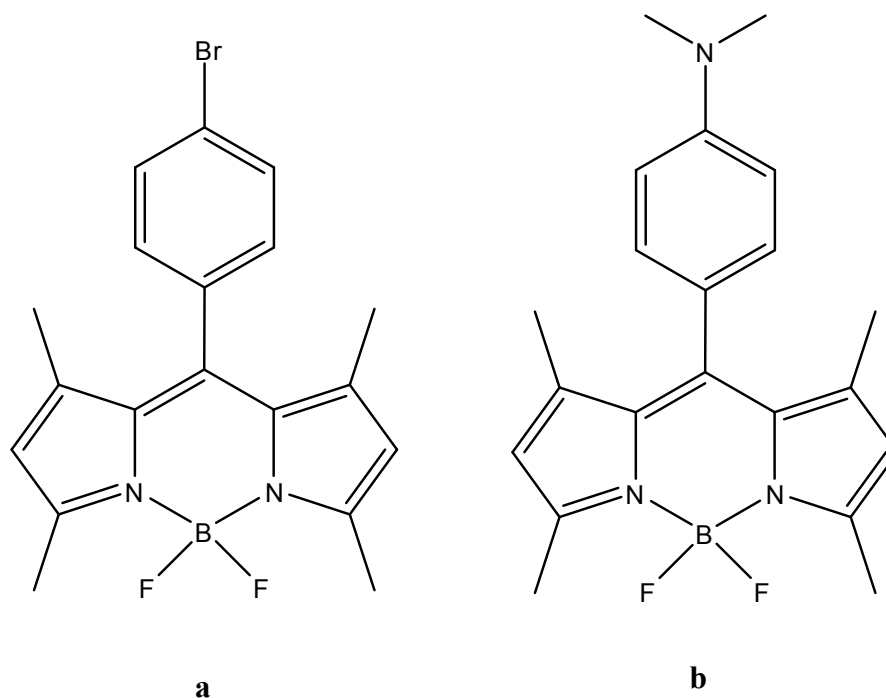


**Fig.4.40:** *a) para-bromophenyl substituted BODIPY b) BODIPY with dimethylamino group.*

For I-BODIPY the torsional angle between phenyl and BODIPY core was reported by Burghart<sup>120</sup> *et al.* as  $77^\circ$ .

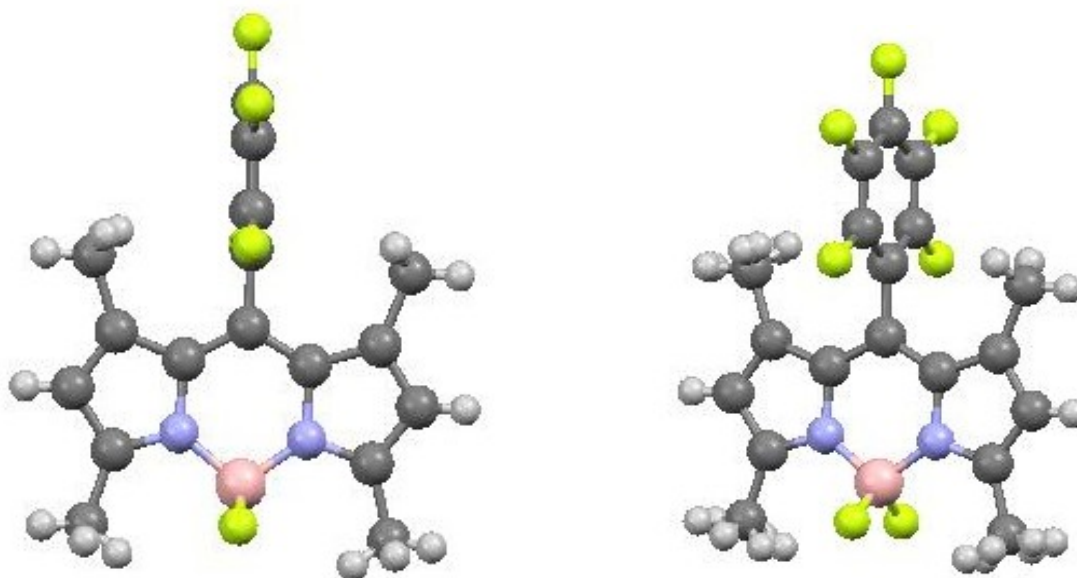


**Fig.4.41:** *The crystal structure of B9.*

### 4.2.3. Steady State Absorption and Emission

**B9** and **B10** show strong absorption and intense emission, as shown by data in Table-4.4. Molar extinction coefficients are similarly high. Main absorption band for F-BODIPY is very close to emission of Argon ion laser at 514 nm. A sulfonated rhodamine derivative Alexa Fluor 514® is one of the fluorophores which is perfectly adapted for this wavelength. Nevertheless it is very expensive. **B9**, which has a fluorescence quantum yield almost unity, is a new and cheaper fluorophore. Absorption and fluorescence emission spectra of **B10** ( $\lambda_{exc} = 504$  nm) and **B9** ( $\lambda_{exc} = 515$  nm) in THF are given in Fig.4.42.

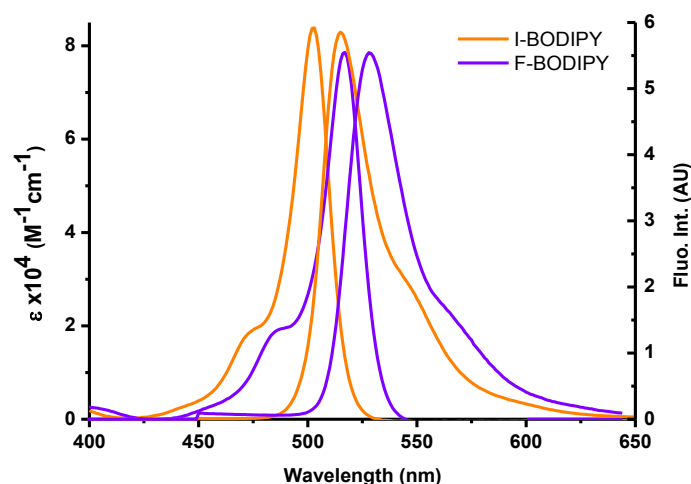


**Fig.4.42** Electronic absorption and fluorescence emission spectra of **B10** ( $\lambda_{exc} = 504$  nm) and **B9** ( $\lambda_{exc} = 515$  nm) in THF.

The phenyl group attached on the *meso* site does not affect the absorption or emission wavelength maximum. However, as a result of its free rotation, the molecule can lose its excited state energy via non-irradiative molecular motions. This decreases the fluorescence quantum yield and also luminescence lifetime. 1, 7 substitution can limit this rotation<sup>112</sup>. Therefore, the quantum yield of **B9** is almost unity and **B10** is close to unity. This phenyl group of **B10** is more flexible than **B9**. This explains the shorter lifetime of **B10**.

**Table-4.4:** The spectroscopic data for **B9** and **B10** in air-equilibrated THF

Sample	$\lambda_{max}$ (nm)	$\epsilon$ ( $M^{-1} cm^{-1}$ )	$\lambda_{em}$ (nm)	$\Phi_f$	$\tau$ (ns)
<b>B9</b>	516	78600	527	0.98	6.1
<b>B10</b>	504	82000	515	0.9	2.8

#### 4.2.4. Transient Absorption

Transient absorption (TRABS) spectroscopy was employed to follow the evolution of the excited **B9** and **B10** molecules. Fig.4.43 (black curve) shows the TRABS spectrum recorded at 500 ps time delay. The TRABS spectrum was built by connecting two spectra after excitation at 510 nm and 355 nm. No TRABS spectral evolution was observed during the lifetime of excited states. The spectrum is dominated by a band with negative intensity centred at 530 nm and positive bands at 350 nm and 420 nm. The negative spectral feature is due to both stimulated emission, responsible for the red side of the band, and bleach of the ground-state absorption, accounting for the blue side of the band. A more accurate analysis of TRABS spectrum, accounting for the ground state bleaching and stimulated emission spectral shapes, reveals a presence in the absorption of excited state of a relatively narrow absorption feature close to the ground state absorption wavelength (blue trace Fig.4.43).

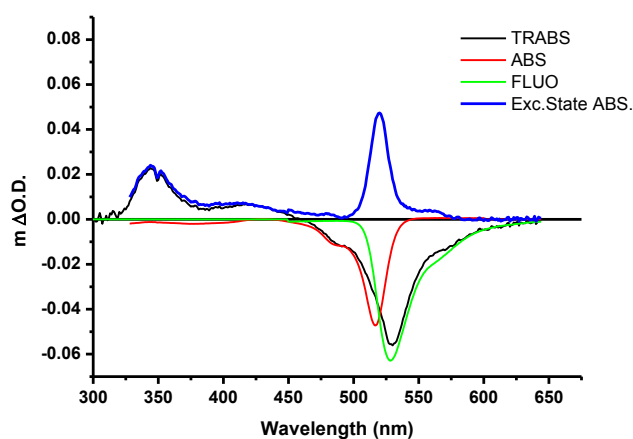


**Fig.4.43:** The excited state absorption spectrum of **B9** in THF ( $\lambda_{exc}=510nm + \lambda_{exc}= 355nm$ ).

Figure 4.44 (black curve) shows TRABS spectrum recorded at 500ps time delay after excitation at 500 nm. No TRABS spectral evolution was observed during the lifetime of excited states. The spectrum is dominated by a band with negative intensity centred at 510 nm and a large weak positive band between 400 and 450 nm. The negative spectral feature is due to both stimulated emission, responsible for the red side of the band, and bleach of the ground-state absorption, accounting for the blue side of the band. The blue curve is the excited state absorption spectrum calculated from TRABS spectrum accounting for the ground state bleaching and stimulated emission spectral shapes.

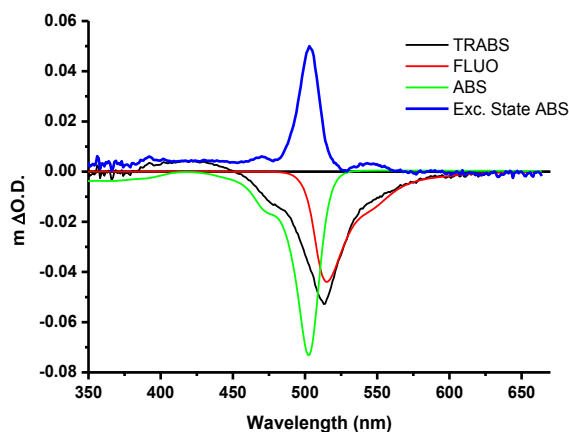


**Fig.4.44:** The excited state absorption spectrum of I-BODIPY in THF ( $\lambda_{exc}=500$  nm).

#### 4.2.5. Two Photon Absorption

Two photon microscopy (TPM) can be more suitable for biological imaging due to its advantages of penetration depth and its red shifted excitation light. In the TPM technique, two photon absorption is strongly dependent on the intensity of the incident light, and therefore, excitation only takes place in a small volume centred at the focal plane, giving intrinsic sectioning and greatly reducing background fluorescence from out-of-focus excitation. Because the two-photon excitation is limited to the focal plane, photodamage and bleaching to the sample are minimized<sup>160</sup>. Additionally, the greatly reduced absorption and scattering of NIR light allows for deeper penetration into biological samples<sup>161</sup>.

The fluorophore which will be used in TPM, must have a high two-photon absorption cross section and the fluorescence quantum yield. In this part, we will present **B10** molecule as a candidate for TPM. As mentioned in previous sections, it has high fluorescence quantum yield, 0.9. Rhodamine B is known to be a bright two-photon dye. For two-photon cross section experiment we have used Rhodamine as reference. Fig.4.45 and 4.46 present two photon cross section values and of **B10** and Rhodamine B dependence on wavelength respectively.

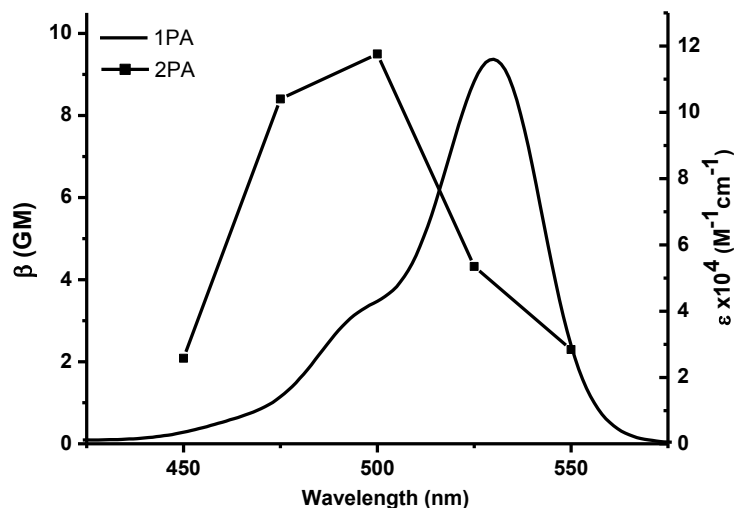


**Fig.4.45:** Comparative one and two photon absorption spectra of Rhodamine B.

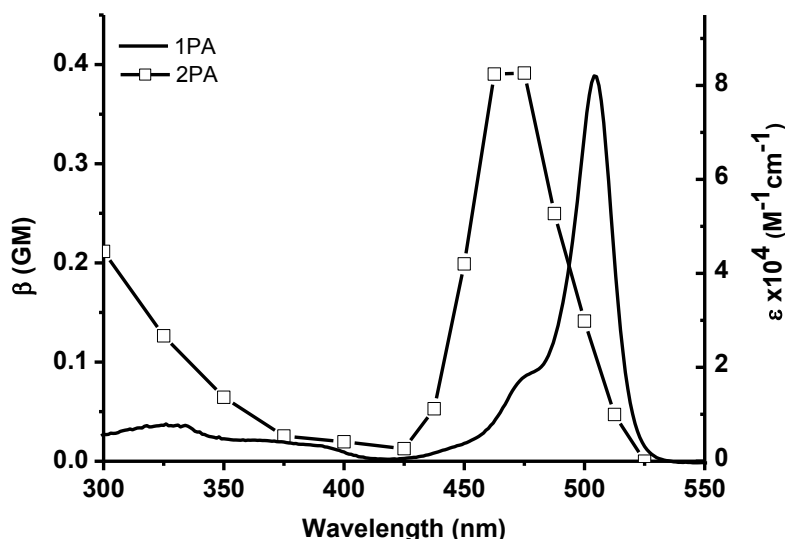


**Fig.4.46:** Comparative one and two photon absorption spectra of **B10**.

Their one-photon absorption spectra are also presented in the graphs for comparison. A small blue shift is observed on the maxima of two photon absorption peaks. We did not observe such a shift in BF<sub>2</sub>-dipyrrromethenes. This phenomenon can be explained as follows: When a molecule absorbs a photon, it is promoted from ground state to excited state. This excited state is a level which is allowed by selection rules due to symmetry. When a molecule is excited by two-photon absorption, symmetry rules now allow promoting electron another excited state which has different symmetry. If a molecule is centrosymmetric its excited state symmetry is different for one- and two photon absorption. If a molecule is non-centrosymmetric, its excited state symmetry is same. As a result **B10** and Rhodamine B are centrosymmetric dyes. Therefore their one- and two-photon absorption spectra are different.

#### 4.2.6. Photodegradation

The photostability of **B9** and **B10** were evaluated on radiation in air-equilibrated solutions. **B9** in acetonitrile solution is irradiated at 512 nm with a excitation beam power of 3.5 mW as well as **B10** in acetonitrile solution is irradiated at 504 nm with a excitation beam power of 3.4 mW. Quantum yield of photodegradation of **B9** and **B10** are estimated  $2.7 \cdot 10^{-5}$  and  $1.8 \cdot 10^{-5}$ , respectively. As mentioned before, according to our measurements quantum yield of photodegradation of fluorescein is  $7.5 \cdot 10^{-5}$ , which is the same order of magnitude as literature value<sup>157</sup>. Considering these results, it can be concluded that **B9** and **B10** are photostable dyes for imaging applications.

#### 4.2.7. Conclusion

As mentioned before, *meso* substitution of BODIPY dyes, does not affect of wavelength and it allows functionalizing molecule by inserting different substitutions. **B9** molecule with perfluorinated phenyl ring can be used for biological labelling applications. The dye has a high extinction coefficient and high quantum yield of fluorescence. Photostability of **B9** and **B10** is in the same order with fluorescein dye which is widely used for imaging studies and known as a stable dye. Compare to Rhodamine B dye, **B10** shows lower two-photon cross-section. However the information is useful for TPA-based applications.

The excited state absorption spectra of these dyes are given also. The calculated spectra have similar features as excited absorption spectra of aza-BODIPY dyes given before. This kind of treatment of transient absorption signal was not reported before to get the excited state absorption spectra of BODIPY dyes. In this point of view, this study can be accepted as a pioneer work.

## PART III

### Ultrafast photoinduced electron transfer in BODIPY-BAPTA sensors

#### 4.3.1. Introduction

Fluorescent sensors are useful tools for cation sensing in the domains of biology, medicine, environmental sciences and chemical oceanography.<sup>10</sup> A fluorescent sensor consists of two parts: An ionophore for cation recognition and a fluorophore as signalling unit. In our molecular system the ionophore is BAPTA [1,2-bis(*o*-aminophenoxy) ethane-*N,N,N',N'*-tetraacetic acid)<sup>30</sup>, which has a well adapted cavity for recognition of calcium. As the fluorophore, BODIPY is used since it has high molar extinction coefficient, high fluorescence quantum yield and excitation wavelength in the visible part of spectrum. Despite there being a wealth of fluorinophores available, relatively few reports of spectroscopic characterization of fast processes have been made. The structures of studied compounds in ester forms **B7** and **B8** are presented in Fig.4.47. Their free acid forms were also studied, which will be named as **B7-fa** and **B8-fa**. In cellular applications the esters can permeate the cell membrane and by hydrolyzed in the cytoplasm, to give the more chelating free acids.

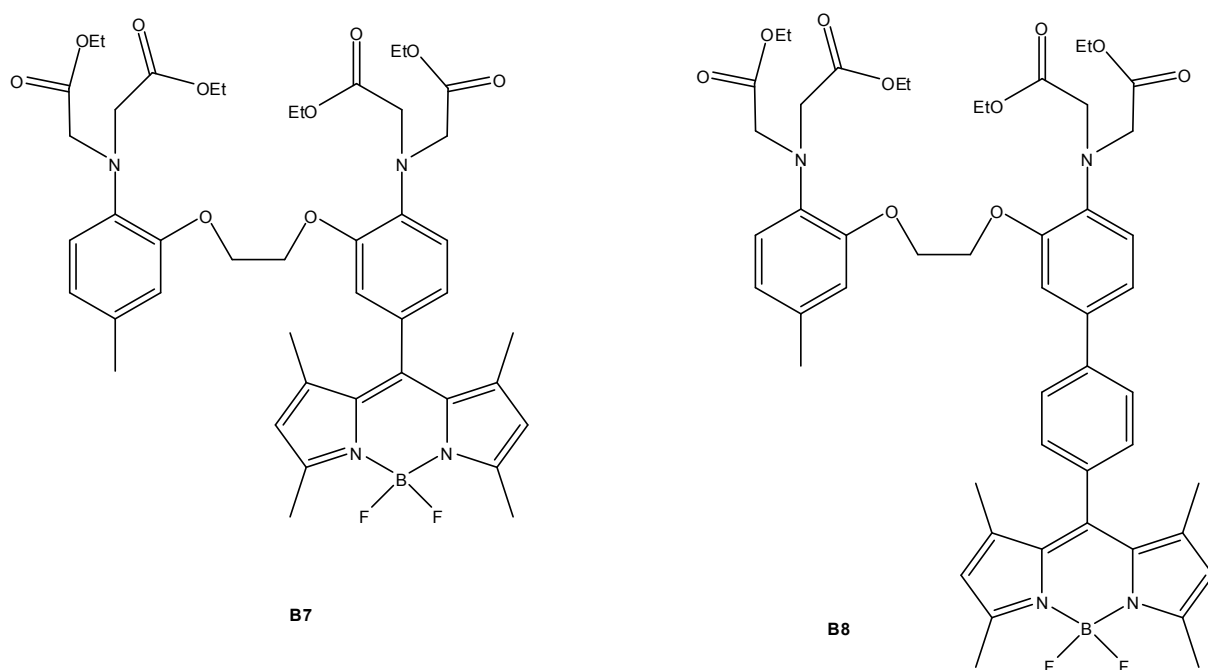


**Fig.4.47:** The structures of **B7** (left) and **B8** (right) esters.

### 4.3.2. Principles

Besides the excellent calcium recognition property, the BAPTA ionophore was chosen as a part of compounds **B7** and **B8** due to its oxidation potential being compatible with photoinduced electron transfer towards the excited BODIPY. This disposition of electronic levels ensures an electron transfer from BAPTA towards BODIPY in the absence of calcium binding and thus, an efficient fluorescence quenching of BODIPY. On blocking this quenching pathway, fluorescence is anticipated to be restored.

Indeed, ionophore BAPTA contains an electron rich group (amino group) and acts as electron donor (D). The fluorophore BODIPY plays the role of an electron acceptor (A). After excitation of the fluorophore (transition HOMO-1 to LUMO is the lowest-gap optically active transition), an electron is transferred from the highest occupied molecular orbital (HOMO) to the lower lying singly occupied molecular orbital (HOMO-1). This photo-induced electron transfer (PET) causes fluorescence quenching of fluorescence. Upon cation binding, the oxidation potential of the donor is changed so that the relevant molecular orbital becomes lower in energy than that of the fluorophore; consequently, PET is not possible anymore and fluorophore starts to exhibit fluorescence (see Fig.4.48). In other words, fluorescence intensity is switched from **OFF** to **ON** in the presence of cation.

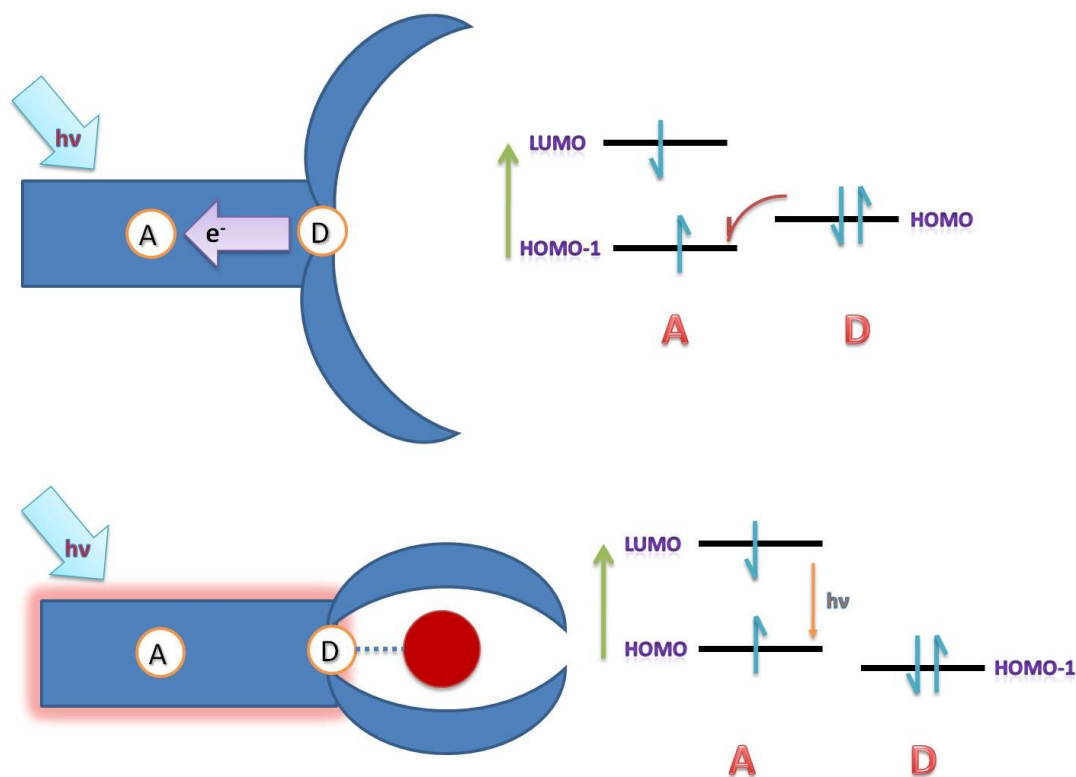


**Fig.4.47:** The principle of photoinduced electron transfer sensors (blue rectangular block: BODIPY part, semi circles: BAPTA part).

Quantum chemical calculations, performed using MOPAC software, confirm the situation explained above. One aniline of BAPTA connected with BODIPY is used for more simple calculations by taking the dielectric constant of the environment as 20. In Figures 4.48 and 4.49, molecular orbitals involved in the PET are depicted. HOMO-1 and LUMO are located on the BODIPY fragment of the compounds and represents the molecular orbitals which involve the lowest-gap optically active transition. The aniline of BAPTA is almost perpendicular with respect to the BODIPY part for molecule **B7** due to steric hindrance introduced by  $\alpha$ -methyls. According to calculations the angle between them is found at  $88^\circ$ . The electronic systems of these two parts of compound **B7** are deconjugated. Thus, HOMO located on BAPTA is not affected by the transition between HOMO-1  $\rightarrow$  LUMO and is involved in PET as electron donating orbital.

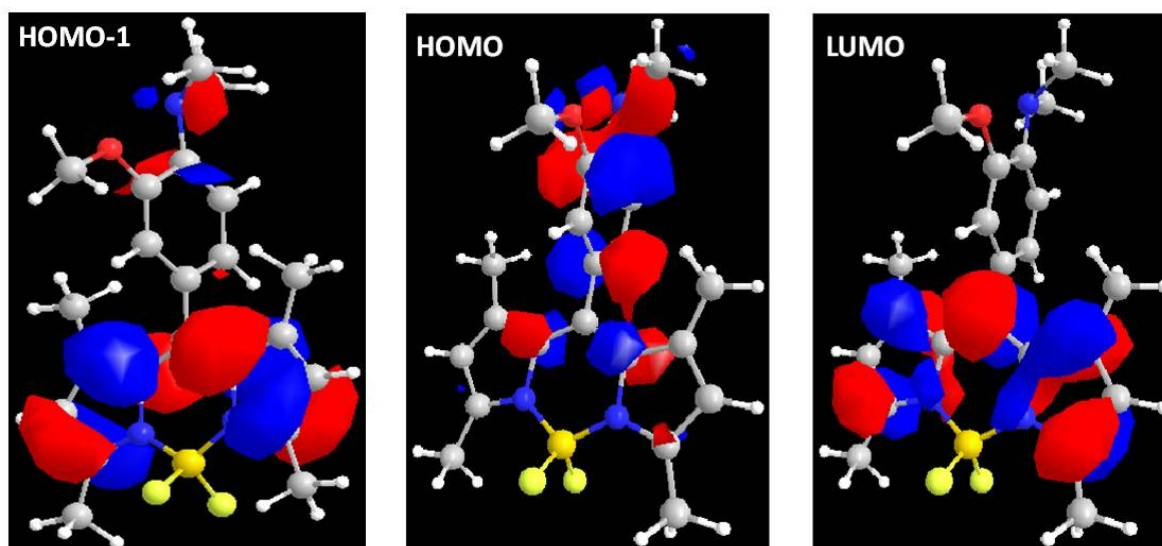


**Fig.4.48:** The HOMO-1, HOMO and LUMO orbitals on molecule **B7**.

Despite the fact that the structure of **B7** contains aniline and the structure of **B8** contains diphenylamine as electron donors, globally the molecular orbital location remains the same and supposed photophysical behaviour should not exhibit large differences.

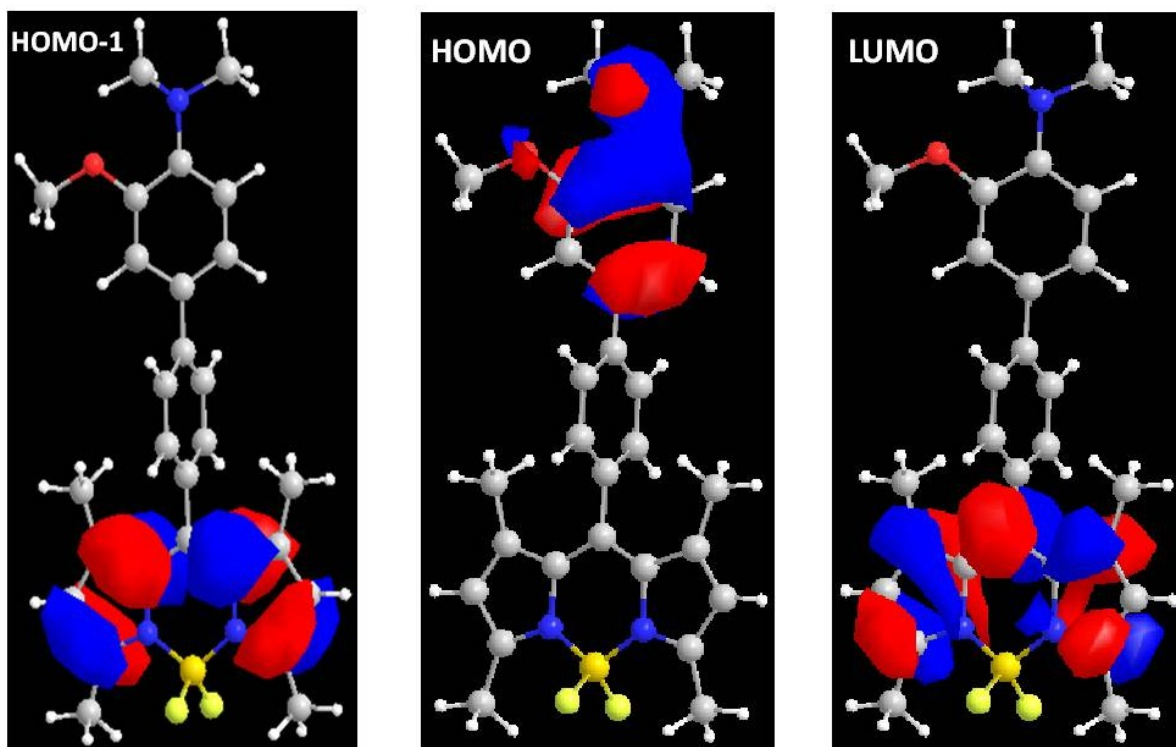


**Fig.4.49:** The HOMO-1, HOMO and LUMO orbitals on molecule **B8**.

#### 4.3.3. Fluorescence Titration with $\text{Ca}^{2+}$ Analyte

The binding of  $\text{Ca}^{2+}$  was studied in an environment similar to the intracellular one. The lithium salts **B7** and **B8** were dissolved in Milli-Q water containing 0.1 M KCl and 0.03 M MOPS (3-[N-morpholino]propanesulfonic acid) and the pH was adjusted to 7.20. Absorption and fluorescence emission spectra measured as a function of  $\text{Ca}^{2+}$  concentration are shown in Fig.4.50 and Fig.4.51 for **B7** and **B8**, respectively. The free  $\text{Ca}^{2+}$  concentrations were adjusted by use of EGTA as described by Tsien<sup>30</sup>. In the absence of  $\text{Ca}^{2+}$ , very weak fluorescence intensity was observed. A large increase of the fluorescence intensity and fluorescence quantum yield was observed upon addition of calcium, without a change of the position of the maxima. The lone electron pair of the amino group of the BAPTA moiety is known to be involved in the binding of  $\text{Ca}^{2+}$ , thus calcium coordination partially blocks the PET process and increases fluorescence yield. In addition, absorption spectra do not change much. It can be explained that the energy levels of fluorophore –BODIPY- are not affected by the presence of  $\text{Ca}^{2+}$  and complexation phenomena as it was supposed after MOPAC calculations.

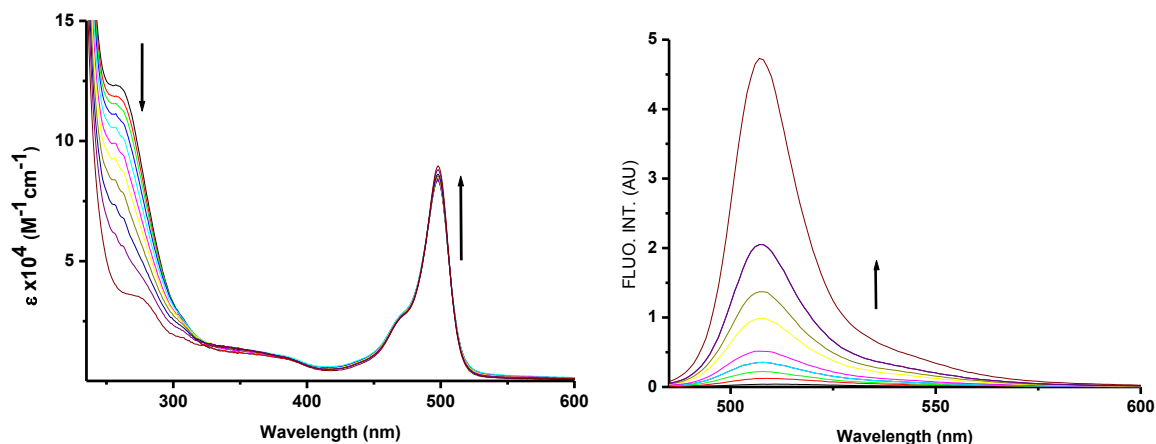


**Fig.4.50:** The change in the absorption and emission spectra of **B7** in water by addition of  $\text{Ca}^{2+}$  ( $\lambda_{exc}=475 \text{ nm}$ ).

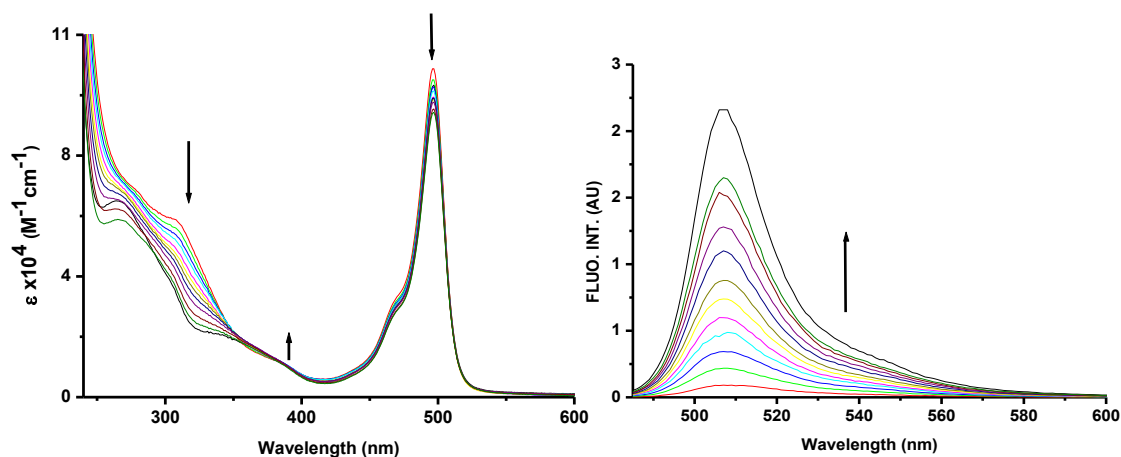


**Fig.4.51:** The change in the absorption and emission spectra of **2** in water by addition of  $\text{Ca}^{2+}$  ( $\lambda_{exc}=475 \text{ nm}$ ).

The dissociation constants  $K_d$  of the complexes between  $\text{Ca}^{2+}$  and **B7** and **B8** were determined in a buffered aqueous solution (pH 7.20) by fluorometric titration as a function of  $\text{Ca}^{2+}$  concentration, using the fluorescence emission spectra. Nonlinear fitting of equation (57) to the steady-state fluorescence data  $F$ , recorded as a function of  $[\text{Ca}^{2+}]$ , yields values of  $K_d$ , the fluorescence signals  $F_{\min}$  and  $F_{\max}$  at minimal and maximal  $[\text{Ca}^{2+}]$ , respectively (corresponding to the free and  $\text{Ca}^{2+}$  bound forms of the ligand, respectively), and  $n$  (the number of calcium cations bound per ligand). Equation (57) assumes that the absorbance of the sample is small ( $<0.1$ ) and that  $\text{Ca}^{2+}$  complex formation in the excited state is negligible.

$$[\text{Ca}^{2+}]^n = K_d \frac{(F - F_{\min})}{(F_{\max} - F)} \quad (57)$$

Equation 57 was linearized and  $K_d$  was obtained by plotting  $\log [(F - F_{\min})/(F_{\max} - F)]$  versus the log of free  $\text{Ca}^{2+}$  in Fig.4.52.

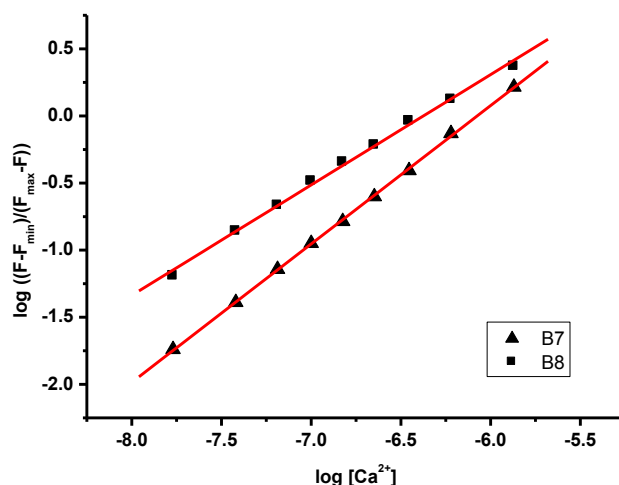


**Fig.4.52:** The Hill-plot of **B7** and **B8**.

The calcium dissociation constants,  $K_d$ , were obtained 0.55 and 5.75 for **B7** and **B8**, respectively, which is a similar value to known BAPTA calcium indicators<sup>162</sup>.  $F_{\max}/F_{\min}$  ratio of **B7** is 122 as well as 23 for **B8**. The data obtained for ester derivatives of **B7** and **B8** in THF are summarized in Table-4.5.

**Table 4.5:** The spectroscopic data for **B7** and **B8**

	$\lambda_{\max}$ (nm)	$\epsilon$ ( $\text{M}^{-1}\text{cm}^{-1}$ )	$\lambda_{\text{em}}$ (nm)	$\Phi_{\text{fluo}}$
<b>B7</b>	501	79 500	514	0.004
<b>B8</b>	501	82 800	512	0.03

#### 4.3.4. Transient Absorption

##### 4.3.4.1.a. Molecule **B7** in THF

In Fig. 4.53, on the left, the transient absorption spectrum of **B7** in THF is shown up to 1ns time delay. We observe positive bands at 420, 525 and 570 nm as well as a wide negative band between 470 and 560 nm. The band at 420 nm and negative band at 520 nm relax in 30ps. While they are relaxing, the positive bands at 525 and 570 nm start to grow-in at the same rate. It can be concluded that there is a precursor-successor relationship between them. These bands are also visible on longer scale experiments (shown on the right) and they have a relaxation time of 1ns. As the observed spectral range is larger, one more band located at 330 nm can be observed also with 1ns relaxation time. The band at 425 nm forms also in 1 ns. The

negative band at 470 nm shows biexponential decay kinetics. Considering these results, the positive band at 420 nm can correspond to excited singlet state absorption band and the negative band at 520 nm is stimulated emission band. After the singlet relaxes, other positive bands appear with a precursor-successor relationship. Due to this relationship, as we expected PET for **B7**, these bands at 525 and 570 nm can be attributed to the anion radical bands of BODIPY fragment and the band at 330 nm is the cation radical band of BAPTA. While radical bands relax, a new band at 425nm starts to grow up. This new band has long lifetime. In 10 ns time window, we have not observed any relaxation of this band. This could be attributed to triplet-triplet absorption band of BODIPY. The biexponential kinetics of negative band at 470 nm, which is ground state bleaching, can be explained with the decay of radicals and recovery of the ground state with triplet relaxation.

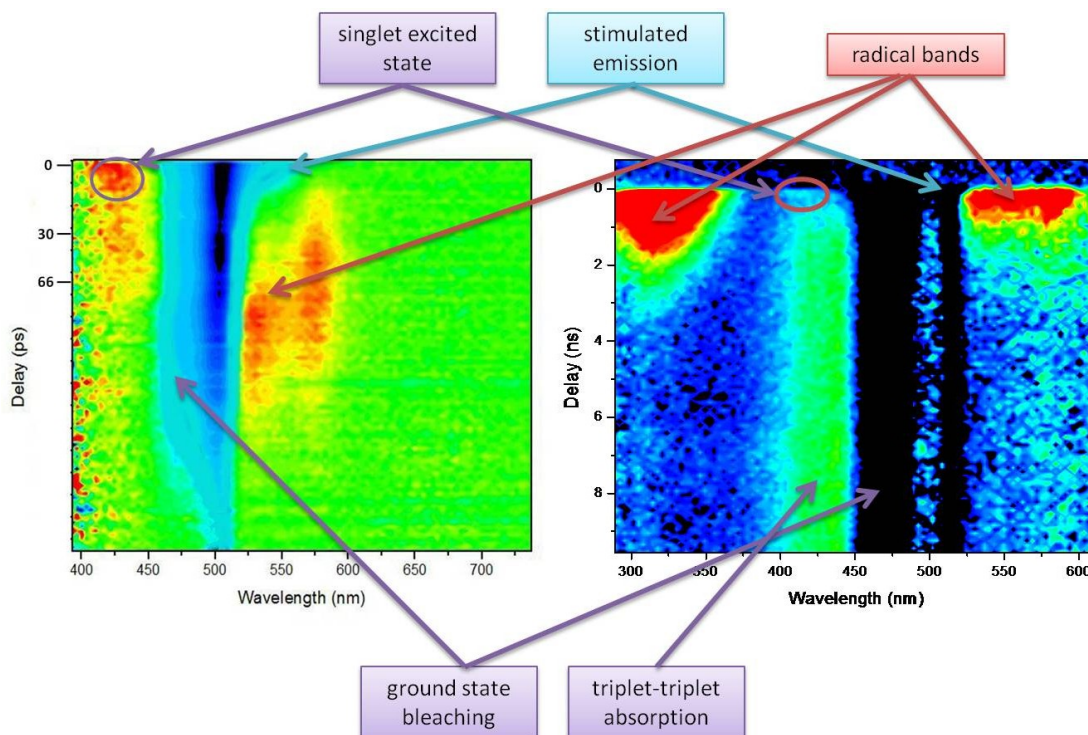
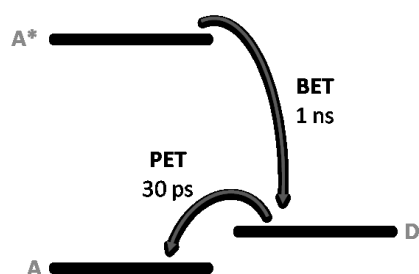


**Fig.4.53:** The transient absorption spectra of **B7** in THF at 0-1 ns (left) and at 0-10 ns (right) ( $\lambda_{exc}=500$  nm).

The model of PET is shown in scheme 1. Photoinduced electron transfer (PET) by excitation occurs in 30 ps. The back electron transfer (BET) rate can be obtained from the relaxation time of radical bands. Relaxation of radicals apparently gives rise to the BODIPY triplet state. The formation of triplets does not affect the behaviour of the system as a sensor. We will make a more detailed discussion about triplet formation in the conclusion part.



**Scheme 1:** *The model for PET and BET for B7 in THF.*

#### 4.3.4.1.b. Protonated B7 in THF

As it was shown before, complexation changes the oxidation potential of the donor, which moves its HOMO energy lower than fluorophore HOMO energy. Obviously, in THF it is impossible to hydrolyze the compound and to make complexation with  $\text{Ca}^{2+}$ . A possible solution to observe photophysical behaviour going upon complexation would be simple protonation of amino group of donor since it should produce similar effect as calcium binding. In Fig.4.54, it is shown the transient absorption spectrum for **B7** in THF in the presence of  $\text{HClO}_4$  in solution.

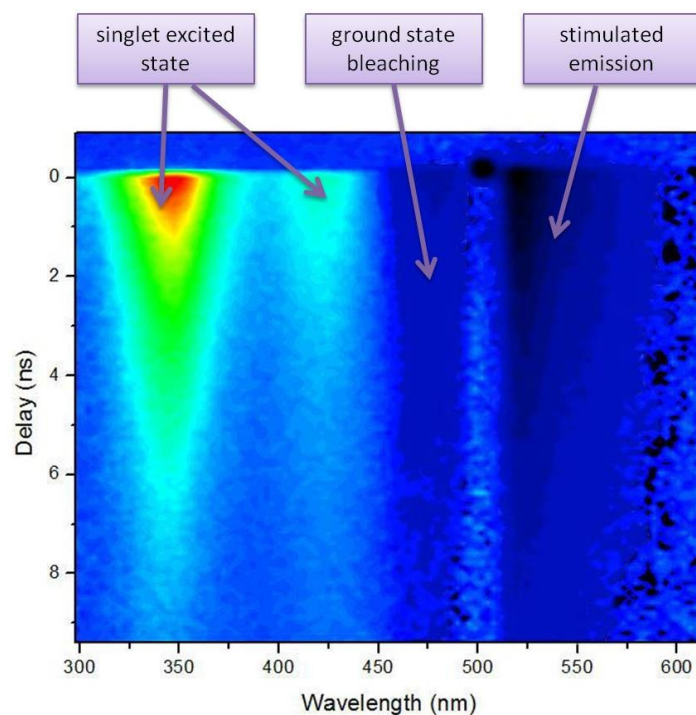


**Fig.4.54:** *Transient absorption spectrum of B7 in THF in the presence of  $\text{HClO}_4$  ( $\lambda_{exc} = 500\text{nm}$ ).*

Positive bands, located at 330 nm and 420 nm, are the singlet excited state absorption bands. The negative band at 480 nm corresponds to ground state bleaching and above 500 nm we

could observe stimulated emission band. All these bands relax with the same time constant of 4 ns. This number is also compatible with fluorescence lifetime.

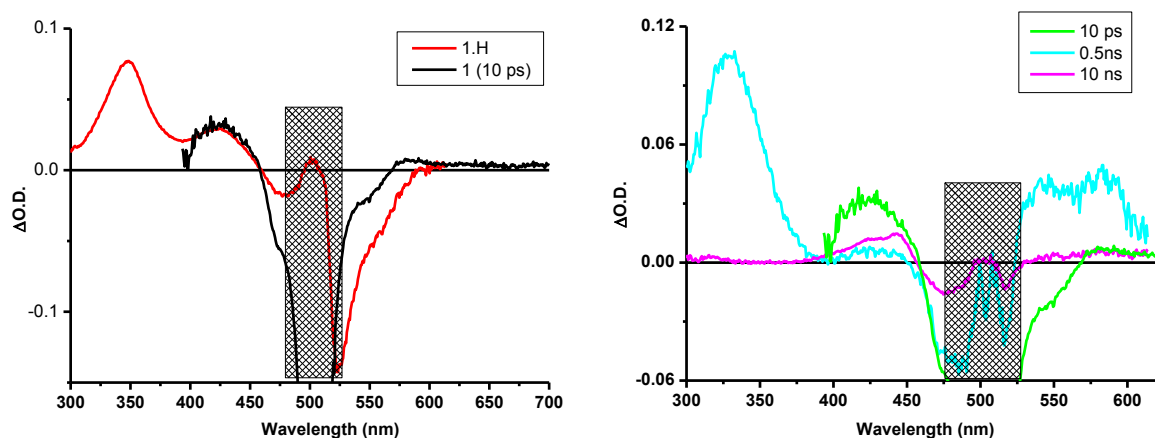


**Fig.4.55:** a) Comparison of transient absorption spectra of singlet excited states of **B7** and **B7.H**.

b) Transient absorption spectra of **B7** for different time delays ( $\lambda_{exc} = 500\text{nm}$ ).

Fig.4.55a shows the transient absorption spectrum of **B7** taken in 10 ps (black curve) and the spectrum of protonated **B7** (red curve). (Amplitudes are adapted for better comparison). Both spectra have the same absorption band at 425 nm; as pointed out before, it is the singlet excited state absorption band. For the protonated molecule, as there is no electron transfer, evidently, this excited singlet is the only possible excited state.

On the right in Fig.4.55b, the spectra belonging to **B7** at different time delays are presented. The green curve contains the excited singlet absorption band together with ground state bleaching and stimulated emission bands recorded in 10 ps delay. In the cyan curve, taken in 0.5 ns, the radical absorption is dominant. After all these bands relax in 10 ns, the spectrum turns as shown into pink curve containing triplet-triplet absorption band and ground state bleaching.

#### 4.3.4.1.c. B7-fa in water

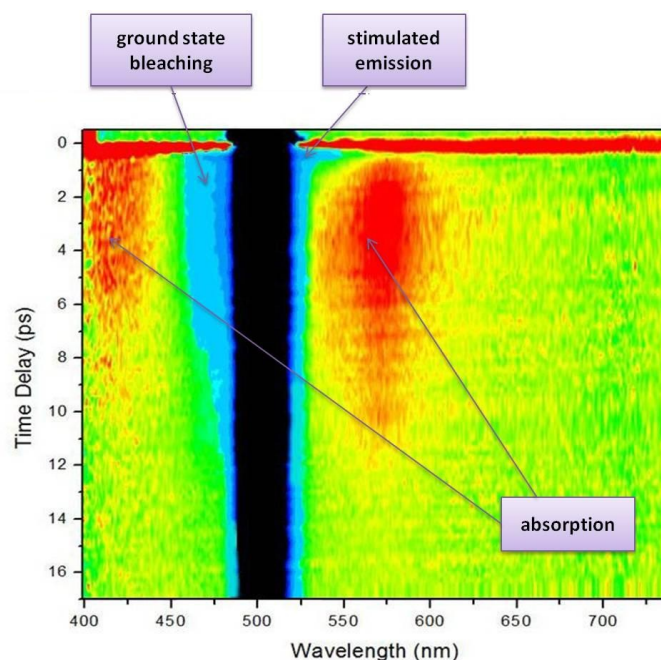
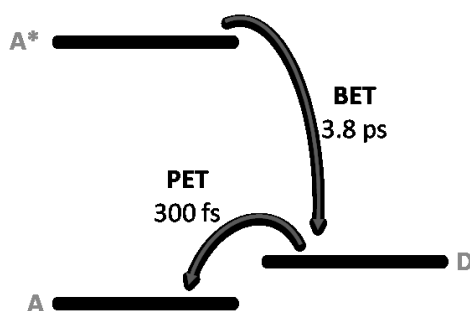


**Fig.4.56:** The transient absorption spectra of **B7-fa** in water ( $\lambda_{exc} = 500\text{nm}$ ).

The transient absorption spectrum for **B7-fa** in water is given in Fig.4.56. At zero delay, a wide positive band can be seen. This band is related to non-linear optical phenomena taking place in the solvent under action of the pump pulse. It is strong and superposed with the excited singlet state absorption band. By fitting the gain band at 530 nm, the relaxation time of singlets is found to be 300 fs. While the gain band disappears, new absorption bands appear at 420 and 570 nm. These new bands are the cation and anion radical absorption bands, respectively. They relax in 3.8ps. Until now, the behaviour of **B7-fa** in water and **B7** in THF is very similar. However, no triplet formation was observed. A discussion will be presented in the conclusion part. In scheme 2, the PET and BET processes for **B7-fa** in water are summarized.



**Scheme 2:** The model for PET for **B7-fa** in water.

#### 4.3.4.1.d. B7-fa with Ca in water

$\text{Ca}(\text{ClO}_4)_2$  is added in solution to obtain a complex. In Fig.4.57, the transient absorption spectrum of molecule **B7-fa**. $\text{Ca}^{2+}$  complex is shown. There are positive bands at 330 and 420 nm like the protonated case in THF. Gain and ground state bleaching bands are hardly seen due to the scattering of pump beam. Positive bands, excited singlet absorption bands, have a decay time of 500 ps. Again here complexation blocks the PET.

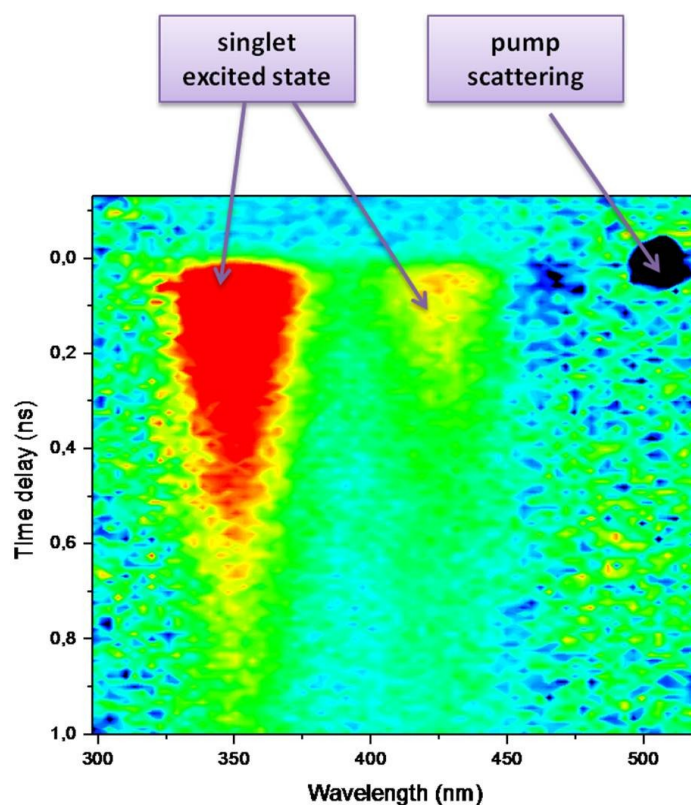


**Fig.4.57:** The transient absorption spectra of **B7-fa**. $\text{Ca}^{2+}$  in water ( $\lambda_{exc} = 500\text{nm}$ ).

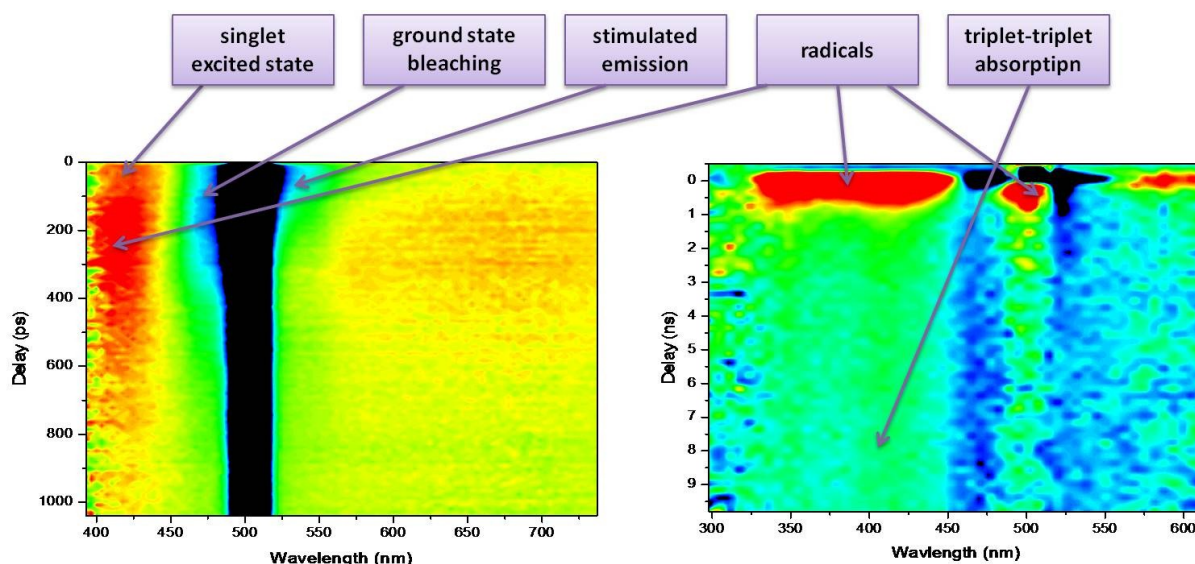
#### 4.3.4.2. a. Molecule B8 in THF

Fig.4.58 presents the transient absorption spectra for **B8** in two different delay ranges: 1 ns on the left and 10 ns on the right. Transient signals show similarities with **B7**. A positive signal at 425 nm with biexponential decay kinetics is observed. The first component decays in 30 ps and the second one decays in 350 ps. After the fast component relaxes, other positive bands at 340 nm and a wide band at between 550 and 800 nm start to form. These bands have a relaxation time of 350 ps which is the same with the second component of 425 nm band. We start to observe this broad band in the 10 ns window too. Negative band at 470 nm, also has the same kinetics with same time constants.

As a conclusion of these results, excited singlet state absorption band at 425 nm has a lifetime of 30 ps, which is seen also in ground state bleaching signal at 470 nm and in stimulated

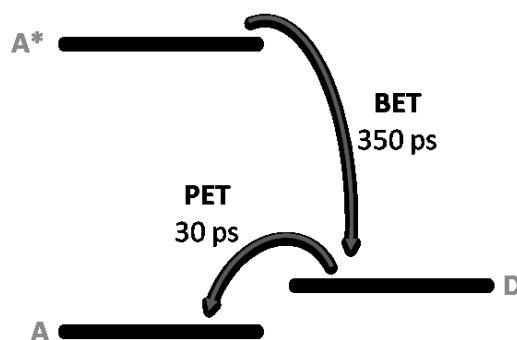
emission band at 520 nm. The positive band at between 550 and 800 nm can be attributed to the anion radical of BODIPY and the band at 340 nm can be attributed to the BAPTA cation radical, as we expected an electron transfer from BAPTA part to BODIPY part. These bands decay in 350 ps. After all the other bands relax, a band still remains at 425 nm. This band can be the triplet-triplet absorption band of BODIPY.

Different from molecule **B7**, molecule **B8** has a phenyl group between BAPTA and BODIPY parts. This makes the BODIPY part more flexible and easily turn around. This can be the reason why the signals are slightly different from molecule **B7**. As mentioned in first chapter, electron transfer rate is given  $k_{ET} \sim e^{-\beta r} e^{-\frac{(\Delta G + \lambda)^2}{4\lambda RT}}$ , which means the distance between electron donor and acceptor parts has an effective role on electron transfer. This distance difference also causes the changes in signals of **B7** and **B8**.



**Fig.4.58:** The transient absorption spectra of **B8** in THF at 0-1ns (left) and at 0-10ns (right) ( $\lambda_{exc} = 500nm$ ).

Scheme 3 explains the PET and BET briefly. We have observed the triplet state formation for this molecule too. However it is much weaker compare to molecule **B7**.



**Scheme 3:** The model for PET for **B8** in THF

#### 4.3.4.2.b. Protonated Molecule B8 in THF

We studied the situation of complex by adding  $\text{HClO}_4$  in solution for the reason explained before. In Fig.4.59, the transient absorption spectrum of **B8.H** is given. There are positive bands at 330nm and 420 nm similarly in **B7**. At 470nm there is ground state bleaching band and at 510nm there is the gain band. All bands have a lifetime of 2.5 ns.

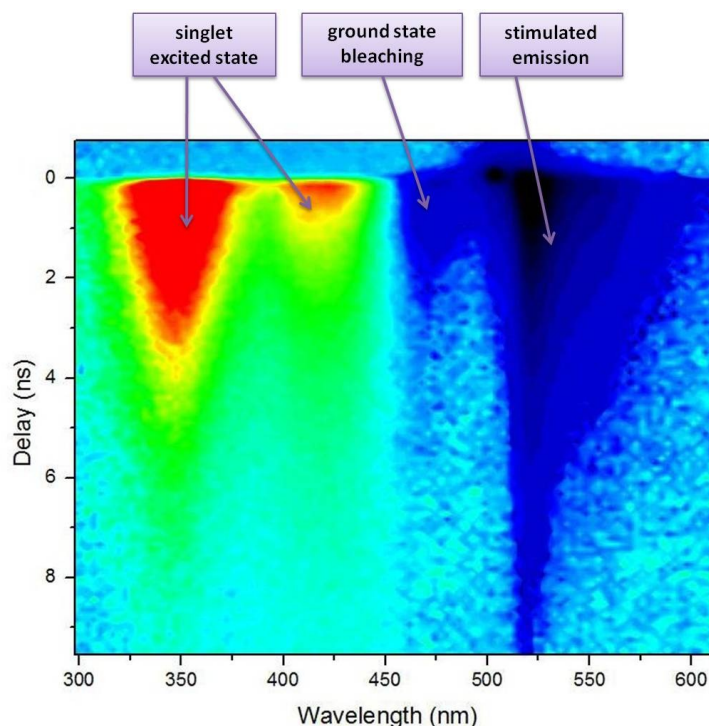


**Fig.4.59:** The transient absorption spectra of molecule **B8.H** in THF ( $\lambda_{exc} = 500\text{nm}$ ).

#### 4.3.4.2.c. Molecule B8-fa in water

The transient absorption spectrum of molecule **B8-fa** in water is shown in Fig.4.60. Excited singlet absorption band at 425 nm relaxes in 1.2 ps. On ground state bleaching signal and stimulated emission signal we observed the same relaxation with the same time constant. After this fast relaxation, there is a band which still remains at 425 nm and a new band appears between 600-800 nm. These bands decay in 21 ps and are attributed to anion radical absorption bands of BODIPY. There are no triplet states observed for this molecule.

The model for relaxation pathway is given on the right of the spectrum.

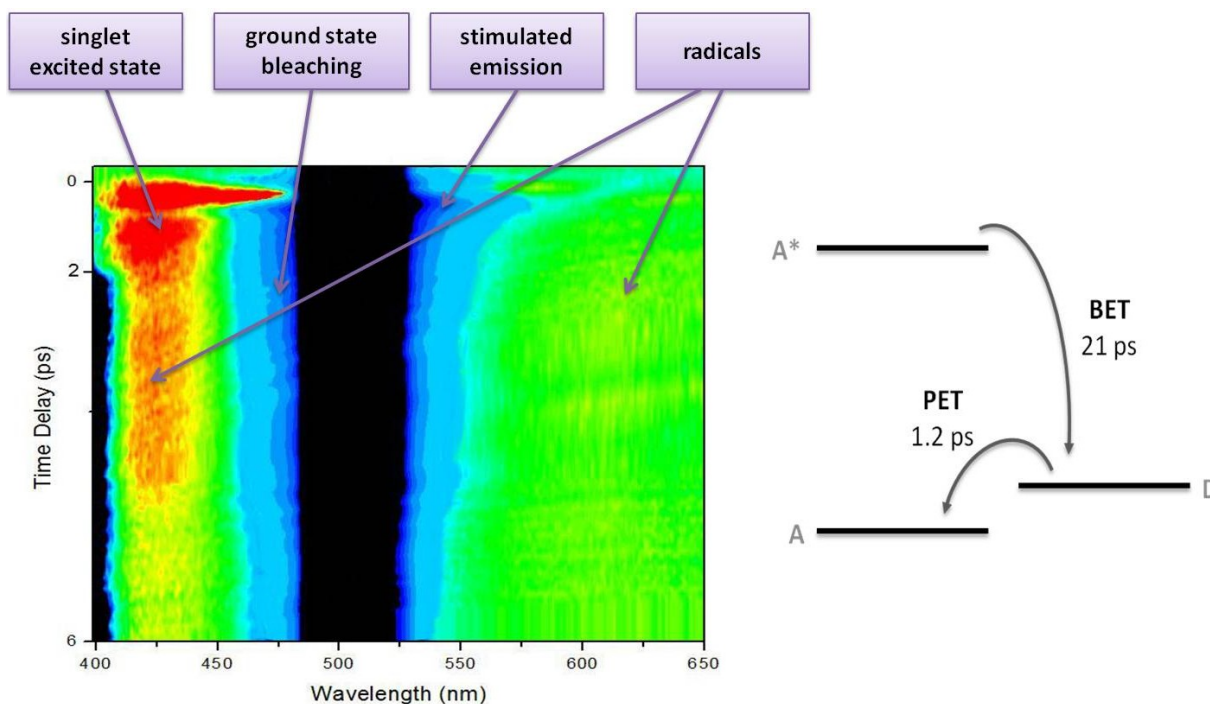


**Fig.4.60:** The transient absorption spectra of **B8-fa** in water (left), the model for relaxation (right), ( $\lambda_{exc} = 500\text{nm}$ ).

#### 4.3.4.2.d. Molecule **B8-fa** with $\text{Ca}^{2+}$ in water

$\text{Ca}(\text{ClO}_4)_2$  is added in solution for getting a complex of **B8-fa**. $\text{Ca}^{2+}$  Fig.4.61 shows the transient absorption spectrum of molecule 2. $\text{Ca}^{2+}$  complex. There are positive bands at 330 and 420 nm like the protonated case **B8.H** in THF. The gain band at 500 nm and ground state bleaching band at 460 nm are perturbed by the scattering of pump beam. Positive bands, excited singlet absorption bands, have a decay time of 760 ps. Complexation with  $\text{Ca}^{2+}$  blocks the PET.

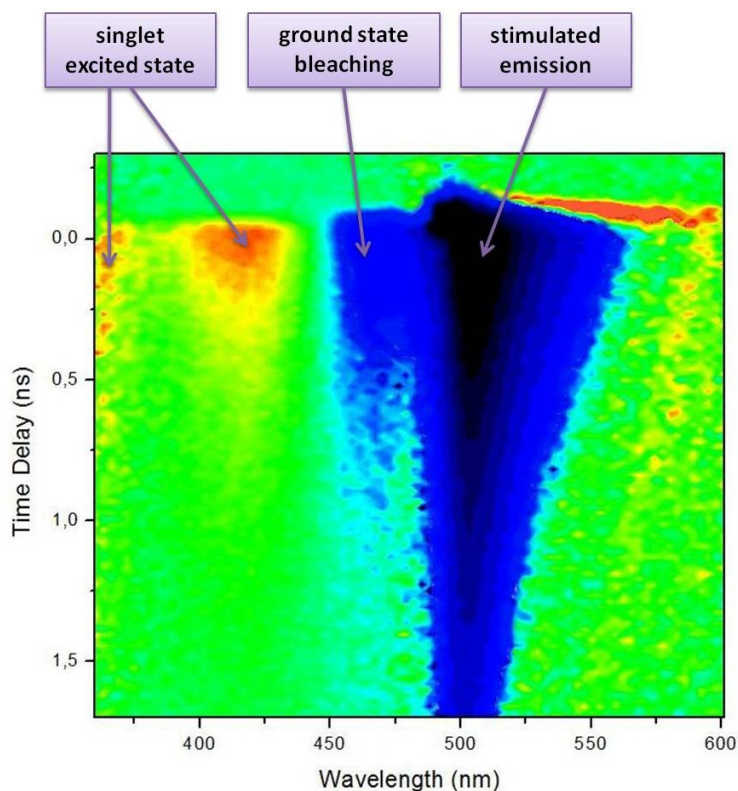


**Fig.4.61:** The transient absorption spectra of molecule **B8**.Ca<sup>2+</sup> in water ( $\lambda_{exc} = 500\text{nm}$ ).

#### 4.3.5. Discussion

BAPTA has a well adapted cavity for recognition of calcium. However its usage with living organism could be hazardous due to its optical responses in the UV, the light wavelengths harmful for life. By using a signalling unit which absorbs in the visible has solved this problem. In this system BODIPY is used as a signalling unit which absorbs visible light and it can be modified for different wavelength by adding substituent. By optically active transition of BODIPY via excitation, causes photoinduced electron transfer (PET) which quenches fluorescence. We have observed PET for compound **B7** in 30 ps in THF and in 300 fs in water as well as for compound **B8** 30 ps in THF and 1.2 ps in water. When BAPTA binds Ca<sup>2+</sup>, due to the changes of its oxidation potential, PET does not occur, which allow to switch the fluorescence ON.

Until now, we neglected to explain one phenomenon we have observed in compounds **B7** and **B8** in THF. As it could be seen in Fig.4.53 and 4.58 on nanosecond time scale, the transient spectra contain a long living feature appearing after the radical relaxes. We expected that the radical relaxation should be a last process in excited state relaxation which entirely recovers the ground state. Yet, it appears that the radical relaxation apparently is related with triplet formation. Surprisingly, this process takes place only in THF and not in water.

Any excited state relaxation process involves dissipation of energy from electronically excited molecular system to environment. This energy may appear as light, as heat, as electrical energy or in some chemical form. The heat-generating relaxation process is usually related to the driving force which is caused as a result of the difference of energy between excited state and ground state. In our experiments after radical bands relaxation by BET causes a large amount of heat-generation because of the big driving force ( $>2$  eV). Normally this energy is dissipated by vibrational coupling between ground state vibrational modes of molecule and solvent environment. Finally, excess vibrational energy flows away from relaxed molecule. In some cases, when this energy flow rate is slower enough due to weak solvent-solute vibrational coupling and the electronic reconfiguration allows that, an upper-state crossing can be observed. Triplet population in THF in our experiments is likely due to this upper-state transition by vibrational coupling.  $S_0 \rightarrow T_1$  transition thus can be observed when a large quantity of vibrational energy is released after back electron transfer. The water case is more complicated since the BET in water is faster than in THF. Yet, supposing a strong vibrational coupling via hydrogen bonding, water probably dissipates the excess vibrational energy much faster than THF and thermal triplet state population becomes less probable.

## Chapter 5

### Photochemionics

#### *Introduction*

In this chapter, an artificial molecular communication system is considered (see Fig.5.1), which is largely inspired by nature. In living organisms, ion fluxes play the principle role in communication inside and between cells. Compatible ion-ejection and detection systems are required to achieve this communication, for example in an ion shuttle where processes of complexation, photo-decomplexation, ion migration and fluorescence signalling of ions are required. Ultrafast spectroscopy is employed to characterize many of the fast processes concerning electron transfer, fluorescence and isomerisation. This approach potentially has wide application fields such as artificial molecular devices and networks, small computing elements, nanoscopic logic elements for medical diagnosis, sensing devices where an analyte can trigger an optical response and adaptive materials. Combination of the two complementary processes is represented in Fig.5.1, where the photoejection of an ion, “light-in, ion-out”, and ion-induced fluorescence, “ion-in, light-out”, is harnessed to establish connection between distinct functional molecules. In the figure ion is represented as black sphere and orange and green semi-circles are the binding sites of molecular systems. In this chapter, molecular systems which can be used as “light-in, ion-out” part of communication will be described.

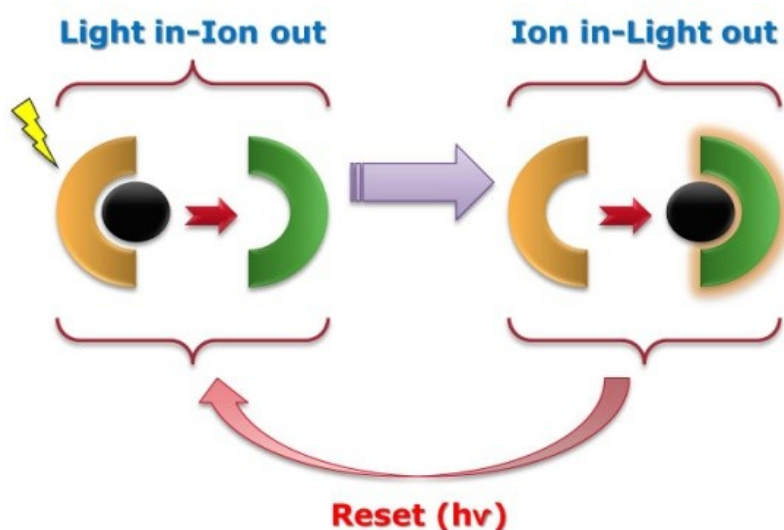


**Fig.5.1:** Principles of communication between molecules.

## PART I

### *BAPTA-Anthracene systems*

#### 5.1.1. Introduction

As detailed in the previous chapter, BAPTA (1,2-bis(2-aminophenoxy)ethane-N,N,N',N'-tetraacetic acid)<sup>30</sup> has a well adapted cavity for  $\text{Ca}^{2+}$ , with a binding constant of  $K_d \sim 100\text{nM}$ .  $\text{Ca}^{2+}$  is an important second messenger in living organisms and is involved in many biological processes. Since changes on its intra- and extracellular concentrations are responsible for cellular activity<sup>163</sup>, controlling its concentration is an important task.

In current BAPTA-Anthracene systems, BAPTA is used as an ionophore for recognition of  $\text{Ca}^{2+}$  with anthracene being a polyvalent photoactive subunit. The studied compounds also contain two covalently attached to BAPTA anthracene molecules; each anthracene being attached to different BAPTA aniline units.

Anthracene molecules are known to dimerize on UV light radiation. Two anthracenes can form an intramolecular excimer in the excited state followed by photodimerization. A new restricted receptor geometry of compound would not be optimal for  $\text{Ca}^{2+}$  coordination and the cation could be photo-released definitively (see Fig.5.2). In this manner, the  $\text{Ca}^{2+}$  release in principle could be controlled by light.

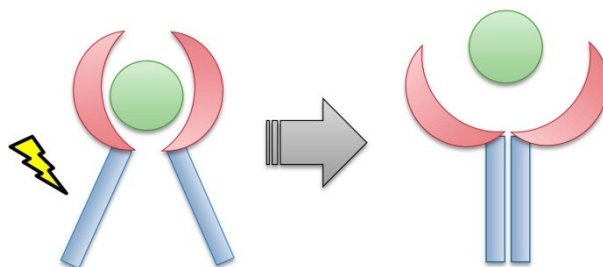


**Fig.5.2:** *The working principle of BAPTA-Anthracene system (green sphere: ion, red parts: BAPTA and blue parts: anthracenes).*

In this research, the behaviour of a series of BAPTA-Anthracene molecules and notably the fast processes therein were studied in different media.

#### 5.1.2. Photochemistry of Anthracene

Anthracene and its derivatives are widely used in many systems (dendrimers, rotaxanes, etc.) due to their photochemical and photophysical properties. In Fig.5.3, the Jablonski-Perrin diagram for an anthracene molecule is given. An absorption band in the range of 350-390 nm

exhibiting vibronic fine structure bands with an extinction coefficient of  $9000 \text{ M}^{-1}\text{cm}^{-1}$  has been attributed to a  $S_1 \leftarrow S_0$  transition<sup>10</sup>. The band associated with the  $S_2 \leftarrow S_0$  transition has a high extinction coefficient (about  $200000 \text{ M}^{-1}\text{cm}^{-1}$ ) but this band is typically not used for photochemical experiments because the absorption of photoproducts are located also in the same UV region and can lead to unwanted secondary processes<sup>10</sup>.

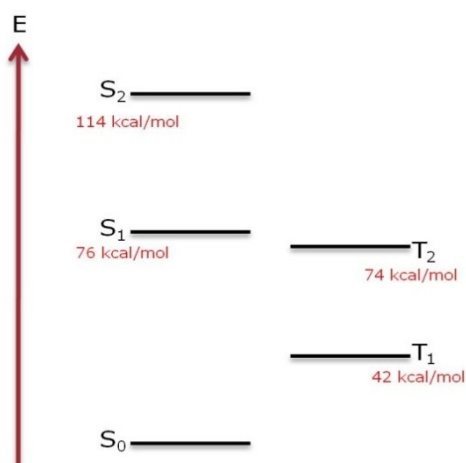


**Fig.5.3:** Jablonski-Perrin diagram for an anthracene molecule.

The intersystem crossing efficiency is very high, with a quantum yield of  $S_1 \rightarrow T_2$  is 0.7<sup>10</sup>. Triplet state of anthracene can sensitize the formation of singlet oxygen, which can react with the anthracene leading to formation of endoperoxide which then decomposes partly to anthraquinone<sup>164</sup> (Fig.5.4).

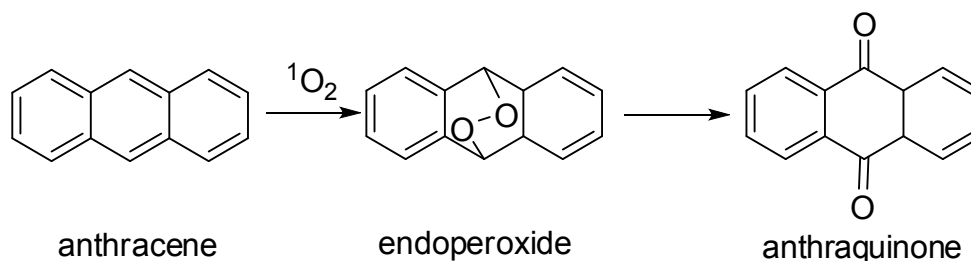


**Fig.5.4:** The photo-oxidation reaction of anthracene

In concentrated solutions of anthracene and its derivatives, one anthracene in its excited state can approach another anthracene in ground state to form an excimer. Excimer fluorescence is observed around 530 nm and does not show a structured band<sup>165</sup>.

Anthracene is also known to form photodimers<sup>9</sup>. Different substitutions and different orientation leads different dimers. Two types of dimer can be formed; head-to-tail and head-to-head, as represented in Fig.5.5.

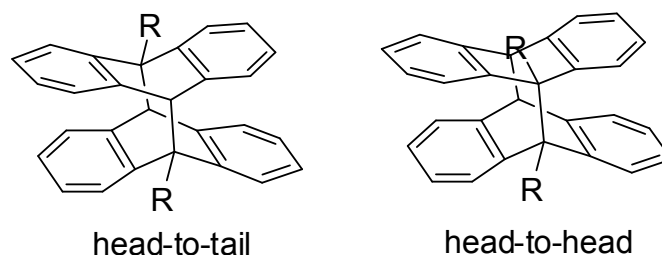


**Fig.5.5:** The types of anthracene dimers

Photodimers can return to monomeric anthracene by irradiation (generally at 254 nm) or by heating. The thermal return can take from seconds to years depending on their substitutions<sup>9</sup>.

### Transient Absorption of Anthracene

Anthracene is a well known molecule and its behaviour in the excited state has been extensively studied<sup>166-169</sup>. Transient absorption experiments on 9-Methoxyanthracene were performed in MeOH in order to compare all later results on the same experimental set-ups.

Fig.5.6 shows the transient absorption spectrum of 9-Methoxyanthracene in MeOH. A positive band at 580 nm is attributed to the absorption band of the excited singlet state<sup>169</sup> which has a decay time of 4 ns. The rest of the spectrum is more complicated due to the superposition of many processes. Around 400 nm we start to observe the structured ground state bleaching signal which is superposed with structured bands of stimulated emission. Additionally, 9-Methoxyanthracene triplet-triplet absorption bands are also located at 400 nm and 420 nm<sup>170</sup>. The decay time of stimulated emission at 460 nm is 4 ns. To summarize: excited singlet absorption is located between 520-650 nm and at 380 nm, triplet-triplet absorption bands are at 400 nm and at 420 nm.

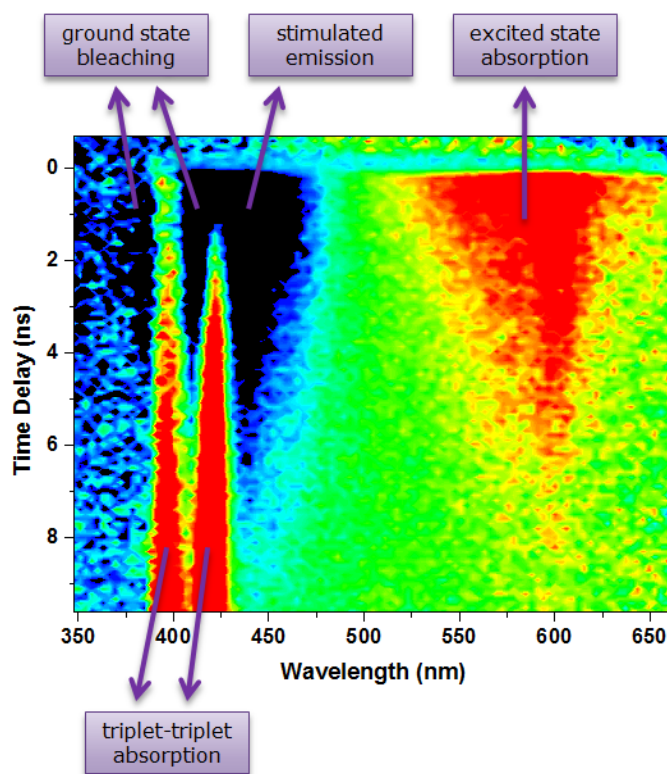


**Fig.5.6:** Transient absorption of 9-Methoxyanthracene in MeOH ( $\lambda_{exc}=355\text{nm}$ ).

### 5.1.3. First Generation (G1)

**G1** molecules are the structurally simplest case, which connect together the molecular subunits (see Fig.5.7). It consists of BAPTA which is connected with an anthracene unit on each aromatic ring via a methylene spacer. A related molecule with one anthracene was reported in the literature<sup>171</sup>.

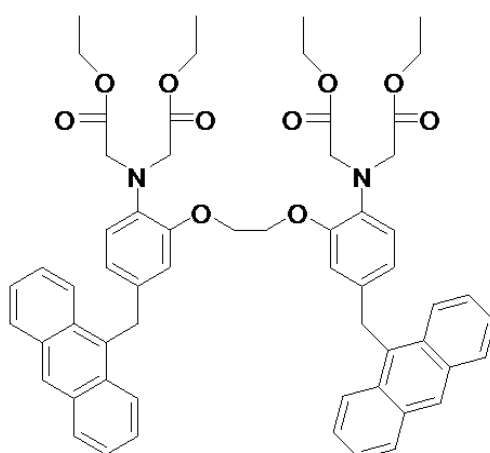


**Fig.5.7:** The structures of 1<sup>st</sup> (G1) generation of BAPTA-Anthracene systems.

### 5.1.3.a. Steady-State Measurements

The electronic absorption and fluorescence spectra of **G1** are shown in Fig.5.8. Absorption spectrum shows the usual structured spectrum of anthracene with maxima at 390, 370, 352, 335 nm. The band at 293 nm is attributed to the absorption of the aniline of BAPTA. The fluorescence spectrum also shows structured emission which belongs to the monomer. It has maxima at 396, 416 and 441 nm. The broad band at 525nm can be due to the excimer emission. Quantum yield of fluorescence is calculated 0.038 (anthracene in EtOH is used as reference). 44% is due to monomer emission and 56% is due to excimer emission.

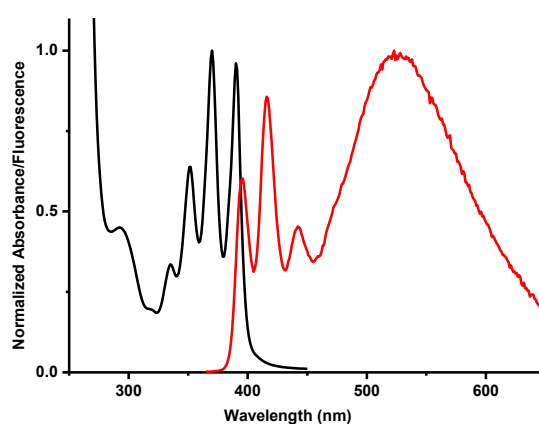


**Fig.5.8:** Normalized absorption spectrum (black), Fluorescence spectrum (red) ( $\lambda_{exc} = 352\text{nm}$ ) in DCM.

### 5.1.3.b. Transient Absorption

#### **G1 in MeOH/DCM**

In Fig.5.9, on the left spectrum, a broad positive band at between 550 nm and 650 nm is observed (Fig.5.10, spectrum at 0 ps), which shows biexponential decay. The first component decays in 12 ps and second component relaxes on a longer time scale. Comparing the transient absorption result of single anthracene, the fast component is attributed to excited singlet absorption. The second component and the band between 650 nm and 700 nm have same decay time (Fig.5.10, spectrum at 0.5 ns). These bands can be thought of as the anion radical absorption band of anthracene, having been monoreduced by a photoinduced electron transfer process involving BAPTA (aniline) donor. In literature, it is reported that anion radical of anthracene shows a band at 330 nm and a second band over 550 nm which has less intense absorption compare to 330 nm band<sup>169</sup>. In the 10 ns window (Fig.5.9, on the right), we can hardly see the anion radical absorption band at over 550 nm, because of the low temporal resolution (Fig.5.10, spectrum at 1 ns). On the other hand we are able to see the anion radical

absorption band at 330 nm. The cation radical of aniline possesses an absorption band at around 480 nm<sup>172</sup>. These bands decay in 3.5 ns. Triplet-triplet absorption band of anthracene at 430 nm forms after the radical absorption bands relaxes (Fig.5.10 spectrum in 10 ns).

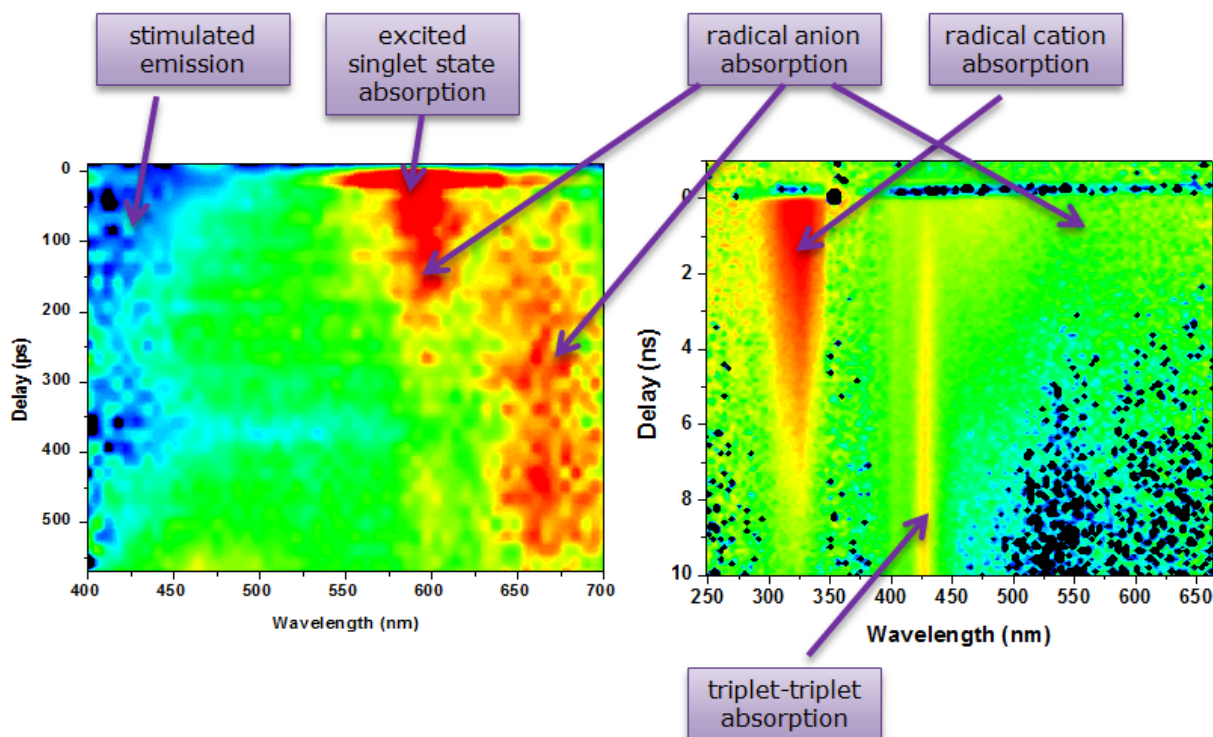


**Fig.5.9:** The transient absorption of **G1** in MeOH/DCM up to 600 ps delay (left), up to 10 ns delay (right) ( $\lambda_{exc}=355$  nm).

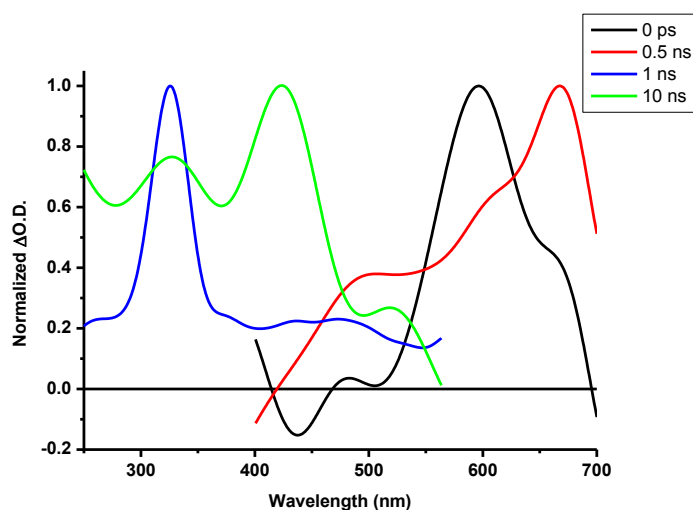


**Fig.5.10:** Normalized transient absorption spectra at different delays.

Kotani *et al.* reported the transient signal of excimer of molten state anthracene at 400 nm and 950 nm<sup>173</sup>. However no excimer formation was observed on the transient absorption spectrum at 400 nm. The band at 950 nm is out of our measuring range. Surprisingly we have seen an

emission band at 530nm in time-resolved fluorescence experiments with a fluorescence life time of 3.5 ns, which is attributed to excimer emission. If we compare the intensity of emission of monomer at 420 nm the intensity of this band at 530 nm is 20%.

It could be probable that a small fraction of **G1** molecules could form excimers. Having in mind that the fluorescence lifetime of the free anthracene is in the range 2.5-4 ns, the **G1** singlet lifetime is 12 ps (at least 200 times less) and the intensity part of excimer fluorescence is 56% (from steady state experiments), we can conclude that if the excimers are formed in the studied solutions of **G1**, its concentration should be at least 1/400 of that of **G1** molecules. Nevertheless, even such low concentration of excimers can produce distinguishable fluorescence signal on the background of quenched singlet anthracene emission. Yet, the detection of transient absorption signal of these intermolecular excimers at these concentrations is unrealistic.

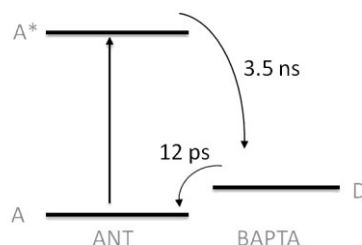


**Fig.5.11:** *The model for relaxation pathway of G1.*

Fig.5.11 summarizes the relaxation pathway for **G1** molecules. As a conclusion, excimer formation and electron transfer in **G1** molecules are in competition. The redox potential of donor (BAPTA aniline) and anthracene units is more suitable for electron transfer. For **G1** molecules, PET is the dominant phenomenon and it takes place in 12 ps. Even so, excimer emission was observed. This means PET is dominant procedure, nevertheless excimer forms even it is with low probability.

### **1G.H in MeOH/DCM**

In case of complexation with  $\text{Ca}^{2+}$ , the redox potential of BAPTA increases, which makes its HOMO level lower than HOMO level of anthracene. In the complexation situation it is expected the blocking of PET. In our time-resolved measurements, we used the esterified form of **G1** in MeOH/DCM. The amino group of BAPTA was protonated in order to get similar effect as  $\text{Ca}^{2+}$  binding.

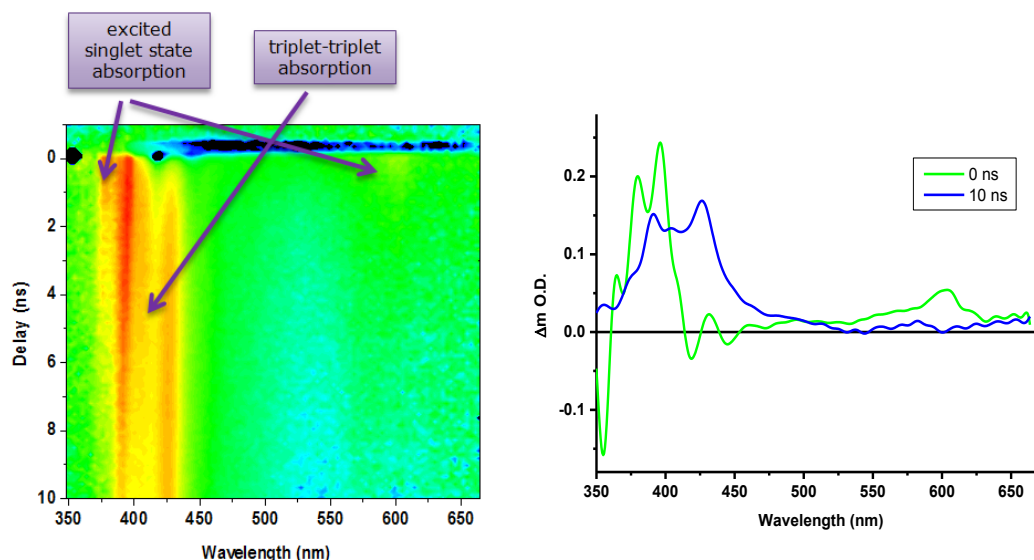


**Fig.5.12:** The transient absorption of **G1.H** in MeOH/DCM up to 10ns delay ( $\lambda_{exc}=355$  nm).

Fig.5.12 presents transient absorption spectrum of **G1.H** in MeOH/DCM. The positive bands at 380 nm and 550-650 nm (spectrum at 0 ns delay) are the excited singlet state absorption bands. They have a decay time of 2.5 ns which is the same with fluorescence lifetime. Triplet-triplet absorption band at 380 nm shows rising kinetics in 2.5 ns. The ground state bleaching, stimulated emission and triplet-triplet absorption bands are located at between 400 and 450 nm. The superposition of all these bands do not allow make an appropriate fit on the kinetics which results in an incompatibility of the time constants. It is summarized in Fig.5.13 the relaxation behaviour of **G1.H**.

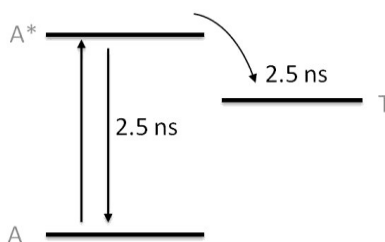


**Fig.5.13:** The model for relaxation pathway of **G1.H**.

### **G1 Hydrolyzed**

Hydrolyzed molecules were prepared in order to study their behaviour in case of complexation with  $\text{Ca}^{2+}$ . In Fig.5.14, the absorption and fluorescence spectra for **G1** molecule are presented with different pH conditions. Fluorescence spectra are corrected. At low pH, the amino group of BAPTA is protonated completely, which blocks the electron transfer. We observe the increase in fluorescence emission compared to pH=7. In the presence of  $\text{Ca}^{2+}$ , an increase in fluorescence emission intensity was also observed; however this increase is not as

pronounced as in the protonated case. It can be concluded that complexation with  $\text{Ca}^{2+}$  is only partially blocking PET.

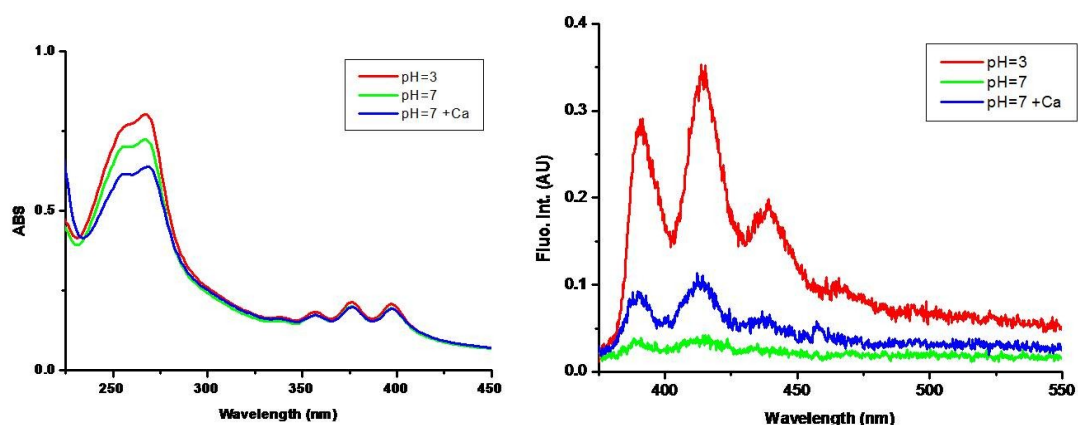


**Fig.5.14:** The absorption (left) and fluorescence (right) spectra of hydrolyzed **G1** molecule in water at different pH values.

#### 5.1.4. Second Generation (G2)

In **G2** molecules, the BAPTA was equally substituted in the *para* position, this time the fluorophores were linked via an amide spacer. It has the advantage of having a longer spacer, which should allow anthracene fluorophores to approach one another more easily to interact. The anthracene units were also modified by introducing oxygen at position 9 which renders the anthracene units more electron rich and hence they become less good acceptors (Fig.5.15). After these new modifications, a possible electron transfer between the donor and acceptor BAPTA and anthracene units may be anticipated to become less feasible, ideally favouring a photodimerization reaction which would ultimately lead to  $\text{Ca}^{2+}$  ejection.

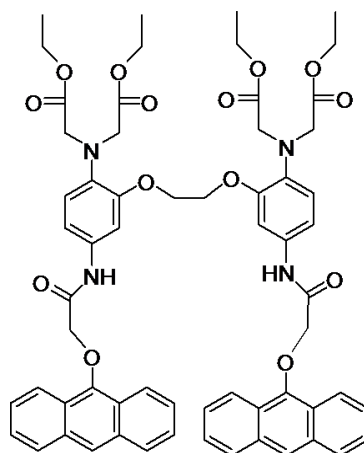


**Fig.5.15:** The structure of 2<sup>nd</sup> generation of BAPTA-Anthracene systems (**G2**).

### 5.1.4.a. Steady-State Measurements

The longer spacer of **G2** molecules makes the molecule more flexible, which should further influence efficiency in dimer formation. Since the energy difference between anti-syn conformers is only few  $\text{kJ}\cdot\text{mol}^{-1}$ , two different dimer orientations, head-head (hh) and head-tail (ht), are possible for **G2** molecules (Fig.5.16).

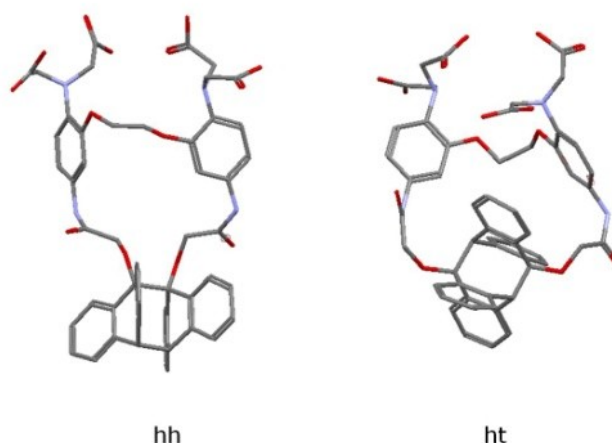


**Fig.5.16:** The dimer models of for **G2**.

The absorption and emission spectra of **G2** in DCM are shown in Fig.5.17. Dilute samples were prepared in order not to have intermolecular interaction ( $c < 5\cdot 10^{-4}$  M). They are also degassed to prevent to 9,10-anthraquinone formation by oxidation of anthracene.

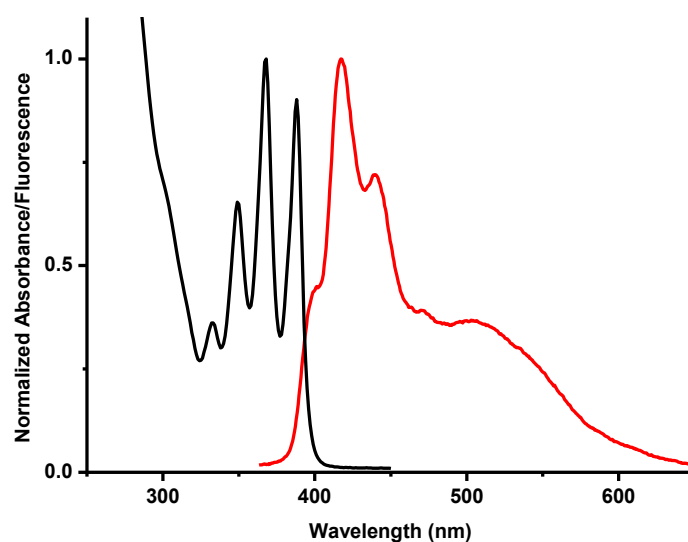


**Fig.5.17:** Normalized absorption spectrum (black) and fluorescence spectrum (red) ( $\lambda_{exc} = 357\text{nm}$ ) of **G2** in DCM.

Similar to **G1**, the spectra of **G2** molecules also show structured bands of anthracene with maxima at 334, 350, 369, 380 nm. The absorption band of aniline of BAPTA part is a

shoulder on the band corresponding to the  $S_2 \leftarrow S_0$  transition at shorter wavelengths. The fluorescence spectrum shows a lower energy structured band of monomer emission of anthracene with maxima at 393, 416, 440 nm. The band at 506 nm is attributed to either an excimer emission band or an exiplex, both of which respect the same kinetic scheme. The fluorescence quantum yield is 0.026. 58% is due to monomer and 42% is due to excimer.

### 5.1.4.b. Dimerization

Dimerization studies were performed on irradiating the degassed **G2** in DCM ( $c$  is less than  $3 \cdot 10^{-6}$  M) at 366 nm. Changes in the absorption spectrum are shown in Fig.5.18. The monomer bands of anthracene at 250, 258, 330 and 450 nm show a decrease in absorption in time, in addition to this the band at 270 nm starts to grow up which is due to dimers. The dimerization is complete in 90 min.

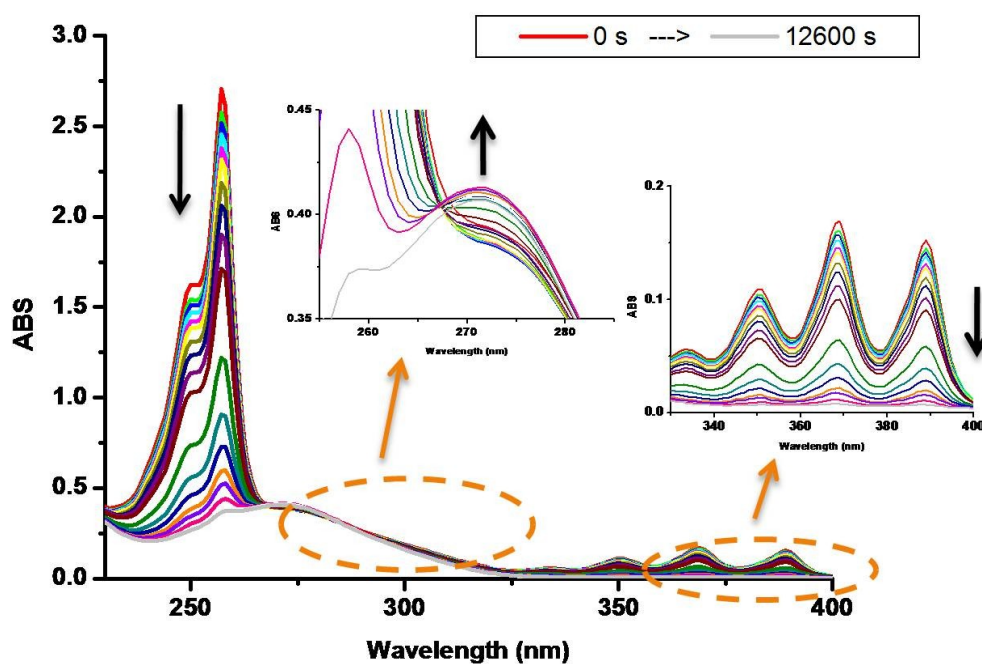


**Fig.5.18:** Changes in absorption of irradiating at 366 nm in DCM.

### 5.1.4.c. Transient Absorption

#### **2G in DCM**

The transient absorption spectrum is presented in Fig.5.19. The bands, located at 370 nm and between 500-600 nm, are attributed to singlet excited state absorption bands of anthracene, which decay in 2.3 ns. In transient absorption measurements with fs pulses, this band shows a

fast decay in 6 ps. After the decay of these bands a band at between 500-550 nm is observed which shows no relaxation in 50 ns. The triplet-triplet absorption bands are observed at 400 nm and 425 nm, which form in 5.4 ns. From time resolved fluorescence experiments, we have seen the fluorescence emission due to monomer at 420 nm has biexponential decay, the first component is faster than 20 ps and second component is 5.4 ns. The excimer emission at 530 nm shows biexponential decay, one fast (<20 ps) and another 12 ns.

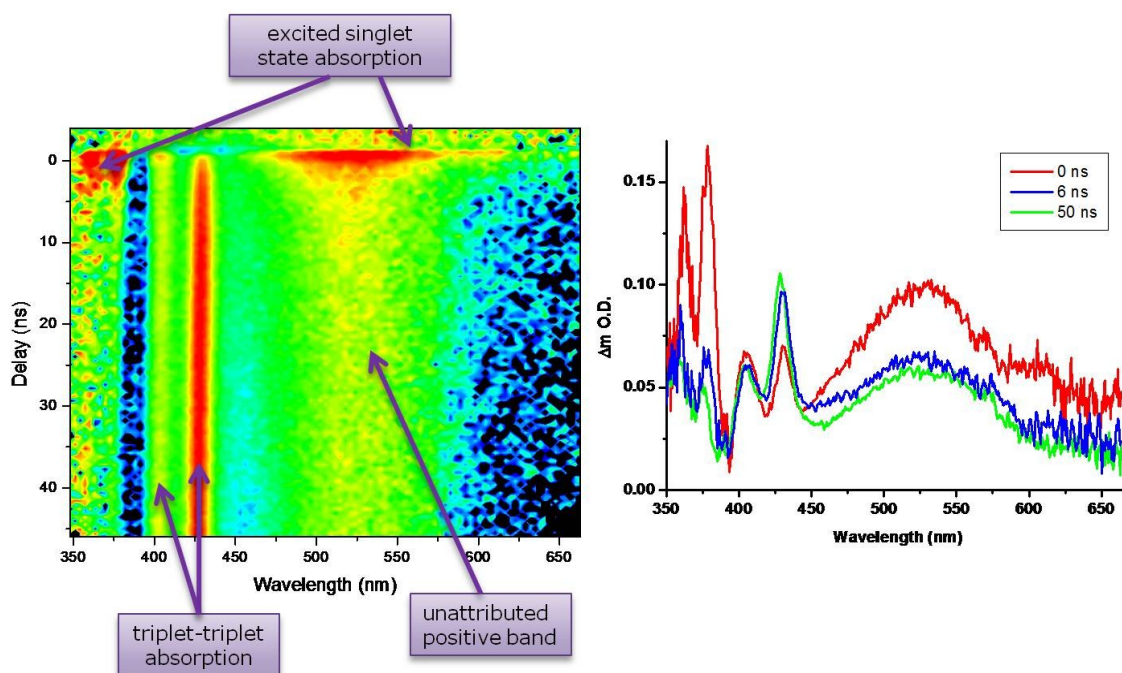


**Fig.5.19:** Transient absorption spectrum ( $\lambda_{exc} = 357\text{nm}$ ) of **G2** with esters in DCM.

All results are summarized on Fig.5.20. There are different photochemical and photophysical phenomena which are not directly connected to each other. Considering time resolved fluorescence and transient absorption results, it can be said that excited anthracene can relax by following different pathways. 30% of excited anthracene molecules undergo an ISC and populates the triplet states in 5.4 ns. The formation of triplet states observed in transient absorption spectrum and fluorescence lifetime of monomer emission are proved this situation. 70% of excited anthracene molecules forms excimer/exciple with a non-excited anthracene in 6 ps, which relaxes in 12 ns. The transient absorption signal of excimers is over 900 nm which is out of our measuring rate, however an emission which may be due to excimers is observed. The long living band at 500-550 nm, stays after relaxation of singlets. While information in the literature about the excited photodimer is scarce, it is unlikely to be located in this spectral region. The exciple absorption band may be anticipated in the NIR region<sup>174</sup>.

## 2G.H in DCM

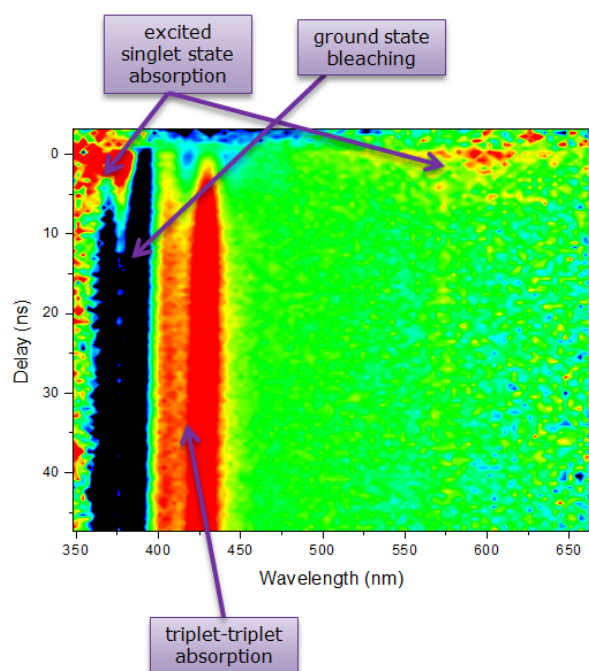


**Fig.5.20:** Transient absorption spectrum ( $\lambda_{exc} = 357\text{nm}$ ) of **G2.H** in DCM.

It is shown on Fig.5.20 transient absorption spectrum of protonated **G2** molecules. The excited singlet bands at 375 and 550-650 nm bands have a decay time of 5.4 ns and triplet rise time is also 5.4 ns. Fluorescence lifetime of the monomer at 425 nm is 5.4 ns and the emission at 510 nm has a biexponential relaxation, 5.4 ns and 22 ns which is due to excimer formation shown in Fig.5.21. Comparing the intensity of monomer and excimer, it can be said excimer formation is estimated at just 1%. However no other absorption band similar in to that observed at 550 nm in the previous spectrum is observed.

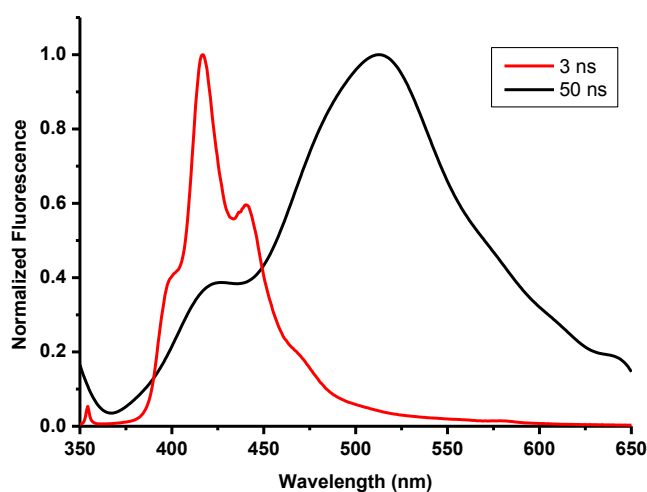


**Fig.5.21:** Fluorescence emission spectral shapes of 2G.H taken after different time delays.

#### 5.1.4. Third Generation (G3)

Third generation photoejectors (**G3**) have a similar structure (Fig.5.22) to **G2**. However they have longer spacer with 3 carbons, which should allow anthracene units of molecules to interact with each other more easily, compared to **G2**.

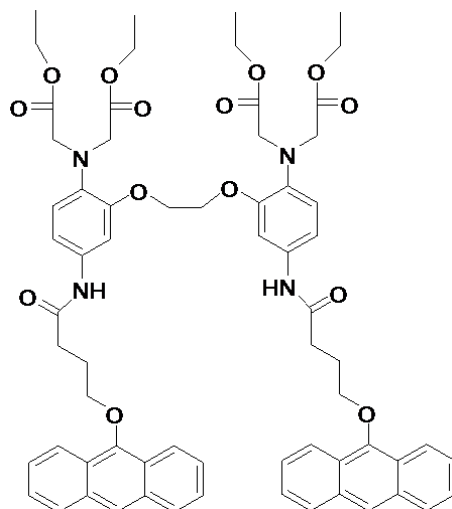


**Fig.5.22:** The structure of 3<sup>rd</sup> generation of BAPTA-Anthracene systems (**G3**).

#### 5.1.4.a. Steady-State Measurements

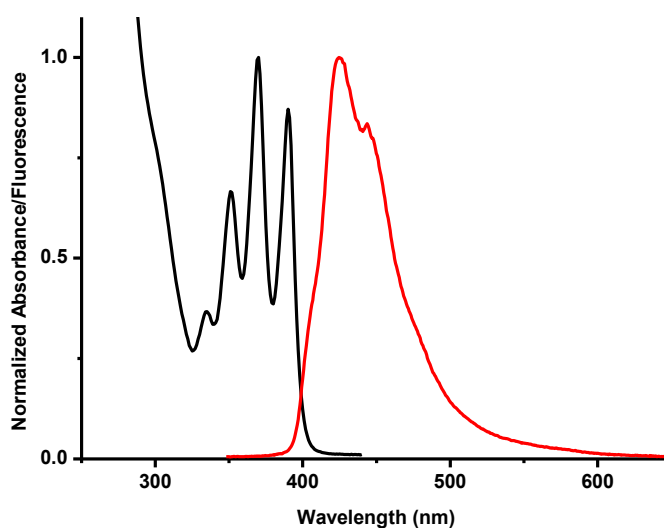


**Fig.5.23:** Normalized absorption spectrum (black) and fluorescence spectrum (red) ( $\lambda_{exc} = 357\text{nm}$ ) of molecules **G3** in DCM.

The absorption spectrum (Fig.5.23) shows the classical structured band of anthracene with maxima at 390, 370, 352 and 336 nm, which corresponds  $S_1 \leftarrow S_0$  transition. Aniline-like absorption bands appear as a shoulder on the band associated with the  $S_2 \leftarrow S_0$  transition. The emission spectrum (Fig.5.23) also shows structured spectra with the bands at 399, 420 and

440 nm. No red shifted bands due to excimers are observed. The quantum yield of fluorescence is estimated to be 0.039.

### 5.1.4.b. Dimerization

The changes on the absorption spectrum of degassed **G3** in DCM ( $c < 5 \cdot 10^{-6} \text{M}$ ), by radiation at 366 nm as a function of time, are shown in Fig.5.24. The monomer bands of anthracene between 250 and 258 nm and between 330 and 450 nm show a decrease in absorption in time, in addition to this the band at 272 nm starts to grow up. The dimerization process is faster compared to **G2** and is completed in 30 min. The thermal return is also faster.

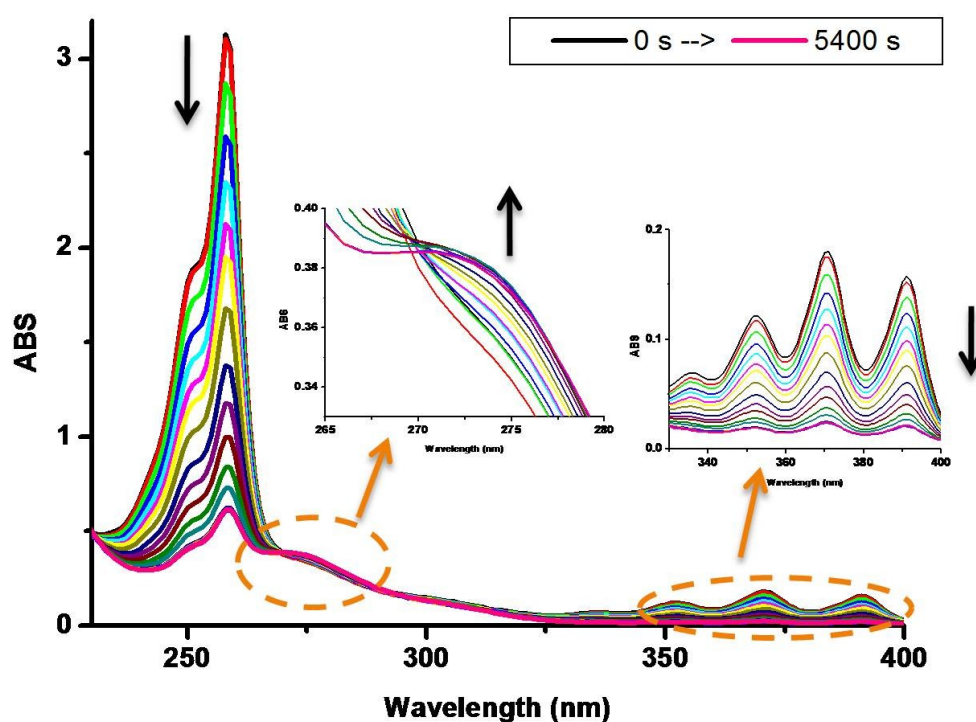
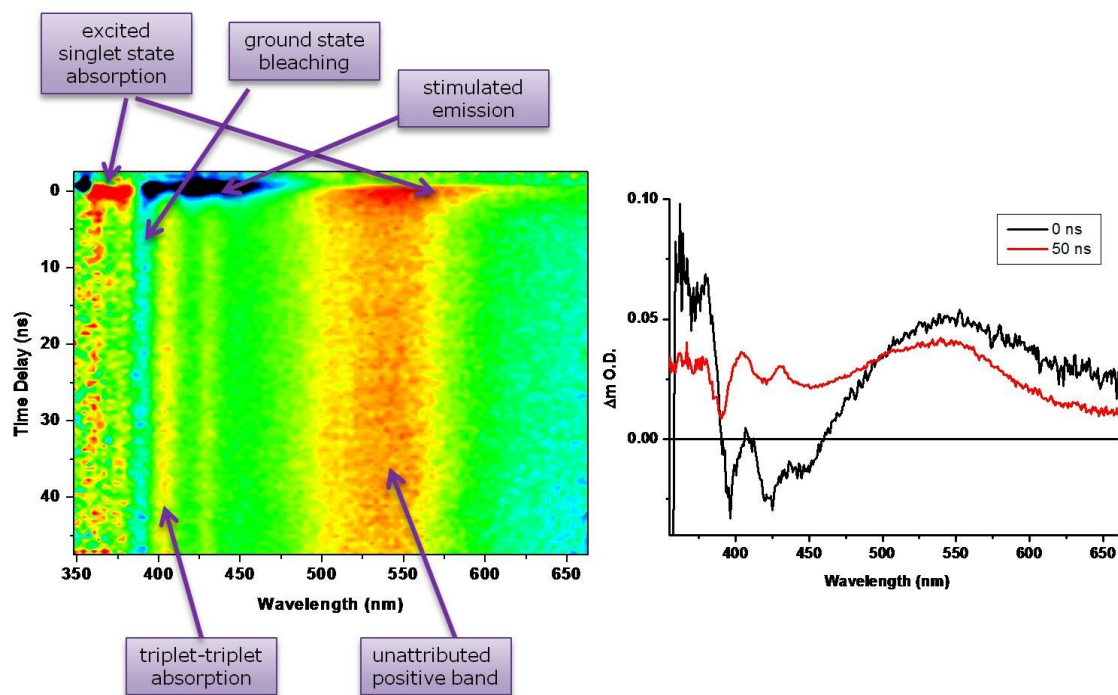


Fig.5.24: Changes in absorption on irradiating at 366 nm in DCM.

### 5.1.4.b. Transient Absorption

#### 3G in DCM

The transient absorption spectrum of **G3** in DCM is shown in Fig.5.25. The singlet excited state absorption bands are located at 370 nm and between 500-600 nm and relaxes in 2 ns. The stimulated emission band at 450 nm decays also in 2 ns, which is the same as the fluorescence lifetime.



**Fig.5.25:** Transient absorption spectrum ( $\lambda_{exc} = 357\text{nm}$ ) of **G3** in DCM.

The formation of the triplet-triplet absorption bands at 400 nm, 420 nm and stimulated emission bands are superposed. After the excited singlet bands relax, a band between 500 and 550 nm stays without relaxing in a 50 ns window. As it was discussed for **G2** molecules, excited anthracene molecules can relax in different pathways. The anthracene molecules undergo ISC and form triplets in 2 ns. The triplet-triplet absorption bands and stimulated emission bands are superposed and do not allow making an appropriate fit of triplet formation kinetics, however from the fluorescence lifetime and excited singlet absorption decay is helpful to estimate ISC rate. In the other relaxation pathway, the excited anthracene molecules form photoproduct in 2 ns. Excimer emission was not observed for these molecules.

### **G3.H in DCM**

The transient absorption spectrum of **G3** molecules in case of protonation in DCM is presented in Fig.5.26. Singlet excited state absorption band between 500 nm and 600 nm is decaying in 6 ns which is same decay time as the stimulated emission bands at 440 and 425 nm. The triplet-triplet absorption band forms in 6 ns also. In time-resolved experiments, the fluorescence lifetime is 6 ns too. No photoproduct absorption or any excimer/exiplex emission was observed.

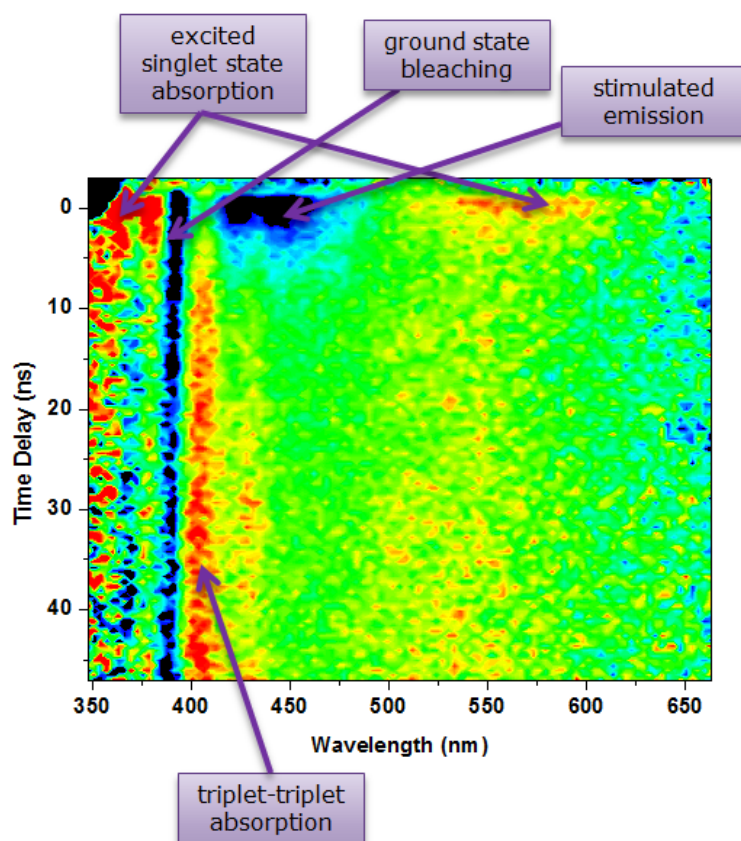


**Fig.5.26:** Transient absorption spectrum ( $\lambda_{exc} = 357\text{nm}$ ) of **G3.H** in DCM.

The transient absorption spectrum of **G3** molecules in case of protonation in DCM is presented in Fig.5.26. Singlet excited state absorption band between 500 nm and 600 nm is decaying in 6 ns which is same decay time as the stimulated emission bands at 440 and 425 nm. The triplet-triplet absorption band forms in 6 ns also. In time-resolved experiments, the fluorescence lifetime is 6 ns too. No photoproduct absorption or any excimer/exiplex emission was observed.

### 5.1.5. Hydrolyzed molecules

Fig.5.27 shows the absorption and emission spectra of **G2** and **G3** molecules in the absence and presence of  $\text{Ca}^{2+}$  in water. Adding  $\text{Ca}^{2+}$  causes shifts on the structured bands of anthracene between 350 and 400 nm. For **G2** molecules, the absorption band at 250 nm is not affected and a new band appears at 260 nm, which is the  $\pi^* \leftarrow \pi$  band of aniline receptor due to the fact that nitrogen is involved in complexation. We have observed decrease in the bands at 248 nm and 255 nm is observed for **G3**.

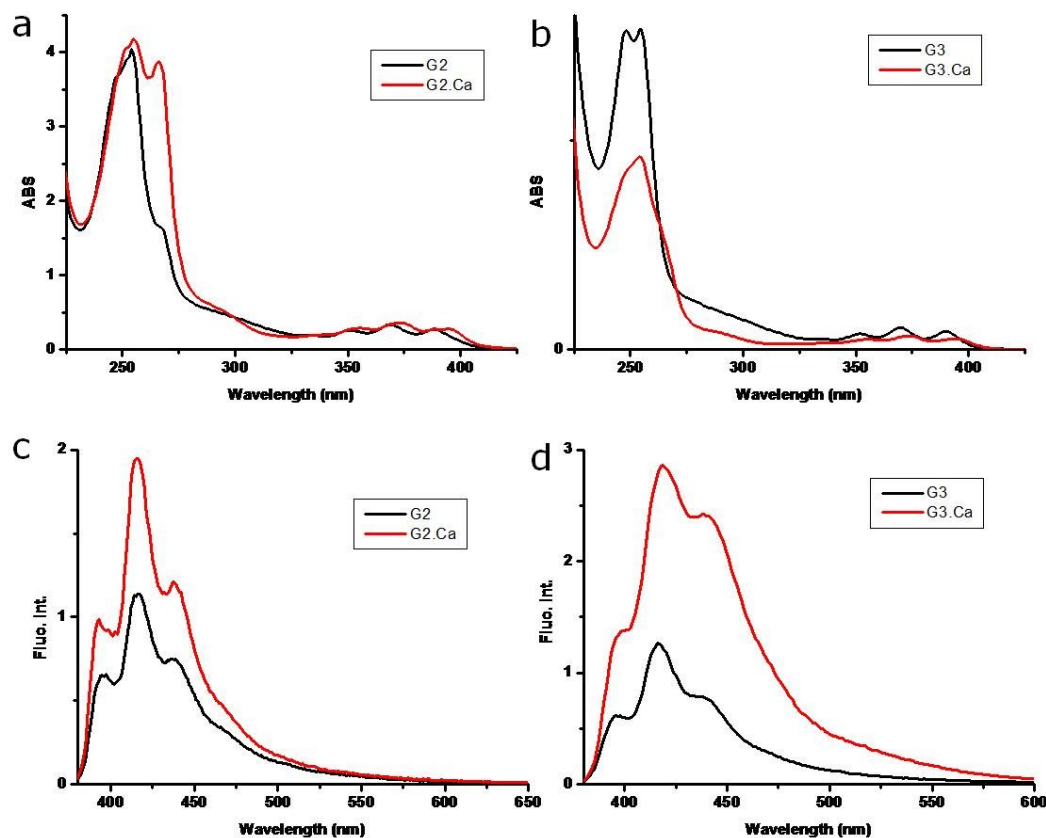


**Fig.5.27: a),b) absorption spectra of G2 and G3 c),d) emission spectra of G2 and G3**

On the bottom the fluorescence spectra of the molecules **G2** (c) and **G3** (d) are shown. Increase of  $\text{Ca}^{2+}$  concentration causes an increase on the fluorescence intensity also. Intensity of fluorescence increases 1.7 times for **G2** and 3.5 times for **G3**.

Fig.5.28 presents the transient absorption spectra of hydrolyzed **G2** and **G3** molecules and its complexes with  $\text{Ca}^{2+}$  at water in different time delays. Black curves represent the spectrum taken immediately after the pump arrives. In 50 ns the wide band located between 500-600 nm and the band at 440 nm decays entirely. The band at 520 nm still remains.

On addition of  $\text{Ca}^{2+}$ , similar spectra were observed at short time scales shown by green curves. In 50 ns, bands are relaxed and the spectra appear like the spectra shown in blue curves. The wide structureless bands on spectra taken in 50 ns are due to a phenomenon called solvated electron. The long living band at 520 nm can be the same photoproduct in previous results that we have observed in DCM.

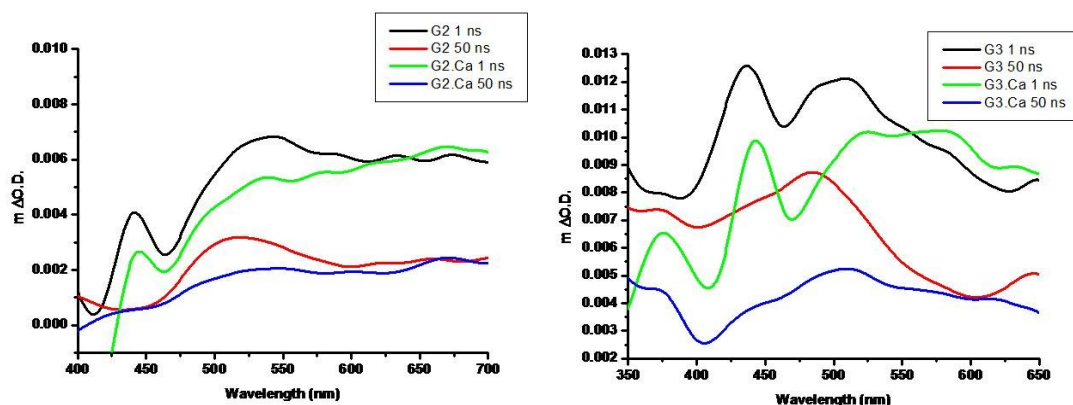


**Fig.5.28:** The transient absorption spectra of **G2**, **G3** and **G2. Ca<sup>2+</sup>**, **G3. Ca<sup>2+</sup>** at different time delays.

### 5.1.6. Conclusion

The calcium ion is an important second messenger in living organisms and is involved in many biological processes. Changes on intra- and extracellular Ca<sup>2+</sup> concentrations are responsible for cellular activity. Various synthetic receptors have been developed to control the concentration of calcium ion. BAPTA is one of the best adapted sensors for Ca<sup>2+</sup>, which is used in our studies herein. Anthracene molecules as fluorophores were expected to dimerize to eject the Ca<sup>2+</sup> from the cavity of BAPTA. In addition to dimerization, they also show different relaxation pathways via triplets or electron transfer etc. Additionally the behaviour appears somewhat different in aqueous environments as compared to more conventional organic solvents. Some additional changes were made to get rid of these redundant relaxation pathways. Structurally modified molecules show dimerization in water. This is a good result since these molecules are designed to be used in biological environment. Time-resolved studies give evidence that presence of calcium prevents dimerization. Time-resolved measurements cannot give information about the ejection of cation, complementary experiments may resolve this question.

Thus, results presented herein are encouraging although it is still necessary to confirm the ejection of Ca<sup>2+</sup>.

## PART II

### Azobenzene-Lariat Ether System

#### 5.2.1. Introduction

The term lariat ether refers to a crown ether or similar macrocyclic derivative with one or more side arms to enhance metal cation complexation ability by giving some three-dimensionality to the binding (Fig.5.29).<sup>33</sup>

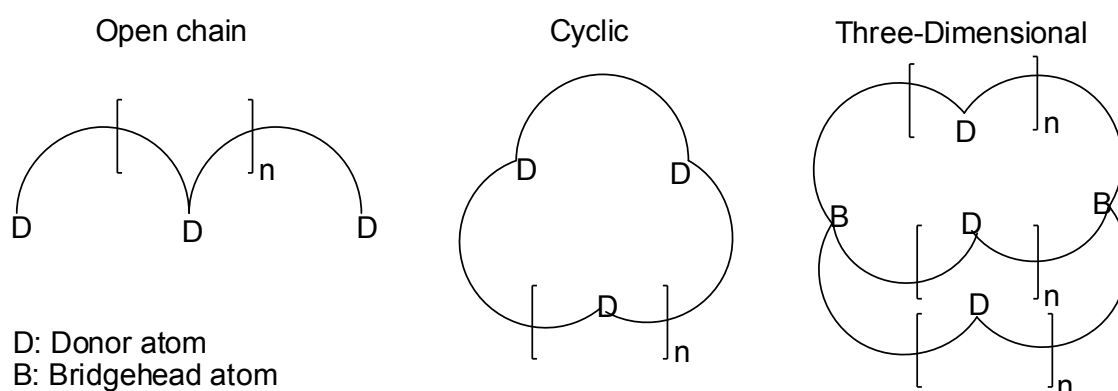


**Fig.5.29:** General chemical structures of cation binding macrocycles.

Shinkai *et al.*<sup>175-177</sup> suggested several photo responsive crown compounds. To control the cation-binding function they used trans-cis photoisomerisation of azobenzenes.

The azobenzene-capped diazacrown ether<sup>175</sup> **95** in Fig.5.30 shows changes in its cation binding behaviour by photoinduced isomerisation between the trans and cis isomers. It is reported that the trans-isomer of **95** binds  $\text{Li}^+$  and  $\text{Na}^+$  and the cis-form binds larger cations such as  $\text{K}^+$  and  $\text{Rb}^+$ .

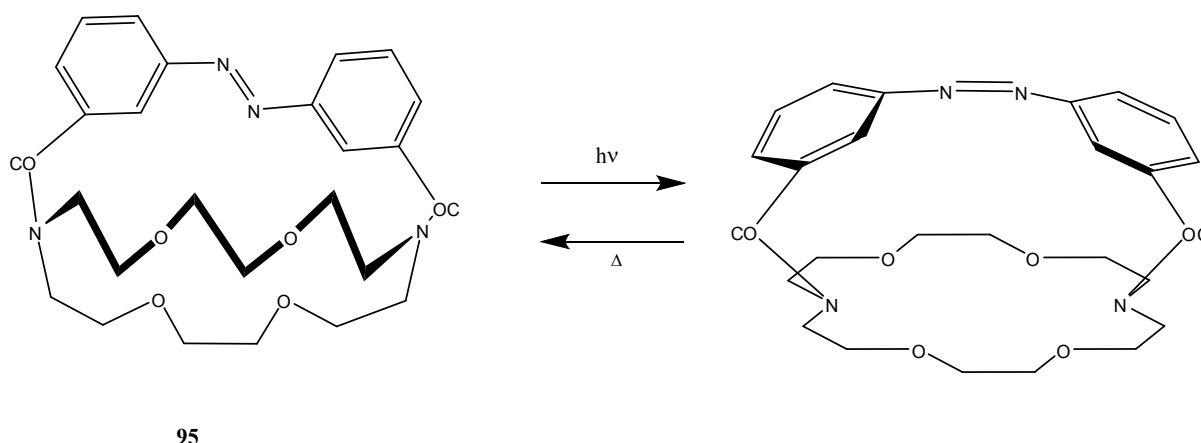
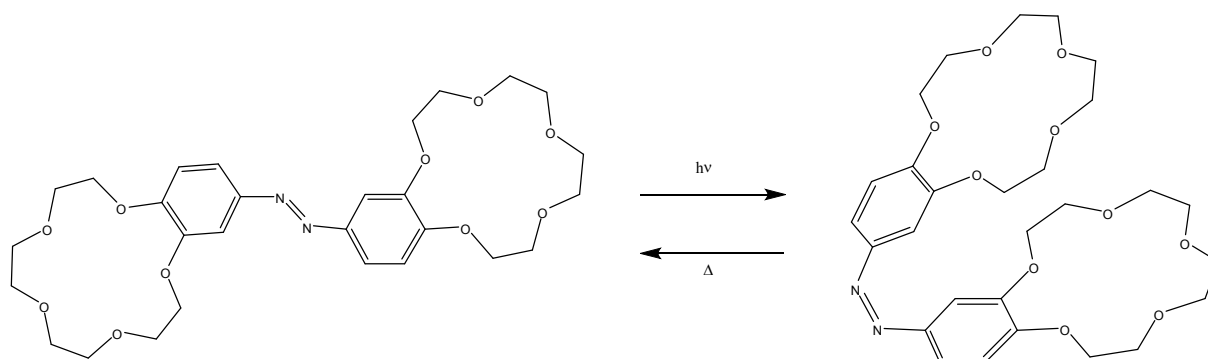


**Fig.5.30:** The isomerisation of azobenzene-capped diazacrown ether.

Bis(15-crown-5) azobenzene<sup>176</sup> **96** binds  $\text{Na}^+$  in the trans-isomer. The cis isomer can capture larger cations such as  $\text{K}^+$  by forming a sandwich type complex (Fig.5.31).



<sup>96</sup>  
**Fig.5.31:** The isomerisation of bis(15-crown-5) azobenzene.

Azobenzenophane-type crown ethers **97** are the first examples for photocontrolled crown ethers which exhibit ‘all-or-nothing’ changes in cation-binding ability<sup>177</sup>. It is reported that trans isomer totally lack of affinity to metal cations. Due to the cis-isomers can form the crown-like cavity, they can bind several of the alkali metal cations (Fig.5.32).

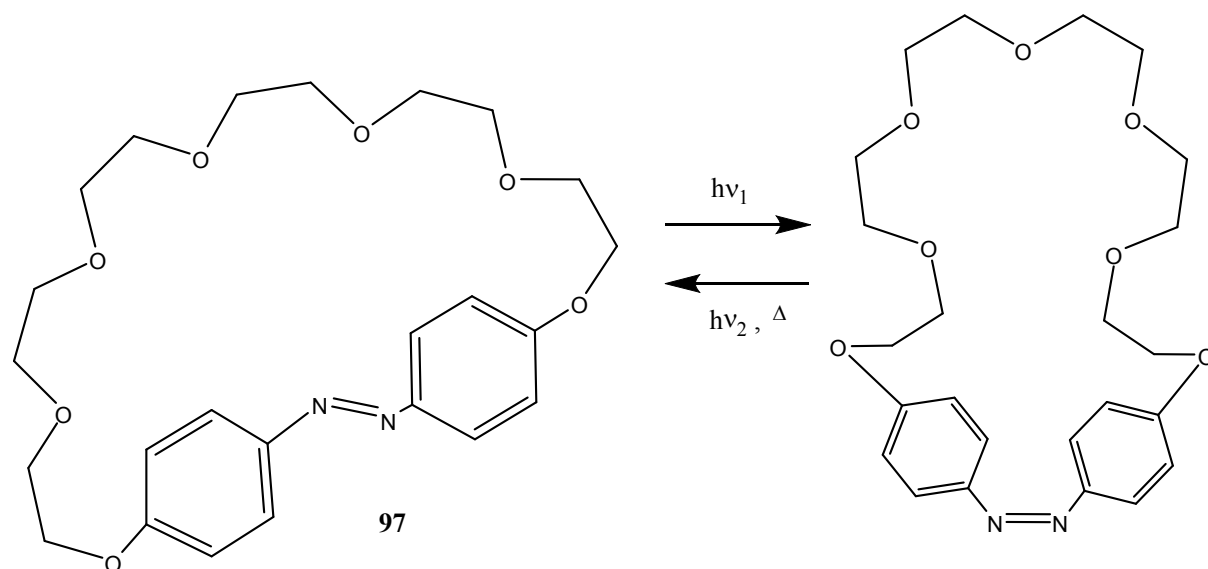


**Fig.5.32:** The isomerisation of Azobenzenophane-type crown ethers.

In this part an azobenzene-lariat ether (ABLE) system will be presented where ion release is anticipated to be based on the isomerisation of azobenzene. In Fig.5.33, the principle is explained for the studied lariat ether–azobenzene system which has high ion affinity of calcium cation. As explained in previous examples, cis isomer prefers to complexation with cation. The illumination of cis isomer causes changes in geometry cis to trans whereas trans form has lack of cation affinity and results as the cation release.

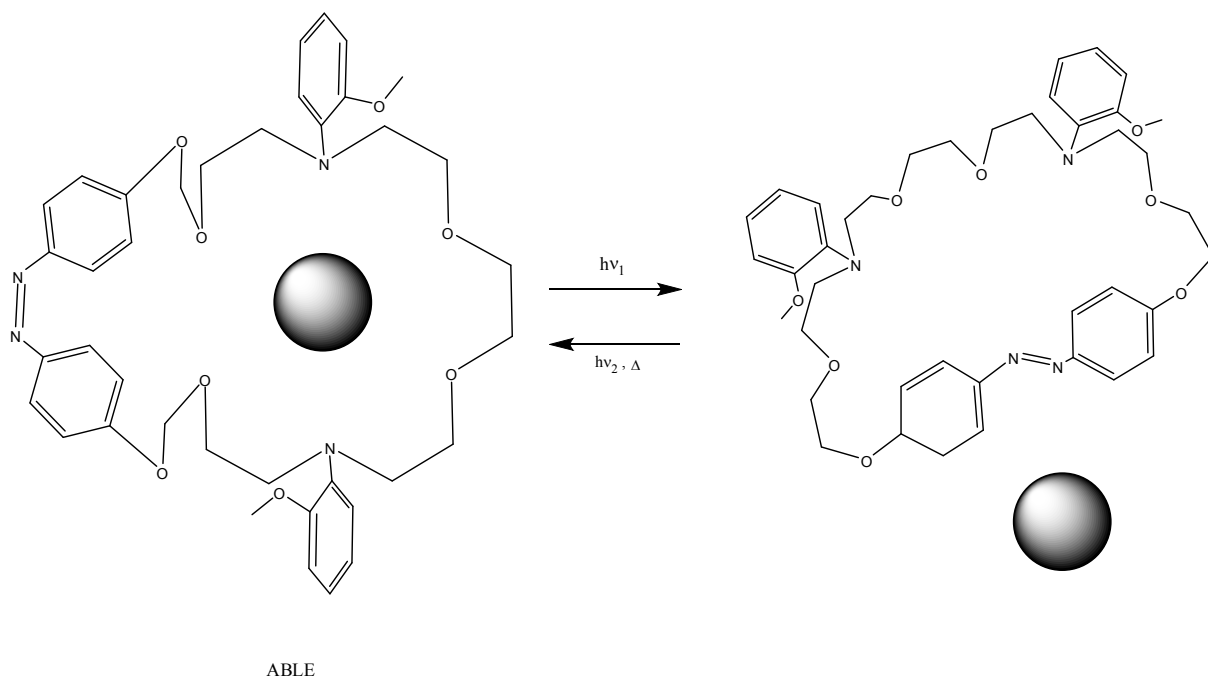


**Fig. 5.33:** *The working principle of Azobenzene-Lariat Ether system (ABLE).*

### 5.2.2. Steady State Absorption

The absorption spectra of **ABLE** is given in Fig.5.34. The black curve is the absorption spectrum of the **trans-ABLE**. When it is illuminated at 360 nm, trans-cis isomerisation occurs. The absorption spectrum of cis-azobenzene, which is shown as the red curve, has an absorption band at 450 nm. The absorption of lariat ether hides the other absorption bands of cis-azobenzene. Addition of  $\text{Ca}^{2+}$  into solution makes small changes in the absorption spectrum. Complex spectrum is shown as the green curve. The band at 450 nm and 300 nm is decreasing due to the effect of complexation with  $\text{Ca}^{2+}$ . When we irradiate the complex at 450 nm, we have observed the spectrum shown as the blue curve, which is very similar to the **trans-ABLE**.

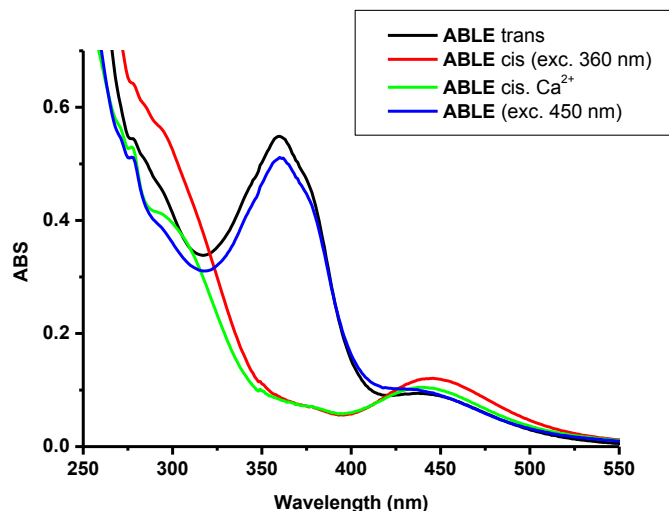


**Fig.5.34:** The absorption spectra of *ABLE* and its complex with  $\text{Ca}^{2+}$ .

### 5.2.3. Transient Absorption

Transient absorption and quantum chemical calculation of azobenzene were reported in the literature<sup>178-186</sup>. The transient absorption results were analyzed considering the information in literature. The generally accepted relaxation scheme of azobenzene molecules is given in Fig.5.35. The energy surfaces were calculated theoretically. The validity of model is proven experimentally by various groups<sup>178,183-186</sup>.

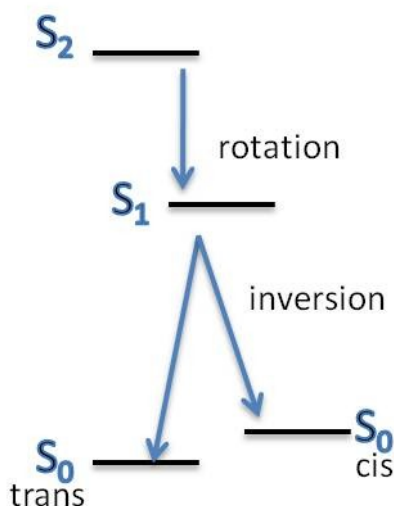


**Fig.5.35:** Relaxation scheme for azobenzene.

Relaxation pathway is as follows: after excitation of molecules in trans form to  $S_2$  state, they relax very quick towards  $S_1$  by rotation. After, evolving on the  $S_1$  surface, these molecules turn again to the flat form. Finally they relax to the ground state either the trans form or by inversion to the cis form.

In transient absorption experiments, the **ABLE** molecule in acetonitrile is excited at 350nm. During the experiment the sample is continuously irradiated with a LED at 450nm to keep the majority of the molecules in trans form.

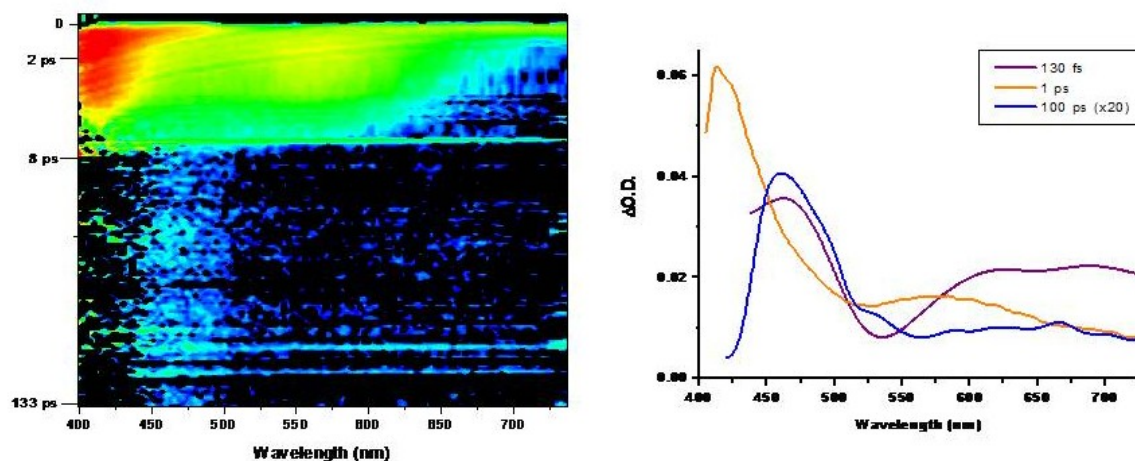


**Fig.5.36:** Transient absorption results of **ABLE** (left: 2D map and right: spectra at different time delays).

In Fig.5.36 on right side, the spectra at different delay times are shown. The purple coloured curve is observed just after excitation. This spectrum belongs to  $S_2$  state of molecules in trans form. This spectrum is relaxing in 180 fs. This fast relaxation was reported by Satzger *et al.*<sup>184</sup>, as 130 fs for simple azobenzene and in Lednev *et al.*<sup>178</sup>, less than 200 fs. Considering that **ABLE** molecule has substitutions and the solvent used is acetonitrile, the measured lifetime is in a similar range.

The orange coloured curve, which belongs to  $S_1$  state of molecules, is relatively long-lived with a decay time of 3 ps. The molecules relax by inversion. This relaxation time was reported as 2.9 ps in ethanol<sup>184</sup> and 2.5 ps in hexane<sup>178</sup>.

The blue coloured curve is observed at longer delays. The spectrum belongs to the absorption of a new photoproduct, which is very long living and very weak. Therefore the spectrum is multiplied in order to be more visible. This photoproduct is the cis form of molecules. Transformation from the cis to the trans form can be either achieved thermally or by irradiation.

#### 5.2.4. Conclusion

In this part an azobenzene-lariat ether system is presented. This system is designed as the “light in, ion out” part of communication system between molecules. In steady state experiments, the trans-cis and cis-trans photoisomerisation process is clearly observed by excitation at proper wavelength. Complexation with  $Ca^{2+}$  causes slight changes in steady state

spectrum. By irradiating the complex, the absorption spectrum of the trans form is observed again. In transient absorption the rate of trans-cis photoisomerization is obtained. The cis-trans isomerisation rate and ejection of  $\text{Ca}^{2+}$  could not be observed due to that the continuum in experimental setup does not allow to measure transient absorption signal below 400 nm. The development of experimental setup and observation of the cation release will be a future research aim.

## General Conclusion

In this thesis, intramolecular charge transfer, electronic energy transfer and photoinduced electron transfer processes of a range of molecules and molecular assemblies were studied. Ultrafast transient absorption measurements and complementary steady state absorption and fluorescence measurements were used for characterization. Ultrafast transient absorption measurements were done in two different time regimes. For the femtosecond regime, a classical pump-probe setup used with 30 fs FWHM pulses. For the picosecond regime, a time gated pump-probe method with 20 ps FWHM pulses used and detection was made with a streak camera.

Amphiphilic azacrown-containing hemicyanine dyes were studied using Langmuir-Blodgett techniques in the presence of various cations. For understanding the behaviour the first molecule was studied in solution. A non-amphiphilic version was used in order to get better solubility. The molecule was studied in various solvents. Absorption and emission maxima show solvatochromic shifts, which mean the dipole moment of the molecule changes in excited state. Quantum chemical calculations and application of different theories (Lippert, Kaswiski, Liptay) shows that ground state dipole moment is higher than excited state dipole moment.

Complexation studies for this molecule were previously reported<sup>62</sup> for  $\text{Li}^+$  and  $\text{Na}^+$ . They have observed hypsochromic shifts in absorption and emission spectra due to suppression of charge transfer by complexation. We have observed similar shifts by complexation with  $\text{Ca}^{2+}$  and  $\text{Ba}^{2+}$ . The absorption spectra of the complexes show two bands: one is the same with the non-complexed molecule and the other is blue shifted due to cation complexation. To explain the observation of these two bands in the complex spectra, a sandwich model was proposed. Two molecules are sharing a cation and form a sandwich. However one of the molecules is less affected by cation which causes the non-complex absorption band. The other molecule is slightly shifted relative to other and binds cations, which gives the blue shifted absorption band.

In emission spectra of the complex, the excitation at the corresponding wavelengths of two absorption bands, gives similar emission. This situation can be explained by decomplexation. However, in the transient absorption spectrum, no transient signal was observed due to a decomplexation process as seen in previous work<sup>37,39</sup>. Another explanation for this situation is energy transfer, which is reported between dimer molecules which consist of different

monomers in fs scale<sup>93</sup> and can be much faster in dimer consisting of the same monomers. The quantum chemical calculations showed also that HOMO and LUMO orbitals are placed in different molecules.

In time-resolved fluorescence experiments and the gain band of transient absorption spectra, the emission is shifting to longer wavelengths during 116 ps, while the fluorescence lifetime is 230 ps and solvation in acetonitrile is 120 fs. The fluorescence anisotropy decay time for the complex found for  $\text{Ca}^{2+}$  is 115 ps and for  $\text{Ba}^{2+}$  it is 124 ps. Theoretical calculations were done by using the relationship between moment of inertia and fluorescence anisotropy decay time derived from Langevin equation. Calculation of moment of inertia for complex was done presuming that after the energy transfer between the molecules in the sandwich, the excited molecule is relaxing by turning around the fixed crown end and take apart. The results are compatible with the calculation of reference dyes. This model also explains the shift of fluorescence emission in time.

An amphiphilic version of the molecules was studied at the air-water interface. The changes of the isotherms were investigated by varying concentration of cation in the water subphase. Later monolayers are deposited on silica plates in order to get their absorption and emission spectra. The molecules form aggregates at the air-water interface. Their fluorescence microscopy images are smooth and homogenous. In the low cation concentration subphase, the absorption and emission spectra show shifts to shorter wavelengths. Cations behave like structure breakers and new organization on the films is no more aggregates. They can be dimers due to their red shifted emission. Increasing the cation concentration causes the movement of maxima of emission to longer wavelengths as well as new band start to observe in absorption spectra. In case of high cation concentration, the emission spectra show a blue shifted band compared to the pure water subphase prepared monolayer (aggregates). This fluorescence microscopy image of this film is also homogenous. This new organization on the film is the aggregates with cations. This structure will be useful for many applications such as iono- and photosensitive artificial membranes. Their conductivity studies and multilayer deposition research can be a future aim.

NIR emitting aza-BODIPY dyes were studied by time-resolved methods in order to investigate their suitability for Photodynamic Therapy applications and imaging. The first synthesis of  $\text{BF}_2$ -azadipyromethenes was reported in 1940s. The research on these molecules has started with O'Shea's group from 2002 and has resulted with synthesis of several dyes<sup>113,133,134</sup>. They have indirectly observed the singlet oxygen generation properties of

halogenated molecules. Until now, the photophysical process in the excited state was not reported in detail.

Steady state absorption and fluorescence measurements show that BF<sub>2</sub>-azadipyrrromethene dyes are therapeutically interesting red-light absorbing photosensitizers. Evolution of the singlet ( $S_n \leftarrow S_1$ ) and triplet ( $T_n \leftarrow T_1$ ) transient absorption signatures of compounds allows direct spectroscopic determination of the intersystem crossing efficiency and rate to the non-emissive triplet state of Br substituted BF<sub>2</sub>-azadipyrrromethene and the lifetime of this PDT-active excited state. An intersystem crossing efficiency of 72% was determined with a triplet lifetime of 21 μs. Singlet oxygen generation quantum yield of Br substituted BF<sub>2</sub>-azadipyrrromethene is estimated at 74 %, or 0.77 compared to C<sub>60</sub>. These photophysical properties make Br-substituted BF<sub>2</sub>-azadipyrrromethene molecules good candidates as PDT agents. The NIR absorption and emission properties, TPA cross sections and very high photostability properties of BF<sub>2</sub>-azadipyrrromethene dyes make them suitable for different applications such as imaging.

Differently functionalized BODIPY dyes were investigated with respect to photostability, two photon absorption and ion sensing. BODIPY dye functionalized by inserting *meso* substitution perfluorinated phenyl ring can be used for biological labelling applications. The dye has a high extinction coefficient and high quantum yield of fluorescence. Photostability of perfluorinated BODIPY is in the same order with fluorescein dye which is widely used for imaging studies and considered a stable dye.

BODIPY dyes are widely used and studied compounds. In this thesis we have calculated the excited state absorption spectra of these dyes by using transient absorption and steady state absorption and emission spectra. Similar features were observed by comparison our calculated spectra of BODIPY and aza-BODIPY containing molecules.

The combination of two complementary processes, the photoejection of an ion, “light-in, ion-out”, and ion-induced fluorescence, “ion-in, light-out”, may be harnessed to establish connection between distinct functional molecules. Separate processes of ion-ejection and ion-detection with artificial systems have been demonstrated with varying degrees of success in terms of efficiency.

For ion detection two new fluorescent calcium probes based on a BAPTA linked, directly or via phenylene spacer, to a BODIPY fluorescent group were studied. Fluorescence emission, time-resolved studies of their ion-regulated photoinduced electron transfer and investigation of their Ca<sup>2+</sup> binding properties by fluorometric titrations are also reported.

By optically active transition of BODIPY via excitation, causes photoinduced electron transfer (PET) which quenches fluorescence. We have observed PET for directly linked compound in 30 ps in THF and in 300 fs in water as well as for phenylene spacer involved compound 30 ps in THF and 1.2 ps in water. When BAPTA binds  $\text{Ca}^{2+}$ , due to changing of its oxidation potential, PET does not occur, which allows switching the fluorescence ON.

Various molecular compounds are considered where light is a stimulus to provoke ion-release. One of these compounds is BAPTA (1,2-bis(o-aminophenoxy)ethane-N,N,N',N'-tetraacetic acid) decorated with two anthracenes where photodimerization is anticipated to lower the calcium binding affinity. BAPTA linked anthracene systems are investigated in three generations; each generation has longer spacer between units. Steady state absorption, emission and time-resolved studies showed that the photodimerization is in competition with photoinduced electron transfer.

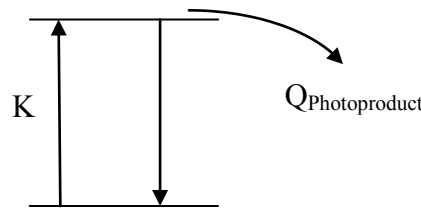
As a second ion-release system, a lariat ether-azobenzene system was studied. Isomerisation of azobenzene results ion release. The isomerisation process was investigated by transient absorption experiments. The isomerisation rate is found to be 3 ps for this system.

The processes of intramolecular charge transfer, electronic energy transfer, photoinduced electron transfer, photoisomerization and photodimerization are the fundamental and most important photoinduced processes at the molecular level. This thesis gives results of various molecular systems, which shows these processes. To understand the behaviour of molecular systems and the processes they have involved is an important to issue in order to develop them. In future work, molecular systems such as ion- photon-sensitive membranes, PDT agent aza-BODIPY dyes, perfluorinated BODIPY dyes can be developed for commercial applications. Artificial systems involving processes of ion-ejection and ion-detection can be develop with different and more efficient subunits.

# APPENDIX

## Calculation of Photodegradation Quantum Yield

The reaction scheme to study the photodegradation is presented below. We suppose that all photoexcited states relax *in fine* to the ground state except a part denoted  $Q_{\text{photoproduct}}$  which represents a quantum yield of photodegradation or other irreversible photoreaction:



The Stark-Einstein law, states that for each photon of light absorbed by a chemical system, only one molecule is activated for subsequent reaction. According to this “photoequivalence law”, equation 1 can be written. Number of excited molecules  $N_{\text{exc}}$  is equal to number of absorbed photons  $K_{\text{abs}}$  :

$$K_{\text{abs}} = K(1 - 10^{-\epsilon c}) = N_{\text{exc}} \quad (1)$$

$K$  is incident photon number. It can be found from

$$K = \frac{Wt}{hv} \quad (2)$$

where  $W.t$  (power by time, Watts by second) multiplication gives the energy dose (Joules) of radiation. If we divide it to one photon energy, result is the number of photons.

According to our photoreaction scheme, some molecules undergo an irreversible photoreaction (photodegradation) with a quantum yield of  $Q$ . This photoreaction yields that number of molecules reaching the ground state after being excited can be find as follows:

$$N_{\text{relax}} = N_{\text{exc}}(1 - Q) \quad (3)$$

or

$$N_{\text{relax}} - N_{\text{exc}} = -N_{\text{exc}}.Q \quad (4)$$

According to the equation 4, the changes of the ground state population in time can be written as

$$\frac{dN_G}{dt} = -\frac{dN_{\text{exc}}}{dt}.Q \quad (5)$$

Substituting equation 1 into equation 4 and having in mind the photon flux (equation 2), one obtains for slowly varying steady state absorption ( $1 - 10^{-\frac{N_G \epsilon}{V}}$ )

$$\frac{dN_G}{dt} = -K \left(1 - 10^{-\frac{N_G \epsilon}{V}}\right) Q = -\frac{W}{hv} \left(1 - 10^{-\frac{N_G \epsilon}{V}}\right) Q \quad (6)$$

Initial condition is  $N_G=N$  at the beginning of the experiment ( $t=0$ ), and  $c_0 = \frac{\varepsilon}{V}$  for 1cm cell. If the absorption ( $N_G\varepsilon/V$ ) of initial solution is small, we can develop the exponent into Taylor series

$$10^{ax} = e^{xa \ln 10} = 1 + xa \ln 10 + \dots \quad (7)$$

Taking the first term from the series 7, the differential equation 6 becomes

$$\frac{dN_G}{dt} = -\frac{W}{h\nu} \left(1 - \left(1 - \frac{N_G\varepsilon}{V} \ln 10\right)\right) Q = -\frac{W\varepsilon \ln 10 Q}{h\nu V} N_G \quad (8)$$

The solution of the equation 8 is

$$N_G = \exp\left(-\frac{W\varepsilon Q \ln 10}{h\nu V} t\right) \quad (9)$$

It corresponds to the exponential relaxation of ground state population (and accordingly steady state absorption) with a time constant

$$\tau = \frac{h\nu V}{W\varepsilon Q \ln 10} \quad (10)$$

Thus, the quantum yield of irreversible photoreaction (photodegradation) can be found from the exponential kinetic of steady state absorption decay upon irradiation as follows:

$$Q = \frac{h\nu V}{W\varepsilon \ln 10 \tau} \quad (11)$$

(In the conditions of real experiment, it is necessary to account for the reflection losses on the input window of the cell as well as permanent stirring of solution is required in order to have an uniform distribution of molecular concentration in the cell)

## References

- (1) Marlin, D. S.; Bill, E.; Weyhermüller, T.; Rentschler, E.; Wieghardt, K. *Angew. Chem.Int. Ed.* **2002**, 41, 4775.
- (2) Speiser, S. *J. Lumin.* **2003**, 102-3, 267.
- (3) Balzani, V. *Handbook of Electron Transfer in Chemistry*, Wiley-VCH, Weinheim; **2001**.
- (4) Kohen, E.; Santus, R.; Hirschbergen *Photobiology*, Academic Press. **1995**.
- (5) Balzani, V.; Venturi, M.; Credi, A. *Molecular Devices and Machines*, Wiley-VCH, Weinheim; **2003**.
- (6) de Silva, A. P.; Gunaratne, H.; Gunnlaugsson, T.; Huxley, A. J. M.; McCoy, C. P.; Rademacher, J.; Rice, T. E. *Chem. Rev.* **1997**, 97, 1515.
- (7) Henbest, K.; Rodgers, M. A. J. Photochemical Techniques, in *Electron Transfer in Chemistry* (ed V. Balzani), Wiley-VCH Verlag GmbH, Weinheim, Germany; **2001**
- (8) Birks, J. B. *Photophysics of Aromatic Molecules*, Wiley-Interscience, London, **1970**.
- (9) Turro, N. J. *Modern Molecular Photochemistry*, University Science Books, Mill Valley California. **1991**.
- (10) Valeur, B. *Molecular Fluorescence Principles and Applications*, Wiley-VCH Verlag GmbH, Weinheim, FRG, **2001**.
- (11) Lakowicz, J. R. *Principles of Fluorescence Spectroscopy*, Springer, New York, **2006**.
- (12) Raymo, M.; Giordani, S.; Drive, M.; Florida, C. G. *J. Am. Chem. Soc.* **2001**, 123, 4651.
- (13) de Silva, A. P.; Huxley, A. J. M. *Applied Fluorescence in Chemistry, Biology and Medicine*; ed. W. Rettig, B. Strehmel, S. Schrader and H. Seifert, Springer, Berlin, **1999**
- (14) Nishida, H.; Katayama, Y.; Ueno, K. *Chem. Lett.* **1982**, 1853.
- (15) Bourson, J.; Badaoui, F.; Valeur, B. *J. Fluoresc.* **1994**, 4, 275.
- (16) Bourson, J.; Pouget, J.; Valeur B. *J. Phys. Chem.* **1993**, 97, 4552.
- (17) Alihodzic, S.; Zinic, M.; Cimerman, Z. *Tet. Lett.* **1993**, 34, 8345.
- (18) Huston, M. E.; Haider, K. W.; Czarnik, A. W. *J. Am. Chem. Soc.* **1988**, 110, 4460.
- (19) Fabbrizzi, L.; Licchelli, M.; Pallavicini, P.; Taglietti, A. *Inorg. Chem.* **1996**, 35, 1733.
- (20) Arman, S. Van; Czarnik, A. W. *J. Am. Chem. Soc.* **1990**, 112, 5376.
- (21) Kumar, C. V.; Asuncion, E. H. *J. Am. Chem. Soc.* **1993**, 115, 8547.
- (22) Jones, G.; Oliveira, M. E.; Cundall, R. B. *Photochem. Photobiol.* **1990**, 52, 451.
- (23) Santis, G. D; Sacchi, D. *Inorg. Chem.* **1995**, 34, 3581.

- (24) Iwata, S.; Tanaka, K. *J. Chem. Soc. Chem. Commun.* **1995**, 1491.
- (25) Kavarnos, G. J.; Turro, N. *J. Chem. Rev.* **1986**, 86, 401.
- (26) Grampp, G. *Angew. Chem. Int. Ed.* **1993**, 32, 691-693.
- (27) Marcus, R. A. *Angew. Chem. Int. Ed.* **1993**, 32, 1111-1121.
- (28) Valeur, B.; Leray, I. *Inorg. Chim. Acta* **2007**, 360, 765-774.
- (29) Valeur, B.; Leray, I. *Coord. Chem. Rev.* **2000**, 205, 3-40.
- (30) Tsien, R. Y. *Biochemistry* **1980**, 2396-2404.
- (31) Parkesh, R.; Mohsin, S.; Lee, T. C.; Gunnlaugsson, T. *Chem. Mater.* **2007**, 19, 1656-1663.
- (32) Gryniewicz, G.; Poenie, M.; Tsien, R. Y. *J. Biol. Chem.* **1985**, 260, 3440-50.
- (33) Steed, J. W.; Atwood, J.L. *Supramolecular Chemistry*, John Wiley & Sons, New York, **2009**.
- (34) Bourson, J. *J. Phys. Chem.* **1989**, 93, 3871.
- (35) Letard, J.F.; Laupoyade, R.; Rettig, W. *Pure Appl. Chem.* **1993**, 63, 1705.
- (36) Ushakov, E.N.; Alfimov, M. *Russ. Chem. B+*. **1997**, 46, 463.
- (37) Martin, M. M.; Plaza, P.; Meyer, Y. H.; Badaoui, F.; Bourson, J.; Lefèvre, J.P.; Valeur, B. *J. Phys. Chem.* **1996**, 100, 6879-6888.
- (38) Dumon, P.; Jonusauskas, G.; Dupuy, F.; Pee, P.; Rulliere, C.; Letard, J.-F.; Lapouyade, R. *J. Phys. Chem.* **1994**, 98, 10391-10396.
- (39) Mathevet, R.; Jonusauskas, G.; Rulliere, C.; Letard, J.F.; Lapouyade, R. *J. Phys. Chem.* **1995**, 99, 15709-15713.
- (40) Tulyakova, E. V.; Fedorova, O. A.; Fedorov, Y. V.; Jonusauskas, G.; Anisimov, A.V. *J. Phys. Org. Chem.* **2008**, 21, 372-380.
- (41) Fedorov, Y. V.; Fedorova, O. A.; Andryukhina, E. N.; Shepel, N. E.; Mashura, M. M.; Gromov, S. P.; Kuzmina, L. G.; Churakov, A. V.; Howard, J. A. K.; Marmois, E.; Oberlé, J.; Jonusauskas, G.; Alfimov, M. V. *J. Phys. Org. Chem.* **2005**, 18, 1032-1041.
- (42) Berera, R.; Stokkum, I. H. M.; van; Kodis, G.; Keirstead, A. E.; Pillai, S.; Herrero, C.; Palacios, R.; E.; Vengris, M.; Grondelle, R.; van; Gust, D.; Moore, T.; Moore, A. L.; Kennis, J. T. M. *J. Phys. Chem.* **2007**, 111, 6868-77.
- (43) Emmelius, M.; Pawlowski, G.; Vollman, H. W. *Angew. Chem. Int. Ed.* **1989**, 28, 1445.
- (44) Wurthner, F.; Wortmann, R.; Matschiner, R.; Lukaszuk, K.; Sens, R. *Angew. Chem. Int. Ed.* **1998**, 37, 2765.
- (45) Vannikov, A. V.; Grishina, A. D. *Nauchn. Fotogr.* **1989**, 25, 74.
- (46) Bricks, J. *J. Photochem. Photobiol.* **2000**, 132, 193-208.

- (47) Callan, J. F.; de Silva, A.P.; Magri, D. C. *Tetrahedron* **2005**, 61, 8551-8588.
- (48) Ito, F.; Nagamura, T. J. *Photochem. Photobiol. Rev.* **2007**, 8, 174-190.
- (49) Hossain, M. Z.; Ernst, L. A.; Nagy, J. L. *Neurosci. Lett.* **1996**, 184, 183.
- (50) Soper, S. A.; Mattingly, Q. L. *J. Am. Chem. Soc.* **1994**, 116, 3744.
- (51) Das, S.; Thomas, K. G.; Thomas, K. J. Kamat, P. V.; George, M. V. *J. Phys. Chem.* **1994**, 98, 9291.
- (52) Lanzafame, J. M.; Muentner, A. A.; Brumbaugh, D. V. *Chem. Phys.* **1996**, 210, 79.
- (53) Möbius, D. *Adv. Mater.* **1995**, 7, 437.
- (54) Tyutyullkov, N.; Tadjer, A. *Polymethine Dyes*; Kliment Ohridski University Press: Sofia, **1991**.
- (55) Williams, C. H. G. *Trans. R. Soc. Edinburg*, **1856**, 21, 377.
- (56) Majznych, M.; Henary, M. *Top. Heterocycl. Chem.* **2008**, 14, 1-9.
- (57) Mishra, A.; Behera, R. K.; Behera, P. K.; Mishra, B. K.; Behera, G. B. *Chem Rev.* **2000**, 100, 1973-2012.
- (58) Haughland, R. *Molecular Probes. Handbook of Fluorescent Probes and Research Chemicals*, 9th ed. Molecular Probes Inc, Eugene, OR. **2002**.
- (59) El-Gezawy, H.; Rettig, W. *Chem. Phys.* **2006**, 327, 385-394.
- (60) Lapouyade, R.; Czeschka, K.; Majenz, W.; Rettig, W.; Gilabert, E.; Rulliere, C. *J. Phys. Chem.* **1992**, 96, 9643-9650.
- (61) Rettig, W. *Chem. Matter. Sci.* **1994**, 169.
- (62) Thomas, K. J.; Thomas, K. G.; Manojkumar, T. K.; Das, S.; George, M. V. *Proc. Ind. Acad. Sci.* **1994**, 106, 1375-1382.
- (63) Gromov, S. P.; Alfimov, M. V. *Dokl. Akedem. Nayk. SSSR* **1990**, 1135.
- (64) Gromov, S. P.; Fedorova, O. A.; Ushakov, E.; Alfimov, M. *Dokl. Akedem. Nayk. SSSR* **1991**, 1134.
- (65) Brazykin, A. V.; Fox, M. A.; Federova, O. A.; Ushakov, E.; Alfimov, M. *J. Am. Chem. Soc.* **1992**, 114, 6381.
- (66) Alfimov, M. V.; Churakov, A. V.; Federov, Y. V.; Federova, O. A.; Vedernikov, A. I. *J. Chem. Soc., Perkin Trans. 2* **1997**, 2249.
- (67) Sahay, A. K.; Mishra, B. K.; Behera, G. B.; Shah, D. O. *Ind. J. Chem.* **1988**, 561.
- (68) Mishra, J. K.; Sahay, A. K.; Mishra, B. K. *Ind. J. Chem.* **1991**, 30A, 886.
- (69) Carpenter, M. A.; Willand, C. S.; Penner, T. L.; Williams, D. J.; Mukamel, S. *J. Phys. Chem.* **1992**, 96, 2810.
- (70) Li, H.; Zhou, D.; Xie, X. H. *J. Chem. Soc. Faraday Trans.* **1996**, 92, 2585.

- (71) Rajesh, K.; Sharath M. S.; Chandra, H. J, K.; Radhakrishnan, T. *Langmuir* **2007**, 23, 8560-8568.
- (72) Schildkraut, J.; Penner, T.; Willand, C.; Ulman, A. *Opt. Lett.* **1988**, 13, 134-136.
- (73) Anceau, C. Brasselet, S.; Zyss, J. *J.Chem.Phys. Lett.* **2005**, 411, 98-102.
- (74) Inglot, K.; Kaleta, A.; Martynski, T.; Bauman, D. *Dyes and Pigments* **2008**, 77, 303-314.
- (75) Lambacher, A.; Fromherz P. *J. Phys. Chem.* **2001**, 105, 343-346.
- (76) de Silva, P. A.; McClenaghan, N. D. *Chem. Eur. J.* **2002**, 8, 21.
- (77) Suppan, P. J. *Photochem. Photobiol.* **1990**, 50, 293-330.
- (78) Onsager, L. *Yale Uni. Cont.* **1936**, 58, 1486-1493.
- (79) Ooshika, Y. L. *J. Phys. Soc. Japan* **1954**, 9, 594.
- (80) Lippert, E. Z. *Electrochem.* **1957**, 61, 962-975.
- (81) Stewart, J. P MOPAC2009, James. Stewart Computational Chemistry, Colorado Springs, CO, USA, **2008**
- (82) Kawski, A. Z. *Naturforsch.* **2002**, 57A, 255-262.
- (83) Liptay, W. Z. *Z. Naturforsch.* **1965**, 20A, 1965.
- (84) Gampp, H.; Maeder, M.; Meyer, C. J.; Zuberbühler, A. D. *Math. Consider., Talanta* **1985**, 32, 95-101.
- (85) Baskin, J. *Chem. Phys. Lett.* **1997**, 275, 437-444.
- (86) Baskin, J. S.; Chachisvilis, M.; Gupta, M.; Zewail, A. H. *J.Phys. Chem.* **1998**, 102, 4158-4171.
- (87) CHEMOffice, CambridgeSoft.
- (88) Weaver, M. J. *J. Molecular Liquids* **1993**, 60, 57.
- (89) McManis, G. E.; Nielsen, R. M. A., G.; Weaver, M. J. *J. Am. Chem. Soc.* **1989**, 111, 5533.
- (90) Hubbard, P. S. *Phys. Rev.* **1963**, 131, 1155.
- (91) Anna, J. M.; Kubarych, K. J. *J. Chem. Phys.* **2010**, 133, 174506.
- (92) Mathevet, R.; Jonusauskas, G. *J.Phys. Chem.* **1995**, 99, 15709-15713.
- (93) Kühn, O.; Chernyak, V.; Mukamel, S. *J. Chem. Phys.* **1996**, 105, 8586.
- (94) Rosenthal, S. J.; Xie, X. H.; Du, M.; Fleming, G. R. *J. Chem. Phys.* **1991**, 95, 4715.
- (95) Robert, G. *Langmuir-Blodgett Films*. Plenum Press: New York; **1990**.
- (96) Ulman, A. *An Introduction to Ultrathin Organic Films*, Academic Press: London **1991**.
- (97) Vollhardt, D. *Colloid. Surface A* **2001**, 176, 117.

- (98) Vollhardt, D. *Adv. Colloid. Interfac.* **1996**, 64, 143.
- (99) Triebs, A.; Kreuzer, F. H. *Liebigs Ann. Chem.* **1968**, 718, 208-223.
- (100) Li, Z.; Mintzer, E.; Bittman, R. *J. Org. Chem.* **2006**, 71, 1718.
- (101) Marmé, N.; Knemeyer, J.P.; Sauer, M.; Wolfrum, J. *Bioconjugate Chem.* **2003**, 14, 1333-1339.
- (102) Faulds, K.; McKenzie, F.; Smith, W. E.; Graham, D. *Angew. Chem.* **2007**, 119, 1861-1863.
- (103) Bonardi, L.; Ulrich, G.; Ziessel, R. *Syn. Lett.* **2006**, 2, 0450-0454.
- (104) Ziessel, R.; Bonardi, L.; Ulrich, G. *Dalton Trans.* **2006**, 2913-8.
- (105) Arbeloa, T. *Chem. Phys. Lett.* **1999**, 299, 315-321.
- (106) Chen, X.; Lenhert, S.; Hirtz, M.; Lu, N.; Fuchs, H.; Chi, L. *Acc. Chem. Res.* **2007**, 393-401.
- (107) Qin, W.; Baruah, M.; Stefan, A.; Auweraer, M.; Boens, N. *ChemPhysChem* **2005**, 6, 2343-51.
- (108) Palma, A.; Tasiar, M.; Frimannsson, D. O.; Vu, T. T.; Méallet-Renault, R.; O'Shea, D. F. *Org. Lett.* **2009**, 11, 3638-41.
- (109) Atilgan, S.; Kutuk, I.; Ozdemir, T. *Tet. Lett.* **2010**, 51, 892-894.
- (110) de Wael, E. V.; Pardoën, J. A.; van Koeveeringe, J. A.; Lugtenburg, J. *Recueil des Travaux Chimiques des Pays-Bas* **1977**, 96, 306-309.
- (111) Kollmannsberger, M.; Rurack, K.; Resch-Genger, U.; Daub, J. *J. Phys. Chem.* **1998**, 102, 10211.
- (112) Loudet, A.; Burgess, K. *Chem. Rev.* **2007**, 107, 4891-932.
- (113) Gorman, A.; Killoran, J.; O'Shea, C.; Kenna, T.; Gallagher, W. M.; O'Shea, D. F. *J. Am. Chem. Soc.* **2004**, 126, 10619-31.
- (114) Lim, S. H.; Thivierge, C.; Nowak-Sliwinska, P.; Han, J.; van den Bergh, H.; Wagnières, G.; Burgess, K.; Lee, H. B. *J. Med. Chem.* **2010**, 53, 2865-74.
- (115) Beer, G.; Rurack, K.; Daub, J. *Chem. Commun.* **2001**, 1138-1139.
- (116) Ziessel, R.; Rihn, S.; Harriman, A. *Chem. Eur. J.* **2010**, 11942 - 11953.
- (117) Olivier, J.H.; Haefele, A.; Retailleau, P.; Ziessel, R. *Org. Lett.* **2010**, 12, 408-11.
- (118) Ozlem, S.; Akkaya, E. U. *J. Am. Chem. Soc.* **2009**, 131, 48-9.
- (119) Yamada, K.; Toyota, T.; Takakura, K. *New J. Chem.* **2001**, 667-669.
- (120) Chen, J.; Burghart, A.; Burgess, K. *J. Org. Chem.* **2000**, 65, 2900-29006.
- (121) Burghart, A.; Kim, H.; Welch, M. B.; Thoresen, L. H.; Reibenspies, J.; Burgess, K. *J. Org. Chem.* **1999**, 64, 7813-7819.

- (122) Li, M.; Wang, H.; Zhang, X.; Zhang, H. *Spectrochim. Acta. A*, 2004, 60A, 987.
- (123) Zhang, X.; Zhang, H. *Spectrochim. Acta. A* **2005**, 61A, 1045.
- (124) Zhang, X.; Wang, H.; Li, J. S.; Zhang, H. *Anal. Chim. Acta* **2003**, 481, 101.
- (125) Wu, Y.; Peng, X.; Guo, B.; Fan, J.; Gao, Y. *Org. Biomol. Chem.* **2005**, 3, 1387.
- (126) Baki, C. N.; Akkaya, E. U. *J. Org. Chem* **2001**, 66, 1512.
- (127) Bricks, J.; Kovalchuk, A.; Rurack, K. *J. Am. Chem. Soc.* **2005**, 127, 13522.
- (128) Martin, V. V.; Rothe, A.; Gee, K. R. *Bioorg. Med. Chem. Lett.* **2005**, 15, 1851.
- (129) Rurack, K.; Kollmannsberger, M.; Resch-Genger, U.; Daub, J. *J. Am. Chem. Soc.* **2000**, 122, 968.
- (130) Basaric, N.; Baruah, M.; Qin, W.; Boens, N. *Org. Biomol. Chem.* 2005, 3, 2755.
- (131) Rogers, M. A. T. *J. Am. Chem. Soc.* **1943**, 596-597.
- (132) Flavin, K.; Lawrence, K.; Bartelmess, J.; Tasiar, M.; Navio, C.; Bittencourt, C.; O'Shea, D. F. Guldi, D. M.; Giordani, S. *ACS Nano* **2011**, 5, 1198-206.
- (133) Killoran, J.; Allen, L.; Gallagher, J. F.; Gallagher, W. M.; O'Shea, D. F. *Chem. Commun.* **2002**, 317, 1862-3.
- (134) McDonnell, S. O.; O'Shea, D. F. *Org. Lett.* **2006**, 8, 3493.
- (135) Gallagher, W. M.; Allen, L. T.; O'Shea, C.; Kenna, T.; Hall, M.; Gorman, A.; Killoran, J.; O'Shea, D. F. *Brit. J. Cancer.* **2005**, 92, 1702-10.
- (136) McDonnell, S. O. Hall, M. J. Allen, L. T. Byrne, A. Gallagher, W. M.; O'Shea, D. F. . *J. Am. Chem. Soc.* **2005**, 127, 16360-1.
- (137) Hall, M. J.; Allen, L. T.; O'Shea, D. F. *Org. Biomol. Chem* **2006**, 4, 776-80.
- (138) Killoran, J.; O'Shea, D. F. *Chem. Commun.* **2006**, 1503.
- (139) Coskun, A.; Yilmaz, M. D.; Akkaya, E. U. *Org. Lett.* **2007**, 9, 607.
- (140) Gawley, R. E.; Mao, H.; Haque, M. M.; Thorne, J. B.; Pharr, J. S. *J. Org. Chem.* **2007**, 2187.
- (141) Murtagh, J.; Frimannsson, D. O.; O'Shea, D. F. *Org. Lett* **2009**, 11, 5386-9.
- (142) Zhao, W.; Carreira, E. M. *Angew. Chem.* **2005**, 44, 1677.
- (143) Zhao, W.; Carreira, E. M. *Chem. Eur. J.* **2006**, 12, 7254.
- (144) Tasiar, M.; O'Shea, D. F. *Bioconjugate Chem.* **2010**, 21, 1130-3.
- (145) Loudet, A.; Bandichhor, R.; Burgess, K.; Palma, A.; McDonnell, S. O.; Hall, M. J.; O'Shea, D. F. *Org. Lett.* **2008**, 10, 4771-4.
- (146) Byrne, A. T.; O'Connor, A. E.; Hall, M.; Murtagh, J.; O'Neill, K.; Curran, K. M.; Mongrain, K.; Rousseau, J. A.; Lecomte, R.; McGee, S.; Callanan, J. J.; O'Shea, D. F.; Gallagher, W. M. *Brit. J. Cancer* **2009**, 101, 1565-73.

- (147) Arbogast, J.W.; Footne, C.; Kao, M. *J. Am. Chem. Soc.* **1992**, *4*, 2277-2279.
- (148) Nastasi, F.; Puntoriero, F.; Campagna, S.; Diring, S.; Ziessel, R. *PhysChemPhys.* **2008**, *10*, 3982.
- (149) Galletta, M.; Campagna, S.; Quesada, M.; Ulrich, G.; Ziessel, R. *Chem. Commun.* **2005**, 4222.
- (150) Galletta, M.; Puntoriero, F.; Campagna, S.; Chiorboli, C.; Quesada, M.; Goeb, S.; Ziessel, R. *J. Phys. Chem.* **2006**, *110*, 4348-58.
- (151) Nicolini, C.; Baranski, J.; Schlummer, S.; Palomo, J.; Lumbierres-Burgues, M.; Kahms, M.; Kuhlmann, J.; Sanchez, S.; Gratton, E.; Waldmann, H.; Winter, R. *J. Am. Chem. Soc.* **2006**, *128*, 192.
- (152) Bestvater, F.; Spiess, E.; Stobrawa, G.; Hacker, M.; Feurer, T.; Porwol, T.; Berchner-Pfannschmidt, U.; Wotzlaw, C.; Acker, H. *J. Microscopy* **2002**, *208*, 108-15.
- (153) Makarov, N. S. *Ultrafast Two-Photon Absorption in Organic Molecules: Quantitative Spectroscopy and Applications*, **2010**, PhD Thesis
- (154) Makarov, N. S.; Drobizhev, M.; Rebane, A. *Opt. Express* **2008**, *16*, 4029-47.
- (155) He, G. S.; Prasad, P. N. *IEEE J. Quantum Elect.* **2010**, *46*, 931-936.
- (156) Bouit, P.A.; Kamada, K.; Feneyrou, P.; Berginc, G.; Toupet, L.; Maury, O.; Andraud, C. *Adv. Mater.* **2009**, *21*, 1151-1154.
- (157) Meallier, P. *Dyes and Pigments* **1999**, *40*, 95-98.
- (158) Wang, D.C.; He, C.; Fan, J.L.; Huang, W.; Peng, X.J. *Acta Cryst.* **2007**, *63*, 2900.
- (159) Yu, Y.H.; Shen, Z.; Xu, H.Y.; Wang, Y.W.; Okujima, T.; Ono, N.; Li, Y.Z.; You, X.Z. *J. Mol. Struct.* **2007**, *827*, 130-136.
- (160) Zipfel, W. R.; Williams, R. M.; Webb, W. W. *Nat. Biotechnol.* **2003**, *21*, 1369-1377.
- (161) Helmchen, F.; Denk, W. *Nat. Methods* **2005**, *2*, 932-940.
- (162) Bergh, V.; Boens, N.; Schryver, F. C.; Ameloot, M.; Steels, P.; Gallay, J.; Vincent, M.; Kowalczyk, A. *Biophys. J.* **1995**, *68*, 1110-9.
- (163) Stryer, L. *Biochemistry*, ed. W. H. Freeman, New York, **1988**.
- (164) Stevens, B.; Perez, S. R.; Ors, J. A. *J. Am. Chem. Soc.* **1974**, *96*, 6846.
- (165) Bouas-laurent, H.; Castellan, A.; Desvergne, J.P. *Pure Appl. Chem.* **1980**, *52*, 2633.
- (166) Zimmermann, C. *J. Photochem. and Photobiol.* **1999**, *125*, 47-56.
- (167) Hamanoue, K.; Hirayama, S.; Nakayama, T.; Teranishi, H. *J. Phys. Chem.* **1980**, *84*, 2074-2078.
- (168) Dvornikov, A. S.; Bouas-Laurent, H.; Desvergne, J.-P.; Rentzepis, P. M. *J. Mater. Chem.* **1999**, *9*, 1081-1084.

- (169) Martin, M. M.; Plaza, P.; Changuenet-barret, P. *J. Phys. Chem.* **2002**, 2351-2358.
- (170) Worrall, D. R.; Williams, S. L.; Wilkinson, F.; Crossley, J. E.; Bouas-Laurent, H.; Desvergne, J.P. *J. Phys. Chem.* **1999**, 103, 9255-9261.
- (171) de Silva P.A.; McClenaghan, N. D. *J. Am. Chem. Soc.* **2000**, 122, 3965-3966.
- (172) Shida, T. *Electronic absorption spectra of radical ions*; Elsevier Amsterdam; **1988**.
- (173) Katoh, R.; Katoh, E.; Nakashima, N.; Yuuki, M.; Kotani, M. *J. Phys. Chem.* **1997**, 5639, 7725.
- (174) Wasielewski, M. R.; Yang, C. N. *J. Am. Chem. Soc.* **1990**, 112, 2823.
- (175) Shinkai, S.; Nakaji, T.; Nishida, Y.; Ogawa, T.; Manabe, O. *J. Am. Chem. Soc.* **1980**, 102, 5860.
- (176) Shinkai, S.; Ogawa, T.; Kusano, Y.; Manabe, O. *Chem. Lett.* **1980**, 283-286.
- (177) Shinkai, S.; Minami, T.; Kusano, Y.; Manabe, O. *J. Am. Chem. Soc.* **1983**, 105, 1851 – 1856.
- (178) Lednev, I. *Chem. Phys. Lett.* **1998**, 290, 68-74.
- (179) Ohshima, A.; Momotake, A.; Arai, T. *Adv. Mater.* **2005**, 6, 633-643.
- (180) Schmidt, B.; Sobotta, C.; Malkmus, S.; Laimgruber, S.; Braun, M.; Zinth, W.; Gilch, P. *J. Phys. Chem.* **2004**, 108, 4399-4404.
- (181) Cattaneo, P.; Persico, M. *ChemPhysChem* **1999**, 4739-4743.
- (182) Hagiri, M.; Ichinose, N.; Zhao, C.; Horiuchi, H.; Hiratsuka, H.; Nakayama, T. *Chem. Phys. Lett.* **2004**, 391, 297-301.
- (183) Fujino, T.; Arzhantsev, S. Y.; Tahara, T. *J. Phys. Chem.* **2001**, 105, 8123-8129.
- (184) Satzger, H.; Root, C.; Braun, M. *J. Phys. Chem.* **2004**, 108, 6265-6271.
- (185) Tahara, R.; Morozumi, T.; Nakamura, H.; Shimomura, M. *J. Phys. Chem.* **1997**, 101, 7736.
- (186) Janus, K.; Sworakowski, J. *J. Phys. Chem.* **2005**, 109, 93-101.